A New Limit on the Electron Electric Dipole Moment: Beam Production, Data Interpretation, and Systematics

A dissertation presented

by

Nicholas Richard Hutzler

to

The Department of Physics

in partial fulfillment of the requirements

for the degree of

Doctor of Philosophy

in the subject of

Physics

Harvard University

Cambridge, Massachusetts

February 2014

Thesis advisor   Author

John M. Doyle   **Nicholas Richard Hutzler**

A New Limit on the Electron Electric Dipole Moment: Beam Production, Data Interpretation, and Systematics

Abstract

The charge distribution associated with an electron has surprising implications for a number of outstanding mysteries in physics. Why is the universe made out of matter versus anti-matter, instead of both equally? What new particles and interactions lie beyond the current reach of accelerators like the LHC? Models which propose answers to these questions, such as Supersymmetry, tend to predict a small, yet potentially measurable, asymmetric interaction between an electron and an electric field, characterized by an electric dipole moment (EDM). Despite over six decades of experimental searching, no EDM of any fundamental particle has ever been measured; however, these experiments continue to provide some of the most stringent limits on new physics. Here, we present the results of a new search for the electron EDM, $d_e = (-2.1 \pm 3.7_{\mathrm{stat}} \pm 2.5_{\mathrm{syst}}) \times 10^{-29}$ e cm, which represents an order of magnitude improvement in sensitivity from the previous best limit. Since our measurement is consistent with zero, we present the upper limit of $|d_e| < 8.7 \times 10^{-29}$ e cm with 90 percent confidence.

Contents

Contents

Citations to Previously Published Work

Portions of the research described in this dissertation were published in the following references:

1. The ACME Collaboration: Jacob Baron, Wesley C Campbell, D Demille, John M Doyle, Gerald Gabrielse, Yulia V Gurevich, Paul W Hess, Nicholas R Hutzler, Emil Kirilov, Ivan Kozyryev, Brendon R O'Leary, Cristian D Panda, Maxwell F Parsons, Elizabeth S Petrik, Benjamin Spaun, Amar C Vutha, and Adam D West. Order of Magnitude Smaller Limit on the Electric Dipole Moment of the Electron. *Science*, 343(6168):269-272, January 2014.

2. The ACME Collaboration: Wesley C Campbell, Cheong Chan, David Demille, John M Doyle, Gerald Gabrielse, Yulia V Gurevich, Paul W Hess, Nicholas R Hutzler, Emil Kirilov, Brendon R O'Leary, Elizabeth S Petrik, Benjamin Spaun, and Amar C Vutha. Advanced cold molecule electron EDM. *EPJ Web of Conferences* 57:02004, August 2013.

3. Emil Kirilov, Wesley C Campbell, John M Doyle, Gerald Gabrielse, Yulia V Gurevich, Paul W Hess, Nicholse R Hutzler, Brendon R O'Leary, Elizabeth Petrik, Benjamin Spaun, Amar C Vutha, and David DeMille. Shot-noise-limited spin measurements in a pulsed molecular beam. *Physical Review A*, 88(1):013844, July 2013.

4. Nicholas R Hutzler, Hsin-I Lu, and John M Doyle. The buffer gas beam: an intense, cold, and slow source for atoms and molecules. *Chemical Reviews*, 112(9):4803-27, September 2012.

5. Nicholas R Hutzler, Maxwell F Parsons, Yulia V Gurevich, Paul W Hess, Elizabeth Petrik, Ben Spaun, Amar C Vutha, David DeMille, Gerald Gabrielse, and John M Doyle. A cryogenic beam of refractory, chemically reactive molecules with expansion cooling. *Physical chemistry chemical physics : PCCP*, 13(42):18976-85, November 2011.

6. Amar C Vutha, Benjamin Spaun, Yulia V Gurevich, Nicholas R Hutzler, Emil Kirilov, John M Doyle, Gerald Gabrielse, and David DeMille. Magnetic and electric dipole moments of the $H^3\Delta_1$ state in ThO. *Physical Review A*, 84(3):034502, September 2011.

7. Amar C Vutha, Wesley C Campbell, Yulia V Gurevich, Nicholas R Hutzler, Maxwell Parsons, David Patterson, Elizabeth Petrik, Benjamin Spaun, John M Doyle, Gerald Gabrielse, and David DeMille. Search for the electric dipole moment of the electron with thorium monoxide. *Journal of Physics B: Atomic, Molecular and Optical Physics*, 43(7):74007, April 2010.

Acknowledgments

This research would not have happened without my amazing co-workers, collaborators, and adviser. I would like to especially thank Amar Vutha, who taught me which way to turn the screws when I first started, and John Doyle, for always spending time to help me figure things out. Thanks also to Dave DeMille and Jerry Gabrielse, from whom I was lucky to learn a great deal.

Thanks to the entire Doyle group, past and present, for of all the advice, laughs, and good times. Special thanks to Dave Patterson and the laser cooling experiment for adopting me before and after my time with ACME.

Thanks to the Physics incoming class of 2007 for making graduate school fun, and to the staff for always being there to help out.

Thanks to my family and friends, especially Mary, for distracting me from my research.

For Mary.

Chapter 1

Electric Dipole Moments

1.1 Introduction

A dipole moment $\vec{d}$ in an electric field $\vec{\mathcal{E}}$ has an interaction energy $U = -\vec{d} \cdot \vec{\mathcal{E}}$. Searches for electric dipole moments (EDMs) of fundamental particles are typically carried out by looking for energy shifts of a particle in an electric field, and in particular a shift which reverses when the electric field is reversed. A very powerful technique to search for the EDM of the electron is to search for interactions of the EDM with the electric field inside an atom or molecule, which can be around one million times larger than any static field which could be created in the laboratory[140, 209]. The best limits on the electron EDM come from heavy atoms[202] and molecules[126, 16], where the heavy, highly-charged nucleus creates a large and relativistically enhanced[209, 57] effective electric field $\mathcal{E}_{\text{eff}}$ experienced by the valence electrons. The previous best limit on the electron EDM, $|d_{\text{e}}| < 10.6 \times 10^{-28}$ e cm, was obtained from a precision spin precession measurement in a beam of polar YbF molecules[126, 135].

Molecules present a number of powerful advantages for electron EDM searches. First, they can be aligned (or polarized) in modest laboratory electric fields, which leads to around a thousand-fold improvement in sensitivity-per-molecule versus atom-based experiments. Second, their strong alignment in the laboratory electric field suppresses the two effects which ultimately limited the best atom-based electron EDM measurement[202]: motional electric fields, and geometric phases. The YbF experiment[126] found that these effects were indeed suppressed to negligible levels, therefore proving that polar molecules are an effective system for electron EDM searches. The ThO molecule has a number of additional advantages, including resistance to stray magnetic fields[243, 244], and the ability to reverse the internal electric field of the molecule without reversing external fields, as first demonstrated with the PbO EDM experiment[29, 77].

1.1.1 EDMs in the Standard Model, and Beyond

The electron EDM is intimately related to two major open questions in physics:

1. Why is the universe made out of matter instead of anti-matter, or equal parts of both?

2. What new particles and forces lie outside the reach of particle accelerators and dark matter detectors?

Let us first discuss the problem of the matter/anti-matter asymmetry, or "baryon asymmetry of the universe" (BAU)[207]. We know that all observable large-scale structures in the universe are made from matter (as opposed to anti-matter) since

matter and anti-matter annihilate when they come in contact. A universe containing large amounts of both matter and anti-matter would be filled with the gamma radiation from these annihilations, which we simply do not observe. How, then, did the universe "decide" to choose one over the other? Were unequal amounts created in the Big Bang? Are there processes which proceed with different rates for matter and anti-matter? In either case, the laws of nature have some asymmetry between matter and anti-matter, and the physical origin of this asymmetry is not known.

There are three "fundamental" symmetries of Nature: charge inversion (C), parity inversion (P), and time reversal (T). Each of these symmetries may be regarded as a mathematical operation on a set of physical laws, with the following effects:

C: Invert the sign of electric charges ($+ \leftrightarrow -$), and invert matter $\leftrightarrow$ anti-matter.

P: Invert the sign of all spatial coordinates $x \to -x$, $y \to -y$, $z \to -z$.

T: Invert time $t \to -t$, or equivalently reverse momenta, both linear ($\vec{p} \to -\vec{p}$) and angular ($\vec{L} \to -\vec{L}$).

All classical physics, as well as non-relativistic quantum mechanics, is completely symmetric under each of these operations (which is why they are called symmetries.) If all matter/anti-matter in the universe were swapped, or if the universe was mirrored about its origin, or if all momenta were instantaneously reversed, classical physics predicts that everything in the universe would proceed in a manner completely described by the same equations that we use to describe our universe.[1]

---

[1] T-reversal seems the most odd since the universe seems to have an "arrow of time." However, this does not violate T-symmetry: systems tend to their most probable state, but they are not forbidden from occupying a less-ordered state. See the book by Sachs[206] for a discussion of entropy in the context of T-symmetry.

These three symmetries used to be regarded as true symmetries observed by Nature; however, it turns out that *none* of these are true symmetries of Nature. The first to be overturned was P, when Chien-Shiung Wu found that radioactive nuclei tend to emit their decay products along the direction of their nuclear spin[252]. To see why this fact implies P violation, consider a ^{60}Co nucleus with its nuclear spin aligned along the z axis. Wu found that the electron (or β particle) emitted by the nucleus when it undergoes a radioactive β-decay is preferentially emitted in a particular direction along the z axis. Now, consider the mirror-image of the nucleus[2], as shown in Figure 1.1. The mirror-image particle is spinning in the same direction, but now the decay products are emitted in the opposite direction with respect to the nuclear spin. However, the mirror-image particle *does not exist*, since Wu found that real ^{60}Co nuclei do not emit their decay products in this way. This is why Wu's finding proved that P is not a true symmetry of nature.

Several other symmetry violations were observed later[109, 156], including C, CP, and T. One symmetry which so far still stands is CPT symmetry[109, 140], that is, under the combined inversion of charges, parity, and time reversal, all known physics is completely symmetric. CPT symmetry is much harder to break, since it is a fairly general feature of many quantum field theories. For the sake of simplicity, we shall assume that CPT is a good symmetry. Under this assumption CP and T are equivalent.

Similar to how ^{60}Co decays violate P symmetry, a fundamental particle (such as an electron) which possesses both a spin $\vec{S}$ and an EDM $\vec{d}$ would violate both P and

---

[2]In three spatial dimensions, a reflection about one axis is equivalent to a reflection all three axes plus a few rotations.
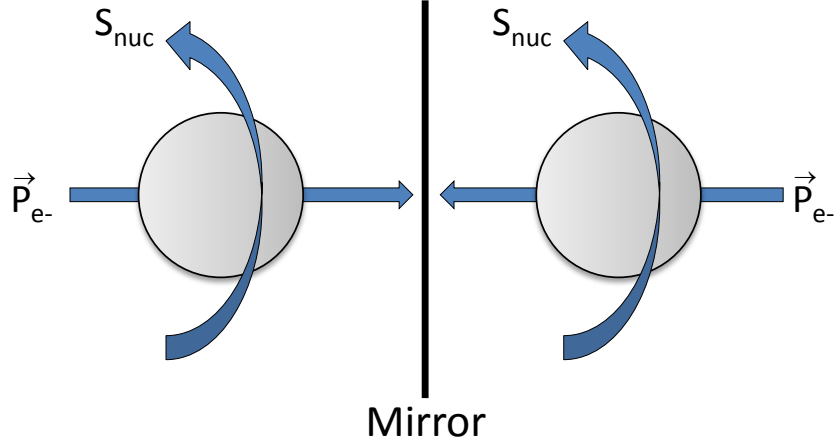
Figure 1.1: Beta decay of ^{60}Co[252]. The drawing on the left indicates what happens for a real nucleus: the electron momenta (P_{e^-}) are emitted in the direction opposite to the nuclear spin (S_{nuc}) direction. The drawing on the right indicates the mirror-image (P-reversed) process, which does not occur in Nature.

T symmetry. To see why, consider the situation shown in Figure 1.2. Since an EDM is a vector quantity, let us assume that the EDM and spin are aligned in the electron, $\vec{S}\|\vec{d}$. The dipole relates to a spatial charge distribution, and will therefore reverse under P but not T. The spin is an angular momentum, and will therefore reverse under T but not P. Therefore, applying either P or T will yield an electron where the spin and EDM are anti-aligned, $\vec{S}\|(-\vec{d})$. We know from the spectra of atoms that all electrons are indistinguishable, so it cannot be the case that some electrons have $\vec{S}\|\vec{d}$ and others have $\vec{S}\|(-\vec{d})$, since these particles could be distinguished by their energy shifts in a combined electric and magnetic field. We also know from atomic spectra that the spin degree of freedom (up, down) is the *only* internal degree of freedom for an electron; this is why we can put only two electrons in an atomic *s* orbital.

One might wonder why there is any motivation to find new symmetry violations, since they are all known to be violated anyway. The answer relates to one of our initial
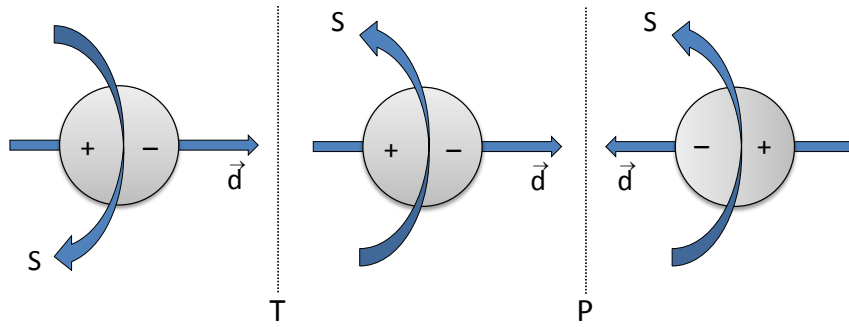
Figure 1.2: P and T applied to a fundamental particle with both spin S and electric dipole moment d. We can see that application of either P or T results in a different relative orientation of S and d, and therefore a different particle.

question of explaining the matter/anti-matter asymmetry (BAU). Andrei Sakharov determined three requirements for generating a BAU[207], one of which is CP violation. CP violation has already been observed in the kaon system, and is a very well understood part of the Standard Model (SM) of particle physics. However, the amount of CP violation which comes from the SM is too small to observe the BAU[73], and no other sources of CP violation are known. Observation of a permanent electron EDM would be a window into this unknown physics.

In the SM, CP violation comes from the Cabibbo-Kobayashi-Maskawa ("CKM") mechanism in the quark sector[23]. When a quark interacts with a weak force boson, it can turn into another quark and acquire a non-trivial ($\neq \pm 1$) complex phase, as shown in Figure 1.3. This phase is completely non-trivial; that is, it cannot be eliminated by some basis change, and is therefore physical. To see intuitively why a non-trivial phase corresponds to T-violation, notice that a Hamiltonian containing a non-trivial complex phase cannot be Hermitian, and therefore the time-evolution operator $\exp(-iHt/\hbar)$ is not unitary.
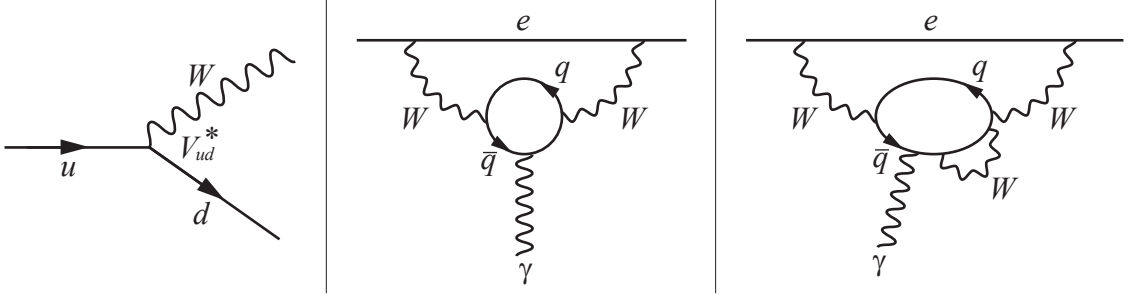
Figure 1.3: Some important Feynman diagrams for the electron EDM. Left: the CKM mechanism results in non-trivial phases (contained in the quantity V_{ud}^*) at vertices where two quarks and a W boson interact. Center: This diagram modifies the electron interacting with an external photon and therefore could possibly cause an interaction identical to an EDM. However, this diagram is left-right symmetric and therefore T-invariant, and hence could not possibly cause an EDM. Right: This single diagram does cause an electron EDM of magnitude $\approx 10^{-38}$ e cm[122], however the sum of all third-order diagrams cancel[194].

Since the only known CP violating physics in the SM resides in the quark sector, the SM electron EDM prediction is suppressed to very low values. In order for some SM interaction (Feynman diagram) to create an electron EDM, it must violate CP and therefore requires a quark-weak vertex, like the one shown in the left pane of Figure 1.3. This rules out one-loop diagrams, since quarks do not interact directly with electrons. We can draw a two-loop diagram (see Figure 1.3, center pane), but this diagram is not T violating; time goes from left to right, so the time-reversed diagram is identical. We can draw single three-loop diagrams (Figure 1.3, right pane) which give a non-zero electron EDM, and Hoogeveen[122] calculated that these diagrams give rise to $|d_e| \approx 10^{-38}$ e cm. Later, Pospelov and Khriplovich[194] found that all three-loop diagrams cancel, and nobody has yet bothered to calculate the four-loop diagrams. This means that the SM prediction for d_e is not known, though based on Hoogeveen's calculation a commonly quoted result is $|d_{e,SM}| \lesssim 10^{-38}$ e cm.

7

Because the SM does not have enough CP violation to explain the BAU, there must be physics beyond the SM which violates CP. Fortunately, many models of new physics introduce new particles and interactions, many of which could violate CP and cause "large" electron EDMs. One very exciting candidate is Supersymmetry (SUSY), which was introduced to stabilize the Higgs mass to radiative corrections but might also have applications to the BAU, dark matter, and a number of other open questions in physics. To understand how a new particle could cause a large electron EDM, consider a new particle X with mass m_X which couples to the electron with a CP violating phase ϕ. Analogous to how the similar interaction with a photon causes a magnetic moment of $(\alpha/\pi)\mu_B$, we can make a dimensional argument[55] to estimate that

$$cd_e \sin\phi m_X^2 \sim (\alpha/\pi)\mu_B m_e^2 \quad \Rightarrow \quad d_e \sim \sin\phi \frac{m_e^2}{m_X^2}\frac{\alpha}{\pi}\frac{\mu_B}{c} \approx (10^{-24} \text{ e cm}) \times \frac{m_H^2}{m_X^2}\sin\phi,$$

(1.1)

where $m_H = 126$ GeV is the Higgs mass. Our upper limit of $\approx 10^{-28}$ e cm therefore puts some very strict limitations on CP-violating physics due to new particles; if we make the natural assumption that $\sin\phi \approx 1$, then we are probing energy scales around one hundred times larger than the Higgs mass! For more general discussions, the reader is referred to the many reviews of the importance of EDMs in new physics[4, 17, 24, 87, 89, 169, 171, 195, 54, 55].

1.1.2 EDMs in Atoms and Molecules

A possible experimental signature of a permanent electron EDM, d_e, is an energy shift E_{EDM} of one or more unpaired valence electrons interacting with the effective,

internal electric field $\vec{\mathcal{E}}_{\text{eff}}$ of an atom or molecule:

$$E_{\text{EDM}} = -\vec{d}_{\text{e}} \cdot \vec{\mathcal{E}}_{\text{eff}}. \tag{1.2}$$

At first glace, there appear to be a few problems with this approach. First, in the absence of applied fields the Hamiltonian of the valence electrons is rotationally symmetric, and therefore $\langle\vec{\mathcal{E}}_{\text{eff}}\rangle = 0$ since an average electric field is a vector quantity which must point in a specific direction. This difficulty is overcome by polarizing the atom or molecule in an external electric field $\vec{\mathcal{E}}_{\text{lab}}$, which breaks the symmetry of the Hamiltonian and eigenstate wavefunctions, and allows $\langle\mathcal{E}_{\text{eff}}\rangle \propto P$, where $0 \leq P < 1$ is the polarization[55]. As we shall now see, polarizing an atom or molecule requires opposite-parity states with a small energy difference.

An atomic or molecular state can only have an energy shift in an electric field if the state does not have well-defined parity. To see why this is the case, consider an atomic state $|\psi\rangle$ of well defined parity, that is, $\Pi\,|\psi\rangle = \pm\,|\psi\rangle$, where Π is the parity operator which inverts spatial coordinates, $\Pi\,|\vec{r}\rangle = |-\vec{r}\rangle$. Since an electric dipole $\vec{d}$ is a parity-odd quantity, $\Pi^{\dagger}\vec{d}\Pi = -\vec{d}$, there can be no linear Stark shift in this state since

$$\langle\psi|\vec{d}\cdot\vec{\mathcal{E}}_{\text{lab}}|\psi\rangle = \langle\psi|(\pm)\vec{d}(\pm)|\psi\rangle \cdot \vec{\mathcal{E}}_{\text{lab}} \tag{1.3}$$

$$= \langle\psi|\Pi^{\dagger}\vec{d}\Pi|\psi\rangle \cdot \vec{\mathcal{E}}_{\text{lab}} \tag{1.4}$$

$$= \langle\psi|-\vec{d}|\psi\rangle \cdot \vec{\mathcal{E}}_{\text{lab}} \tag{1.5}$$

$$\langle\psi|\vec{d}\cdot\vec{\mathcal{E}}_{\text{lab}}|\psi\rangle = -\langle\psi|\vec{d}\cdot\vec{\mathcal{E}}_{\text{lab}}|\psi\rangle \tag{1.6}$$

$$\Rightarrow \langle\psi|\vec{d}\cdot\vec{\mathcal{E}}_{\text{lab}}|\psi\rangle = 0. \tag{1.7}$$

Such a state can, of course, have a quadratic Stark shift, provided that there is some state of opposite parity $|\psi'\rangle$ such that $\langle\psi'|\vec{d}\cdot\vec{\mathcal{E}}_{\text{lab}}|\psi\rangle \neq 0$. If the energy spacing between two states of opposite parity $|\psi_\pm\rangle$ is ΔE, then the perturbed eigenstate will be

$$|\psi(\mathcal{E}_{\text{lab}})\rangle \approx |\psi(0)\rangle + \frac{\langle\psi'|\vec{d}\cdot\vec{\mathcal{E}}|\psi\rangle}{\Delta E}|\psi'(0)\rangle. \tag{1.8}$$

The admixture of the opposite-parity state $|\psi'\rangle$ into $|\psi\rangle$ is approximately the polarization of the state $|\psi\rangle$,

$$P \approx \frac{\langle\psi'|\vec{d}\cdot\vec{\mathcal{E}}|\psi\rangle}{\Delta E}, \tag{1.9}$$

in the limit where $P \ll 1$. If we make the approximation that the dipole matrix element is approximately an atomic unit $\langle\psi'|\vec{d}\cdot\vec{\mathcal{E}}|\psi\rangle \approx ea_0 \approx h\times 1 \text{ GHz}/(\text{kV/cm})$, we can see that $P \approx 1 \text{ GHz} \times\mathcal{E}_{\text{lab}}[\text{kV/cm}]/(\Delta E \times h)$.

In atoms, polarization is achieved by mixing electronic states of opposite parity which are typically spaced by $\Delta E_{electronic} \gtrsim h \times 100$ THz. This means that the polarization of atoms is typically $P \lesssim 10^{-3} \times [\mathcal{E}_{\text{lab}}/(100 \text{ kV/cm})]$, so achieving $P > 10^{-3}$ is difficult. Heteronuclear diatomic molecules have rotational states of opposite parity which (for oxides and fluorides, common choices for EDM experiments) are typically spaced by $\Delta E_{rotational} \lesssim 100$ GHz, so achieving order-unity polarization in the lab frame is possible with fields of $\lesssim 100$ kV/cm. The result is that molecules are typically 10^3 times more sensitive to EDMs than atoms. As we will see later on, certain molecules (such as ThO[244]) can be fully polarized in laboratory fields of < 10 V/cm.

The second apparent problem with using atoms or molecules to measure EDMs is less obvious, and was noticed by Schiff in 1963[213]. Since neutral atoms or molecules

are not accelerated in a uniform laboratory electric field, the average electrostatic force on every particle must be zero, $\langle \vec{F}_{el} \rangle = 0$. If the electrons experience an average electric field $\langle \vec{\mathcal{E}}_{\text{int}} \rangle$, then they will experience a force $\langle \vec{F}_{el} \rangle = -e \langle \vec{\mathcal{E}}_{\text{int}} \rangle = 0$ and therefore $\langle \vec{\mathcal{E}}_{\text{int}} \rangle = 0$. However, this argument fails when relativity is taken into account[209]. The intuitive reason how Schiff's Theorem is evaded is that the electron EDM will undergo Lorentz contraction due to its non-zero velocity, and that this contraction can be large near a heavy nucleus[57]. Therefore, while $\langle \vec{\mathcal{E}}_{\text{int}} \rangle = 0$ may be strictly true, $\langle \vec{d}_e \cdot \vec{\mathcal{E}}_{\text{int}} \rangle$ need not be zero due to the spatial dependence of d_e as the electron orbits the nucleus. We define the effective electric field $\mathcal{E}_{\text{eff}}$ by $\langle \vec{d}_e \cdot \vec{\mathcal{E}}_{\text{int}} \rangle = d_e \mathcal{E}_{\text{eff}}$.

Sandars[209] found that not only is the effective electric field non-zero, is actually *enhanced* due to these relativistic effects. The electron will experience an effective electric field which is related to the lab field by the enhancement factor $R = \mathcal{E}_{\text{eff}} / \mathcal{E}_{\text{lab}}$, which can be several hundred (e.g. the Thallium atom has $R = -573(20)$[193, 202]). For molecules, the effective electric field $\mathcal{E}_{\text{eff}}$ is more relevant than the enhancement factor R, since $\mathcal{E}_{\text{eff}} \propto P$ is no longer proportional to $\mathcal{E}_{\text{lab}}$ once the polarization is order unity. The effective electric field scales as the cube of the atomic number Z^3 (due to the relativistic nature of the effect), which is why heavy atoms are used in electron EDM searches[140]. Since the effect only occurs near the heavy nucleus, atoms or molecules must have core-penetrating electron wavefunctions (valence electrons typically in $s-$shells) to exhibit a large EDM shift.

The shot noise limit for the determination of a spin precession frequency (see [140] and Section 4.4.1) sets the best possible experimental electron EDM sensitivity to be

$$\delta d_e = \frac{\hbar}{2\mathcal{E}_{\text{eff}} \tau \sqrt{N}}, \tag{1.10}$$

where $\mathcal{E}_{\text{eff}}$ is effective electric field experienced by the electron, N is the total number of measurements, and τ is the amount of time the electrons were allowed to precess before being measured. We shall see that the ThO molecule offers a large $\mathcal{E}_{\text{eff}}$, and buffer gas beam technology[167, 46, 129] offers large count rates and long interrogation times.

1.2 Thorium monoxide electron EDM

The thorium monoxide (ThO) molecule possesses a metastable electronic state $H^3\Delta_1$ in which we perform the electron EDM measurement. The H state is separated from the ground $X^1\Sigma_1^+$ state by ≈ 5300 cm^{-1}[83], and has a radiative decay lifetime of ≈ 1.8 ms[243]. ThO is a Hund's Case (c) molecule[36], though both states H and X are well described in the Hund's case (a) basis[188]. The ThO H state combines a number of scientific and technical advantages, some of which we will list here.

Large effective electric field. The effective electric field in ThO is 84 GV/cm[224], with an estimated error of 15%. This field is over 6 times as large as the effective electric field in the YbF experiment[126] (which is not fully polarized), and over 1000 times larger than the $\mathcal{E}_{\text{eff}}$ achieved in the Tl experiment [202]. This larger internal effective electric field leads to larger energy shifts due an EDM, and therefore better experimental sensitivity.

Small magnetic moment. The magnetic moment of a $^3\Delta_1$ molecular state is very small due to near-perfect cancellation of the spin and orbital magnetic moments (see [228, 117, 36, 244, 247, 142], and Section 2.1.2). The magnetic moment of the ThO $H, J = 1$ state is $-\mu_B \times 0.00440(5)$, where μ_B is the Bohr Magneton[244]. This small

magnetic moment makes the measurement very insensitive to magnetic field offsets, imperfections, and noise, as will be discussed in Section 5.2.

Large polarizability. One of the most significant advantages of the ThO molecule is the fact that it has a very large polarizability, which has a number of advantages[68]. In particular, the two systematic effects which limited the best atomic experiment[202] were related to relativistic (motional) magnetic fields, and geometric phases. The large stark shift in molecules suppresses these effects, as will be discussed in Section 5.2.

Furthermore, ThO can be completely polarized in modest laboratory fields[244] (~ 10 V/cm), thereby avoiding the technical challenges of high voltages. The ability to completely polarize ThO in a small lab electric field is in fact a general feature of molecular states with non-zero projection of electronic angular momentum on the internuclear axis ($\Lambda > 0$)[117]. In such molecular states, there are two opposite-parity sublevels called $\Lambda-$doublets (or $\Omega-$doublets for Hund's case (c) molecules) which are spaced by an amount much smaller than the rotational constant (≈ 360 kHz for ThO[79] and ≈ 10 MHz for PbO[166], compared to the rotational splitting of ≈ 40 GHz for both molecules). Complete polarization means that the effective electric field of the molecule is maximally aligned in the lab frame, and we can fully realize the large effective field of ThO. This also means that the effective field (and therefore expected EDM shift) is independent of the magnitude of the laboratory electric field, unlike partially polarized species. EDM experiments with fully polarized species can therefore operate at several different values of $|\mathcal{E}_{\text{lab}}|$ as a systematic check without sacrificing sensitivity. Complete polarization also allows spectroscopic reversal of the

molecule, as discussed in the next paragraph.

Spectroscopic reversal. When a molecule is completely polarized, the two states with the molecular dipole aligned and anti-aligned with the lab field can typically be spectroscopically resolved with modest laboratory electric fields[36]. These two states are commonly called the "Ω-doublet" states since, as discussed above, they arise from the mixing of Ω-doublets (see Section 2.4.2). These two states also have the effective electric field of the molecule aligned in opposite directions, meaning that the electron EDM interaction can be reversed simply by addressing the other Ω-doublet state. This is commonly called "spectroscopic reversal" since it reverses the electron EDM interaction without reversing any laboratory fields, and has very powerful systematic rejection abilities[67, 137, 29]. Since the molecular $g-$factors in the two Ω-doublet states are nearly equal[29] (see Section 6.3), the Ω-doublet reversal can be used to suppress magnetic field noise and offsets, as well as magnetic fields due to leakage currents. Geometric phases, another significant systematic effect in atomic systems[56, 202], are nearly equal and opposite in the different Ω-doublet states, which allows even further suppression[245] on top of that already provided by the large tensor Stark shift [126, 192]. Finally, the Ω-doublet reversal can be performed very quickly using acousto-optic modulators (much faster than switching even a small electric field), which reduces sensitivity to slow experimental drifts, for example from the molecular beam (see Section 4.3.5).

Simple spectroscopy. The spectrum of ThO has been widely studied, both experimentally and theoretically,[84, 85, 81, 33, 32, 78, 189, 246, 151, 250, 165, 105, 71, 82, 188, 79, 80, 248, 41, 83], since its first spectroscopic observation in 1951[150].

The spectrum is free of hyperfine or isotope structure. The term assignments and molecular constants were known sufficiently well so that laser spectroscopy could be performed with relative ease. Additionally, all required spectroscopy lasers are in the red or near IR where diode, fiber, and tapered amplifier laser technology can be used to create simple, stable, and robust laser systems.

High flux beam source. Due to some very unique chemistry of the Thorium-Oxygen system[136, 118, 101, 60, 20, 3, 2, 1], ThO is a chemically and thermodynamically favored species at high temperatures. This is perhaps one of the reasons why ThO can be created in laser ablation in relatively large numbers ($\approx 10^{13}$ molecules per ablation pulse[130]) compared to many similar chemically reactive molecules[129, 46]. Additionally, ThO_2 is a nuclear material, and as such its material properties have been studied extensively, including a method for creating dense, sintered targets[11] that are excellent for laser ablation[130]. By combining these dense targets with the stability and robustness of a neon cooled buffer gas beam source[130], the beam source can be operated with $\gtrsim 90\%$ duty cycle for several months before the apparatus must be opened and the ablation targets replaced.

Chapter 2

Molecules

In this chapter we will calculate a number of important features present in the spectra of diatomic molecules. The first section will present a brief overview of the important features in the spectrum of the H state in ThO, in particular the interaction with external fields. The following sections will go into details about how to derive these results in a general setting.

2.1 Summary: Structure of the $^3\Delta_1$ EDM State

In this section we will discuss the level structure of the ThO H state. The H state is well described in the Hund's case (a) basis[36] as a $^3\Delta_1$ state, and it therefore has total electron spin $S = 1$, projection of total electronic angular momentum $\vec{L}$ on the internuclear axis $\hat{n}$ of $|\Lambda| = |\vec{L}\cdot\hat{n}| = 2$, and spin projection $|\Sigma| = |\vec{S}\cdot\hat{n}| = 1$. We choose the internuclear axis to point from the negative (O) to the positive (Th) nucleus in the polar molecule, so that the molecular dipole is aligned along $\hat{n}$ (be aware that the

opposite convention is common). The angular momentum projections satisfy $\Lambda + \Sigma = \Omega$, so $\Omega = \pm 1$. We will write the most general eigenstates as $|H; \Lambda, S, \Sigma; J, M, \Omega\rangle$[36], where J is the total angular momentum (electronic plus molecule nuclear rotation), and M is the projection of J on the laboratory Z_{lab} axis. We will typically leave out the Λ, S, Σ part of the wavefunction and use the basis $|H; J, M, \Omega\rangle$ the majority of the time. We will only consider the lowest vibrational ($v = 0$) level of the molecule. The EDM measurement is performed in the $J = 1$ level, though we shall see that the other rotational levels are important.

In zero external fields, the molecule Hamiltonian is invariant under inversion of the coordinate system so the good eigenstates are[36]

$$|H; J, M, \pm\rangle = \frac{1}{\sqrt{2}} \left(|H; J, M, +\Omega\rangle \pm |H; J, M, -\Omega\rangle \right).$$

In the absence of perturbations these two states are degenerate, though the degeneracy is lifted due to the rotation of the molecule[37, 157]. The splitting between the $|H; J, M, \pm\rangle$ is equal to $aJ(J + 1)$, where $a = h \times 181(1)$ kHz for the ThO H state (see Ref. [84] and Section D.3). The splitting in the $J = 1$ state is therefore around 360 kHz.

In a magnetic field $\mathcal{B}$ and electric field $\mathcal{E}$ (both along Z_{lab}), the Hamiltonian in the linear Stark (fully polarized) regime is given by

$$H = -Mg(J)\mu_{\text{B}}\mathcal{B} - \eta(J)\tilde{\mathcal{N}}M\mu_{\text{B}}|\mathcal{E}|\mathcal{B} - \tilde{\mathcal{N}}d(J)|\mathcal{E}| - M\tilde{\mathcal{N}}\tilde{\mathcal{E}}\mathcal{E}_{\text{eff}}d_{\text{e}}. \qquad (2.1)$$

From left to right, these terms represent magnetic spin precession, electric field dependence of the magnetic g-factors, the DC Stark shift, and the electron EDM interacting with the effective internal electric field. Here $g(J)$ and $d(J)$ are the g-factor and electric dipole moment of the Jth rotational state (respectively), d_{e} is the

electron EDM, $\mathcal{E}_{\text{eff}}(1) = 84$ GV/cm[224] is the internal effective electric field, μ_{B} is the Bohr magneton, and $\mathcal{N} = \pm 1$ describes whether the molecule is aligned or anti-aligned with respect to the lab electric field (see Section 2.1.1). A tilde over a quantity indicates the sign (± 1) of a quantity which is reversed in the experiment, $\tilde{\mathcal{B}} = \text{sign}(\vec{B} \cdot \hat{z}), \tilde{\mathcal{E}} = \text{sign}(\vec{\mathcal{E}} \cdot \hat{z})$, and $\tilde{\mathcal{N}} = \mathcal{N}$ for consistency. We use the convention that a positive g-factor means that the projection of the angular momentum and magnetic moment are aligned.

2.1.1 Stark Shift

In the limit where the molecule is fully polarized, the opposite parity states $|H; J, M, \pm\rangle$ are fully mixed by the electric field and the good eigenstates are $|H; J, M, \pm\Omega\rangle$ $= \frac{1}{\sqrt{2}}|H; J, M, +\rangle \pm \frac{1}{\sqrt{2}}|H; J, M, -\rangle$. The Stark shift of the states is given by[36, 117]

$$\langle H; J, M, \Omega | \vec{D} \cdot \vec{\mathcal{E}}_{\text{lab}} | H; J, M, \Omega \rangle = \frac{M\Omega D_{\parallel} \mathcal{E}_{\text{lab}}}{J(J+1)} \tag{2.2}$$

$$= \frac{D_{\parallel} \mathcal{N} |\mathcal{E}_{\text{lab}}|}{J(J+1)} \tag{2.3}$$

$$= d(J)\mathcal{N}\mathcal{E}_{\text{lab}}, \tag{2.4}$$

where we have defined

$$\mathcal{N} = M\Omega\hat{\mathcal{E}}_{\text{lab}}, \tag{2.5}$$

$\hat{\mathcal{E}}_{\text{lab}} = \text{sign}(\vec{\mathcal{E}}_{\text{lab}} \cdot Z_{\text{lab}})$ is the sign of the lab electric field relative to the lab $z-$axis, $D_{\parallel} = 1.67(4)ea_0 = 2.14(5)$ MHz/(V/cm) is the molecule-frame electric dipole moment[244], and $d(J) = D_{\parallel}[J(J+1)]^{-1}$ is the dipole moment for the Jth rotational state. We will typically write $d(1) = d$. The Stark Hamiltonian is given by $H_{Stark} = -\vec{D} \cdot \vec{\mathcal{E}}_{\text{lab}}$, so states with $\mathcal{N} = +1$ (-1) are shifted down (up) in energy. We define the quantity $\mathcal{N}$
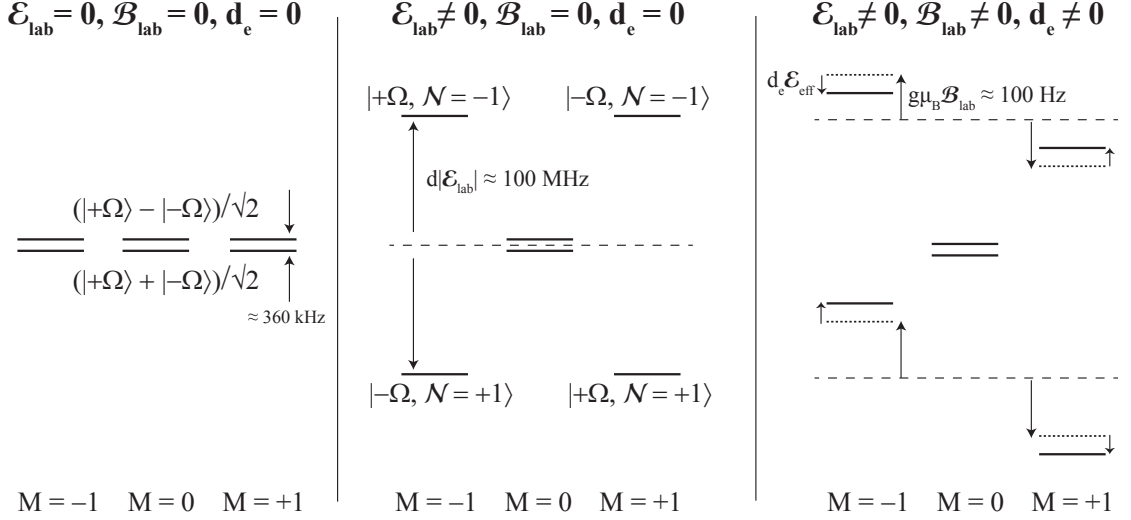
Figure 2.1: Level structure of the $H^3\Delta_1, J = 1$ state of ThO, and their shifts in external fields. The $J = 1$ state is split into three Zeeman sublevels $M = -1, 0, +1$, and each Zeeman sublevel is split in two by Ω-doubling. *Left:* In the absence of external electric and magnetic fields, the eigenstates are the Ω-doubled parity eigenstates $(|\Omega = +1\rangle \pm |\Omega = -1\rangle)/\sqrt{2}$, which are split by $\Delta_\Omega \approx 360$ kHz. The upper and lower states have well-defined, opposite parity. *Center:* In a large electric field $(d\mathcal{E}_{\text{lab}} \gg \Delta_\Omega)$, the molecule is fully polarized. The good quantum numbers for the $M = \pm 1$ Zeeman levels (the $M = 0$ levels only have a small perturbation from the $H, J = 2$ level) are now J, M, Ω. The sign of the Stark shift is proportional to $\mathcal{N} = M\Omega\hat{\mathcal{E}}_{\text{lab}}$. The molecule-fixed dipole moment of the ThO H state is $d = h \times 1.07(3)$ MHz/(V/cm)[244], and the magnitude of the Stark shift is ≈ 100 MHz under typical experimental conditions. *Right:* An external magnetic field and the electron EDM (interacting with the molecule effective electric field) shift the Zeeman sublevels in each $\mathcal{N}$ state proportional to $M\mathcal{B}_{\text{lab}}$ and $d_e\mathcal{E}_{\text{eff}}$, respectively. For the ThO $H, J = 1$ state, the magnetic moment is $g\mu_B = -0.00440(5)\mu_B \approx 6\text{Hz/mG}$[244, 142], and the magnitude of the Zeeman shift is ≈ 100 Hz under typical experimental conditions. Given the effective electric field $\mathcal{E}_{\text{eff}} = 84$ GV/cm of the ThO H state[224], $(10^{-28}$ e cm$) \times \mathcal{E}_{\text{eff}} \approx 2$ mHz. The Zeeman and EDM shifts are much smaller than the Stark shift, and do not change the eigenstates appreciably.

because one of the experimental switches we perform is to change which of these two states is addressed by the lasers (see Section 4.2).

We can also define the direction of the molecular internuclear axis in the lab frame $\hat{n}_{lab}$ using the above quantum numbers. Since the molecular dipole is aligned along the internuclear axis, we have $\text{sign}(\vec{D} \cdot \vec{\mathcal{E}}_{\text{lab}}) = \text{sign}(\vec{n} \cdot \vec{\mathcal{E}}_{\text{lab}}) = \hat{n}_{lab}\hat{\mathcal{E}}_{\text{lab}} = -\mathcal{N}$, so $\hat{n}_{lab} = -\mathcal{N}\hat{\mathcal{E}}_{\text{lab}}$.

2.1.2 Zeeman Shift

The experiment is performed with fully polarized molecules, so we only need to consider the Zeeman effect in the states $|H; \Lambda, S, \Sigma; J, M, \pm\Omega\rangle$, which for a Hund's case (a) molecule is given by[36, 117]

$$\langle H; J, M, \Omega|\vec{\mu} \cdot \vec{\mathcal{B}}_{\text{lab}}|H; J, M, \Omega\rangle = \frac{MG_\| \mu_{\text{B}}\mathcal{B}_{\text{lab}}}{J(J+1)} \tag{2.6}$$

$$= Mg(J)\mu_{\text{B}}\mathcal{B}_{\text{lab}}, \tag{2.7}$$

where μ_{B} is the Bohr Magneton, $G_\|\mu_{\text{B}}$ is the molecule-frame magnetic dipole moment, and $g(J)$ is the g-factor for the Jth rotational level. We will typically abbreviate $g(1) = g$. For the ThO H state, $g(1) = -0.00440(5)$[244, 142], and we find that the higher J levels do not scale as $[J(J+1)]^{-1}$ as expected, as discussed in Chapter 6.

The general expression for the molecule-frame magnetic $g-$factor is $G_\| = (g_S\Sigma + g_L\Lambda)\Omega$, i.e. a sum of the spin and orbital contributions from the electrons. If we enter $g_S = -2$ and $g_L = -1$ into the equation and use the values of $\Lambda = \pm2, \Sigma = \mp1, \Omega = \pm1$ for a $^3\Delta_1$ state, we find that $G_\| = 0$ exactly (see Figure 2.2). The cancellation is not perfect due to the fact that g_S is not exactly 2 even for a single electron[112],

and due to mixing of other electronic states with $g-$factors of order unity[188]. We will consider these effects in detail in Chapter 6.

Figure 2.2: Schematic representation of the g-factor suppression in a $^3\Delta_1$ state. As described in the text, this state has $\Lambda = +2$, $\Sigma = -1$, and $\Omega = +1$. The orbital part contributes a magnetic moment $\mu_L = g_L \Lambda \mu_B = -2\mu_B$ and the spin part contributes $\mu_S = g_S \Sigma \mu_B \approx +2\mu_B$. When combined, these magnetic moments nearly cancel.

2.1.3 $\mathcal{E}$-field dependence of g-factors

The first two terms in Eq. (2.1) are mathematically equivalent to a magnetic g-factor which depends on the molecule orientation $\mathcal{N}$ and electric field $\mathcal{E}$,

$$g(J, \mathcal{N}, \mathcal{E}) = g(J) + \eta(J)|\mathcal{E}|\mathcal{N}, \tag{2.8}$$

where η depends on the molecular state[29]. For the ThO H state, $\eta(1) = 0.79(1)$ nm/V, so for a typical field of $\mathcal{E} \approx 100$ V/cm, the g-factor is modified by $\approx 10^{-5}\mathcal{N} \approx 10^{-3}g(1)\mathcal{N} \approx 4 \times 10^{-5}\mathcal{N}$. This effect is considered in detail in Chapter 6.

2.1.4 EDM Shift

We use the convention that a positive $\mathcal{E}_{\text{eff}}$ points from the positive to the negative nucleus, which is the same convention used by the authors who calculated the internal field[224, 155]. ThO (and WC) has a positive $\mathcal{E}_{\text{eff}}$, meaning that it points *against* the internuclear axis (which points from the O to the Th in our convention), so write

$\vec{\mathcal{E}}_{\text{eff}} = -\mathcal{E}_{\text{eff}}\hat{n}$. The EDM energy shift is therefore

$$\Delta E_{EDM} = -\vec{d}_{\text{e}} \cdot \vec{\mathcal{E}}_{\text{eff}} = -(d_{\text{e}}\vec{S}) \cdot (-\mathcal{E}_{\text{eff}}\hat{n}) = +d_{\text{e}}\mathcal{E}_{\text{eff}}\Sigma = -d_{\text{e}}\mathcal{E}_{\text{eff}}\Omega = -M\mathcal{N}\hat{\mathcal{E}}_{\text{lab}}d_{\text{e}}\mathcal{E}_{\text{eff}},$$

$$(2.9)$$

where we used that $\Omega = -\Sigma$ in the ThO H state. Notice that $d_{\text{e}}\vec{S}$ appears in the formula instead of $(d_{\text{e}}\vec{S})/|S|$, since the length of S is included in the definition of $\mathcal{E}_{\text{eff}}$. In other words, $|\Delta E_{EDM}| = |d_{\text{e}}\mathcal{E}_{\text{eff}}|$ is always true by definition regardless of S.

2.2 Molecular Structure

Molecules have a number of internal degrees of freedom not available to atoms, which make them promising candidates for a large number of exciting applications such as precision measurement, quantum computation, and quantum simulation[48, 149]. In addition to excitations of the electrons (which are very similar in atoms), the nuclei in the molecule can rotate and vibrate. This gives rise to a large number of states, which we will briefly discuss below. For this entire thesis, we will restrict ourselves to heteronuclear diatomic molecules.

2.2.1 Electronic states

The valence electrons in a molecule can be electronically excited, very similar to electronic excitation in atoms. Radiative lifetimes, range of wavelengths, and selection rules are also very similar, and will be discussed in more detail later on. The electronic states in a molecule are characterized by their angular momenta, which are summarized by a term symbol. Atomic term symbols are written as $^{2S+1}L_J$,

where $S, L,$, and J are the spin, orbital, and total angular momenta of the electronic state, respectively. Molecular term symbols are written as $^{2S+1}\Lambda_\Omega$, where S is the total electron spin, $\Lambda = |\vec{L} \cdot \hat{n}|$ is the projection of the total electron orbital angular momentum $\vec{L}$ on the internuclear axis $\hat{n}$, and $\Omega = |\vec{J} \cdot \hat{n}|$ is the projection of the total electron angular momentum $\vec{J}$ on the internuclear axis. Atomic terms symbols use $S, P, D, F, \ldots$ to indicate $L = 0, 1, 2, 3, \ldots$, while molecular term symbols use $\Sigma, \Pi, \Delta, \Phi, \ldots$ to indicate $|\Lambda| = 0, 1, 2, 3, \ldots$. There is another quantum number $\Sigma = |\vec{S} \cdot \hat{n}|$, which satisfies the rule $\Sigma + \Lambda = \Omega$. This Σ should not be confused with the Σ appearing in the term symbol which indicates $\Lambda = 0$ (similar to the overuse of S in atomic term symbols).

Ω/Λ-Doubling

At first glance, states with opposite signs of Λ, Σ, and Ω might appear to be degenerate due to the parity invariance of the molecule (ignoring small P-violating effects[139]). However, these two states are in fact only nearly-degenerate, and lead to a very important feature of certain molecules called Ω- or Λ-doubling[1].

There is a simple, intuitive picture to understand why these two states are not degenerate. Consider the case $|\Omega| = 1$. The Ω eigenstates look like $e^{\pm i\Omega\phi}$, where ϕ is the axial angle about the internuclear axis[36]. Notice that these are not parity eigenstates, since they are neither even nor odd under a space inversion ($\phi \to -\phi$). The parity eigenstates are the even and odd combinations of these functions, $\sin(\Omega\phi)$ and $\cos(\Omega\phi)$, and are shown pictorially in Figure 2.3. Now, say that the molecule is

---

[1]These doublets are typically called Λ-doublets in case (a) molecules, and Ω-doublets in case (c) molecules since Λ is not a good quantum number in this case.
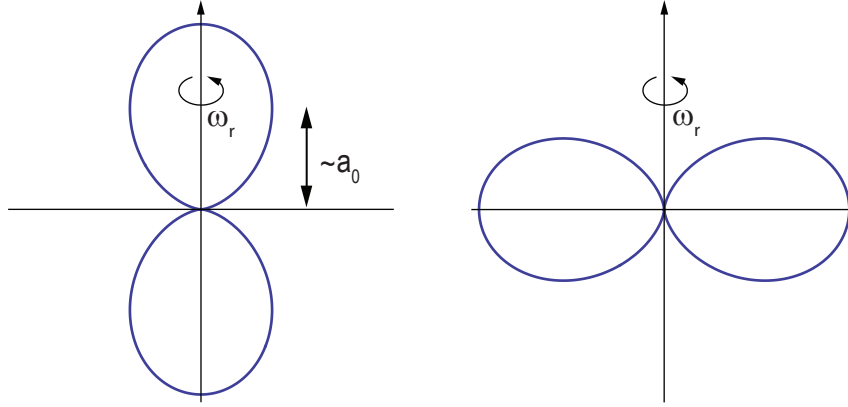
Figure 2.3: Intuitive understanding of Ω-doubling for the case of $|\Omega| = 1$. The wavefunctions shown are the parity eigenstates $\sin(\Omega\phi)$ and $\cos(\Omega\phi)$.

rotating with angular frequency ω_r about the indicated axis. The energies of these states differ by $\sim I_e\omega_r^2$, where $I_e \approx \mu_e a_0^2 \approx m_e a_0^2$ is the moment of inertia for the electron cloud and ω_r is the rotation frequency. The energy splitting is therefore

$$\Delta E_\Omega \approx I_e\omega_r^2 \approx m_e a_0^2 \left(\frac{2E_r}{\mu_n a_0^2}\right) \approx m_e a_0^2 \left(\frac{2BJ^2}{m_n a_0^2}\right) \approx \frac{m_e}{\mu_n}BJ^2, \qquad (2.10)$$

where μ_n is the reduced nuclear mass. For the ThO H state this corresponds to $\Delta E_\Omega \approx$ a few hundred KHz, which is very close to the actual spacing of 362(2) kHz in $J = 1$ (see Section D.3).

In reality, this effect is due to perturbative couplings between electronic states, as discussed later in this chapter. However, this simple explanation is very useful for building intuition about the physical origin of the splitting.

2.2.2 Rotation and vibration

The nuclei in a diatomic molecule are bound by a potential $V(R)$ which depends on the nuclear separation R. This potential typically supports a number of

bound states called vibrational levels, which correspond to motional excitations of the nuclei[117, 36]. The nuclei have some mean, ground-state separation R_e at the potential minimum, and for small perturbations about R_e the molecular potential can be approximated by a quadratic, harmonic oscillator potential. The vibrational energy levels can therefore be approximated by the levels of a simple harmonic oscillator, with the vth level having energy $E(v) = hc\omega_e(v + 1/2)$. The constant ω_e has units of wavenumbers (cm^{-1}) and depends on the molecular electronic state. Typical vibrational frequencies are in the range of $c\omega_e = 1 - 100$ THz. The level with $v = 0$ is called the ground vibrational state, and is the only state we will consider in this thesis.

The nuclei in a diatomic molecule can also rotate. If we make the approximation that the two nuclei constitute a rigid rotor, then the energy levels are given by the usual quantum mechanical rigid rotor levels[117, 36] $E(J) = hcB_eJ(J + 1)$, where J is the number of rotational quanta, and B_e has units of wavenumbers (cm^{-1}) and depends on the molecular electronic state. Typical rotational frequencies are $cB_e = 1 - 100$ GHz.

Real molecules are of course neither perfectly harmonic, nor are they rigid rotors. The energy levels of a rotating and vibrating molecule are typically expanded in a power series called the Dunham expansion[36],

$$E(v, J) = hc\sum_{k\ell} Y_{k,\ell}(v + 1/2)^k[J(J + 1)]^{\ell}. \tag{2.11}$$

In our notation, $Y_{1,0} = \omega_e$ and $Y_{0,1} = B_e$. The other terms are typically referred to by their traditional names ($Y_{2,0} = \omega_e x_e, Y_{0,2} = D_e$, etc.), but we will not go over these here. Take note that the signs of these terms sometimes differ based on convention.

2.2.3 Hunds' Cases

The quantum numbers discussed so far correspond to a particular choice of basis known as Hund's case (a). This is a fairly common choice of basis, and will be the most useful for our discussions of ThO, but there are several others[36]. Hund's case (a) is valid when the spin-orbit coupling $A\vec{L} \cdot \vec{S} = A\Lambda\Sigma$ is large compared to the rotational constant B. In words, it means that the electron spin is strongly coupled to the internuclear axis, and the energy cost of changing the orientation of the electron spin is larger than the energy cost of increasing the molecular rotation. In this case, state with different values of $|\Sigma|$ can be viewed as different electronic states, each with their own rotational manifold.

On the other hand, Hund's case (b) is a valid basis when the opposite is true; in this case, the spin is weakly coupled to the internuclear axis, and each rotational state has several sub-levels corresponding to different values of Σ. This case is common for molecular states with a single valence electron and no orbital angular momentum, such as $^2\Sigma$ states.

Lastly, Hund's case (c) is something of a sub-case of (a), where the spin-orbit coupling is so large that Λ and Σ are no longer good quantum numbers by themselves. This is typically the case for heavy, relativistic molecules (such as ThO), when the spin-orbit constant is comparable to the energy of electronic excitation, so that states with different Σ can be regarded as different electronic states with different molecular constants. Some molecules (again such as ThO) may be case (c) in general, but may have a subset of electronic states which are well described in the (a) basis.

We will not go further into the different cases, except to remind the reader that

Table 2.1: Hund's cases (a)-(c), along with their good quantum numbers, and limit when the description is valid (adapted from Brown and Carrington[36]). Here $N = J - S$ is the total non-spin angular momentum, $J_e = L + S$ is the total electronic angular momentum, A is the spin-orbit constant, B is the rotational constant, and ΔE_{el} is the typical electronic spacing in the molecule.

Case	Quantum numbers	Limit
(a)	$\Lambda, S, \Sigma, J, \Omega$	$A\Lambda \gg B_e J$
(b)	Λ, N, S, J	$A\Lambda \ll BJ$
(c)	J_e, Ω, J	$A\Lambda \gg \Delta E_{\text{el}}$

real molecules are never purely described in one basis or another, but must in fact be written as a sum of basis states. This shall be important for our discussion of the Zeeman effect in ThO, where we must consider an intermediate (a)-(b) case to correctly describe the states (see Chapter 6).

2.3 Matrix Elements for Spherical Tensor Operators

Computing matrix elements involving molecular states is difficult. Unlike atoms, which have no internal or "body" frame, molecules have quantities which exist either in the lab frame, or the internal, co-rotating molecular frame. As discussed in Chapter 5 of Brown and Carrington[36], quantities such as angular momentum obey different quantities in the lab and molecule frames. As a specific example, consider the usual angular momentum operators J_X, J_Y, J_Z in the lab frame. Now apply a rotation operation to these operators to obtain the operators in the molecule frame J_x, J_y, J_z. We then find that $[J_x, J_y] = -iJ_z$ (see [36],§5.3.1), which is fundamentally different from the usual lab-frame relationship $[J_X, J_Y] = iJ_Z$. This may not seem important,

but when one remembers that all angular momentum algebra is built upon this commutation relation, the difficulty becomes clear: we cannot perform any calculations involving angular momentum in the molecule frame (nuclear rotation, electron spin, etc.) using the usual angular momentum algebra.

There are two approaches to overcoming this difficulty. The first is to look at large tables of matrix elements, such as those contained in [145] or [212]. They have the significant advantage of simplicity, and offer quick answers to questions such as "can a magnetic field change J in a molecule[2]?" The downside is that the physics is swept under the rug, either by avoiding it entirely or because the notation is so outdated that nobody can understand it anymore. The other approach is the one taken by Brown and Carrington[36], which is to overcome the "anomalous commutation relationship" problem by rotating the molecule-frame quantities into the lab frame, using the usual angular momentum algebra, and then rotating back to the molecule frame. The advantage is that mastery of this technique allows one to compute nearly anything involving molecules, and understand the physics. The downside is that the math can quickly become very cumbersome (see p. 772 in [36], for example), and the only thorough reference on the subject (Brown and Carrington[36]) is notoriously difficult to navigate. Here, we will take the latter approach. Due to the difficulty involved with trying to decipher Brown and Carrington, we will compile some of the important results in this section.

We will use p to denote an index of a spherical tensor operator in the laboratory frame, q to denote an index of a spherical tensor operator in the molecule (body)

---

[2]Yes, it can; this fact will be very important in Chapter 6.

frame, capital X, Y, Z to indicate coordinates in the lab, and lower case x, y, z to indicate coordinates in the molecule frame. Consider a rank 1 spherical tensor operator $\vec{A}$ which is defined in the lab frame, for example a laboratory electric field $\vec{\mathcal{E}}$. An operator which is defined in the molecule frame would be something like the total electron spin $\vec{S}$ or internuclear axis $\hat{n}$, which (in the absence of fields forcing alignment of these quantities in the lab frame) are rotating about in the molecule frame, and therefore cannot be expressed in the lab frame without knowing the rotational state of the molecule.

We will use the notation $T_p^1(A)$ to denote the pth component (where $p = 0, \pm 1$) of the spherical tensor version of $\vec{A}$ in the lab frame. In the case where $\vec{A} = A_X \hat{X} + A_Y \hat{Y} + A_Z \hat{Z}$ is naturally expressed in Cartesian coordinates, the spherical tensor indices are given by $T_0^1(A) = A_Z$, $T_{\pm 1}^1 = \mp 2^{-1/2}(A_X \pm iA_Y)$. In particular, if we consider the angular momentum operator $\vec{J}$, we find that $T_0^1(J) = J_Z$, and $T_{\pm 1}^1 = \mp 2^{-1/2} J_\pm$.

2.3.1 Transforming Between Lab and Molecule Frames

Very often we find ourselves wanting to express molecule quantities in the lab frame, and vice-versa. This will be especially important when we want to look at the interaction between a lab and molecule quantity, for example the electric dipole interaction between a lab electric field and the molecule internuclear axis. Before continuing, the reader should keep in mind that many of these relations look complicated and involve quantities with confusing physical interpretation (a physicist may wonder: through which Euler angles do we rotate to get into the molecule frame?),

but we shall see that their matrix elements turn out to be simple and rely only on quantities with clear physical interpretation.

To rotate a rank k spherical tensor from one frame to the other, we use the rotation matrices,

$$T_p^k(A) = \sum_q \mathcal{D}_{p,q}^{(k)}(\omega)^* T_q^k(A), \qquad T_q^k(A) = \sum_p (-1)^{p,-q} \mathcal{D}_{-p,-q}^{(k)}(\omega)^* T_p^k(A). \qquad (2.12)$$

The rotation matrix $\mathcal{D}_{p,q}^{(k)}(\omega)$ is defined such that if we consider an eigenstate of angular momentum $|J, M\rangle$ in some coordinate system X, Y, Z, and then rotate the coordinate system through Euler angles (ϕ, θ, χ), we obtain

$$R(\phi, \theta, \chi) |J, M\rangle = \sum_{M'} |J, M'\rangle \, \mathcal{D}_{M'M}^J(\phi, \theta, \chi). \qquad (2.13)$$

We typically abbreviate $(\phi, \theta, \chi) = \omega$. Notice that this rotation does not change J, which makes sense; rotations will never change the length of a vector, just the projection on some axis.

As mentioned above, the rotation matrices will turn into physically meaningful observables when we compute matrix elements. We will list some of the most important relationships below; see Brown and Carrington[36], Chapter 5 for derivations and details. Equation (2.15) is the Wigner-Eckart Theorem, where $\langle J || T_p^1(J) || J' \rangle = \delta_{J,J'} [J(J+1)(2J+1)]^{1/2}$ is the reduced matrix element. In this equation, J can be replaced with any angular momentum operator (L or S, for example).

$$\langle J, M|T_p^1(J)|J', M'\rangle = (-1)^{J-M} \begin{pmatrix} J & 1 & J' \\ -M & p & M' \end{pmatrix} \langle J||T_p^1(J)||J'\rangle \quad (2.14)$$

$$= (-1)^{J-M} \begin{pmatrix} J & 1 & J' \\ -M & p & M' \end{pmatrix} \delta_{J,J'} [J(J+1)(2J+1)]^{1/2} \quad (2.15)$$

$$\langle J, M, \Omega|\mathcal{D}_{p,q}^{(k)}(\omega)^*|J', M', \Omega'\rangle =$$

$$(-1)^{M-\Omega} [(2J+1)(2J'+1)]^{1/2} \begin{pmatrix} J & k & J' \\ -\Omega & q & \Omega' \end{pmatrix} \begin{pmatrix} J & k & J' \\ -M & p & M' \end{pmatrix} \quad (2.16)$$

$$\sum_p \langle J, M, \Omega|T_p^1(J)\mathcal{D}_{-p,q}^{(1)}(\omega)^*|J', M', \Omega'\rangle =$$

$$(-1)^{J-\Omega}\delta_{J,J'}\delta_{M,M'} [J(J+1)(2J+1)]^{1/2} \begin{pmatrix} J & 1 & J \\ -\Omega & q & \Omega' \end{pmatrix} \quad (2.17)$$

2.3.2 Matrix elements using multiple frames

We often find ourselves wanting to compute matrix elements for interactions between the lab and molecule frame. For example, a lab-quantized magnetic field $\vec{\mathcal{B}}$ will interact with molecule-quantized electron spin $\vec{S}$ and add a term $-g_S\mu_B\vec{B}\cdot\vec{S}$ to the Hamiltonian, where g_S is the electron $g-$factor and μ_B is the Bohr Magneton. How we compute this dot product when the two quantities are defined in different frames? The dot-product is defined as

$$\vec{B}\cdot\vec{S} = \sum_p (-1)^p T_p^1(B)T_{-p}^1(S), \quad (2.18)$$

so the key is to take the molecule-quantized tensor $T_q^1(S)$, rotate into the lab frame to obtain $T_p^1(S)$, and then compute the usual lab-frame dot product above. We will work out this (and other) specific examples in the next few sections, and stick to generalities for now.

For a quantity $\vec{P}$ in the lab frame and $\vec{Q}$ in the molecule frame, we compute $\vec{P} \cdot \vec{Q}$ by calculating

$$\vec{P} \cdot \vec{Q} = \sum_p (-1)^p T_p^1(P) T_{-p}^1(Q) \tag{2.19}$$

$$= \sum_{p,q} (-1)^p T_p^1(P) \mathcal{D}_{-p,q}^{(k)}(\omega)^* T_q^k(A) \tag{2.20}$$

$$\langle \alpha, \beta | \vec{P} \cdot \vec{Q} | \alpha', \beta' \rangle = \sum_{p,q} (-1)^p \langle \alpha | T_p^1(P) \mathcal{D}_{-p,q}^{(k)}(\omega)^* | \alpha' \rangle \langle \beta | T_q^k(A) | \beta' \rangle . \tag{2.21}$$

Here α, α' are quantum numbers in the lab frame, and β, β' are quantum numbers in the molecule frame. It may not be apparent from the above expression, but we are now in a position where can use normal angular momentum algebra to solve the problem; the left-hand element in the sum uses only the lab frame, and the right-hand element only uses the molecule frame. The appearance of the q index in the term $\mathcal{D}_{-p,q}^{(k)}$ may make it seem that we are still mixing coordinate systems, but remember that $\mathcal{D}_{-p,q}^{(k)}$ is just some entry in a rotation matrix whose matrix elements are given by Eq. (2.16).

We cannot proceed further in this general case without knowing the specific forms of the operators. In the next few sections we will work through examples of how to compute such matrix elements. We will typically work in the Hund's case (a) basis since the ThO electronic states have known decomposition in this basis[189]. We will write the states as $|J, M, \Omega; \Lambda, S, \Sigma\rangle$. Here the semicolon divides the lab frame

32

quantum numbers J, M, Ω from the molecule frame quantum numbers Λ, S, Σ.

2.4   Stark Shift

The Stark Hamiltonian is $H_{stark} = -\vec{D} \cdot \vec{\mathcal{E}}$, where $\vec{D}$ is the molecule-frame dipole moment and $\vec{\mathcal{E}}$ is a lab-frame electric field. Using Eq. (2.21) with $\vec{P} = \vec{\mathcal{E}}$, $\vec{Q} = \vec{D}$, $\alpha = (J, M, \Omega)$, and $\beta = (\Lambda, S, \Sigma)$,

$$\langle J, M, \Omega; \Lambda, S, \Sigma | \vec{D} \cdot \vec{\mathcal{E}} | J', M', \Omega'; \Lambda', S', \Sigma' \rangle =$$

$$\sum_{p,q} (-1)^p \langle J, M, \Omega | T_p^1(\mathcal{E}) \mathcal{D}_{-p,q}^{(1)}(\omega)^* | J', M', \Omega' \rangle \langle \Lambda, S, \Sigma | T_q^1(D) | \Lambda', S', \Sigma' \rangle . \quad (2.22)$$

Let's proceed piece-by-piece. Since the electron spin does not contribute to the electric dipole moment of the molecule (ignoring the electron electric dipole moment, which is a good approximation), we can factor this matrix element into

$$\langle \Lambda, S, \Sigma | T_q^1(D) | \Lambda', S', \Sigma' \rangle = \langle S, \Sigma | S', \Sigma' \rangle \langle \Lambda | T_q^1(D) | \Lambda' \rangle = \delta_{SS'} \delta_{\Sigma\Sigma'} \langle \Lambda | T_q^1(D) | \Lambda' \rangle .$$

$$(2.23)$$

This is very similar to the selection rules for atoms in an electric field: we cannot change anything relating to the spin (S, Σ), but can only change the orbital angular momentum Λ. The quantity $\langle \Lambda | T_q^1(D) | \Lambda' \rangle$ is called the reduced matrix element, and is typically written as $\langle \Lambda | T_0^1(D) | \Lambda' \rangle = D_\parallel$ and $\langle \Lambda | T_{\pm 1}^1(D) | \Lambda' \rangle = D_\perp$, the on-diagonal and off-diagonal (or parallel and perpendicular) dipole moments, respectively. These quantities are not easy to calculate in real molecules, and are typically measured (or calculated using advanced techniques.)

The other term in Eq. (2.22) is simple since it is just a rotational matrix element and some constants,

$$\langle J, M, \Omega | T_p^1(\mathcal{E}) \mathcal{D}_{-p,q}^{(1)}(\omega)^* | J', M', \Omega' \rangle = T_p^1(\mathcal{E}) \langle J, M, \Omega | \mathcal{D}_{-p,q}^{(1)}(\omega)^* | J', M', \Omega' \rangle$$

$$= T_p^1(\mathcal{E})(-1)^{M-\Omega} \left[(2J+1)(2J'+1) \right]^{1/2} \begin{pmatrix} J & 1 & J' \\ -\Omega & q & \Omega' \end{pmatrix} \begin{pmatrix} J & 1 & J' \\ -M & -p & M' \end{pmatrix}. \quad (2.24)$$

Since we are taking the electric field $\mathcal{E}$ as an input parameter, the quantities $T_0^1(\mathcal{E}) = \mathcal{E}_Z$, $T_{\pm 1}^1(\mathcal{E}) = \mp 2^{-1/2}(\mathcal{E}_X \pm i\mathcal{E}_Y)$ are simply constants. Combining all of these, we have

$$\langle J, M, \Omega; \Lambda, S, \Sigma | \vec{D} \cdot \vec{\mathcal{E}} | J', M', \Omega'; \Lambda', S', \Sigma' \rangle =$$

$$\sum_{p,q} (-1)^p T_p^1(\mathcal{E})(-1)^{M-\Omega} \delta_{SS'} \delta_{\Sigma\Sigma'} \langle \Lambda | T_q^1(D) | \Lambda' \rangle \times \cdots$$

$$[(2J+1)(2J'+1)]^{1/2} \begin{pmatrix} J & 1 & J' \\ -\Omega & q & \Omega' \end{pmatrix} \begin{pmatrix} J & 1 & J' \\ -M & -p & M' \end{pmatrix}. \quad (2.25)$$

This equation is complex, but only involves things which we can easily calculate, input, or look up. As an explicit example, let's calculate the energy shift (Stark shift) for a lab electric field in the Z direction, i.e. $T_0^1(\mathcal{E}) = \mathcal{E}_Z, T_{\pm 1}^1(\mathcal{E}) = 0$. We take $p = 0$ (since the $\mathcal{E}$ field is in the Z direction) and $q = 0$ (since we are considering matrix

elements between a state and itself, i.e. not changing Ω) to write

$$
\begin{aligned}
\Delta E_{Stark} &= \langle J, M, \Omega; \Lambda, S, \Sigma| - \vec{D} \cdot \vec{\mathcal{E}} |J, M, \Omega; \Lambda, S, \Sigma\rangle \\
&= -T_0^1(\mathcal{E}) D_{\parallel} (-1)^{M-\Omega} [(2J+1)(2J'+1)]^{1/2} \begin{pmatrix} J & 1 & J \\ -\Omega & 0 & \Omega \end{pmatrix} \begin{pmatrix} J & 1 & J \\ -M & 0 & M \end{pmatrix} \\
&= -\mathcal{E}_Z D_{\parallel} (-1)^{M-\Omega} (-1)^{J-\Omega} (-1)^{J-M} \frac{M\Omega}{J(J+1)} \\
&= -\mathcal{E}_Z D_{\parallel} (-1)^{2(J-\Omega)} \frac{M\Omega}{J(J+1)} \\
\Delta E_{Stark} &= -\mathcal{E}_Z D_{\parallel} \frac{M\Omega}{J(J+1)},
\end{aligned}
\tag{2.26}
$$

where in the last step we used that J and Ω differ by the number of rotational quanta, which is an integer. This is the classic result[117] for the Stark shift of a molecule with $|\Lambda| > 0$.

2.4.1 Molecule Orientation and the Quantum Number $\mathcal{N}$

Consider a state with $J = |\Omega| = 1$, such as the $J = 1$ rotational level of the ThO H state. From the equation above, we can see that $\text{sign}(\Delta E_{Stark}) = -\text{sign}(\mathcal{E}_Z M\Omega) = -\hat{\mathcal{E}}_Z M\Omega$, assuming that we take $D_{\parallel} > 0$. Define the quantity

$$
\mathcal{N} = \hat{\mathcal{E}}_Z M\Omega,
\tag{2.27}
$$

which is -1 for the states which are shifted up, and $+1$ for the states which are shifted down, so that

$$
\Delta E_{Stark} = -|\mathcal{E}_Z| D_{\parallel} \frac{\mathcal{N}}{J(J+1)} = -d(J)\mathcal{E}_Z \mathcal{N}.
\tag{2.28}
$$

This number $\mathcal{N}$ is relevant for the EDM measurement since one of our switches (see Section 4.2) is to change the laser frequency addressing the molecules, which has

the effect of switching $\mathcal{N}$. This is commonly called an "$\Omega-$doublet reversal," even though we are actually changing $\mathcal{N}$. We can also define the direction of the molecular internuclear axis in the lab frame $\hat{n}_{lab}$ using the above quantum numbers. Since the molecular dipole is aligned along the internuclear axis, $\text{sign}(\vec{D} \cdot \vec{\mathcal{E}}) = \text{sign}(\vec{n} \cdot \vec{\mathcal{E}}_Z) = \hat{n}_{lab}\hat{\mathcal{E}}_Z = -\mathcal{N}$, so

$$\hat{n}_{lab} = -\mathcal{N}\hat{\mathcal{E}}_Z. \tag{2.29}$$

This $\mathcal{N}$ should not be confused with the very common molecular quantum number $N = J - S$ used in Hund's case (b) molecules[36, 157]. We will never use $N = J - S$ in this thesis apart from this warning, and in Table 2.1.

2.4.2 Molecular polarization: linear vs. quadratic Stark regime

We often talk about a molecule being "fully polarized," so we should clarify what exactly this means. Consider two states of opposite parity, spaced in energy by 2Δ, and connected by an E1 matrix element $\langle 1| - \vec{d} \cdot \vec{\mathcal{E}}|2 \rangle = -d\mathcal{E}$. The Hamiltonian for this simple system is

$$H = \begin{pmatrix} +\Delta & -d\mathcal{E} \\ -dE & -\Delta \end{pmatrix}, \tag{2.30}$$

which we can easily diagonalize to find the eigenenergies

$$E_\pm = \pm\Delta\sqrt{1 + (d\mathcal{E}/\Delta)^2}. \tag{2.31}$$

When $d\mathcal{E} \ll \Delta$, we are in the quadratic Stark regime, where $E_\pm \approx \pm\Delta \pm (d\mathcal{E})^2/2\Delta$. The physical interpretation of this limit is that the electric field is inducing a dipole $\propto |\mathcal{E}|$, so there is an energy shift $d\mathcal{E} \propto \mathcal{E}^2$. When $d\mathcal{E} \gg \Delta$, we are in the linear Stark regime, where $E_\pm =\approx \pm d\mathcal{E}$, and the eigenstates are $(|1\rangle \pm |2\rangle)/\sqrt{2}$.

Typical values for d are approximately 1 atomic unit, $d \approx ea_0 \approx h \times 1 \, \mathrm{MHz/(V/cm)}$. In words, this means that for every MHz of energy spacing between opposite-parity states connected by an E1 matrix element, we require approximately 1 V/cm of external field to start entering the linear Stark regime, or to "polarize the molecule."

We often discuss the polarization P of the molecule, which is defined as $E_\pm = Pd\mathcal{E}$ and satisfies $0 \leq P < 1$. From Eq. (2.31), we can see that

$$P = \frac{\epsilon}{\sqrt{1 + \epsilon^2}}, \text{ where } \epsilon = \frac{d\mathcal{E}}{\Delta}. \tag{2.32}$$

In the two limits discussed above, we can approximate this quantity by

$$P \approx \begin{cases} \epsilon + \mathcal{O}(\epsilon^2) & \epsilon \ll 1 \\ 1 - \frac{1}{2\epsilon^2} + \mathcal{O}(\epsilon^{-3}) & \epsilon \gg 1 \end{cases} \tag{2.33}$$

For the ThO H state, the two closest states of opposite parity are the Ω-doublet states, spaced by $aJ(J+1)$ where $a = 181(1)$ kHz (see Section D.3). Since the dipole moment of the H state is $D_\parallel = 2.14(2) \, \mathrm{MHz/(V/cm)}$[244], we can see that a field of 10 V/cm should result in a polarization of $P > 0.999$. On the other hand, a molecule which requires mixing rotational levels spaced by ≈ 10 GHz, such as YbF[125, 126], only achieves $P \approx 0.5$ with external fields of ≈ 10 kV/cm. The fact that our molecule is "fully polarized" has a number of advantages, which we will encounter throughout this thesis.

2.5 Zeeman Shift

The Zeeman shift is simlar to the Stark shift, but the reduced matrix element is more complicated. The Zeeman effect comes from the external field interacting with the electron spin and orbital angular momenta, $H_{Zeeman} = -\vec{\mu} \cdot \vec{\mathcal{B}} = -g_S \mu_\mathrm{B} \vec{S} \cdot \vec{\mathcal{B}} -$

$g_L \mu_\mathrm{B} \vec{L} \cdot \vec{\mathcal{B}}$, where g_S and g_L are the spin and orbital $g-$factors, respectively, and μ_B is the Bohr Magneton. The values of g_S and g_L depend on the molecular states (due to perturbations[38, 36]), but are typically ≈ -2 and ≈ -1 respectively. Let us consider the $\vec{S} \cdot \vec{\mathcal{B}}$ term first:

$$\langle J, M, \Omega; \Lambda, S, \Sigma | \vec{S} \cdot \vec{\mathcal{B}} | J', M', \Omega'; \Lambda', S', \Sigma' \rangle =$$

$$\sum_{p,q} (-1)^p \langle J, M, \Omega | T_p^1(\mathcal{B}) \mathcal{D}_{-p,q}^{(1)}(\omega)^* | J', M', \Omega' \rangle \langle \Lambda, S, \Sigma | T_q^1(S) | \Lambda', S', \Sigma' \rangle . \quad (2.34)$$

The first matrix element is exactly analogous to the corresponding Stark term (equation 2.24),

$$\langle J, M, \Omega | T_p^1(\mathcal{B}) \mathcal{D}_{-p,q}^{(1)}(\omega)^* | J', M', \Omega' \rangle =$$

$$T_p^1(\mathcal{B})(-1)^{M-\Omega} [(2J+1)(2J'+1)]^{1/2} \begin{pmatrix} J & 1 & J' \\ -\Omega & q & \Omega' \end{pmatrix} \begin{pmatrix} J & 1 & J' \\ -M & -p & M' \end{pmatrix}, \quad (2.35)$$

where $T_0^1(\mathcal{B}) = \mathcal{B}_Z$, $T_{\pm 1}^1(\mathcal{B}) = \mp 2^{-1/2}(\mathcal{B}_X \pm i\mathcal{B}_Y)$ are input parameters. The reduced matrix element is easy to compute using the Wigner-Eckart Theorem (Eq. 2.15), and the fact that the S operator cannot change Λ,

$$\langle \Lambda, S, \Sigma | T_q^1(S) | \Lambda', S', \Sigma' \rangle = \langle \Lambda | \Lambda' \rangle \langle S, \Sigma | T_q^1(S) | S', \Sigma' \rangle$$

$$= \delta_{\Lambda,\Lambda'} (-1)^{S-\Sigma} \begin{pmatrix} S & 1 & S' \\ -\Sigma & q & \Sigma' \end{pmatrix} \delta_{S,S'} [S(S+1)(2S+1)]^{1/2}. \quad (2.36)$$

We can combine these results to obtain the complicated (but easy to evaluate)

38

expression for Zeeman matrix elements,

$$\langle J, M, \Omega; \Lambda, S, \Sigma | \vec{S} \cdot \vec{\mathcal{B}} | J', M', \Omega'; \Lambda', S', \Sigma' \rangle = \sum_{p,q} (-1)^p T_p^1(\mathcal{B}) \delta_{\Lambda,\Lambda'} \delta_{S,S'} \times \cdots$$

$$(-1)^{S-\Sigma+M-\Omega} [S(S+1)(2S+1)]^{1/2} [(2J+1)(2J'+1)]^{1/2} \times \cdots$$

$$\begin{pmatrix} S & 1 & S' \\ -\Sigma & q & \Sigma' \end{pmatrix} \begin{pmatrix} J & 1 & J' \\ -\Omega & q & \Omega' \end{pmatrix} \begin{pmatrix} J & 1 & J' \\ -M & -p & M' \end{pmatrix}. \quad (2.37)$$

For the operator $\vec{L} \cdot \vec{B}$, we will obtain the same result but with $S \to L$ and $\Sigma \to \Lambda$. As with the Stark case, we will explicitly evaluate the most commonly used instance of this: the Zeeman energy shift diagonal in all quantities with a magnetic field in the $Z-$direction, $T_0^1(\mathcal{B}) = \mathcal{B}_Z, T_{\pm1}^1(\mathcal{B}) = 0$. Since $M = M', \Omega = \Omega', \Sigma = \Sigma'$ for this matrix element, only the $p = q = 0$ term in the sum will contribute,

$$\langle J, M, \Omega; \Lambda, S, \Sigma | \vec{S} \cdot \vec{\mathcal{B}} | J, M, \Omega; \Lambda, S, \Sigma \rangle$$

$$= \mathcal{B}_Z (-1)^{S-\Sigma+M-\Omega} [S(S+1)(2S+1)]^{1/2} (2J+1) \times \cdots$$

$$\begin{pmatrix} S & 1 & S \\ -\Sigma & 0 & \Sigma \end{pmatrix} \begin{pmatrix} J & 1 & J \\ -\Omega & 0 & \Omega \end{pmatrix} \begin{pmatrix} J & 1 & J \\ -M & 0 & M \end{pmatrix}$$

$$= \mathcal{B}_Z (-1)^{2J+2S-2\Sigma+M-\Omega} [S(S+1)(2S+1)]^{1/2} (2J+1) \times \cdots$$

$$\frac{\Sigma}{[S(S+1)(2S+1)]^{1/2}} \frac{\Omega}{[J(J+1)(2J+1)]^{1/2}} \frac{M}{[J(J+1)(2J+1)]^{1/2}}$$

$$= \mathcal{B}_Z \frac{\Sigma M \Omega}{J(J+1)}, \quad (2.38)$$

where we used the fact that both $S - \Sigma$ and $J - \Omega$ are integers to get rid of the power of -1. The corresponding term for $\vec{L} \cdot \vec{\mathcal{B}}$ will be the same but with $\Sigma \to \Lambda$. We can

combine these results to compute the Zeeman shift,

$$\langle J, M, \Omega; \Lambda, S, \Sigma | H_{Zeeman} | J, M, \Omega; \Lambda, S, \Sigma \rangle$$

$$= \mu_{\mathrm{B}} \langle J, M, \Omega; \Lambda, S, \Sigma | - g_S \vec{S} \cdot \vec{\mathcal{B}} - g_L \vec{L} \cdot \vec{\mathcal{B}} | J, M, \Omega; \Lambda, S, \Sigma \rangle$$

$$= -\mathcal{B}_Z \mu_{\mathrm{B}} (g_S \Sigma + g_L \Lambda) \frac{M\Omega}{J(J+1)}. \tag{2.39}$$

The quantities Σ and Λ are signed, so $\mathrm{sign}(g_S\Sigma + g_L\Lambda) \propto \mathrm{sign}(\Omega)$. Define the parallel $g-$factor $G_\| = \Omega(g_S\Sigma + g_L\Lambda)$, which is independent of the signs of Ω, Λ, Σ, so that

$$\langle J, M, \Omega; \Lambda, S, \Sigma | H_{Zeeman} | J, M, \Omega; \Lambda, S, \Sigma \rangle = -\mathcal{B}_Z \mu_{\mathrm{B}} G_\| \frac{M\Omega^2}{J(J+1)}. \tag{2.40}$$

Recall that we are considering a Hund's case (a) basis. The Zeeman effect in a Hund's case (b) basis is not the same, and in particular as different scaling with J. Real molecules are some intermediate case between (a) and (b); we will discuss this in more detail in Chapter 6, or see Ref. [21].

2.6 Rotational Perturbations: Spin-Orbit, Uncoupling, Ω-doubling

The rotational part of the Hamiltonian is given by

$$H_{rot} = B_{v=0}\vec{R}^2 = B_{v=0}(\vec{J} - \vec{L} - \vec{S})^2 = B_{v=0}(J^2 + L^2 + S^2 - 2\vec{J}\cdot\vec{L} - 2\vec{J}\cdot\vec{S} + 2\vec{L}\cdot\vec{S}), \tag{2.41}$$

where $B_{v=0}$ is the rotational constant in the $v = 0$ level. These interactions between J, L, and S have important consequences, and are typically called "spin-orbit" effects. The $B_{v=0}J^2$ term gives us the usual rotational energy $E_{rot} = B_{v=0}J(J+1)$, and the terms L^2, S^2 merely give some constant energy offset, so let's focus on the dot

products. It is very important to notice that none of these terms will mix states of different J, since J is an absolutely good quantum number in the absence of external fields when the Hamiltonian is rotationally symmetric. A summary of these perturbations can be found in Table 6.1.

2.6.1 Spin-Orbit, $L \cdot S$

The term $2B_{v=0}\vec{L}\cdot\vec{S}$ is called the spin-orbit term. There is generally a term $A\vec{L}\cdot\vec{S}$ due to the motion of the electrons themselves (as opposed to the molecular rotation), and often $A \gg B_{v=0}$, so we shall ignore the contributions from the $B_{v=0}$ term. The diagonal elements of this perturbation are

$$\langle J, M, \Omega; \Lambda, S, \Sigma | H^{SO} | J, M, \Omega; \Lambda, S, \Sigma \rangle = A\Lambda\Sigma. \tag{2.42}$$

In ThO, this means that the $^3\Delta_{1,2,3}$ (H, Q, W) states are split by $2A$ (plus a significant number of higher order terms[37]). The splitting of $W - Q$ is not precisely known, and the spacing is generally not uniform due to other perturbations[157], but we will write $A = 405$ cm$^{-1} = 12$ THz in the future when considering couplings between the H and Q states.

The off-diagonal matrix elements satisfy[157] $\Delta\Lambda = \pm 1$ and $\Delta\Sigma = \mp 1$. This interaction is responsible for mixing between the H and the B, C states, which is one of the main contributors to the non-zero $g-$factor in the H state (see Section 6.2.2). The spin-orbit interaction is actually much more complicated[157] than our treatment here; however, this treatment is sufficient for our purposes.

2.6.2   Spin Uncoupling, $J \cdot S$

The operator $J \cdot S$ is called the $S-$uncoupling operator[157] and satisfies $\Delta \Lambda = \Delta J = \Delta S = 0$, $\Delta \Sigma = \Delta \Omega = \pm 1$. In words, this operator is responsible for changing Σ, the projection of the spin on the internuclear axis, and therefore changing Ω. To see why the operator has this name, consider a molecular state (e.g. $^3\Delta_{1,2,3}$) which has a number of fine structure components split by $\sim A$. When $A \gg B_{v=0}$, the spin-orbit splitting is much larger than any matrix elements from the operator $B_{v=0} J \cdot S$, so we can regard the states $^3\Delta_{1,2,3}$ as distinct states with a small perturbative coupling between them. In other words, we are in the Hund's case (a) limit[36, 157] where the spin is strongly coupled to the internuclear axis. On the other hand, if $A \ll B_{v=0}$, then each rotational level is split into a number of fine-structure components spaced by $\sim A$ and we are in the Hund's case (b) limit, where the electron spin is not strongly coupled to the internuclear axis. The perturbation $J \cdot S$ therefore "uncouples" the spin from the internuclear axis as it becomes larger and larger, which we shall see happens as J is increased. In addition, this term will mix states of different Σ and Ω, so these are not strictly good quantum numbers in a rotating molecule. This has a number of important consequences, but for us the most important result is that it will change the Zeeman spectrum of the molecular state[157, 239, 212, 21, 36], which we will explore further in Chapter 6.

Since this term is important for some of the measurements we have performed with ThO, we will go through it in detail. This term is partially worked out in Brown and Carrington[36] on p. 170. We will start with an equation very similar to Eq. (2.22) above, using the fact that J is quantized in the lab and S in the molecule,

$$\langle J, M, \Omega; \Lambda, S, \Sigma | \vec{J} \cdot \vec{S} | J', M', \Omega'; \Lambda', S', \Sigma' \rangle$$

$$= \sum_{p,q} (-1)^p \langle J, M, \Omega | T_p^1(J) \mathcal{D}_{-p,q}^{(1)}(\omega)^* | J', M', \Omega' \rangle \langle \Lambda, S, \Sigma | T_q^1(S) | \Lambda', S', \Sigma' \rangle$$

$$= \sum_{p,q} (-1)^p \langle J, M, \Omega | T_p^1(J) \mathcal{D}_{-p,q}^{(1)}(\omega)^* | J', M', \Omega' \rangle \langle S, \Sigma | T_q^1(S) |, S', \Sigma' \rangle \langle \Lambda | \Lambda' \rangle$$

$$= \sum_{p,q} (-1)^p \langle J, M, \Omega | T_p^1(J) \mathcal{D}_{-p,q}^{(1)}(\omega)^* | J', M', \Omega' \rangle \langle S, \Sigma | T_q^1(S) |, S', \Sigma' \rangle \delta_{\Lambda,\Lambda'}$$

$$= \sum_{q} \langle S, \Sigma | T_q^1(S) |, S', \Sigma' \rangle \delta_{\Lambda,\Lambda'} \left[\sum_{p} (-1)^p \langle J, M, \Omega | T_p^1(J) \mathcal{D}_{-p,q}^{(1)}(\omega)^* | J', M', \Omega' \rangle \right]$$

$$(2.43)$$

The sum over p term is given in Eq. (2.17). The term $\langle S, \Sigma | T_q^1(S) |, S', \Sigma' \rangle$ can be evaluated using the Wigner-Eckart Theorem (Eq. 2.15). Continuing,

$$= \sum_{q} (-1)^{S-\Sigma} \begin{pmatrix} S & 1 & S' \\ -\Sigma & q & \Sigma' \end{pmatrix} \delta_{S,S'} [S(S+1)(2S+1)]^{1/2} \delta_{\Lambda,\Lambda'} \times \cdots$$

$$(-1)^{J-\Omega} \delta_{J,J'} \delta_{M,M'} [J(J+1)(2J+1)] \begin{pmatrix} J & 1 & J \\ -\Omega & q & \Omega' \end{pmatrix} \qquad (2.44)$$

$$= (-1)^{J+S-\Sigma-\Omega} \delta_{J,J'} \delta_{M,M'} \delta_{S,S'} \delta_{\Lambda,\Lambda'} [S(S+1)(2S+1)]^{1/2} \times \cdots$$

$$[J(J+1)(2J+1)]^{1/2} \sum_{q} \begin{pmatrix} S & 1 & S \\ -\Sigma & q & \Sigma' \end{pmatrix} \begin{pmatrix} J & 1 & J \\ -\Omega & q & \Omega' \end{pmatrix} \qquad (2.45)$$

$$= (-1)^{J+S-\Sigma-\Omega} \delta_{J,J'} \delta_{M,M'} \delta_{S,S'} \delta_{\Lambda,\Lambda'} [S(S+1)(2S+1)]^{1/2} \times \cdots$$

$$[J(J+1)(2J+1)]^{1/2} \begin{pmatrix} S & 1 & S \\ -\Sigma & \Sigma-\Sigma' & \Sigma' \end{pmatrix} \begin{pmatrix} J & 1 & J \\ -\Omega & \Omega-\Omega' & \Omega' \end{pmatrix} \qquad (2.46)$$

where we used the sum rule[36] for Wigner-3j symbols that the bottom row must sum to 0 to have non-zero values. We are interested in the off-diagonal elements which

will mix states of different Ω. They are

$$\langle J, M, \Omega \pm 1; \Lambda, S, \Sigma \pm 1 | \vec{J} \cdot \vec{S} | J, M, \Omega; \Lambda, S, \Sigma \rangle$$

$$= (-1)^{J+S-\Sigma-\Omega} \left[S(S+1)(2S+1) \right]^{1/2} \left[J(J+1)(2J+1) \right]^{1/2} \times \cdots$$

$$\sum_q \begin{pmatrix} S & 1 & S \\ -\Sigma \mp 1 & \pm 1 & \Sigma \end{pmatrix} \begin{pmatrix} J & 1 & J \\ -\Omega \mp 1 & \pm 1 & \Omega \end{pmatrix}$$

$$= (-1)^{2J+2S-2\Sigma-2\Omega} \left[S(S+1)(2S+1) \right]^{1/2} \left[J(J+1)(2J+1) \right]^{1/2} \times \cdots$$

$$(\pm 1) \left[\frac{(S \mp \Sigma)(S \pm \Sigma + 1)}{2S(S+1)(2S+1)} \right]^{1/2} (\pm 1) \left[\frac{(J \mp \Omega)(J \pm \Omega + 1)}{2J(J+1)(2J+1)} \right]^{1/2}$$

$$= \frac{1}{2} \sqrt{(S \mp \Sigma)(S \pm \Sigma + 1)(J \mp \Omega)(J \pm \Omega + 1)} \tag{2.47}$$

$$= \frac{1}{2} \sqrt{[S(S+1) - \Sigma(\Sigma \pm 1)][J(J+1) - \Omega(\Omega \pm 1)]}. \tag{2.48}$$

The expectation value of the spin-uncoupling term appearing in the rotational Hamiltonian (Eq. 2.41) is therefore

$$\langle J, M, \Omega \pm 1; \Lambda, S, \Sigma \pm 1 | -2B_{v=0} \vec{J} \cdot \vec{S} | J, M, \Omega; \Lambda, S, \Sigma \rangle =$$

$$- B_{v=0} \sqrt{[S(S+1) - \Sigma(\Sigma \pm 1)][J(J+1) - \Omega(\Omega \pm 1)]}. \tag{2.49}$$

which agrees with the formula given in the literature[145, 21, 157].

2.6.3 Ω-doubling, $J \cdot J_e$

As discussed earlier, the molecular rotation breaks the degeneracy between states with opposite signs of Λ, Σ, and Ω. In light of Eq. (2.41), we can now see precisely why this occurs. The lifting of the degeneracy between the $\pm \Omega$ states requires some coupling between then, but we now know of several terms which can change Ω and give

this coupling. In general, the calculation of Ω-doubling parameters is very complicated and highly dependent on the electronic state in question[37]. However, for a $^3\Delta$ state, the Ω-doublet splitting is well-approximated by $aJ(J+1)$, where a is a constant. For the ThO H state, $a = 181(1)$ kHz for the ThO H state, as we will discuss in Appendix D.3.

2.7   Optical Absorption Cross Sections and Branching Ratios

The starting point for computing the absorption cross section σ of an electronic transition $|g, J\rangle \to |e, J'\rangle$ in a molecule is[42]

$$\sigma = \frac{\lambda^2}{2\pi} \frac{2J'+1}{2J+1} \frac{\gamma_p}{\gamma_{tot}}, \qquad (2.50)$$

where $J'(J)$ is the angular momentum of the upper (lower) state, γ_{tot} is the "total width" of the transition, and γ_p is the "partial width" of the transition. The total width includes all broadening mechanisms (natural, doppler, etc.), and can be thought of as the "actual" width: if you scan a laser across the transition and measure the absorption, the width of the spectral feature will be γ_{tot}. We introduce this notation to distinguish the total width from the partial width, which is the result of spontaneous decay from $|e, J'\rangle \rightsquigarrow |g, J\rangle$ *only*. The quantity γ_p is given by

$$\gamma_p = \frac{4}{3} \frac{1}{2J'+1} \frac{\omega^3}{4\pi\epsilon_0 hc^3} |\langle e, J' | e\vec{r} | g, J \rangle|^2, \qquad (2.51)$$

where $e\vec{r}$ is the electric dipole operator. There is an unfortunate overuse of the letter e; when it appears in a ket it is the excited state, and is otherwise the charge of

an electron. This formula is very similar to the usual expression for the Einstein A-coefficient given in standard atomic physics texts[97]; indeed, γ_p is the rate at which the decay $|e, J'\rangle \rightsquigarrow |g, J\rangle$ occurs.

First, let us consider the case when the excited state radiatively decays to a number of states $|g_i\rangle$, and there are no other broadening mechanisms. Here γ_{tot} is the total decay rate, which is the sum of each partial decay rate $\gamma_{tot} = \sum_i \gamma_{p,i}$. If we define the branching ratio $\xi_i = \gamma_{p_i}/\gamma_{tot}$, then the cross section has the relatively simple form

$$\sigma_i = \frac{\lambda^2}{2\pi}\frac{2J'+1}{2J+1}\xi_i, \tag{2.52}$$

where σ_i is the optical absorption cross section for the transition $|g_i, J\rangle \to |e, J'\rangle$. When $\xi = 1$ we obtain the formula for a "closed transition," where the excited state decays back down to a single lower state, and is typically the case considered in atomic physics texts.

Notice that we have reduced the problem of finding the optical cross sections to finding the decay branching ratios of the excited state. A molecule can change its vibrational and rotational state during an electronic decay, so we will have to calculate the electronic, vibrational and rotational branching ratios.

2.7.1 Electronic Branching

Generally, the computation of a dipole matrix element between electronic states in a molecule is too difficult for a non-expert. However, we can make some simple estimates based on Eq. (2.51) and selection rules. We shall assume that the term symbol $^{2S+1}\Lambda_\Omega$ is known for both upper and lower states, otherwise we cannot make

a simple estimate. The selection rules for an electric dipole (E1) transition are

$$\Delta S = 0 \qquad \Delta\Sigma = 0 \qquad \Delta\Lambda = \pm 1, 0 \qquad \Delta\Omega = \pm 1, 0. \qquad (2.53)$$

These have the same intuitive explanation as atomic E1 selection rules: a photon cannot flip a spin, and can only change an angular momentum by at most one.

If an electronic state has a known decomposition into term symbols, we can estimate the strength of the transition by assuming that the parts of the states which are connected by an E1 transition have a transition dipole moment equal to one atomic unit $ea_0 \approx 2.5$ D (Debye), so that the partial width is $\propto \lambda^{-3}$, where λ is the wavelength of the transition.

2.7.2 Vibrational Branching - Franck-Condon Principle

As mentioned in Section 2.2.2, vibrational levels typically have an energy spacing that is 10-100 times smaller than electronic spacing. This means that the timescales of the electronic motion are much faster than the timescales of nuclear vibration, and therefore the effect of an electronic transition on the vibrational wavefunction can be treated as diabatic, or "instantaneous." This assumption is called the Born-Oppenheimer approximation, and has a number of important implications[36]. One implication is that the probability of starting in vibrational state ν' and decaying into ν (ignoring all other quantum numbers) is simply given by the re-projection of the old basis onto the new basis, $F_{\nu'\nu} = |\langle v'|v\rangle|^2$. This quantity is called a Franck-Condon factor, and gives us the vibrational branching ratios for an electronic transition. When the internuclear potential can be considered harmonic to good approximation, the

vibrational wavefunction is simply given by the wavefunctions of a harmonic oscillator,

$$\psi_\nu(R;\omega_e,R_e) = \frac{1}{\sqrt{2^\nu \nu!}} \left(\frac{\mu\omega_e}{\pi\hbar}\right)^{1/4} \exp\left(\frac{-\mu\omega_e}{2\hbar}(R-R_e)^2\right) H_\nu\left((R-R_e)\sqrt{\frac{\mu\omega_e}{\hbar}}\right),$$

$$(2.54)$$

where μ is the reduced molecular mass, ω_e is the vibrational constant, R_e is the equilibrium spacing of the nuclei, and H_ν is a Hermite polynomial. The Franck-Condon is now a simple integral

$$F_{\nu'\nu} = |\langle v'|v \rangle|^2 = \int_0^\infty \psi_{\nu'}(R;\omega_e',R_e')\psi_\nu(R;\omega_e,R_e)\,dR \tag{2.55}$$

which can easily be evaluated on a computer. Notice that since $\omega \neq \omega'$ and $R_e \neq R_e'$ in general these values are non-trivial; in the case when $\omega = \omega'$ and $R_e = R_e'$ the orthogonality of the harmonic oscillator solutions gives $F_{\nu'\nu} = \delta_{\nu'\nu}$. This may seem to imply that vibrational transitions within an electronic state are not allowed, but this is only within the approximation of the Born-Oppenheimer approximation. In real molecules these transitions are allowed, though we will not discuss this here[36].

2.7.3 Rotational Branching - Hönl-London Factors

The final and most difficult branching ratio calculation is that of the rotational levels. To begin, we mention the selection rules[117, 36]

$$\Delta J = \pm 1, 0 \qquad \Delta M = \pm 1, 0 \qquad J = 0 \nleftrightarrow J' = 0. \tag{2.56}$$

As a very simple approximation, we could argue (as we did with electronic transitions) that those allowed by selection rules are equally likely. This approximation would be correct to within factors of order unity, though we would end up assuming that some

transitions were allowed when they are not. We shall see that the rotational branching ratios are, not surprisingly, given by products of Clebsch-Gordan coefficients, and are called the Hönl-London factors.

It might be tempting to argue that since rotational energies (timescales) are much lower (smaller) than vibrational energies (timescales), the Born-Oppenheimer approximation should imply that we can simply re-project the old rotational wavefunction onto the new, similar to the Franck-Condon factors. This line of reasoning fails because what we call the "rotational part" of the wavefunction, $|J, M, \Omega\rangle$, depends on the electronic wavefunction: Recall that J includes electronic orbital and spin angular momenta as well as nuclear rotation.

Fortunately, we have already calculated the electric dipole matrix elements in equation Eq. (2.25),

$$\left| \langle J, M, \Omega | \vec{D} \cdot \vec{\mathcal{E}} | J', M', \Omega' \rangle \right|^2 \propto$$

$$(2J+1)(2J'+1) \begin{pmatrix} J & 1 & J' \\ -\Omega & \Omega - \Omega' & \Omega' \end{pmatrix}^2 \begin{pmatrix} J & 1 & J' \\ -M & M - M' & M' \end{pmatrix}^2 . \quad (2.57)$$

We have simplified the expression by omitting reference to S and Σ, since it is assumed that $\Delta S = \Delta \Sigma = 0$ (E1 transition), and we have substituted $p = M - M'$, $q = \Omega - \Omega'$ to satisfy the selection rule that the sum of the bottom row of a 3j symbol must be 0[36]. Since we are principally concerned with finding the relative strengths of different rotational transitions of the same electronic transition, we omit the molecule-fixed dipole moment and $\mathcal{E}$ from the right hand side of the above equation, since these will not change with J. Since the above equation gives the non-normalized transition strength, we merely need to compute this strength for the possible lower states to

find the relative strengths.

By making various assumption and performing sums over M, M', we can arrive at some simple, closed-form results known as the Hönl-London factors. We will not go over these here since Eq. (2.57) is very general, so the reader is referred to the texts by Zare[255], Brown and Carrington[36], or Herzberg[117] for more details.

2.7.4 Molecular transition notation - P, Q, and R branches

There is a commonly used notation in molecular spectroscopy to label transitions according to how they change J. The selection rules for E1 transitions require $\Delta J = -1, 0, 1$. If the difference between the upper state J' and lower state J'' is $-1, 0, 1$, the transition is called a P, Q, R transition (or "branch transition") respectively, as shown in Figure 2.4. We then follow the letter with a number in parentheses indicating the angular momentum of the lower state. The labeling always refers to the angular momentum difference between upper and lower; for example, both an absorption $|J = 0\rangle \rightarrow |J = 1\rangle$ and spontaneous decay $|J = 1\rangle \rightsquigarrow |J = 0\rangle$ would be called $R(0)$ transitions.
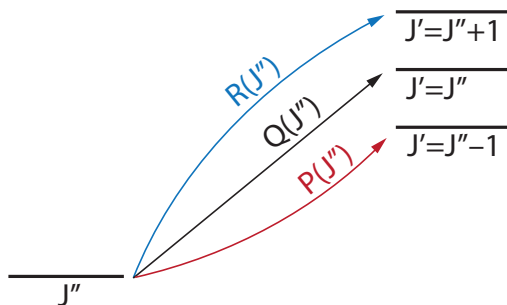
Figure 2.4: P, Q, R notation for rotational state changing transitions in a molecule.

Chapter 3

Buffer Gas Cooled Beams

Much of this section is adapted from a review paper written in 2012 by myself, Hsin-I Lu, and John M. Doyle[129]. I would like to thank them for a significant amount of help, both with gathering information and editing.

3.1 Introduction

Beams of atoms and molecules are important tools for spectroscopy and studies of collisional processes[158, 217, 201, 175]. The supersonic beam technique can create cold beams of many species of atoms and molecules. However, the resulting beam is typically moving at a speed of 300–600 m s^{-1} in the lab frame, and for a large class of species has insufficient flux for several important applications. In contrast, buffer gas beams[167, 46, 129] can be a superior method in many cases, producing cold and relatively slow atoms and molecules (see Figure 3.1) in the lab frame with high brightness and great versatility. There are basic differences between supersonic and

buffer gas cooled beams regarding particular technological advantages and constraints. At present, it is clear that not all of the possible variations on the buffer gas method have been studied. In this review, we will present a survey of the current state of the art in buffer gas beams, and explore some of the possible future directions that these new methods might take.

Compared to supersonic expansion, the buffer gas cooled beam method uses a fundamentally different approach to cool molecules into the few kelvin regime. The production of cold molecules (starting from hot molecules) is achieved by initially mixing two gases in a cold cell with dimensions of typically a few cm. The two gases are the hot "species of interest" molecules, introduced at an initial temperature T_0 typically between 300–10,000 K, and cold, inert "buffer" gas atoms, cooled to 2–20 K by the cold cell. The buffer gas in the cell is kept at a specifically tuned atom number density, typically $n = 10^{14-17}$ cm^{-3}, which is low enough to prevent clustering due to three body collisions involving the target molecule, yet high enough to provide enough collisions for thermalization before the molecules touch (and therefore freeze to) the walls of the cold cell. A beam of cold molecules can be formed when the buffer gas and target molecules escape the cell through a few-millimeter-sized orifice, or a more complicated exit structure, into a high vacuum region as shown in Figure 3.2. For certain buffer gas densities, the buffer gas aids in the extraction of molecules into the beam via a process called "hydrodynamic enhancement" or "hydrodynamic entrainment"[183]. In addition, when the mass of the molecule is larger than that of the buffer gas atom, there is a velocity-induced angular narrowing of the molecular beam, which increases the on-axis beam intensity[183]. Although such enhancement

has long been recognized in room-temperature beams[7], it is seldom employed because it requires intermediate Reynolds numbers, in conflict with the high Reynolds numbers necessary for full supersonic cooling of molecules in the beam. In buffer gas cooled beams, on the other hand, the intermediate Reynolds number regime is often ideal for creation of cold, slow, bright beams, and allows this technique to take full advantage of the intensity enhancement from angular narrowing.

With cryogenic cooling, high gas densities are not needed in the buffer cell to cool into the few kelvin regime. In the case of supersonic beams, the high gas densities required in the source can be undesirable in some situations (see Section 3.2.3). In the case of buffer gas beams, the cryogenic environment and relatively low flow of buffer gas into the high vacuum beam region allows for near 100% duty cycle (continuous) beam operation, without relying on external vacuum pumps. Rather, internal cryopumping provides excellent vacuum in the beam region. This combination of characteristics has led to high-brightness cold molecule sources for both chemically reactive (e.g. pulsed cold ThO, producing 3×10^{11} ground state molecules per steradian during a few ms long pulse[130]) and stable molecules (e.g. continuous cold O_2, producing $\approx 3 \times 10^{13}$ cold molecules per second[183]).

3.1.1   Cold atoms and molecules

In the past two decades, the evaporative cooling of atoms to ultracold temperatures at high phase space density has opened new chapters for physics and led to exciting discoveries, including the realization of Bose-Einstein condensation[8, 64], strongly correlated systems in dilute gases[51, 258], and controlled quantum simulation[220,

Table 3.1: A comparison of supersonic, effusive, and buffer gas cooled beams for selected molecules. The intensity is the number of molecules per quantum state per second, and the velocity is reported in the forward direction. If the angular spread of the beam is known, then the intensity per unit solid angle (i.e. brightness) is given. The ND_3 sources are velocity-selected. For pulsed sources, the intensity is given by the number of molecules per pulse times the pulse rate; if no pulse rate is given then the source is continuous. For chemically reactive molecules, buffer gas sources can provide both significantly higher brightness and slower forward velocity. See Table 3.2 for more data about experimentally realized buffer gas cooled beams.

Method	Species	Intensity $[s^{-1}]$	Rate $[s^{-1}]$	Velocity $[m\ s^{-1}]$
Chemically reactive polar molecules				
Buffer gas	ThO[130]	3×10^{13} sr^{-1}	100	170
Buffer gas	SrF[18]	1.8×10^{12} sr^{-1}	15	140
Buffer gas	CaH[162]	5×10^{9} sr^{-1}	10	40
Supersonic	YbF[231]	1.4×10^{10} sr^{-1}	10	290
Supersonic	BaF[200]	1.3×10^{10} sr^{-1}	20	500
Effusive	SrF[236]	5×10^{11} sr^{-1}	–	650
Effusive	ThO[130, 1]	1×10^{11} sr^{-1}	–	540
Stable molecule with significant vapor pressure at 300 K				
Buffer gas	ND_3[237, 226]	1×10^{11}	–	65
Supersonic	ND_3[26, 27]	1×10^{8}	–	280
Stark Decelerated	ND_3[26, 27]	1×10^{6}	–	13
Effusive	ND_3[134]	2×10^{10}	–	40
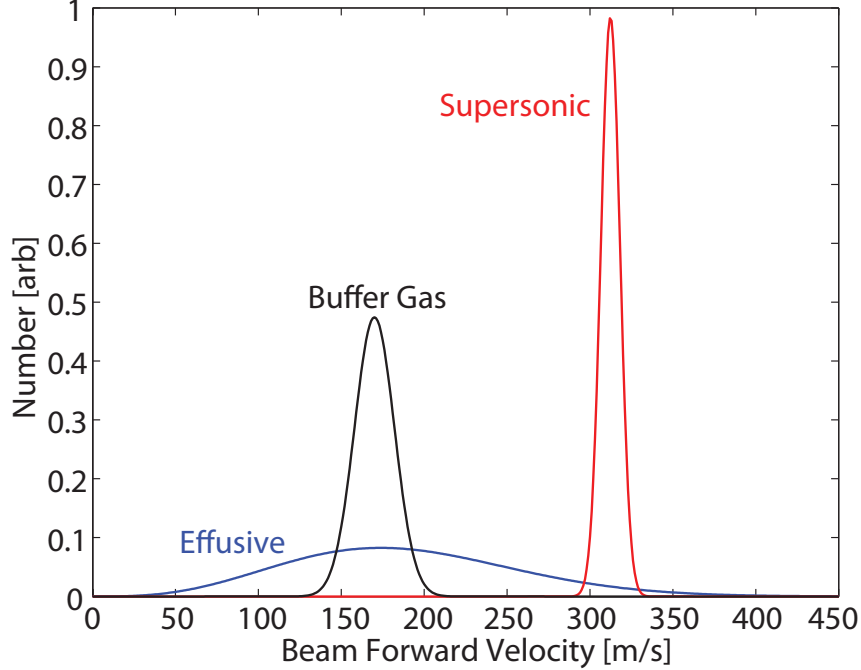
Figure 3.1: Schematic velocity distributions for selected effusive, supersonic, and buffer gas cooled beam sources. The buffer gas cooled beam properties are taken from a ThO source with neon buffer gas[130]. The effusive beam is a simulated room temperature source of a species with mass of 100 amu, and the simulated supersonic source uses room temperature xenon as the carrier gas. Compared to the effusive beam, the buffer gas beam has a much lower temperature (i.e. smaller velocity spread). Compared to the supersonic beam, the buffer gas beam has a comparable temperature but lower forward velocity. Supersonic sources typically have a much higher average forward velocity than the one presented above (≈ 600 m s^{-1} for room temperature argon, or ≈ 1800 m s^{-1} for room temperature helium)[175], and effusive sources for many species (like ThO[130, 1]) would require oven temperatures of > 1000 K, making the distribution much wider and with a much higher mean. The distributions above are normalized; however, for many species the buffer gas source would have considerably higher flux. See Table 3.1 for experimental data about some specific beams.

107]. Meanwhile, the success of cold atom methods and new theory has inspired the vigorous pursuit of molecule cooling. Molecules are more complex than atoms and possess two key features not present in atoms: additional internal degrees of freedom, in the form of molecular rotation and vibration, and the possibility (with polar molecules) to exhibit an atomic unit of electric dipole moment in the lab frame, which can lead to systems with long range, anisotropic, and tunable interactions. The rich internal structure and chemical diversity of molecules could provide platforms for exploring science in diverse fields, ranging from fundamental physics, cold chemistry, molecular physics, and quantum physics[48, 149]. We will list just a few of these applications here.

- Molecules have enhanced sensitivity (as compared to atoms) to violations of fundamental symmetries, such as the possible existence of the electron electric dipole moment[140, 55, 126, 16], and parity-violating nuclear moments[104, 75].

- The internal degrees of freedom of polar molecules have been proposed as qubits for quantum computers[66], and are ideal for storage of quantum information[199, 9, 48].

- The long-range electric dipole-dipole interaction between polar molecules may give rise to novel quantum systems[173, 153, 253].

- Precision spectroscopy performed on vibrational or hyperfine states of cold molecules can probe the time variation of fundamental constants, such as the electron-to-proton mass ratio and the fine structure constant[70, 124, 95, 233, 234].

- Studies of cold molecular chemistry in the laboratory play an important role in understanding gas-phase chemistry of interstellar clouds, which can be as cold as 10 K[214, 127, 143, 221].

- Ultracold chemical reactions have been observed at a temperature of a few hundred nK, with reaction rates controllable by external electric fields[180, 178].

- Molecular collisions in the few partial wave regime reveal the molecular interaction in great detail[47, 103, 148].

The most common way to cool atoms to ultracold temperatures, defined as the temperature (typically $\lesssim 1$ mK) where only $s-$wave collisions occur (for bosons), is laser cooling[111]. This technique relies on continuously scattering photons from atoms to dissipate the atom's motional energy. Typically $\sim 10^4$ photon scattering events are needed to significantly reduce the kinetic energy of the atom. Molecules generally lack closed transitions that can easily cycle this many photons because the excited states of the molecules can decay to many vibrational or rotational states. Because laser cooling molecules is more difficult than it is with atoms (and has only been demonstrated relatively recently[219, 218, 19, 128]), there continue to be broad efforts in developing new molecule cooling methods in order to fully control the internal and motional degrees of freedom of molecules[74, 100, 48, 25]. Additionally, many of these new proposed methods could work well with laser cooling, in some form.

In general, cooling techniques for molecules can be broadly classified into two types: indirect and direct[74, 100]. Hot molecules can be directly cooled through several methods, including supersonic expansion[217, 175] (often followed by beam slowing[238]) and buffer gas cooling[46]. Indirect cooling relies on assembling two

laser-cooled atoms into a bound molecule using photoassociation or magnetoassociation. The resulting molecules have the same translational temperature as their ultracold parent atoms but are typically in a highly excited vibrational state, which can be transferred (typically by a coherent transfer method, such as STIRAP[22]) to the absolute ground state. While indirect methods can access ultracold polar molecules with a high phase space density, these molecules are currently limited to a combination of the small subset of atoms which have been laser and evaporatively cooled, such as the alkali and alkaline earth atoms. Currently, high-density samples of ultracold polar molecules have only been demonstrated with a single species, KRb[177]. Since many atoms are not easily amenable to laser cooling, there is a large class of molecules that are the focus of direct cooling; this class includes many of the molecules that are desirable for the applications listed above[48].

3.1.2 Buffer gas cooling and beam production

At the heart of the buffer gas beam technique is buffer gas cooling[46, 172] (also called collisional cooling), which works by dissipating the energy of the species of interest via elastic collisions with cold, inert gas atoms, such as helium or neon. The first application of this technique was by the De Lucia group[172], who used it to study CO-He collisions at 4 K and later extended it to perform a large number of experiments on different molecules, some of which are discussed in our review paper[129]. Unlike laser cooling, this cooling mechanism does not depend on the internal structure of the species, and can therefore be applied to nearly any atom or small molecule[46], and certain large molecules[187, 186, 184]. Helium maintains a
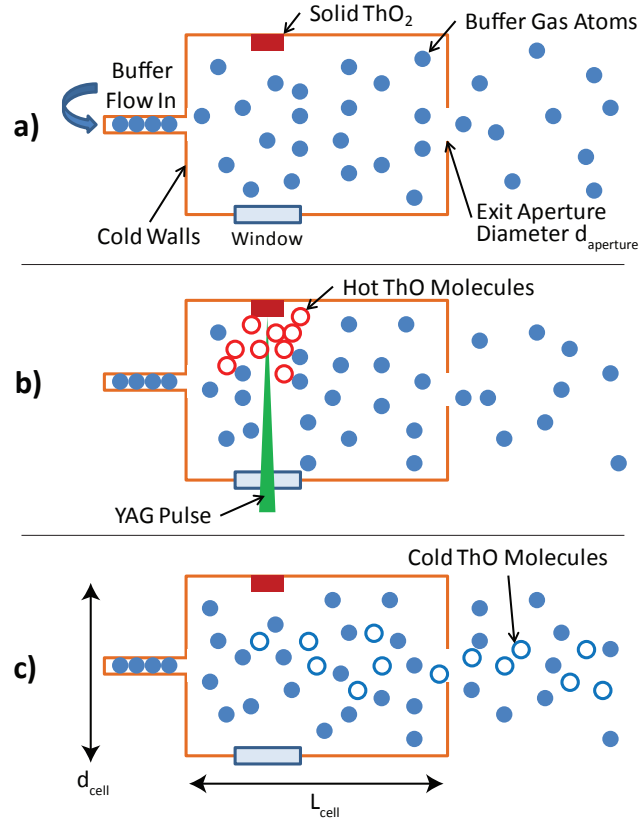
Figure 3.2: A simplified schematic of a buffer gas beam cell, which is maintained at a temperature of few K. (a) The buffer gas (typically helium or neon) enters the cell through a fill line and exits via a cell aperture on the other side of the cell. (b) Introduction of species via laser ablation. (c) The species thermalizes to the buffer gas and forms a molecular beam with the flowing buffer gas.

sufficient vapor pressure down to a few hundred mK[99, 46], and the typical helium-molecule elastic cross section[46] of $\sim 10^{-14}$ cm^2 means that buffer gas cooling and trap loading can be realized with modest cell sizes of a few $\times$ few $\times$ few cm^3. In this thesis we shall focus solely on the production and application of buffer gas beams; for further discussion of the buffer gas cooling technique, the reader is referred to the review by Campbell and Doyle[46] and the references contained therein.

As shown in Figure 3.2, a buffer gas beam is formed simply by adding an exit aperture to one side of a cold cell filled with a buffer gas. A constant buffer gas density is maintained by continuously flowing the buffer gas through a fill line on the other side of the cell. Figure 3.2(b) shows laser ablation, one of several methods used to introduce molecules of interest into the cell (Section 3.3.1). After production and injection of molecules in the buffer gas cell, the molecules thermalize with the buffer gas translationally and rotationally, and are carried out of the cell with the flowing buffer gas, forming a molecular beam (Figure 3.2(c)).

3.2 Effusive and Supersonic Beam Properties

For the sake of comparison, we will briefly review some properties of effusive and supersonic beams. Detailed discussions may be found in existing literature[217, 190, 175].

3.2.1 Characterization of gas flow regimes

In this chapter we will typically use the Reynolds number to characterize gas flow. The Reynolds number is defined as the ratio of inertial to viscous forces in a fluid

flow[98, 241]

$$\mathcal{R} = \frac{F_{intertial}}{F_{viscous}} = \frac{\rho w^2 d^2}{\mu w d} = \frac{\rho w d}{\mu}, \tag{3.1}$$

where ρ is the density, w is the flow velocity, μ is the (dynamic) viscosity, and d is a characteristic length scale (in the case of beams, d is the aperture diameter $d_{aperture}$). The Reynolds number can be related to kinetic quantities by the von Kármán relation[227, 241]

$$\mathcal{M} \approx \frac{1}{2}\mathcal{K}\mathcal{R}, \tag{3.2}$$

where $\mathcal{K} = \lambda/d$ is the Knudsen number, λ is the mean free path, $\mathcal{M} = w/c$ is the Mach number, and

$$c \equiv \sqrt{\frac{\gamma k_B T}{m}} \tag{3.3}$$

is the speed of sound in a gas with specific heat ratio γ and atomic mass m. The mean free path is given by[115]

$$\lambda = (n\sigma\sqrt{2})^{-1}, \tag{3.4}$$

where n is the number density and σ is the elastic collision cross section for the atoms. Near the aperture, the gas atoms are traveling near their mean thermal velocity

$$\bar{v} = \sqrt{\frac{8k_B T}{\pi m}}, \tag{3.5}$$

which for a monoatomic gas ($\gamma = 5/3$) is approximately the speed of sound ($c \approx 0.8\bar{v}$). This means that $\mathcal{M} \approx 1$ near the aperture, or

$$\frac{1}{2}\mathcal{K}\mathcal{R} \approx 1. \tag{3.6}$$

When we discuss the Reynolds number in a buffer gas cell, we specifically mean the Reynolds number of the buffer gas (not the species) at the aperture so that Eq. (3.6)

applies. In general, we shall ignore the species when discussing properties of the gas flow since the species is typically a very small fraction and therefore does not influence the buffer gas flow properties significantly[129].

According to Eq. (3.6), $\mathcal{R} \approx 2\mathcal{K}^{-1} = 2d_{aperture}/\lambda_{b-b}$, or about twice the number of collisions within one aperture diameter of the aperture, i.e. "near" the aperture. In some of the previous buffer gas literature[185], the number of collisions near the aperture is used in lieu of the Reynolds number. In Eq. (3.21) and Eq. (3.22) we will see that the in-cell buffer gas density, buffer gas flow rate, Reynolds number, and number of collisions near the aperture are all linearly related. The possible types of flow can be roughly divided into three Reynolds number regimes:

- *Effusive regime, $\mathcal{R} \lesssim 1$:* In this regime there are typically no collisions near the aperture, so the beam properties are simply a sampling of the thermal distribution present in the cell. This is the regime where effusive beams operate, and will be discussed in Section 3.2.2.

- *Intermediate, or partially hydrodynamic regime, $1 \lesssim \mathcal{R} \lesssim 100$:* Here there are enough collisions near the aperture to change the beam properties from those present in the cell, but not enough so that the flow is fluid-like. Buffer gas beams typically operate in this regime; however, we will see examples of buffer gas beams in all three regimes.

- *Fully hydrodynamic, or "supersonic" regime, $100 \lesssim \mathcal{R}$:* In this regime the buffer gas begins to behave more like a fluid, and the beam properties become similar to those of a beam cooled via supersonic expansion. This is the regime where supersonic beams operate, and will be discussed further in Section 3.2.3.

3.2.2   Effusive beams

In an effusive gas flow from an aperture, the typical escaping gas atom has no collisions near the aperture ($\mathcal{R} \lesssim 1$). Therefore, the resulting beam can be considered as a random sampling of the velocity distribution in the cell. A typical setup is a gas cell with a thin exit aperture, where the thickness of the aperture and the aperture diameter $d_{aperture}$ are both much smaller than the mean free path of the gas at "stagnation" (steady-state) conditions. Note that the effusive beams under discussion in this section are from oven-type effusive sources, i.e. where the vapor pressure of the species of interest is large at the source temperature (as opposed to buffer gas cooled effusive sources, which can operate at temperatures where the species has no appreciable vapor pressure).

The number density in the beam resulting from a differential aperture area dA is given by[190]

$$n_{eff}(R, v, \theta) = n_{eff}(R, \theta) f(v) \, dv \tag{3.7}$$

$$n_{eff}(R, \theta) = \frac{n_0 \cos(\theta)}{4\pi R^2} dA, \tag{3.8}$$

$$f(v) = \frac{32}{\pi^2 \bar{v}^3} v^2 e^{-4v^2/\pi(\bar{v})^2}, \tag{3.9}$$

where R is the distance from the aperture, θ is the angle from the aperture normal, n_0 is the stagnation density in the cell, $n(R, \theta)$ is the total number density distribution integrated over velocity, and $f(v)$ is the normalized velocity distribution in the cell. Notice that Eq. (3.7) is different from the corresponding equation published in[129], which is missing a factor of dv. The velocity distribution in the beam is given by

$$f_{beam}(v) = (v/\bar{v}) f(v) = \frac{32}{\pi^2 \bar{v}^4} v^3 e^{-4v^2/\pi(\bar{v})^2}. \tag{3.10}$$

From the velocity distribution we can extract the mean forward velocity of the beam,

$$\bar{v}_{\parallel,eff} = \int_0^\infty v f_{beam}(v) \, dv = \frac{3\pi}{8}\bar{v} \approx 1.2\bar{v}. \tag{3.11}$$

From the total number density in the beam $n(R,\theta)$, we can extract the FWHM (full-width at half-maximum) of the characteristic angular spread $\Delta\theta$ by solving $n(R, \Delta\theta/2) = \frac{1}{2}n(R,0)$, which gives

$$\Delta\theta_{eff} = \frac{2\pi}{3} = 120°, \tag{3.12}$$

or the characteristic solid angle

$$\Delta\Omega_{eff} = 2\pi(1 - \cos(\Delta\theta_{eff}/2)) = \pi. \tag{3.13}$$

This angular spread is very simple to determine from transverse and longitudinal Doppler spectroscopic data; if a beam has a transverse velocity spread $\Delta v_\perp$ and forward velocity $v_\parallel$, then (see Figure 3.3)

$$\Delta\theta = 2\arctan\left(\frac{\Delta v_\perp/2}{v_\parallel}\right) \tag{3.14}$$

The discussion above ignores the fact that the aperture is an extended source; however, these relationships are valid in the far field.

The rate $\dot{N}$ at which molecules escape the cell and therefore enter the beam is simply the molecular flow rate through an aperture (the same equation commonly used in vacuum engineering),

$$\dot{N} = \frac{1}{4}n_{0,b}\bar{v}_0 A_{aperture}, \tag{3.15}$$

where the subscript 0 indicates in-cell, stagnation conditions. Effusive beams of some species have very large fluxes, such as certain metal atoms or low-reactivity molecules
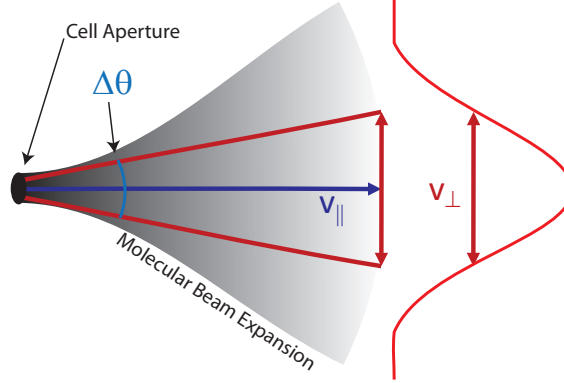
Figure 3.3: An illustration showing the relationship between the forward velocity $v_\parallel$, transverse velocity spread $\Delta v_\perp$, and angular spread $\Delta\theta$ from Eq. (3.14), $\tan(\Delta\theta/2) = (\Delta v_\perp/2)/v_\parallel$. The gray shaded region indicates the spatial extent of the molecular beam, with darker indicating higher density.

with high vapor pressure. For alkali metals[111], the cell (or oven) temperature required to achieve a vapor pressure of 1 torr is between around 500 and 1000 K. The flow through a 1 mm^2 aperture is then around $10^{14} - 10^{15}$ s^{-1}. Note that in this situation there is no buffer gas.

The beam resulting from an effusive source may not be immediately useful for some applications. The large forward velocity (typically several hundred m s^{-1}) can limit experimental interrogation time, and broad velocity distributions can lead to significantly broadened spectral lines. Some atoms can be slowed and cooled using powerful optical techniques[111]; however, molecules have, until recently[219, 218, 19, 128], resisted these optical techniques due to their complex internal structure. In addition, molecules have internal degrees of freedom which can be excited by the large temperatures in an oven. The rotational energy constant for diatomic molecules is typically 1–10 K $\times k_B$, so at typical oven temperatures the molecules can be distributed over hundreds or thousands of rotational states.

3.2.3 Fully hydrodynamic, or "supersonic" beams

In a fully hydrodynamic, or "supersonic," beam, the gas experiences many collisions near the exit aperture (typically $\mathcal{R} \gtrsim 100$), and therefore the beam properties are determined by the flow properties of the gas. In this case we cannot apply simple gas kinetics as in the case of effusive beams, but instead must consider the dynamics of a compressible fluid. Our simple treatment will not do justice to the very large number of supersonic beam techniques, so the reader is referred to reviews and texts on the subject[217, 190, 175, 158].

If there is a small amount of a species of interest mixed (or "seeded") in with the main "carrier" gas, then there are usually enough collisions such that the species will follow the carrier gas flow lines, and will be in thermal equilibrium. Therefore the properties discussed for the carrier gas should be very similar for the species gas as well. The species of interest can be mixed with the carrier gas in the source if the species has significant vapor pressure at the source temperature. The introduction of chemically reactive or refractory species is challenging due to the short mean free path between collisions in the source, and these species are often introduced into the expansion plume[123, 96, 72, 231]. This technique has opened the supersonic expansion technique to a large number of interesting species, thought the brightness of the resulting beam is typically smaller than those which are seeded in the source.

For a monatomic gas with specific heat ratio $\gamma = 5/3$, the number density and temperature in a supersonic expansion are related by[175]

$$\frac{n}{n_0} = \left(\frac{T}{T_0}\right)^{3/2}. \tag{3.16}$$

In the far field (typically more than four times the aperture diameter away from the aperture[190]), the number density will fall off as a point source, $n(R) \propto R^{-2}$, where R is the distance to the aperture. Therefore $T(R) \propto R^{-4/3}$, so unlike in the case of an effusive beam, the temperature decreases as the beam expands. There is a simple intuitive explanation for why cooling should take place in a beam expanding into vacuum: Near the aperture, gas atoms receive collisions primarily in the forward direction, which increases their forward velocity (see Section 3.3.2). Gas expansion into a vacuum is free and adiabatic, so this increase in forward velocity must come at the expense of random thermal motion in order to preserve total energy. Therefore, the beam cools as it expands and accelerates.

The temperature will continue to decrease until the gas density becomes low enough that collisions stop, the gas ceases to act like a fluid, and the gas atoms simply fly ballistically. This transition is often called "freezing" or "quitting," and occurs when the mean number of collisions remaining in the expansion becomes fewer than the number of collisions required to achieve thermalization[190]; this is ≈ 1 for translational temperatures, or more for internal degrees of freedom (see Section 3.3.1). Increasing the backing pressure P_0 can be used to further reduce the temperature of the molecules, though at high enough pressures cluster formation can begin to reduce the beam intensity[119]; however, even from a room-temperature supersonic source, it is not uncommon to have beam-frame temperatures of around 1 K, and techniques exist which can produce molecules with sub-kelvin temperatures[88]. If the species has internal structure (i.e. electronic, vibrational, and rotational states that can be thermally populated), and if there are sufficiently large inelastic, internal-state-changing

collision cross sections with the carrier gas, then the internal temperatures can be thermalized as well[217, 12, 13].

The relationship between the forward velocity and temperature of an ideal monatomic gas expansion is given by[190]

$$v_{\parallel,ss} = \sqrt{\frac{5k_B(T_0 - T)}{m}}. \tag{3.17}$$

If the gas is allowed to expand a long enough distance such that $T \ll T_0$, then the final forward velocity is

$$v_{\parallel,ss} = \sqrt{\frac{5k_B T_0}{m}} = \bar{v}_0 \sqrt{\frac{5\pi}{8}} \approx 1.4\bar{v}_0. \tag{3.18}$$

One of the standard supersonic sources is argon expanding from a 300 K cell, which has a forward velocity of about 600 m s^{-1}. A more technically challenging source uses xenon expanding from a 210 K cell, which has a forward velocity of about 300 m s^{-1}.

The number density as a function of the distance R and the angle θ from the aperture normal is given approximately by[10]

$$n_{ss}(R, \theta) = n(R, 0) \cos^2 \left(\frac{\pi\theta}{2\phi} \right), \tag{3.19}$$

where $\phi \approx 1.4$ for a monatomic gas. We can then find the angular spread $\Delta\theta$ and solid angle $\Delta\Omega$ as in Eqs. (3.12) and (3.13) to be

$$\Delta\theta_{ss} = \phi \approx 1.4 = 79°, \quad \Delta\Omega_{ss} \approx 1.4. \tag{3.20}$$

The above discussion assumes a "sonic nozzle" (i.e. the vacuum-side of the aperture is a hole in a flat plate), though there are many techniques which may be used to reduce the angular divergence of a supersonic expansion[217]. Special nozzle geometries, such as the Even-Lavie pulsed valve[88], de Laval nozzle[205] and conical

nozzles[119, 164] can reduce the angular spread of a supersonic expansion significantly. Other techniques include using slit-shaped apertures[5, 161, 159, 6] to reduce the divergence in one dimension, and aerodynamic focusing[91, 7] for seeded beams with a large seed-carrier mass mismatch. These techniques will typically change other properties of the expansion as well, and the reader is referred to the cited literature for details.

A typical supersonic source has a backing pressure $P_0 \sim 1$ atm, and $d_{aperture} \sim 1$ mm^2. The gas flow rate from the aperture can be on the order of 1 standard liter per second, which would make keeping good vacuum in the apparatus difficult if the beam were to operate continuously. For this reason, supersonic beams are often pulsed to reduce time-averaged gas load on the vacuum system. Continuous, or "Campargue"-type[44, 217] supersonic beams are possible, although they introduce many technical challenges.

3.3   Buffer Gas Cooled Beams

We will present the details of buffer gas cooled beam production and properties in this section. In our treatment, we shall assume that the buffer gas is a noble gas, and that the species of interest is seeded in the buffer gas flow with a low fractional concentration, about 1% or less. We will often refer to the species of interest as "the molecule," even though buffer gas cooled beams of atoms are also of interest. As is typically the case, we shall assume that the species of interest is heavier than the buffer gas; however, the analysis is easily extended to lighter molecules.

Table 3.2: A list of molecules which have been cooled in buffer gas beams, along with any measured properties. The output is either reported as molecules per state per pulse for pulsed (ablation-loaded) beams, or per second for continuous (capillary-loaded) beams. If an angular spread was measured, the brightness is reported as molecules per state per unit steradian (sr) per pulse or per second. $v_\parallel$ is the forward velocity and $\Delta v_\parallel$ is the full-width at half-maximum of the forward velocity distribution. A dash (–) means that the beam property was not reported in the indicated references. Notes: A) beam used a slowing cell, B) species was loaded by capillary and beam was velocity selected or guided by electromagnetic fields, C) flux reported is after beam collimation, D) Output is not reported; this value is estimated by assuming a 10% extraction efficiency.

Species	Output/Brightness	$v_\parallel[\mathrm{m\ s^{-1}}]$	$\Delta v_\parallel[\mathrm{m\ s^{-1}}]$
Molecules			
BaF[200]	1.6×10^{11} sr^{-1} pulse^{-1}	–	–
CaH[162][A]	$5 - 500 \times 10^8$ sr^{-1} pulse^{-1}	40–95	65
CH$_3$F[226][B]	–	45	35
CF$_3$H [226][B]	–	40	35
H$_2$CO[237][B]	–	–	–
ND$_3$[185][B]	$3 - 200 \times 10^8$ s^{-1}	60–150	25–100
ND$_3$[237, 226][B]	$1 - 10 \times 10^{10}$ s^{-1}	65	50
ND$_3$[211][B]	1×10^{11} s^{-1}	100	–
O$_2$[183][B]	3×10^{12} s^{-1}	–	–
PbO[167]	$3 - 100 \times 10^8$ sr^{-1} pulse^{-1}	40–80	30–40
SrF[18]	$1 - 12 \times 10^{10}$ sr^{-1} pulse^{-1}	125–200	60–80
SrO[191]	$3 - 100 \times 10^9$ sr^{-1} pulse^{-1}	65–180	35–50
ThO[130]	$1 - 30 \times 10^{10}$ sr^{-1} pulse^{-1}	120–200	30–45
YbF[223]	$4 - 20 \times 10^9$ sr^{-1} pulse^{-1}	130–250	35–75
YO[128][D]	1×10^9 pulse^{-1}	120	40
Atoms			
K[185]	1×10^{16} sr^{-1} s^{-1}	130	120
Na[167]	$2 - 400 \times 10^8$ sr^{-1} pulse^{-1}	80–135	60-120
Rb[163][C]	3×10^{10} s^{-1}	190	25–30
Yb[183]	5×10^{13} sr^{-1} pulse^{-1}	130	–
Yb[183][A]	5×10^{10} pulse^{-1}	35	–
Yb[43]	–	90–170	25–50

3.3.1 Species production, thermalization, diffusion, and extraction

In this section we present estimates of physical parameters that can be used to support an intuitive understanding of the processes occurring in the buffer gas cell. These derivations will all be approximate, and will vary depending on geometry, species, introduction method, temperature range, density range, etc. However, they are typically correct within an order of unity.

Buffer gas flow through the cell

Consider a buffer gas cell as depicted in Figure 3.2. The cell has a volume of $V_{cell} = A_{cell} \times L_{cell}$, where L_{cell} is the length of the cell interior, and $A_{cell} \approx d^2_{cell}$ is the cross-sectional area (which may be round or square, but has a characteristic length of d_{cell}). L_{cell} is typically a few cm, and A_{cell} is typically a few cm^2. The cell is held at a fixed temperature T_0 by a cryogenic refrigerator, typically between 1 K and 20 K. Buffer gas of mass m_b is introduced into the cell volume by a long, thin tube, or "fill line". The buffer gas exits the cell through an aperture of characteristic length $d_{aperture}$ and area $A_{aperture}$ (for the case where the aperture is a rectangle, $d_{aperture}$ is the shorter dimension). Typical values are $d_{aperture} = 1-5$ mm, and $A_{aperture} = 5-25$ mm^2. A buffer gas flow rate $f_{0,b}$ into the cell can be set with a mass flow controller. Here the subscript "b" refers to the buffer gas, and "0" refers to stagnation conditions in the cell. The most commonly used unit for gas flow is the standard cubic centimeter per minute, or SCCM, which equals approximately 4.5×10^{17} gas atoms per second. Typical flow rates for buffer gas beams are $f_{0,b} = 1 - 100$ SCCM.

At steady state, the flow rate out of the cell is given by the molecular conductance of the aperture, $f_{out} = \frac{1}{4} n_{0,b} \bar{v}_{0,b} A_{aperture}$, where $\bar{v}$ is the mean thermal velocity of the buffer gas inside the cell (Eq. (3.5); about 140 m s^{-1} for 4 K helium or 17 K neon), k_B is Boltzmann's constant, and $n_{0,b}$ is the stagnation number density of buffer gas atoms. Therefore, the number density $n_{0,b}$ is set by controlling the flow via the steady-state relationship $f_{out} = f_{0,b}$, or

$$n_{0,b} = \frac{4 f_{0,b}}{A_{aperture} \bar{v}_{0,b}}. \tag{3.21}$$

With typical cell aperture sizes and temperatures, a flow of 1 SCCM corresponds to a stagnation density of about 10^{15} cm^{-3}, so typical values for the stagnation density are $10^{15} - 10^{17}$ cm^{-3}. Note that in the above equation we assume that the flow through the aperture is purely molecular. At higher number densities the flow can become more fluid-like, and then the flow rate out will change; however, the difference is about a factor of two[190], so the above equation is suitable for approximation.

Combining Eqs. (3.21), (3.6), and (3.4) allows us to relate the buffer gas flow f_0 to the Reynolds number at the aperture,

$$\mathcal{R} \approx \frac{2 d_{aperture}}{\lambda_{b-b,0}} \approx \frac{10 f_{0,b} \sigma_{b-b}}{d_{aperture} \bar{v}_{0,b}}, \tag{3.22}$$

which we shall use to parameterize the flow regime in later sections. Using $\sigma_{b-b} \approx 3 \times 10^{-15}$ and assuming a 4 K helium or 18 K neon buffer source, we find $\mathcal{R} \approx 0.7 \times (f_0/(1 \text{ SCCM})) \times (d_{aperture}/(4.5 \text{ mm}))$, so for our beam source the relationship $\mathcal{R} \approx (f_0/(1 \text{ SCCM}))$ is a good approximation.

Introduction of species

The species of interest can be introduced into the buffer gas cell through a number of methods[46], including laser ablation, light-induced atomic desorption (LIAD[116]), beam injection, capillary filling, and discharge etching. The most commonly used techniques for creation of buffer gas cooled beams are laser ablation and capillary filling, but we shall restrict our discussion to laser ablation since that is the technique we use to create our ThO beam.

In laser ablation (see Figure 3.2), a high energy pulsed laser is focused onto a solid precursor target. After receiving the laser pulse, the solid precursor can eject gas-phase atoms or molecules of the desired species, often along with other detritus. The actual mechanism for how gas phase species results from the ablation of the solid precursor is not simple, and depends on the relationship between the length of the laser pulse, and the time constants for electronic and lattice heating[50, 179]. While pulsed ablation has been studied with pulse widths from femtoseconds to milliseconds, the most common ablation laser (used for the majority of experiments in Table 3.2) is the pulsed Nd:YAG, which can easily deliver up to 100 mJ of energy in a few ns. Either the fundamental (1064 nm) or first harmonic (532 nm) wavelengths are used, and neither seems to have a distinct advantage over the other, except for certain technical conveniences afforded by a visible laser. The ablation laser is typically directed through a converging lens, with the target placed at the focus.

The review by Campbell and Doyle[46] has a partial list of species which have been ablated and buffer gas cooled. Vapors of metals such as Na[167] or Yb[183] can be easily produced by ablation of the solid metal, and the yields are often large

and consistent; however, creation of gas phase molecules by laser ablation can be more complicated, and varies significantly by species and solid percursor production method. Molecules with a stable solid phase (such as PbO[167]) can be created by simply using the solid phase as a precursor, but unstable molecules require careful choice of precursor. It is often the case that the desired diatomic molecule MX has a stable solid form $M_a X_b$ which is a glass or ceramic, as is the case with BaF, CaH, SrF, YO, ThO, and others. In such cases, experience has shown that pressing (and sometimes sintering) a very fine powder of the stable solid often yields the best ablation target[130, 18]. Ablation targets that mix multiple species can also be prepared with guidance from known chemical reactions; for example, a heated mixture of SrF_2+B can be used to create an effusive beam of SrF[236], and Barry *et al.*[18] found that a pressed mixture of SrF_2+B made a superior ablation compared to the several other ablation targets that they tested. In general, ablation targets are best found by trial and error, and several ablation targets may need to be tested before one is chosen[18].

The most important advantage of laser ablation is that it can be used to create a very wide variety of atoms and molecules with high flux[46]. The main drawback is that ablation is typically a "violent," non-thermal process that can result in unusual behavior of the gases in the cell, and in the resulting beam. The dependence of the yield on pulse energy, focus, and location on the target varies significantly by species, and the ablation process can create plasmas and complex plumes[102] with temperatures of several thousand K[63]. However, buffer gas cells can be designed to allow proper thermalization of the species, which can mitigate many of these problems.

It should be noted that regardless of technique, the density of the species is typically (though not in the case of some capillary filling schemes[237, 226]) $< 1\%$ of the number density of the buffer gas. This fact will be important later on, because it allows us to treat the the gas flow properties as being determined solely by the buffer gas, with the species as a trace component.

Thermalization

Before the species flows out of the cell, it must undergo enough collisions with the cold buffer gas to become thermalized to the cell temperature. A simple estimate of the necessary number of collisions can be obtained by approximating the species and buffer gases as hard spheres[65, 141]. The mean loss in kinetic energy of the species per collision with a buffer gas atom results in a mean temperature change of

$$\Delta T_s = -(T_s - T_b)/\kappa, \text{ where } \kappa \equiv \frac{(m_b + m_s)^2}{2m_b m_s}. \tag{3.23}$$

Here T denotes temperature, m denotes mass, and the subscripts "b" and "s" refer to the buffer gas and species of interest, respectively. Therefore, the temperature of the species after $\mathcal{N}$ collisions, $T_s(\mathcal{N})$, will vary as

$$T_s(\mathcal{N}) - T_s(\mathcal{N} - 1) = -(T_s(\mathcal{N} - 1) - T_b)/\kappa \tag{3.24}$$

If we treat $\mathcal{N}$ as large and the temperature change per collision as small, we can approximate this discrete equation as a differential equation:

$$\frac{dT_s(\mathcal{N})}{d\mathcal{N}} = -(T_s(\mathcal{N}) - T_b)/\kappa. \tag{3.25}$$

Solving this differential equation yields the ratio between the species and buffer gas temperatures:

$$\frac{T_s(\mathcal{N})}{T_b} = 1 + \left(\frac{T_s(0)}{T_b} - 1\right)e^{-\mathcal{N}/\kappa} \tag{3.26}$$

$$\approx 1 + \frac{T_s(0)}{T_b}e^{-\mathcal{N}/\kappa}, \tag{3.27}$$

where in the last equality we have assumed that the species is introduced at a temperature much larger than the cell (and therefore buffer gas) temperature, i.e. $T_s(0) \gg T_b$. If we estimate $m_b \sim 10$ amu, $m_s \sim 100$ amu, $T_b \sim 10$ K, and $T_s(0) \sim 1000$ K, the species should be within a few percent of the buffer gas temperature after ~ 50 collisions.

If the species is loaded via ablation, then the buffer gas will itself be heated and require some time (potentially much longer than the time required for ~ 50 collisions) to cool back down to the cell temperature. This effect can be very significant for sources operating with cells below 4 K, but is not a concern for the ThO beam.

The mean free path of a species molecule in the buffer gas cell is given by[115]

$$\lambda_{s-b,0} = \frac{(n_{0,b}\sigma_{b-s})^{-1}}{\sqrt{1 + m_s/m_b}} \approx \frac{A_{aperture}\bar{v}_{0,b}}{4f_{0,b}\sigma_{b-s}\sqrt{m_s/m_b}} \tag{3.28}$$

where σ_{b-s} is the thermally averaged elastic collision cross section (since the cross section typically varies with temperature), we assume $m_s \gg m_b$, and have used Eq. (3.21). For typical values of $\sigma_{b-s} \approx 10^{-14}$ cm^2, this mean free path is ~ 0.1 mm. Therefore, the thermalization length for the species in the buffer gas cell is typically no more than 100×0.1 mm $= 1$ cm.

Note that the above discussion has pertained only to translational temperatures, yet buffer gas cooling is also effective at thermalization of internal states. Typical

rotational relaxation cross sections for molecules with helium buffer gas are of order $\sigma_{rot} \sim 10^{-(15-16)}$ cm^2, which means that around $\sigma_{b-s}/\sigma_{rot} \sim 10-100$ collisions are required to relax (or "quench") a rotational state[46]. Since this is comparable to the number of collisions required for motional thermalization, buffer gas cooling can be used to make samples of molecules which are both translationally and rotationally cold. Vibrational relaxation is less efficient, since the cross sections for vibrational quenching are typically several orders of magnitude smaller than those for translational or rotational relaxation[46]. Several experiments[249, 45, 18] have seen the vibrational degree of freedom not in thermal equilibrium with the rotational or translational degrees of freedom. Further discussion of internal relaxation of molecules may be found elsewhere[158, 46, 217, 190, 172, 13, 12].

Diffusion

Once the species of interest is introduced into the cell and thermalized, we must consider the diffusion of the species in the buffer gas. Understanding the diffusion is crucial since the buffer gas cell is typically kept at a temperature where the species of interest has essentially no vapor pressure, and if it is allowed to diffuse to the cell walls before exiting the cell it will freeze and be lost. The diffusion constant for the species diffusing into the buffer gas is[115]

$$D = \frac{3}{16(n_{0,s} + n_{0,b})\sigma_{b-s}} \left(\frac{2\pi k_B T_0}{\mu} \right)^{1/2},$$ (3.29)

where $\mu = m_s m_b / (m_s + m_b)$ is the reduced mass. It should be noted that different works use different forms for the diffusion coefficient[46, 222], though they agree to within factors of order unity and are all suitable for making estimates. If we make

the approximations $n_{0,s} \ll n_{0,b}$ and $m_s \gg m_b$, we find

$$D = \frac{3}{16 n_{0,b} \sigma_{b-s}} \left(\frac{2\pi k_B T_0}{m_b} \right)^{1/2} = \frac{3\pi}{32} \frac{\bar{v}_{0,b}}{n_{0,b} \sigma_{b-s}}, \tag{3.30}$$

After a time t, a species molecule will have a mean-squared displacement of

$$\langle \Delta x^2 \rangle (t) = 6Dt = \frac{9\pi}{16} \frac{\bar{v}_{0,b}}{n_{0,b} \sigma_{b-s}} t \tag{3.31}$$

from its starting point[182]. Since the characteristic length of the cell interior is the cross-sectional length d_{cell}, we can define the diffusion timescale τ_{diff} as $\langle \Delta x^2 \rangle (\tau_{diff}) = d_{cell}^2 \approx A_{cell}$, or

$$\tau_{diff} = \frac{16}{9\pi} \frac{A_{cell} n_{0,b} \sigma_{b-s}}{\bar{v}_{0,b}}. \tag{3.32}$$

The diffusion time is typically 1-10 ms. Skoff *et al.*[222] performed a detailed theoretical analysis and compared the results to measured absorption images in order to understand diffusion of YbF and Li in a helium buffer gas, and the reader is referred to their paper for more information.

Extraction from the buffer cell

So far we have not considered the beam at all, having focused entirely on the in-cell dynamics. Once the species of interest is created in the gas phase and cooled in the buffer gas cell, it is necessary that the species flow out of the cell so that it can create a beam. As discussed above, extraction of the species from the cell must occur faster than the diffusion timescale τ_{diff}, so an important parameter is the extraction or "pumpout" time. The rate at which the buffer gas out of the cell is given by the molecular conductance of the cell aperture,

$$\dot{N}_b = \frac{1}{4} N_b \bar{v}_{0,b} A_{aperture}/V_{cell}, \tag{3.33}$$

where N_b indicates the total number of buffer gas atoms in the cell, and $\dot{N}_b$ is the

rate at which they are flowing out of the cell. The solution is an exponential decay

with timescale τ_{pump}, the pumpout time, given by

$$\tau_{pump} = \frac{4V_{cell}}{\bar{v}_{0,b} A_{aperture}}. \tag{3.34}$$

The pumpout time is typically around 1-10 ms. Note that the pumpout time also

sets the duration of the molecular pulse in the case of a beam with pulsed loading.

If the buffer gas density in the cell is high enough that the species of interest follows

the buffer gas flow, then this is a good estimate for the pumpout time for the species

of interest as well. We now define[183] a dimensionless parameter to characterize the

extraction behavior of the cell

$$\gamma_{cell} \equiv \frac{\tau_{diff}}{\tau_{pump}} = \frac{4}{9\pi} \frac{n_{0,b}\sigma_{b-s}A_{aperture}}{L_{cell}} \approx \frac{\sigma_{b-s}f_{0,b}}{L_{cell}\bar{v}_{0,b}}, \tag{3.35}$$

where in the last step we used Eq. (3.21) and dropped an order-unity prefactor, as

this is simply an estimate. This parameter γ_{cell} characterizes the extraction behavior,

and can be divided into two limits (see Figure 3.12).

For $\gamma_{cell} \lesssim 1$, the diffusion to the walls is faster than the extraction from the

cell, so the majority of species molecules will stick to the cell walls and be lost. This

"diffusion limit"[183] is characterized by low output flux of the molecular species, and

is typically accompanied by a velocity distribution in the beam that is similar to that

inside the cell[167]. In this limit, increasing the flow (thereby increasing γ_{cell}) has the

effect of increasing the extraction efficiency f_{ext}, defined as the fraction of molecules

created in the cell which escape into the beam. The precise dependence of f_{ext} on γ_{cell} is highly variable, and has been observed to be approximately linear, exponential, or cubic for the various species which have been examined[167, 183, 130, 18].

For $\gamma_{cell} \gtrsim 1$, the molecules are mostly extracted from the cell before sticking to the walls, resulting in a beam of increased brightness. This limit, called "hydrodynamic entrainment" or "hydrodynamic enhancement"[183], is characterized by high output flux of the molecular species, and is typically accompanied by velocity distribution which can vary considerably from that present inside the cell. In this regime, the extraction efficiency plateaus and can be as high as >40%[183], but is typically observed to be around 10%[18, 130, 43]. While the formula for γ_{cell} does not contain the aperture diameter, we shall see in Section 3.3.7 that as the aperture becomes small ($\lesssim 3$ mm diameter), the extraction efficiency drops significantly.

Regardless of the value for γ_{cell}, thermalization must occur on a timescale faster than either τ_{pump} or τ_{diff} to cool the species. Since neither τ_{diff} nor τ_{pump} impose strict constraints on the cell geometry, it is possible to have both good thermalization and efficient extraction, as demonstrated by the large number of high flux, cold beams created with the buffer gas method (see Table 3.2).

By examining Eq. (3.22) for the Reynolds number, which governs the gas flow regime, and Eq. (3.35) for the extraction parameter γ_{cell}, which governs the species extraction regime, we can see that they are related by a factor which depends on the cell geometry,

$$\frac{\gamma_{cell}}{\mathcal{R}} \propto \frac{d_{aperture}}{L_{cell}}. \tag{3.36}$$

This means that, at least in principle, it is possible to separately control the ex-

traction efficiency (governed by γ_{cell}), and the flow regime (governed by $\mathcal{R}$). Most buffer gas sources operate either in the effusive or intermediate flow regimes, and it is experimentally challenging to design a beam which is completely effusive, has good extraction, and sufficient thermalization. A purely effusive beam should have a forward velocity which, according to Eq. (3.11), does not change with source pressure; however, in buffer gas beam sources with good extraction[167, 130, 18, 226] the forward velocity of the molecules indeed changes with source pressure. Slowing cells[183, 162, 129] can offer near-effusive velocity distributions, but typically have $\sim 1\%$ extraction efficiency[183, 162].

3.3.2 Forward velocity

The forward velocity of the species in a buffer gas beam depends on the Reynolds number of the buffer gas flow, and behaves differently in the effusive, intermediate, and supersonic regimes, though it is typically smaller than supersonic or effusive sources (see Figure 3.1, Table 3.1). This behavior is shown schematically in Figure 3.4, and some data from our ThO beam is shown in Figure 3.5

If the beam is in the effusive regime, then there are typically no collisions near the aperture, and the forward velocity of the beam $v_{\parallel,s}$ is given by the forward velocity of an effusive beam (3.11), where the appropriate thermal velocity is that of the species, *i.e.*

$$v_{\parallel,s} \approx \frac{3\pi}{8}\bar{v}_{0,s} \approx 1.2\bar{v}_{0,s} \qquad (\mathcal{R} \lesssim 1). \tag{3.37}$$

In the intermediate regime, the molecules undergo collisions with the buffer gas atoms near (i.e. within one aperture diameter of) the cell aperture, whose average

velocity is $\bar{v}_{0,b}$. This is larger than that of the (typically) heavier species $\bar{v}_{0,s}$ by a factor of $\sqrt{m_s/m_b}$. Since the collisions near the aperture are primarily in the forward direction, the species can be accelerated, or "boosted," to a forward velocity, $v_{\parallel,s}$, which is larger than the thermal velocity of the molecules (just as with supersonic beams[217]). We shall divide the situation where collisions must be considered into three regimes, based on the Reynolds number.
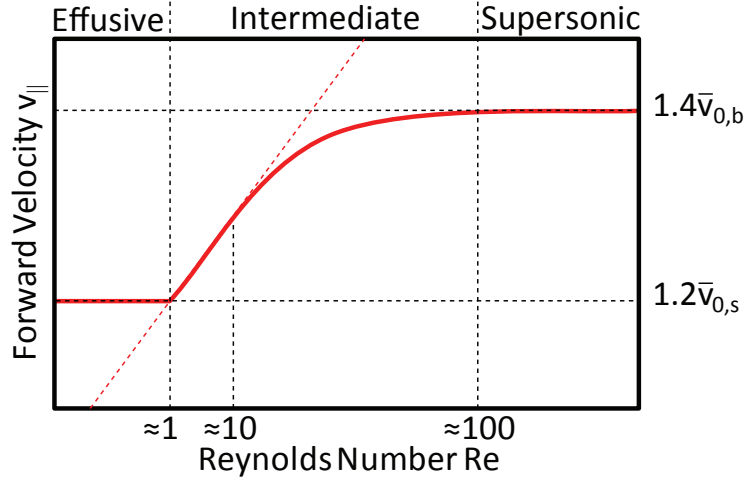
Figure 3.4: A schematic representation of beam forward velocity vs. Reynolds number and buffer gas flow. In the effusive regime ($\mathcal{R} \lesssim 1$), the forward velocity is the thermal velocity of the (heavy) species. In the intermediate regime, collisions of the species with the buffer gas near the aperture accelerate the species; the velocity increase is linear with the Reynolds number until $\mathcal{R} \approx 10$, and then begins to asymptote to the final value. In the supersonic regime ($\mathcal{R} \gtrsim 100$), the species has been fully accelerated to the forward velocity of the (light) buffer gas. Each of these regimes is discussed in detail below.

Few-collision regime: $1 \lesssim \mathcal{R} \lesssim 10$

If there are few collisions, we can estimate the relationship between $\mathcal{R}$ and $v_{\parallel,s}$ with a simple model from Maxwell *et al.*[167]. Near the aperture, the molecules
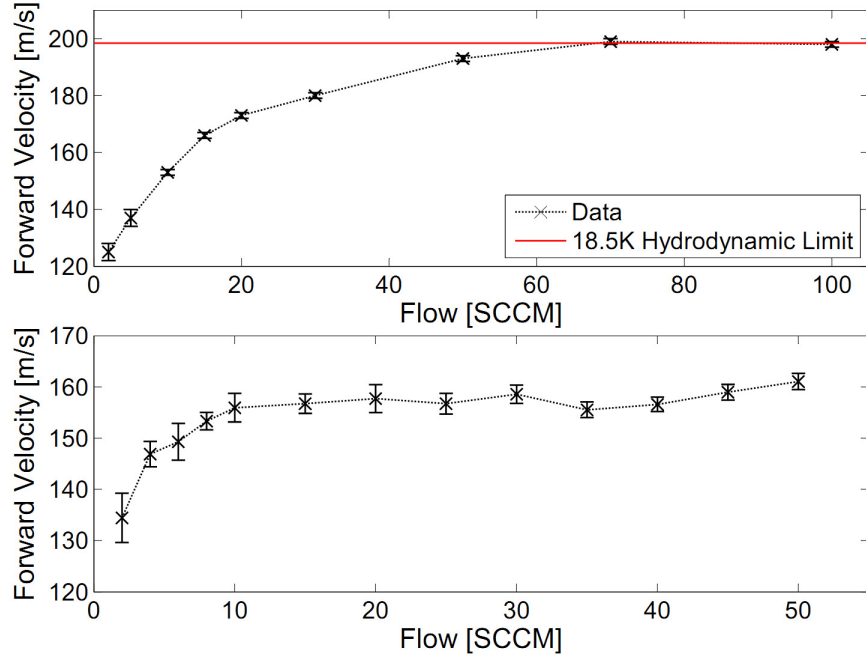
Figure 3.5: Top: Mean forward velocity vs. flow rate with neon buffer gas. The solid line is the hydrodynamic limit for the forward velocity of neon atoms exiting an 18.5 K cell, given by Eq. (3.18). The forward velocity of the molecules with neon buffer gas cooling varies by no more than 10% over a pulse. Bottom: Mean forward velocity vs. flow rate with helium buffer gas. For both plots data, 1 SCCM of flow corresponds to $\mathcal{R} \approx 0.7$ according to Eq. (3.22).

undergo approximately $\mathcal{R}/2$ collisions. Each of these collisions gives the molecules a momentum kick in the forward direction of about $\approx m_b v_b$, so the net velocity boost is $\approx v_b m_b \mathcal{R}/2m_{mol}$. Since there are a small number of collisions, the forward velocity of the buffer gas is approximately given by the mean forward velocity of an effusive beam Eq. (3.11), $v_{\|,b} \approx 1.2\bar{v}_{0,b}$, so for $1 \lesssim \mathcal{R} \lesssim 10$ (we shall justify the $\mathcal{R} \lesssim 10$ cutoff later on),

$$v_{\|,s} \approx \bar{v}_{0,s} + \bar{v}_{0,b}\mathcal{R}\frac{m_b}{m_{mol}}. \tag{3.38}$$

Therefore, the forward velocity should increase linearly with $\mathcal{R}$ (and therefore with in-cell buffer gas density, or buffer gas flow). Several studies[167, 130, 18] have considered the behavior of $v_{\|,s}$ vs. $\mathcal{R}$, and have seen this linear dependence at low $\mathcal{R}$. In Figure 3.6, we compare the measured forward velocity of our ThO beam to this model and find good agreement between the measured and predicted slope.
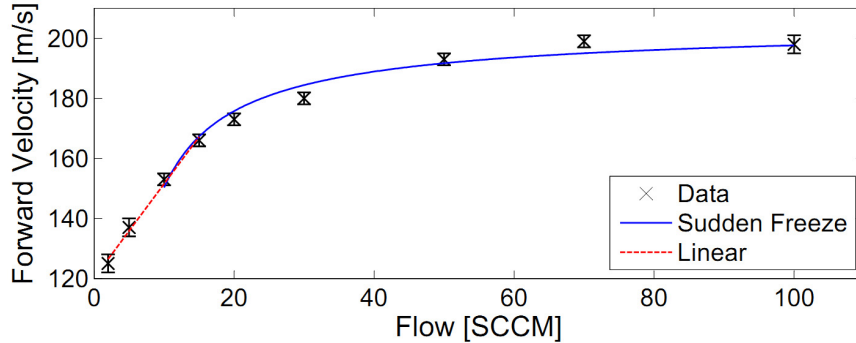
Figure 3.6: Forward velocity for neon buffer gas with a 4.5 mm aperture, along with a linear fit at low flow and a sudden freeze fit at high flow. The linear model has a slope of 3.1±0.8 (m/s)/SCCM, in good agreement with our estimate of 4.5 (m/s)/SCCM presented in the text. The sudden freeze fit is to the function $v = \alpha\sqrt{1 - \beta f^{-4/5}}$, with parameters $\alpha = 205 \pm 6$ m/s, $\beta = 3.0 \pm 0.5$. The parameters are close to the expected values of $\alpha \approx 200$ m/s (the final velocity) from experiment, and $\beta \approx 3$ from the estimate presented in the text. For this data, 1 SCCM of flow corresponds to $\mathcal{R} \approx 0.7$ according to Eq. (3.22).

Intermediate regime: $10 \lesssim \mathcal{R} \lesssim 100$

The above model necessarily breaks down as $v_{\parallel,s}$ approaches $\sim \bar{v}_{0,b}$, since the maximum possible forward velocity is $1.4\bar{v}_{0,b}$ (from Eq. 3.18), the forward velocity of a fully hydrodynamic buffer gas expansion. We therefore expect that the forward velocity should saturate to this value at large enough $\mathcal{R}$, and this behavior has been seen in buffer gas beams with high flow rates[130, 18].

We can model the shape of the velocity vs. flow curve with the "sudden freeze" model[190], in which we assume that the molecules are in equilibrium with the buffer gas until some distance where the density is low enough that the gases decouple, and the molecular beam properties are frozen. The velocity of the buffer gas scales with the density n as

$$v(x) \approx 1.6 v_{\mathrm{p},0} \left[1 - \left(\frac{n(x)}{n_0} \right)^{2/3} \right]^{1/2}, \tag{3.39}$$

where $v_{p,0} = (2k_B T_0/m_{\mathrm{b}})^{1/2}$ is the most probable velocity of the buffer gas in the cell (≈ 120 m/s for 17 K Ne), k_B is Boltzmann's constant, x is the distance from the cell aperture, n_0 is the cell stagnation density, and the collision cross section is estimated to be $\sigma \approx 3 \times 10^{-15}$ cm^2. Introducing the normalized distance $\xi \equiv x/d_{aperture}$, the far-field number density scales as $n(\xi)/n_0 \approx 0.2\xi^{-2}$, so $v(\xi) \approx 1.6 v_{\mathrm{p},0} \sqrt{1 - 0.3\xi^{-4/3}}$. For a monoatomic hard-sphere gas, the location where collisions freeze is given by

$$\xi_0 \approx (0.1\sigma n_0 d_{aperture})^{3/5} \approx 0.2 \left(\frac{f_0}{1 \text{ SCCM}} \right)^{3/5} \tag{3.40}$$

where in the last equality we used $d_{aperture} = 4.5$ mm to get a numerical value for the data presented in Figure 3.6. The 3/5 exponent is model dependent and should be considered approximate. Therefore, if we assume that the molecules and buffer gas

are in equilibrium until the position ξ_0, the final molecule velocity will be given by

$$v(\xi_0) \approx 1.6 v_{p,0} \left[1 - 3 \left(\frac{f_0}{1 \text{ SCCM}} \right)^{-4/5} \right]^{1/2} . \tag{3.41}$$

This sudden-freeze model is valid when there are collisions in the beam, *i.e.* when $\xi_0 \gtrsim 1$, which from equation (3.40) occurs at approximately 10 SCCM neon flow with the 4.5 mm aperture. Below this flow we are in the regime where the forward velocity increases linearly[167], so we can fit a line to the flows $\gtrsim 10$ SCCM and the sudden freeze model for flows ≥ 10 SCCM, as shown in Figure 3.6.

Hydrodynamic regime: $100 \lesssim \mathcal{R}$

Finally, for large enough $\mathcal{R}$, there should be enough collisions to fully boost the molecules to the forward velocity of the buffer gas,

$$v_{\parallel,s} \approx v_{\parallel,b} \approx 1.4 \bar{v}_{0,b} \qquad (\mathcal{R} \gtrsim 100) \tag{3.42}$$

where the cutoff $\mathcal{R} \gtrsim 100$ means that $v_{\parallel,s} \gtrsim 95\% \times v_{\parallel,b}$ according to Eq. (3.18). This limit corresponds to the supersonic flow regime.

With neon buffer gas in an 18 K cell, the forward velocity (see Figure 3.5) approaches a value that is very close to the final velocity of ≈ 200 m/s predicted by Eq. (3.18). With helium buffer gas, the mean forward velocity approaches about 70% of the value 230 m/s predicted by equation (3.18) for a 5 K cell. The lower-than-expected value for the helium-cooled beam is likely due to collisions with the background helium that accumulates due to the limited pumping speed of the activated charcoal, which is not a problem with neon because once it sticks to a 4 K surface, it remains there nearly indefinitely (i.e. has negligible vapor pressure at 4 K). Increasing the

amount of charcoal and improving its placement mitigated this problem; however, the issue persisted. Further discussion is presented in Section 3.3.8.

Time dependence of forward velocity

Interpretation of our helium forward velocity data was additionally complicated by the fact that, unlike with the case of neon buffer gas, it varies in time over the molecule pulse duration, as shown in Figure 3.7. This dependence of beam properties on time after ablation is perhaps due to the finite amount of time required to thermalize the ThO molecules in the buffer gas cell, which is much smaller with neon due to neon's smaller mass mismatch with ThO, and the fact that the heat introduced by ablation results in a smaller fractional change in temperature at 18 K versus 5 K. Additionally, the forward velocity with helium buffer gas varies by as much as $\sim 10\%$ if the ablation spot is moved, and as the charcoal cryopumps become full of helium and the pumping speed changes, as discussed in section Section 3.3.8. These effects were not observed with neon buffer gas.
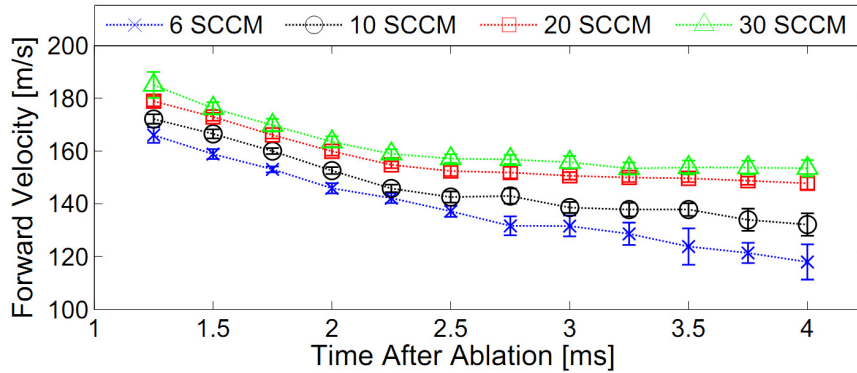
Figure 3.7: Forward velocity vs. time after ablation for several different flows rates of the helium buffer gas. For this data, 1 SCCM of flow corresponds to $\mathcal{R} \approx 0.7$ according to Eq. (3.22).

Isentropic expansion

The boosting effect discussed above can be detrimental if one aims to produce a slow beam, which is one of the benefits of buffer gas beams over supersonic beams and effusive "oven" beams. One would therefore prefer to operate the beam in the effusive flow regime, i.e. at a low Reynolds number. It is possible to keep the Reynolds number fairly low while maintaining good extraction ($\gamma_{cell} > 1$) by using a slit-shaped aperture, as we will now discuss. Consider the aperture as having a short and long dimension, so that $A_{aperture} = d_{short} \times d_{long}$. For a fixed internal cell geometry, buffer gas, species, and cell temperature, we can see from Eqs. (3.22) and (3.35) that $\mathcal{R} \propto d_{short} n_{0,b}$ and $\gamma_{cell} \propto n_{0,b} A_{aperture}$, therefore $\gamma_{cell}/\mathcal{R} \propto d_{long}$. In other words, by increasing d_{long} but keeping $A_{aperture}$ fixed, we can decrease $\mathcal{R}$ without changing γ_{cell} or the buffer gas density. Note that simply changing the aperture size while leaving all other parameters fixed also has the effect of changing $\mathcal{R}$ but not γ_{cell}, though this is not ideal for two reasons: First, the in-cell buffer gas density is constrained to be large enough that the species is thermalized, but small enough that the molecules can diffuse away from the injection point[222], and this method would change the buffer gas density. Second, as we shall see in Section 3.3.7, reducing the aperture size can in fact have a negative effect on the extraction for small enough aperture sizes. For these reasons, earlier buffer gas beam papers tended to use a slit[167] aperture, typically around 1×5 mm. Similar slit apertures are also used in supersonic expansions[217, 175, 5, 161, 159, 6] to reduce Doppler broadening along the slit dimension and allow longer optical interaction lengths.

The downside of high $\mathcal{R}$ flows can also come with a benefit: Isentropic cooling

from the free expansion of a gas, similar to what happens in supersonic beams[175]. This effect was first observed in buffer gas cooled beam from a hot oven[185, 163], and subsequently characterized by with our ThO beam[130] and a beam of SrF[18]. In each case, the molecules were found to cool rotationally and translationally below the temperature of the cell, as we shall see in following sections.

3.3.3   Forward (longitudinal) velocity spread

In the effusive limit, the velocity spread should correspond to the thermal distribution in the cell (see Section 3.2.2). As the Reynolds number is increased, the forward velocity spread (temperature) will begin to decrease due to the isentropic expansion of the buffer gas into the vacuum region. We measured this effect with our ThO beam, and the results are show in Figure 3.8

With helium buffer gas the beam properties once again change as a function of time after ablation. Similar to the analysis for the helium forward velocity in Section 3.3.2, we can measure the time-resolved fluorescence from the molecules to extract spectral properties as a function of time after ablation. Figure 3.8 shows the forward velocity spread for the entire molecule pulse, and the mean instantaneous forward velocity spread extracted from the time-resolved spectra. The instantaneous velocity spread is comparable to that of neon; however, the changing forward velocity of the beam (see Figure 3.7) results in the forward velocity spread of the entire pulse being much larger. With neon, neither the forward velocity nor the forward velocity width change by more than 10% over the duration of the pulse.
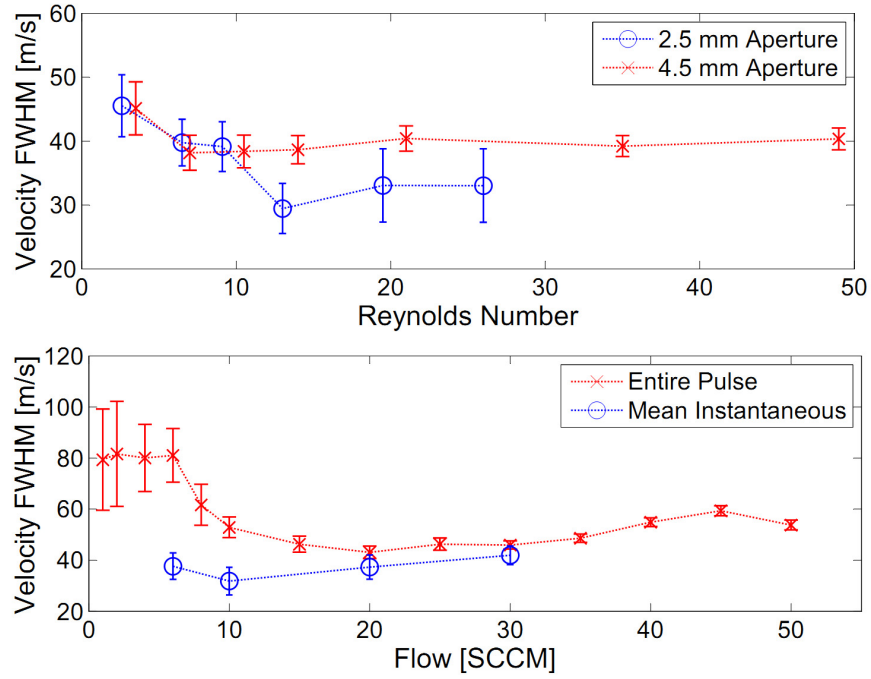
Figure 3.8: Top: The velocity spread in the forward direction with neon buffer gas. Bottom: The velocity spread in the forward direction with helium buffer gas. The data points marked by the × symbols indicate velocity spread averaged over the entire molecule pulse, while the data points marked by the ∘ symbols indicate the mean instantaneous velocity spread obtained from time-resolved fluorescence data. For this data, 1 SCCM of flow corresponds to $\mathcal{R} \approx 0.7$ according to Eq. (3.22).

3.3.4   Transverse velocity spread

Similar to the case with forward velocity, collisions between the species and buffer gas near the aperture can increase the transverse velocity spread above the value expected for an effusive beam. We can estimate the slope of the angular spread vs. flow curve with a simple model. Near the aperture, the buffer gas atoms must follow a convergent trajectory since the flow cross-section narrows from the cell diameter $d_{\text{cell}} \approx 13$ mm to the aperture diameter $d_{aperture} \approx 5$ mm. The typical mean buffer gas velocity normal to the beam axis is given approximately by the flow velocity. The relationship between the in-cell flow velocity v_{cell} and the flow velocity in the aperture, which is approximated by $v_{p,0}$, is given by $d_{\text{cell}}^2 v_{\text{cell}} \approx d_{aperture}^2 v_{p,0}$, or $v_{\text{cell}} \approx v_{p,0}(d_{\text{cell}}/d_{aperture})^2 \approx 18$ m/s. There are $\approx \mathcal{R}/2$ collisions near the aperture, so the change in the transverse spread is given by

$$\Delta v_{\perp,s} \approx \bar{v}_{0,s} + \mathcal{R}\bar{v}_{0,b}\frac{d_{cell}^2}{d_{aperture}^2}\frac{m_b}{m_{mol}}, \qquad (3.43)$$

which gives $\Delta v_{\perp,s} \approx (0.7 \text{ m/s}) \times \mathcal{R}$ for our ThO beam, in good agreement with the typical data fit value of $(0.4 \text{ m/s}) \times \mathcal{R}$ measured for several aperture sizes (see Figure 3.9). The transverse spread downstream displays similar linear increases, however modeling is complicated by the expansion dynamics. Typical slopes for the transverse spread vs. Reynolds number relationship are ~ 1 (m/s)/($\mathcal{R}$).

With neon buffer gas the transverse spread does not change by more than 10% over the duration of a single pulse of molecules, but with helium the transverse spread changes by as much as 30%. The divergence shown in Figure 3.9 was calculated using the mean spectral width, defined as the spectral width of the entire molecule pulse. As with the forward velocity data, the transverse velocity spread with helium buffer
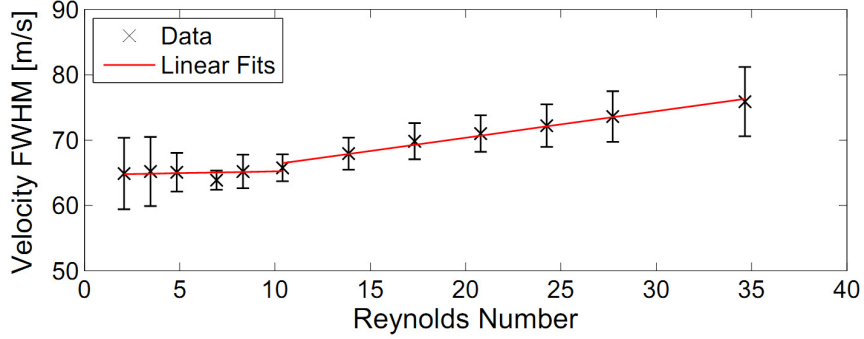
Figure 3.9: The transverse spectral width vs. Reynolds number with neon buffer gas and a 4.5 mm cell aperture, measured at the aperture. At low flows the transverse widths inside the cell and outside the cell are the same, and indicate a thermal distribution of $T \approx 20$ K. The slope of the fit line at these low flows is (0.06 ± 0.27) m/s, consistent with zero. At higher flows the transverse width in the beam begins to linearly increase, with slope (0.41 ± 0.06) m/s. Note that the transition Reynolds number agrees with that from Figure 3.6. For this aperture size, the conversion from flow to Reynolds number is $\mathcal{R} \approx 0.7 \times (\text{flow}/(1 \text{ SCCM}))$.

gas varies by as much as $\sim 10\%$ if the ablation spot is moved, and as the charcoal cryopumps become full of helium; however, the data typically falls within the error bars shown in Figure 3.10. These effects are not observed with neon buffer gas.

3.3.5   Angular spread and divergence

In the range $1 \lesssim \mathcal{R} \lesssim 10$, the forward velocity begins to increase linearly with $\mathcal{R}$ yet the transverse velocity remains constant at $\Delta v_{\perp,s} = 1.5\bar{v}_{0,s}$. Therefore, Eq. (3.14) tells us that the divergence will begin to decrease. As the molecules begin to be boosted to the forward velocity of the buffer gas $v_{\parallel,s} \approx v_{\parallel,b} \approx \bar{v}_{0,b}$, the divergence should approach

$$\Delta\theta = 2\arctan\left(\frac{\Delta v_{\perp,s}/2}{v_{\parallel,s}}\right) \approx 2\sqrt{\frac{m_b}{m_s}}, \tag{3.44}$$

where in the last approximation we assumed that $m_s \gg m_b$ and used Eq. (3.5). The solid angle spread is then approximated by

$$\Delta\Omega = 2\pi(1 - \cos(2\sqrt{m_b/m_s})) \approx \pi m_b/m_s. \tag{3.45}$$

Notice that this can be much smaller than the corresponding spreads of π for an effusive beam (Eq. 3.13), or 1.4 for a supersonic beam (Eq. 3.20). Since experiments with atomic and molecular beams are often performed at a distance from the cell aperture that is many times larger than $d_{aperture}$, this smaller angular divergence contributes to the typically large brightness of buffer gas beams.

As $\mathcal{R}$ is increased to the point where the transverse spread begins to increase yet the forward velocity has reached its maximum, the divergence will stop decreasing. We were able to see this transition from decreasing to increasing divergence for our ThO beam in neon buffer gas, shown in Figure 3.10.

The preceding discussion about the shape of the divergence vs. Reynolds number relationship is not universal, and some experiments have observed very different behavior; using helium buffer gas, both our measurements and those of and Barry *et al.*[18] observed no variation in divergence over combined range of Reynolds numbers $1 \lesssim \mathcal{R} \lesssim 150$. This was due to the fact that the increases in transverse and forward velocities canceled each other almost exactly. This indicates that while there is some proposed "universal shape" for the relationships of $v_\parallel$ and $\Delta v_\perp$ vs. $\mathcal{R}$, the Reynolds numbers where transitions in behavior occur for the two relationships need not overlap, and there is not a similar universal shape for $\Delta\Omega$ vs. $\mathcal{R}$.
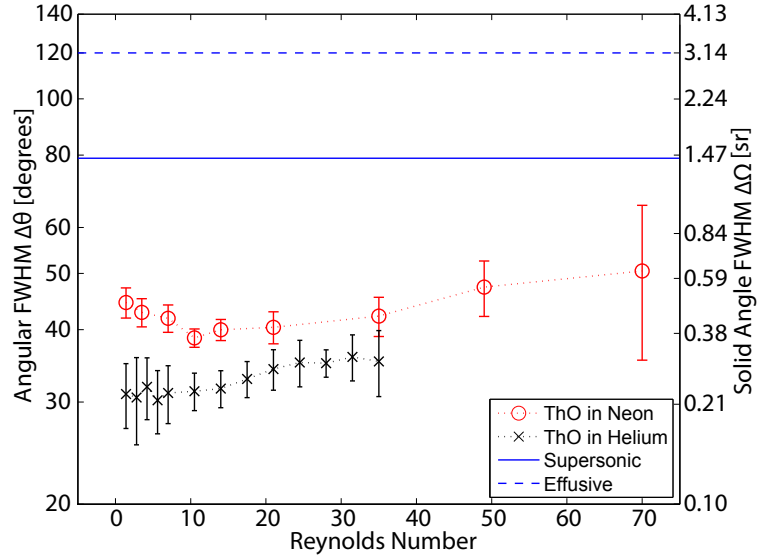
Figure 3.10: Divergence of a ThO beam in both a helium and neon cooled buffer gas beam[130]. For low Reynolds number with neon buffer gas, we are in the regime of linearly increasing forward velocity but constant transverse velocity spread. Eventually the forward velocity stops increasing and the transverse velocity starts increasing, which results in the divergence ceasing to decrease. With helium buffer gas, the divergence is essentially constant, similar to what was seen with SrF in a helium buffer gas cooled beam[18]. In all cases, the divergence compares very favorably to those of supersonic and effusive beams.

3.3.6   Rotational Temperature

As the translational temperature cools, we expect some internal cooling as well. We can observe this in our ThO beam by measuring the rotational temperature. With neon buffer gas we find that the rotational temperature decreases with both increasing Reynolds number and increasing distance from the cell aperture. The rotational temperature does not change after a distance of 2 cm after the cell, indicating that the cooling collisions have stopped before this distance. With helium buffer gas the rotational temperature is largely independent of Reynolds number, distance from the cell, and aperture size as measured with 14 different flows, three different distances after the cell, and three different aperture sizes. The temperature of the molecules just outside of the cell, however, is lower than the cell temperature, even for the lowest flow and largest aperture. This behavior is unexpected: at the lowest flow (1 SCCM) and largest aperture (4.5 mm side square), the flow regime is effusive ($\mathcal{R} \approx 1$) and so we should see no additional cooling below the cell temperature of ~ 5 K. More low-flow helium phenomena, along with possible explanations, are discussed in section Section 3.4.2.

For both buffer gases, the molecules approach some minimum rotational temperature that does not decrease with additional flow. This minimum temperature appears to be about 2-3 K, and is similar for both helium and neon. In fact, the rotational temperature just outside a 9 K cell with a helium buffer gas flow has a similar minimum temperature of 2.9 ± 1.3 K.

The minimum measured rotational temperature, measured 6 cm from the cell, as a function of buffer gas flow and aperture size, was 2.0 ± 0.8 K with neon buffer gas,
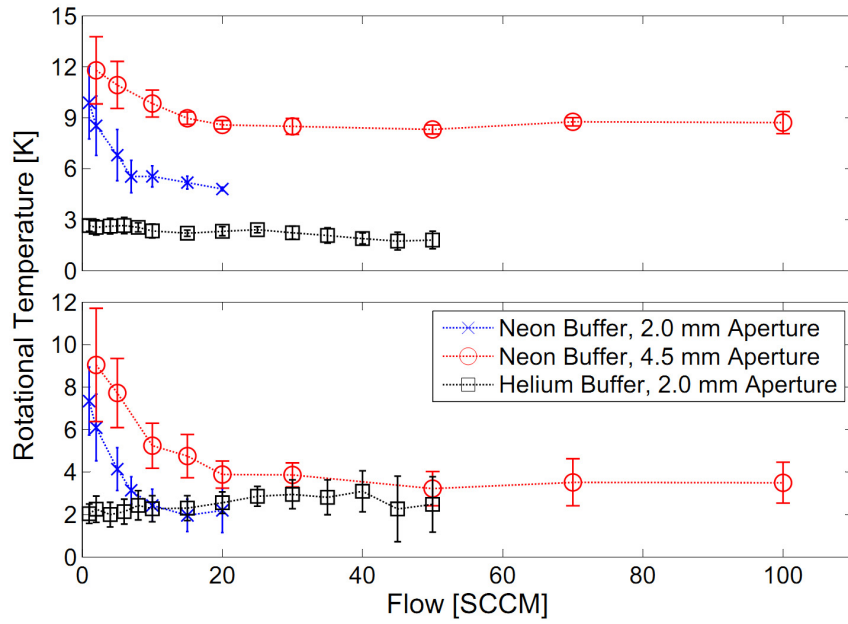
Figure 3.11: Rotational temperatures in the buffer gas cooled beam. Top: temperatures measured 1 mm from the cell aperture. Bottom: final rotational temperatures in the expansion, measured 6 cm after the cell aperture. The cell temperatures are 5±1 K and 18±1 K for helium and neon buffer gases, respectively. The data with a helium buffer gas was taken with a 2.0 mm aperture, while the data with a neon buffer gas was taken with both 2.0 mm and 6.5 mm apertures.

and 1.7 ± 0.5 K with helium buffer gas. These represent an increase of a factor of 8.2 and 2.8 in the $X, J = 0$ population with neon and helium buffer gas, respectively, from the distribution present at the cell temperature.

3.3.7 Measured Cell Extraction and Molecule Production

Figure 3.12 shows our measured molecule flux and extraction fraction. When the flow is large enough to ensure good extraction from the cell (*i.e.* $\gamma_{\text{cell}} \gtrsim 1$), typical molecule outputs are $\sim 10^{11}$ in the $X, J = 0$ absolute ground state, or $\sim 10^{12}$ total molecules (in all states) per pulse, estimated from absorption spectra taken immediately after the cell aperture. Since the temporal width of the pulse is ~ 1 ms (see Figure 3.13), the peak instantaneous output rate is $\sim 10^{14}$ molecules per second per state in $J = 0$, or $\sim 10^{15}$ total number of molecules per second. Behavior of the number of molecules output per pulse is plotted in Figure 3.12. With neon buffer gas, the flow-output behavior is very similar for different aperture sizes larger than about 3.0 mm, and has a maximum output around $\gamma_{\text{cell}} \approx 1 - 2$. With helium buffer gas, the shape of the curve is non-repeatable; specifically, the shape changes if the YAG ablation spot is moved, which is not the case with neon. However, the approximate number output is typically within a factor of two of the data in Figure 3.12 for all conditions.

According to the simple hydrodynamic entrainment theory, the extraction of molecules from the cell is governed by the parameter γ_{cell} from Eq. (3.35). This parameter does not have an explicit dependence on the aperture size; however, we find that there can be a strong dependence on aperture size that varies with gas type.

For neon buffer gas, the extraction fraction is constant for cell apertures larger than about 3 mm, then falls off rapidly with decreasing aperture size. For helium buffer gas, the maximum extraction fraction does not depend significantly on the aperture size. It should be noted that based on previous observations, both published[167, 183] and unpublished, the cell extraction is typically dependent, sometimes in puzzling ways, on species, ablation properties, internal cell geometry, and collimation geometry.
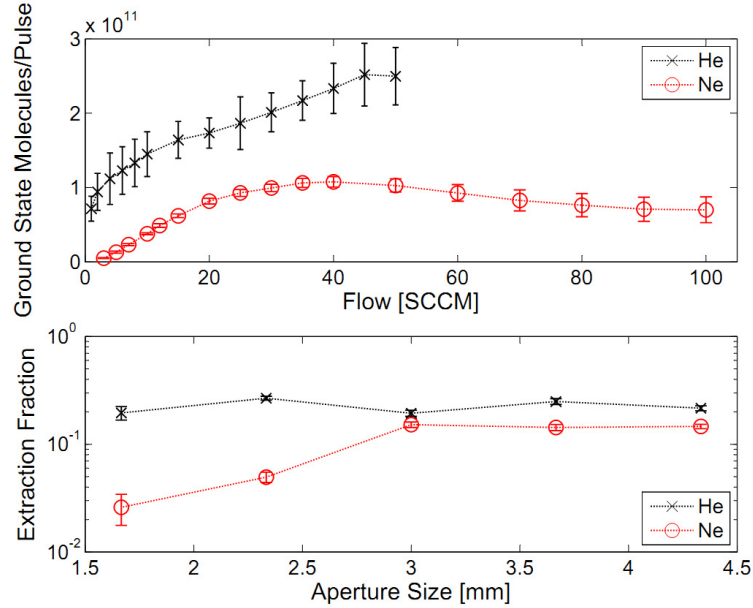
Figure 3.12: Top: Number of absolute ground state molecules output per pulse with helium and neon buffer gases, using a 4.5 mm cell aperture. Bottom: Fraction of molecules extracted out of the cell into the beam, with neon and helium buffer gases.

3.3.8   Effect of buffer gas species on beam properties

For many applications, helium is a natural choice of buffer gas. Helium has large vapor pressure at 4 K (that corresponds to an atom number density of $> 10^{19}$ cm^{-3}), which is a convenient temperature for cryogenics: Many refrigerators can cool to ~ 4

K, as can a simple liquid helium cryostat. Helium also has a large vapor pressure at even lower temperatures (< 1 K), where operating the cell will result in a colder and slower beam[183, 185]. Simple cryogenic techniques can achieve temperatures of ~ 2 K and still handle the necessary heat loads (typically ~ 30 mW); lower temperatures require a more complicated setup.

Our data shows that a beam using neon buffer gas performs nearly as well as one using helium, but with much simpler technical requirements and a much larger cryopumping speed. The minimum rotational temperatures with both helium and neon buffer gas differ by <1 K, despite the fact that the buffer gas cell sits at $\sim$5 K and $\sim$18 K for helium and neon respectively. The forward velocity and divergence of the helium-based beam are slightly lower, however both can vary as much as 30% over a single beam pulse, which is behavior not seen in our neon-based source.

In addition to time variations of beam properties within a single pulse, we find that the properties of helium-based beams also depend significantly on the location of the ablation spot, and on the pumping conditions of the buffer gas out of the beam region. Helium in the beam region can only be pumped by a large surface area adsorbent, such as activated charcoal. As the helium adsorbent fills up, the cryopumping speed begins to change, resulting in a significant change in beam properties. To keep the beam properties consistent, the adsorbent must be emptied periodically (typically every few hours for our apparatus) by heating it and then pumping the helium out of the vacuum chamber. In addition, we find that the performance of our helium-based beam is very sensitive to the amount and placement of both beam collimators and adsorbent: incorrect placement often results in the extinction of the molecular beam,

as we have observed in our apparatus and several other similar apparatus. Correct placement requires much trial and error, and is not currently understood, though has been achieved in a different ThO beam test apparatus in our group. Neither the sensitivity to the ablation spot or the charcoal placement is entirely understood.

Neon, on the other hand, is readily adsorbed by any 4 K surface, including neon ice, allowing for a cryopump of >1000 l/s in the beam region of our apparatus. We have operated the neon-based molecular beam continuously, with 30 SCCM of neon flow, for over 24 hours with little increase in background pressure and no appreciable variation in beam properties. The neon-based beam is also robust to variation of the collimator geometry. We have experimented with several cell-collimator configurations, including changing the cell-collimator distance (*in situ* via a motion feedthrough on the apparatus), and found that for all configurations with the neon-based beam, the collimator performed as expected and we have never had difficulty obtaining consistent, robust beam signal.

Another advantage of a neon-based beam is that because the cell is kept at a higher temperature, the refrigerator cooling the cell can sustain a much higher heat load. We have demonstrated operation of the neon-cooled ThO beam with nearly 10 W of input power from a 200 Hz pulsed YAG (Litron Nano TRL 80-200) and achieved stable production with single-shot yields comparable to those measured with a slower repetition rate, resulting in about a factor of 10 increase in time-averaged yield compared to the data presented earlier.

3.4   Details of the ThO Beam Study

Now that we have presented the measured properties of our molecular beam, we will describe some of the technical details of the beam source and the measurements.

3.4.1   Apparatus

The heart of our cold beam apparatus (see Figure 3.2) is similar to that which is described in earlier buffer gas cooled beam publications[167, 183, 185], and to which the reader is referred for additional technical details. It is a cryogenically cooled, cylindrical copper cell with internal dimensions of 13 mm diameter and 75 mm length. A 2 mm inner diameter tube entering on one end of the cylinder flows buffer gas into the cell. A 150 mm length of the fill line is thermally anchored to the cell, ensuring that the buffer gas is cold before it flows into the cell volume. An open aperture (or nozzle) on the other end of the cell lets the buffer gas spray out as a beam, as shown in Figure 3.2. ThO molecules are injected into the cell via ablation of a ceramic target of ThO_2, located approximately 50 mm from the exit aperture. A pulsed Nd:YAG laser[1] is fired at the ThO_2 target, creating an initially hot plume of gas-phase ThO molecules (along with other detritus of the ablation process). Hot ThO molecules mix with the buffer gas in the cell, and cool to near the cell temperature, typically between 4 and 20 K. The buffer gas is flowed continuously through the cell at a rate $f_0 = 1 - 100$ SCCM (1 SCCM = 1 cm^3/minute of gas at standard conditions, or about 4.5×10^{17} gas atoms per second). This both maintains a buffer gas stagnation

---

[1]For the data in this chapter, we used a Continuum Minilite II. For the EDM search, we used a Litron Nano TRL 80-200.

density of $n_0 \approx 10^{15} - 10^{16}$ cm^{-3} ($\approx 10^{-3} - 10^{-2}$ torr) and extracts the molecules out the aperture into a beam[183]. The result, due to the pulsed introduction of ThO into the cell, is a pulsed beam of ThO molecules (embedded in a continuous flow of buffer gas) over a 1-3 ms period, as shown in Figure 3.13. We have achieved stable operation of the neon based beam with up to a 200 Hz repetition rate; however, the data presented in this chapter was with a repetition rate of 10 Hz. The cell aperture is a square hole of adjustable side length $d_{aperture} = 0 - 4.5$ mm that can be varied *in situ* and continuously while the beam runs.

We use either helium or neon as the buffer gas. The cell temperature T_0 is maintained at 5 ± 1 K for helium, or 18 ± 1 K for neon, and is controlled by the use of resistive heaters thermally anchored to the cell. The cell is surrounded by a radiation shield at 4 K, which is partially covered in activated charcoal to form a cryopump that keeps the helium background pressure low. A second radiation shield at temperature ~ 50 K surrounds the 4 K radiation shield, and both shields have glass windows to allow the transmission of spectroscopy lasers, and holes to allow passage of the molecular beam. The radiation shields and cell are connected by flexible copper braid heat links to a pulse tube refrigerator (Cryomech PT415).

The beam exiting the cell is incident on a conical collimator with a 6 mm diameter orifice located 25 mm from the cell aperture. There are expected to be few collisions this far from the cell aperture, so for our work, the features of this collimator are more akin to those of a simple differentially pumped aperture. For helium buffer gas, the collimator is at a temperature of about 8 K. For neon buffer gas the collimator is heated to 30 K to prevent neon ice formation.

All of the cryogenic apparatus is kept inside a room-temperature vacuum chamber of internal volume ≈ 0.2 m^3. During beam operation, vacuum is maintained by cryopumping of the charcoal and radiation shields, and no external pumping on the vacuum chamber is required. However, a small (60 l/s) turbomolecular pump continuously pumps on the chamber, to pump out any gas released should the cryopumps warm up and stop pumping. The main chamber has a pressure of $< 10^{-5}$ torr during buffer gas flow, as measured with an ion gauge.

The ThO$_2$ target is constructed from ThO$_2$ powder, pressed and sintered as described in existing literature[11]. The targets used in this study were prepared by Elizabeth Petrik. These targets typically yield $\gtrsim$30,000 YAG shots on a single focus site before the yield per shot drops to 50% of the initial value, at which time the focus must be moved to a new spot. The large surface area ($\sim$1 cm^2) of the target should allow for $> 10^7$ shots before target replacement is necessary. While performing our EDM search[16], we found that a target would typically last about 1 month, which indeed corresponds to about 10^7 shots.

3.4.2   Measured Beam Properties

We studied the beam with a variety of buffer gas flows, aperture sizes, and cell temperatures for both helium and neon buffer gases using continuous wave laser spectroscopy from the ThO ground electronic state X ($v = 0$, $\Omega = 0^+$, $B_{v=0}$=0.33 cm^{-1}) to the excited electronic state C ($v = 0$, $\Omega = 1$, $T_0 = 14489.90$ cm^{-1}, $B_{v=0} = 0.32$ cm^{-1})[83] at 690 nm. Two diode lasers are each locked to a stabilized frequency source via a Fabry-Pérot transfer cavity. The frequency of one laser is scanned to

obtain spectra, while the other is kept at a fixed frequency and used to normalize against variation in the ablation yield (typically a few percent from shot-to-shot). The scanning laser detuning, Nd:YAG pulses, and data acquisition are all synchronized via a master control computer. The scanning laser is split into multiple beams and used for absorption transverse to the molecular beam at several distances after the cell aperture, and for laser-induced fluorescence (LIF) parallel to the molecular beam. Absorption data is obtained using silicon photodiodes, and laser-induced fluorescence is collected with either a CCD camera or a photomultiplier tube (PMT).

The rotational temperature was determined by fitting a Boltzmann distribution to the lowest six rotational levels ($J = 0$ to $J = 5$) of the ground state X. Population was determined from the optical density (see Figure 3.13) of absorption on the X to C transition. The lines $R(0)$, $Q(1), \ldots, Q(5)$ were used to obtain the population in $X, J = 0, 1, \ldots, 5$ respectively (the R and Q notation is explained in Section 2.7.4). Some example population distributions are shown in Figure 3.14.

The forward velocity of the ThO beam was measured at distances between about 6 cm and 16 cm from the cell aperture using laser-induced fluorescence (LIF) imaging. A counter-propagating, red-detuned pump beam excites the molecules on the $Q(1)$ or $Q(2)$ line of the $X - C$ transition, and the fluorescence is collected with either a CCD camera or a PMT. The camera gives spatial information about the beam, but since the exposure time is longer than the molecular pulse duration the camera averages over an entire pulse. To get time-dependent information, we use the PMT. We measure the first-order Doppler shift of the molecules by fitting a Gaussian shape to the obtained LIF spectrum and comparing the center to that of a transverse absorption spectrum.
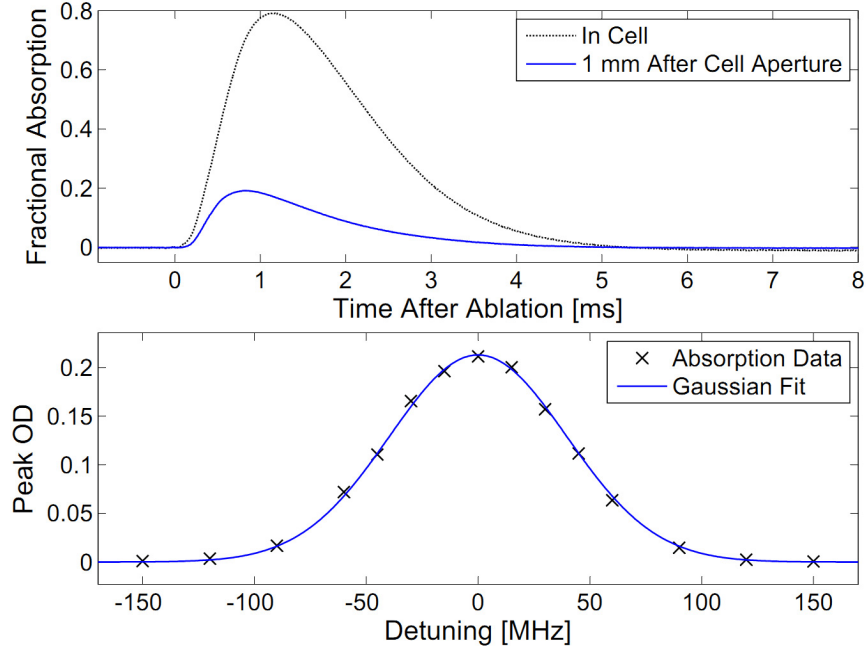
Figure 3.13: Top: An absorption signal of the ThO molecular beam in a 1 SCCM flow of helium buffer gas with a 4.5 mm diameter cell aperture. The laser is fixed spatially, so the time variation of the signal is a result of the molecular beam pulse passing through the laser. The different traces show absorption in the cell (dashed) and 1 mm after the cell aperture (solid). For this data, the laser is locked on the resonance of the X-C Q(1) line. The width and height of the signals depend on buffer gas flow rate, buffer gas species, and cell aperture size; however, the qualitative features are similar. Bottom: By varying the laser detuning, we obtain an absorption spectrum. This curve shows the absorption spectrum of the molecular beam 1 mm after the cell, with the same experimental parameters as in the top figure. Optical density (OD) is defined as $T = e^{-\mathrm{OD}}$, where T is the transmitted fraction of the probe laser light.
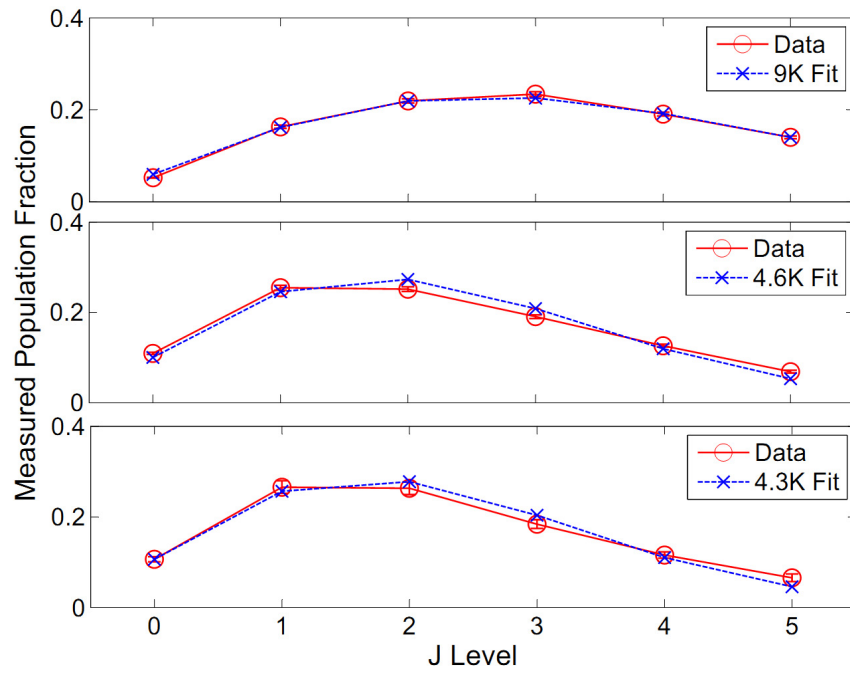
Figure 3.14: Rotational level populations with Boltzmann distribution fits for 30 SCCM neon flow, 4.5 mm aperture. The top, middle, and bottom plots show the distributions near, 2 cm from, and 6 cm from the cell aperture, respectively.

The forward velocity and velocity distribution are then inferred from the first-order Doppler shift and width of the spectrum, respectively.

High-flow neon phenomena

For very high neon flows (Reynolds number $\gtrsim 50$) the beam behavior degrades. The molecule pulse resulting from a single ablation shot begins to decompose into spatially and temporally variegated pulses with different spectral characteristics. This is likely a result of the post-ablation dynamics in the high density buffer gas inside the cell, as we have observed the onset of similar behavior occurring in high-density, ablation-loaded buffer gas cells in other species in the past (unpublished work, particularly by Max Parsons, using Yb and alkali metals). Fortunately, this behavior occurs for flows significantly above the point where the cell extraction is maximum, and therefore is not near the optimal flow for most conceivable beam-based spectroscopy experiments.

Low-flow helium phenomena

For low flows of helium the behavior of the beam is unusual and not in good agreement with other helium buffer gas beam experience[167]. At low flow there should be little extraction and poor thermalization; however, in the data presented here we have evidence of a high-extraction, well-thermalized beam at flows as low as 1 SCCM with aperture size as large as 4.5 mm, or $Re \approx 1$ and $\gamma_{\text{cell}} < 0.1$. At this flow the mean free path in the cell is a few mm, so it is surprising that there is any significant thermalization or extraction. A possible explanation for this behavior is that a helium film builds up in the cell (either on the walls or in the target) as helium

gas flows into the cell between ablation pulses. Then, when the ablation pulse hits and the helium desorbs due to ablation heating, there is a pulse of higher buffer gas pressure at the moment the ThO is introduced into the cell. Additionally, we observe that the phenomena disappear as the cell is heated, in which case we observe the expected[167] increasing extraction with increasing flow.

The strongest evidence that these effects were due to helium film buildup was that we could create a few pulses of a beam with no buffer gas flow at all. Specifically, if we turned off the gas flow after flowing for about a minute, then waited over 20 minutes, we could create a few pulses of a molecular beam by firing the YAG at the target. On the other hand, if we turned off the gas flow after flowing for about one minute, then heated the cell to around 10 K, then let the cell cool back down to 4 K, there would be no beam.

3.5   Applications to Precision Measurements

Molecular beams have important applications in the field of precision measurement. This is made possible by the lack of collisions in the beam region, and enhanced by the large volume of advanced molecular beam production, manipulation, and spectroscopy techniques[158, 201, 217, 175, 230]. Many precision measurements can benefit from the high flux and low forward velocity afforded by buffer gas cooled beams. In this section we will review some molecular beam precision measurements, and discuss how they could benefit from buffer gas cooled beam technology. Applications in other areas, such as laser cooling, collisional studies, and trap loading, are discussed in our review[129].

Electric dipole moments

As discussed in Section 1.1.2, the molecules which have the highest enhancement factor have high-Z atoms with partially filled electron shells, tend to be chemically reactive, have high melting points, and are often free radicals[55]. For this reason, effusive beam sources of these molecules are typically not feasible; the Boltzmann distribution of rotational states at temperatures where the species have appreciable vapor pressure put only a tiny fraction in any single rotational state (however, performing an electron EDM experiment with molecules in a hot vapor cell is possible[29, 77]). A molecular beam for an EDM search should therefore have low temperature, and a low forward velocity to allow the molecules to interact with the fields for a long time. For the types of molecules under consideration, buffer gas cooled beams[167, 130, 18, 16] have considerable advantages over supersonic beams, even those which have specifically optimized for production of chemically reactive polar molecules[231]. As discussed earlier, the brightness for refractory or chemically reactive species can be very high with buffer gas beams, and they have considerably slower forward velocities. In Table 3.1, we can see that a buffer gas cooled ThO beam has a slower forward velocity and over 1000 times the brightness compared to a demonstrated, state-of-the-art YbF supersonic beam, both of which are currently being used for an electron EDM search. These reasons make buffer gas cooled beams an attractive option for electron EDM searches, with some existing supersonic experiments considering switching to buffer gas cooling[222].

Parity violation and anapole moments

The exchange of weak neutral currents between the constituent particles of an atom or molecule can lead to observable parity violating effects in their spectra. Precision examinations of these effects, known as atomic parity violation (APV), allow the study of nuclear and electroweak physics using atomic systems[104]. An experimentally feasible approach to using APV to probe electroweak physics was first proposed in 1974[34], and since then APV has been observed in a number of atoms[110, 104, 235, 15]. Here we will briefly review APV and discuss how buffer gas beams may improve experimental studies of APV; detailed discussions of APV theory and experiments may be found elsewhere[104, 110, 75, 42].

Weak neutral currents. The exchange of a neutral Z_0 boson between the nucleus and the electrons in an atom can give rise a parity-violating, electronic contact potential[34]. This potential can mix atomic states of opposite parity, such as a valence electron in $S_{1/2}$ and $P_{1/2}$ atomic orbitals. This mixing can either be measured by searching for parity violating optical rotation in atomic emission/absorption[15, 34], or by looking for interference between the APV induced state mixing and the mixing provided by an external electric field (the Stark-interference method[58]). APV has been measured in a number of atoms[104, 235], and comparison to theory gives tests of the Standard Model at low energies.

Nuclear anapole moments. Another parity violating effect in an atom is the anapole moment[256, 104, 42], which arises from an exchange of a Z_0 or $W_{\pm}$ boson between nucleons in a nucleus. Like the parity-violating potential above, the interaction is a contact potential between the electrons and nuclear anapole moment.

The observable effect is very similar to that of the weak neutral currents discussed above, with the important exception that the size of the effect will vary depending on the nuclear spin. An experimental signature of an anapole moment is then a difference in parity violating amplitudes between different hyperfine levels. So far only a single anapole moment has been measured, in the ^{133}Cs nucleus[251], though other experiments are underway[75, 69, 131, 200].

Enhancement of parity violation in diatomic molecules. Parity-violating effects have thus far been observed only in atoms, though the search has been extended to diatomic molecules for very compelling reasons. Molecules have states of opposite parity (rotational states, and in some cases Λ- or Ω-doublets[117]) which are typically much closer than opposite parity electronic states in atoms, so the effects of nuclear-spin-dependent parity violation (such as anapole moments) can be greatly enhanced[152, 229, 69, 94]. This mixing can be increased even further by applying external magnetic fields to push rotational states to near-degeneracy.

Similar to the case with an EDM measurement, the shot-noise limited uncertainty in the parity violating amplitude scales as $\propto N^{-1/2}\tau^{-1}$, where N is the total number of interrogated molecules and τ is the time that the molecules spend interacting with the electromagnetic fields. Also similar to the EDM measurements is the choice of molecules, including[75] BiO, BiS, HgF, LaO, LaS, LuO, LuS, PbF, and YbF: These are all heavy free radicals and are therefore prime candidates for production in a buffer gas cooled beam. There are even some molecules which have already been discussed, such as YbF and BaF (Table 3.1), for which a buffer gas beam has been shown to deliver over 100 times the brightness of a supersonic beam, with a slower

forward velocity (allowing the same time τ with a shorter apparatus, easing technical requirements).

Time-variation of fundamental constants

There has been much recent interest in the question of whether or not fundamental constants are truly "constant," or whether their values have changed over time. In particular, the dimensionless fine structure constant $\alpha = e^2/4\pi\epsilon_0\hbar c$ and electron-proton mass ratio $\mu = m_e/m_p$ have attracted special attention due to the possibility of measuring their variation from multiple independent sources. Detailed discussions of the theory and experiments discussed here may be found in reviews[95, 52].

Searches for time-variation of fundamental constants typically take one of two approaches. One is to use high precision laboratory measurements, for example an atomic clock frequency compared at different times[204, 30]. Another is to look at data which may give information about α or μ from a very long time ago, for example by examining astronomical spectra at large redshifts[95, 93], but with comparably smaller precision. The current limits on the variation of μ and α are

$$\frac{\dot{\mu}}{\mu} = (1 \pm 3) \times 10^{-16} \text{ yr}^{-1}$$

from the inversion spectrum of ammonia measured in sources with high redshift[93], and

$$\frac{\dot{\alpha}}{\alpha} = (-1.6 \pm 2.3) \times 10^{-17} \text{ yr}^{-1}$$

from comparing optical clocks[204]. The values for α and μ for laboratory measurements and astrophysical measurements can also be compared[234], and are currently known to agree on the $\lesssim 10^{-7}$ fractional level.

As with EDMs and parity violation, molecules can have large enhancement factors which could allow more sensitive measurements. In particular, the α and μ dependence of fine structure splitting $\omega_f \propto \alpha^2$, rotational splitting $\omega_r \propto \mu$ and vibrational splitting $\omega_v \propto \mu^{1/2}$ are different[95], and if two levels with different hyperfine, rotational, or vibrational character are nearly degenerate there can be significant sensitivity enhancement[92] in changes to both μ and α. This enhancement can be several orders of magnitude compared to atoms, and there are several promising species[95], including CuS, IrC, LaS, LaO, LuO, SiBr, YbF, Cs_2, and Sr_2. Several of these molecules may be difficult to produce through normal beam methods, but are prime candidates for buffer gas beam production.

Chapter 4

Measurement and Data Analysis

The goal of this chapter is to discuss how we extract spin precession phases from the experiment, and how we correlate components of the phase with various experimental parameters. We will not make any attempt to interpret these phases until the next chapter. As we shall discuss in Section 4.3.6, this data analysis routine was developed while the measured EDM value has an unknown, "blind" offset added to prevent operator bias.

4.1   Apparatus overview

Here we will give a brief overview of the experimental apparatus. The work described in this subsection encompasses contributions from nearly every member of the ACME collaboration. Parts in which I had significant involvement are described in detail elsewhere in this thesis.

4.1.1 Beam Source

The buffer gas beam source delivers a 2-3 ms wide pulse of molecules every 20 ms. We use neon buffer gas at a flow rate of 25-40 SCCM. Our ablation laser is a pulsed Nd:YAG laser (Litron Nano TRL 80-200, 1064 nm and 532 nm combined, 15 ns width, 30-50 mJ per pulse), and is incident on a solid piece of ThO_2 to create gas phase ThO. The ablation laser is focused by a 300 mm or 400 mm focal length lens placed approximately one focal length from the target; however, the lens focal length, distance, height, and orientation need to be varied occasionally to maximize output. The number of molecules in the $|X, J = 1\rangle$ state leaving the cell is $\sim 10^{11}$, with a forward velocity of ≈ 200 m/s. The cell aperture diameter is 5 mm. The cell temperature is kept between 16-17 K for normal operation, which requires approximately 2 W of heat put into the cell. This heat can either come from a resistor attached to the cell, or from the YAG itself. We find that with normal operating conditions the YAG delivers approximately 1.5 W into the cell.

The molecules are incident on a 6 mm diameter conical collimator at a distance of 25 mm from the source. This collimator is attached to the 4 K radiation shield, but is kept at around 10 K by thermal standoffs. The next collimator is a 10 mm diameter hole in a flat plate on the outer (~ 50 K) radiation shield. After this collimator, the molecules travel through an "ion sweeper," which is an electric field of magnitude ≈ 200 V/cm provided by two flat copper plates (spaced by 2.5 cm, at +500 V and ground) attached to the room temperature vacuum chamber. The purpose of this electric field is to deflect ions from the beamline and prevent charge accumulation on the main electric field plates in the interaction region. The molecules then travel

through a gate valve and leave the beam source vacuum chamber.

4.1.2   Stem Region

The stem region lies between the beam source and the interaction region, and serves a number of purposes. The first segment in the stem region is where "rotational cooling," or "ground state enhancement" occurs. This segment concentrates population from the $|X, J = 0, 2, 3\rangle$ states into $|X, J = 1\rangle$, which is the only state optically pumped into the EDM sensitive H state. First, a microwave field resonant with the Stark-shifted $|X, J = 0\rangle \leftrightarrow |X, J = 1\rangle$ transition drives Rabi flopping between the states. Given the rotational temperature and distribution of the molecular beam, this results in a population enhancement of $\approx 50\%$ in $X, J = 1$. Next, optical pumping lasers drive the $X \rightarrow C$, $P(2)$ and $P(3)$ transitions ($J = 1 \rightarrow 2$ and $2 \rightarrow 3$, respectively). Since neighboring rotational states in $X^1\Sigma_0^+$ have opposite parity (and no Ω-doublets), we could not move population from $X, J = 2^+$ to $X, J = 1^-$ with an E1 (parity changing) excitation followed by an E1 decay; for this reason, we perform the optical pumping in a 42.5 V/cm electric field to mix the parity of the C state. This results in another enhancement of $\approx 50\%$, for a net gain of a factor of ~ 2.

After the rotational cooling, the molecules pass through a set of adjustable collimators. These are razor blades on the end of a translation stage, which allow us to selectively collimate parts of the beam for systematic checks. These collimators are fully retracted from the beam line during normal operation. Next, the molecules travel through another gate valve, which divides the stem region from the interaction region.

4.1.3   Interaction Region

The interaction region is an aluminum vacuum chamber surrounded by 5 layers of mumetal magnetic shielding. The molecules first travel down a long aluminum tube called the "trunk." The trunk penetrates the 5 layers of magnetic mumetal shields and connects to the interaction region vacuum chamber. The vacuum chamber is surrounded by a $\cos\theta$ coil, which produces a uniform magnetic field in the $\hat{Z}$ direction. The coordinate axes are measured relative to the lab and never change; $+\hat{Z}$ points from east to west, and is collinear with lasers and fields; $+\hat{X}$ points from south to north, and is the direction of the molecule forward velocity; $+\hat{Y}$ points into the floor.

Before entering the electric field, the molecules pass through a collimator which is fixed on the electric field plate assembly. The primary purpose of these collimators is to prevent deposition of the molecular beam on the electric field plates. The electric field is provided by two 12.7 mm thick pieces of Schott Borofloat glass, spaced by 25.1 mm. The interior faces are coated with a $\sim$100 nm thick coating of indium tin oxide (ITO), a transparent conductor. The thickness was reported by the manufacturer but not measured. The exterior sides of the glass plates are covered with a broadband anti-reflection (AR) coating. The plates are held in a kinematic mount by "guard rings" made of gold coated copper which is electrically isolated from the ITO on the plates, though always kept at the same electrical potential. The lasers used to prepare and readout the EDM sensitive H state propagate perpendicularly through the electric field plates, as described in the next section.

4.2 Measurement scheme

Once the molecules have traveled ≈ 10 cm from the edge of the field plates, they encounter a 943 nm laser (see Figure 4.2) resonant with the $|X; J = 0, M = \pm 1\rangle \rightarrow |A; J = 0, M = 0\rangle$ transition. The $\hat{Z}$ axis is the quantization axis, so since the laser propagates along the $\hat{Z}$ direction we can only drive transitions with $\Delta M = \pm 1$. This laser is retroreflected with a rotated polarization so that it can nominally pump out all of the molecules in $|X, J = 1, M = \pm 1\rangle$. The radiative decay $|A; J = 0, M = 0\rangle \rightsquigarrow |H, J = 1\rangle$ populates the state in which the EDM measurement occurs. The decay populates the sublevels $|H; J = 1, M = \pm 1, \mathcal{N} = \pm 1\rangle$ and $|H; J = 1, M = 0^-\rangle$, which is the lower $\Omega-$doublet state. Notice that since the $M = 0$ state is only affected by the quadratic Stark shift (see Section 2.4), it largely remains a parity eigenstate. After a distance of ~ 1 cm, the molecules encounter a 1090 nm laser resonant with the $|H; J = 1, M = \pm 1, \tilde{\mathcal{N}} = \pm 1\rangle \rightarrow |C; J = 1, M = 0, \tilde{\mathcal{P}}\rangle$, where $\tilde{\mathcal{P}} = +1(-1)$ indicates the upper (lower) $\Omega-$doublet state of C, which have opposite parity. Note that $\tilde{\mathcal{P}}$ and $\tilde{\mathcal{N}}$ are fixed for each molecular beam pulse, and are chosen by setting the 1090 nm laser frequency with a system of AOMs. The states $|C; J = 1, M = 0, \tilde{\mathcal{P}} = \pm 1\rangle$ are separated by ≈ 50 MHz, and the $\tilde{\mathcal{N}} = \pm 1$ states are separated by the Stark shift, which is typically ~ 100 MHz for laboratory electric fields. For the remainder of this section we shall suppress $\tilde{\mathcal{N}}$ and $\tilde{\mathcal{P}}$ in the kets for simplicity.

The purpose of this first 1090 nm laser (called the preparation laser) is to spin-polarize the molecules by creating a coherent superposition of the $|H, J = 1, M = \pm 1\rangle$
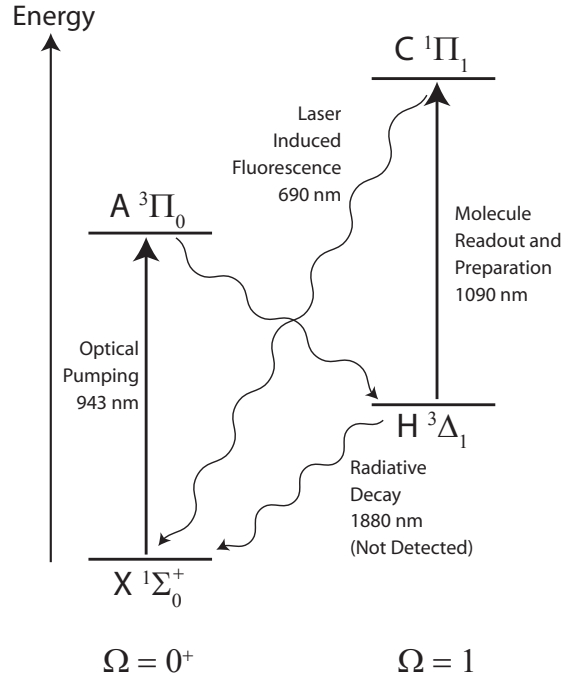
Figure 4.1: Experimentally relevant levels and transitions in ThO[243, 80, 189]. Only the ground vibrational level of each state is used. The ground electronic state is X, and the EDM measurement takes place in H. The term symbols given are approximate[189]. Solid lines indicate electronic transitions excited by lasers in the experiment, and wavy lines indicate light emitted through radiative decays.
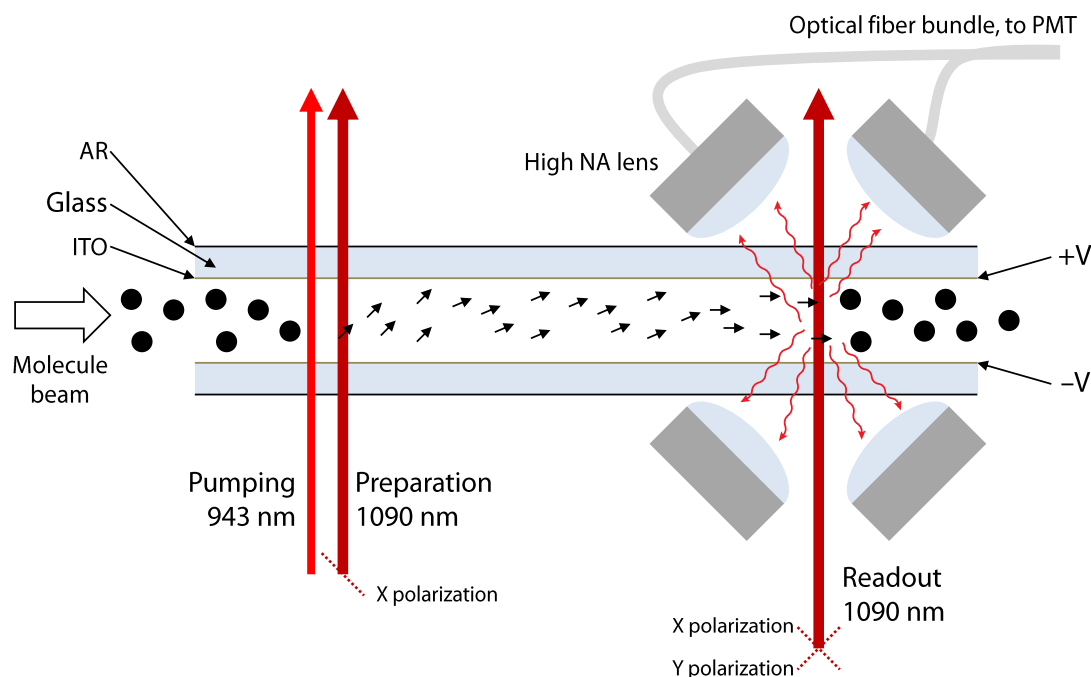
Figure 4.2: A schematic representation of the molecules in the electric field plates. The molecules enter the electric field from the left. The field is provided by two glass plates with a transparent, conducting indium tin oxide (ITO) coating on one side, and a broadband anti-reflection (AR) coating on the other. The incoherent ground state molecules (black circles) are optically pumped into the H state, then spin polarized by the preparation laser. The spins (indicated by the small black arrows) precess in the fields, mostly due to the Zeeman interaction with the magnetic field. After precessing for ≈ 1 ms, the molecules encounter the readout laser, which has modulated linear polarization. Molecules will absorb the readout laser light, then decay to the electronic ground state, emitting a 690 nm photon which is collected by a high numerical aperture lens system. The lenses focus the light into a fiber bundle which takes the photons to a PMT for detection.
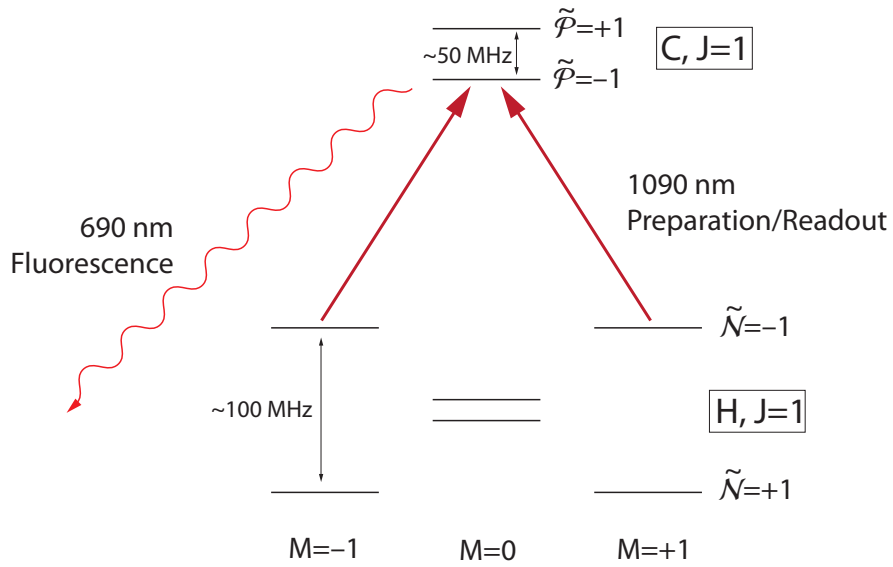
Figure 4.3: Relevant levels in the state preparation and readout. As shown, molecules in the $\tilde{\mathcal{N}} = -1$ state in $|H, J = 1\rangle$ are excited with linearly polarized light at 1090 nm into the $\tilde{\mathcal{P}} = -1$ state in $|C, J = 1\rangle$. The bright superposition decays to the ground state X, and emits a photon at 690 nm. For state preparation the 690 nm photon is not detected. For state readout, the photon is detected and used to determine the molecular spin polarization. The values for $\tilde{\mathcal{N}}$ and $\tilde{\mathcal{P}}$ are chosen by setting the laser frequency, but the same values are used for both preparation and readout.

Zeeman sublevels. Let us write the optical polarization of the preparation laser as[97]

$$\hat{\epsilon}_{\theta'} = \frac{1}{\sqrt{2}}\left(-e^{-i\theta'}\hat{\epsilon}_{+1} + e^{+i\theta'}\hat{\epsilon}_{-1}\right) = \cos(\theta')\hat{\epsilon}_X + \sin(\theta')\hat{\epsilon}_Y. \tag{4.1}$$

Here θ' denotes the laser's linear polarization in the $X - Y$ plane (we are assuming a perfect linear polarization, but will consider other cases in Section 5.2.2). The rotating wave Hamiltonian (on resonance, and up to an overall constant) is[42]

$$H = \begin{pmatrix} 0 & \Omega_R e^{i\theta'} & -\Omega_R e^{-i\theta'} \\ \Omega_R e^{-i\theta'} & 0 & 0 \\ -\Omega_R e^{i\theta'} & 0 & 0 \end{pmatrix}, \tag{4.2}$$

where Ω_R is the Rabi frequency, and we use $\{|C, M = 0\rangle, |H, M = +1\rangle, |H, M = -1\rangle\}$ as our basis. The eigenstates of this Hamiltonian are

$$|D(\theta)\rangle = \frac{1}{\sqrt{2}}\left(e^{-i\theta'}|H, M = +1\rangle + e^{i\theta'}|H, M = -1\rangle\right) \tag{4.3}$$

$$|B_\pm(\theta)\rangle = \frac{1}{\sqrt{2}}\left(-e^{-i\theta'}|H, M = +1\rangle + e^{i\theta'}|H, M = -1\rangle\right) \pm |C, M = 0\rangle. \tag{4.4}$$

Here D denotes the "dark" state, and B denotes the "bright" states. The bright states contain a large admixture of the C state, which decays with ≈ 500 ns radiative lifetime primarily into the X state. Therefore, the two bright states rapidly decay, leaving all molecules (which are being addressed by the laser) in the dark state $|D(\theta)\rangle$, which is a coherent superposition of the Zeeman sublevels. Once the molecules leave the preparation laser, the Ramsey measurement begins.

Since the system is rotationally symmetric about the Z axis (to good approximation), let us set $\theta' = 0$. Our initial molecular state is therefore

$$|\psi(t = 0)\rangle = \frac{|H, M = +1\rangle + |H, M = -1\rangle}{\sqrt{2}}. \tag{4.5}$$

Common mode energy shifts between these levels will simply cause an overall phase which is not detectable, so say that the Zeeman levels have energy shift given by EM, where E includes all Zeeman-level dependent energy shifts (see Section 5.2.7). According to the Schrödinger Equation, after a time τ the molecule wavefunction becomes

$$|\psi(\tau)\rangle = \frac{e^{-i(+E)\tau/\hbar} |H, M = +1\rangle + e^{-i(-E)\tau/\hbar} |H, M = -1\rangle}{\sqrt{2}} \tag{4.6}$$

$$= \frac{e^{-i\phi} |H, M = +1\rangle + e^{i\phi} |H, M = -1\rangle}{\sqrt{2}}, \tag{4.7}$$

where $\phi = \omega\tau = E\tau/\hbar$ is phase accumulated by the molecules. Notice that the sign of the measured phase is equal to the sign of the $M = +1$ energy shift.

After the molecules travel for ≈ 22 cm (corresponding to $\tau \approx 1.1$ ms), they encounter a second 1090 nm "readout" laser. This laser has the same frequency as the preparation laser, but with modulated polarization. Specifically, the linear polarization switches between two orthogonal directions, θ and $\theta + \pi/2$, with a 10 μs full period. This period is short enough that each molecule will be illuminated by both polarizations during the flight through the laser, which is a few mm wide. Consider what happens when the molecules are illuminated by the θ polarization. The molecule will be reprojected into the bright/dark basis $|B(\theta)\rangle, |D(\theta)\rangle$, where we suppress the $\pm$ subscript on B since $\langle\psi(\tau)|B_+(\theta)\rangle = \langle\psi(\tau)|B_-(\theta)\rangle$. The molecules will be projected on the bright (dark) state with probability P_B (P_D), given by

$$P_B = \frac{1 - \mathcal{C}}{2} + \mathcal{C} |\langle\psi(\tau)|B(\theta)\rangle|^2, \quad P_D = \frac{1 - \mathcal{C}}{2} + \mathcal{C} |\langle\psi(\tau)|D(\theta)\rangle|^2, \tag{4.8}$$

where $0 \leq \mathcal{C} \leq 1$ is the contrast (see Appendix E), and is a measure of how well we can prepare and read out the quantum state of the molecule. If a molecule is projected

into the bright state, it will decay to the X state (via the C state admixture) and emit a photon at 690 nm. If there are N_0 total molecules interrogated by the laser, then there will be $N_\theta = N_0 P_B$ photons emitted, which we can detect (albeit with finite efficiency, as discussed in Appendix C). After 5 μs, when the readout polarization has rotated by 90 degrees, there will be $N_{\theta+\pi/2} = N_0 P_D$ photons emitted. If we detect these photons, we can compute the asymmetry[243]

$$\mathcal{A} = \frac{N_\theta - N_{\theta+\pi/2}}{N_\theta + N_{\theta+\pi/2}} = \frac{P_B - P_D}{P_B + P_D} = \mathcal{C}\cos(2(\phi - \theta)), \tag{4.9}$$

where ϕ is the phase accumulated by the molecules and θ is a laser polarization. Notice that this quantity is independent of the number of molecules N_0, provided that the same number of molecules was interrogated by the θ and $\theta + \pi/2$ beams. Since the transit time of the molecules across the laser is less than the switching period, this is a good approximation[142]. Even though these polarizations need not be aligned with the lab X and Y axes, we refer to these beams as the "X" and "Y" beams for simplicity.

4.2.1 Magnetic Field, Fringe Number, and $\mathcal{B}$-corrected Asymmetry

To maximize our sensitivity to phase, we want to maximize $\partial\mathcal{A}/\partial\phi$. This occurs when $(\phi-\theta) \approx (2N_{\text{fringe}}+1)\pi/4$, where N_{fringe} is an integer called the "fringe number," a choice of words which will be explained shortly. Intuitively, this means that we want the laser polarization to offset from the molecule polarization by 45° so that the asymmetry is linear in ϕ. Since $\phi \approx g\mu_{\text{B}}\mathcal{B}\tau$ to very good approximation, this means that $(g\mu_{\text{B}}\mathcal{B}\tau-\theta) \approx (2N_{\text{fringe}}+1)\pi/4$. We also want this condition to be satisfied when

Table 4.1: Relationship between asymmetry $\mathcal{A}$ and phase ϕ for various N_{fringe}

N_{fringe}	Asymmetry vs. Phase Relationship
0	$\mathcal{A} \approx +2\mathcal{C}\phi$
1	$\mathcal{A} \approx -2\mathcal{C}\phi\tilde{\mathcal{B}}$
2	$\mathcal{A} \approx -2\mathcal{C}\phi$
3	$\mathcal{A} \approx +2\mathcal{C}\phi\tilde{\mathcal{B}}$

we reverse $\mathcal{B}$, so we will require that $g\mu_{\text{B}}\mathcal{B}\tau \approx N_{\text{fringe}}\pi/4$ and $\theta = (N_{\text{fringe}} + 1)\pi/4$.

In words, we want to choose the magnetic field so that each Zeeman component accumulates a phase which is a multiple of $\pi/4$. Using $|g| = 0.00440(5)$[142], we can see a magnetic field of $\mathcal{B} = \mathcal{B}_{\pi/4} = 20$ mG will give a $\pi/4$ phase. The current source which supplies the coils cannot reliably output 80 mG, so we are restricted to $N_{\text{fringe}} = 0, 1, 2, 3$. Table 4.1 shows the results of Taylor expanding the asymmetry from Eq. 4.9 around these values of N_{fringe}. See Figure 4.4 for an illustration of this idea.

Because we operate at each of these different values of N_{fringe}, the varying relationships between $\mathcal{A}$ and ϕ could become confusing. In an attempt to minimize this confusion, we define the "$\mathcal{B}$-corrected asymmetry" $\hat{\mathcal{A}}$ to satisfy $|\mathcal{A}| = |\hat{\mathcal{A}}|$ and $\hat{\mathcal{A}} \approx 2\mathcal{C}\phi$ for all integer values of N_{fringe}. Notice that $\mathcal{A}$ and $\hat{\mathcal{A}}$ differ by at most a sign (though perhaps a sign correlated with the magnetic field).

4.3   Data analysis

Our experiment is divided into shots, traces, states, blocks, superblocks, and runs. A shot is a single molecule beam pulse resulting from a single shot of the ablation laser. The repetition rate of shots is set by the ablation rate R_{YAG}, typically 50
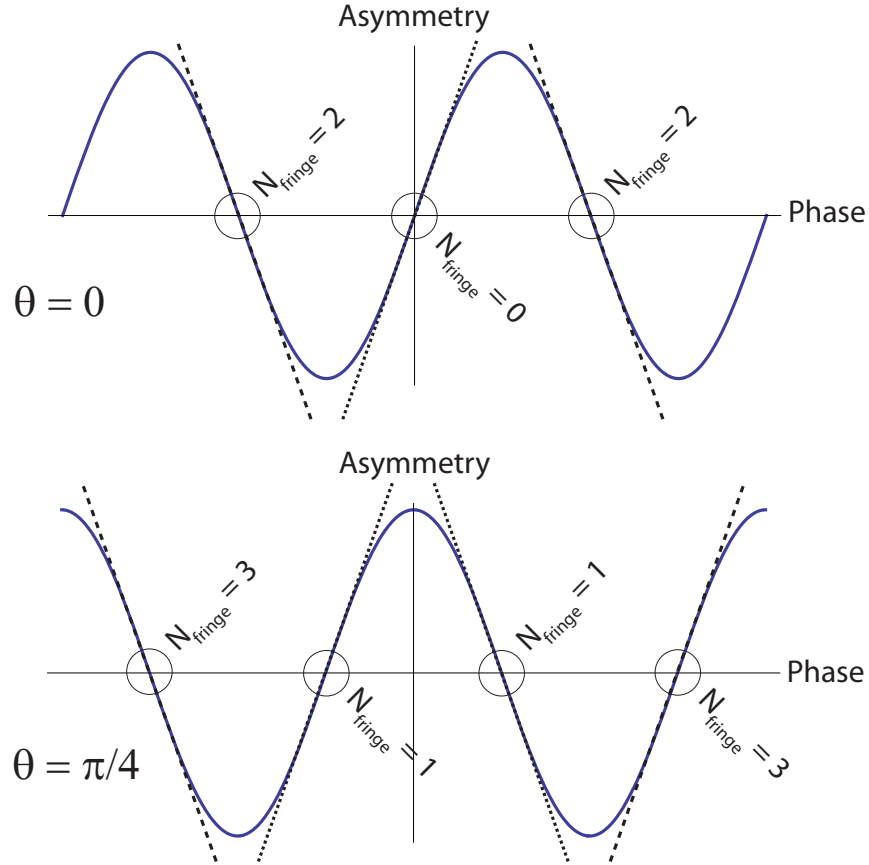
Figure 4.4: Asymmetry $\mathcal{A}$ vs. phase ϕ relationship (Eq. 4.9) for two different values of the polarization offset θ. Top: with $\theta = 0$, we can either linearize around $\phi \approx 0$ or $\phi \approx \pi/2$, corresponding to a fringe number of 0 or 2, respectively. Notice that the slope of $\mathcal{A}/\phi$ does not when we reverse the magnetic field (i.e. $\phi \to -\phi$). Bottom: with $\theta = \pi/4$, the asymmetry vs. phase curve shifts as shown. Now we can either linearize around $\phi \approx \pi/4$ or $3\pi/4$, which correspond to fringe number of 1 or 3, respectively. Notice that now the slope of $\mathcal{A}/\phi$ does switch when we reverse the magnetic field.

Hz. The fluorescence signal from a number N_{avg} (typically 25) of shots is averaged together by the DAQ to form a trace. Nominally, nothing is changed within a trace. The DAQ samples at 5 MS/s, or one value every 200 ns. Each trace is taken in a specific state, that is, a specific set of values for the electric field $\vec{\mathcal{E}}$, magnetic field $\vec{\mathcal{B}}$, Ω-doublet $\mathcal{N}$, pump-probe relative polarization θ, etc. Between traces, a switch or reversal (or several) may be performed, that is, we may reverse the applied electric field, address the other Ω-doublet, etc. A block is a complete set of the $2^4 = 16$ different combinations of $\pm\mathcal{N}, \pm\vec{\mathcal{E}}, \pm\vec{\mathcal{B}}$, and $\pm\theta$. Each block typically has four redundant copies of each state, so there are 64 traces per block. Each block takes about 40 seconds of "clock time," that is, time that has passed on a clock in the lab.
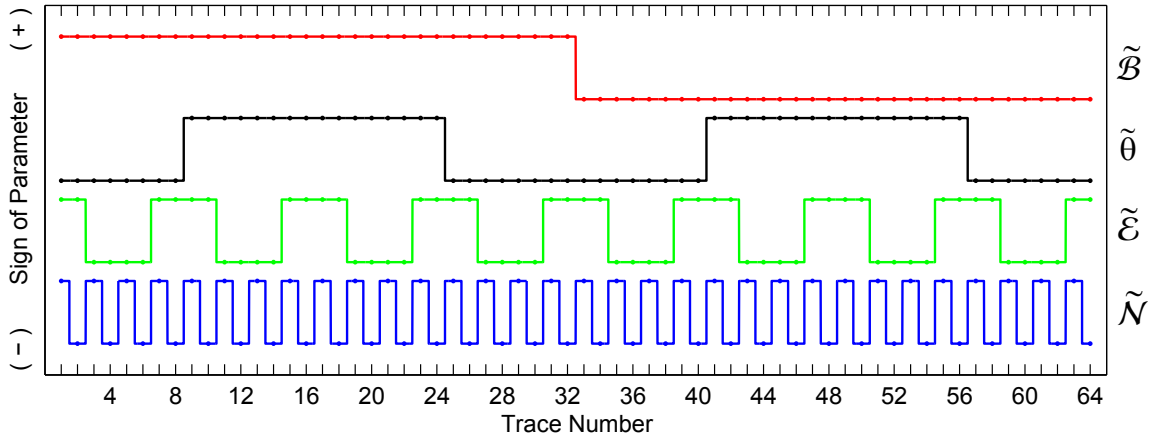
Figure 4.5: Switching order within a single block. The time between traces is ~ 0.5 s. From block-to-block, the initial value of each parameter is randomly chosen to be positive or negative individually (except the magnetic field, whose starting value is always the ending value from the previous run.)

The switches performed in a block $(\tilde{\mathcal{N}}, \tilde{\mathcal{E}}, \tilde{\mathcal{B}}, \tilde{\theta})$ are called the "EDM switches" since these quantities are directly used to measure the EDM, and each block is a

complete EDM measurement. The tilde ˜ indicates the sign of a parameter. There are also a number of other switches (called "superblock switches" or "superswitches") which are performed between blocks: readout state ($C-$state) switching, field plate lead switching, pump-probe global polarization rotation, and interchange of $X \leftrightarrow Y$ probe beam polarizations. A complete set of these switches is called a superblock. These superblock switches function primarily to suppress systematics, and will be discussed further in Section 4.3.7.

A run is a complete set of data taken under some fixed conditions; for example, we may take a run with the laser power turned down, or a run with some experimental timing changed, or a run with best possible conditions. A run typically lasts one to several hours of clock time.

4.3.1 Extracting Counts

The "chopping" of the probe beam results in a modulated PMT signal as shown in Figure 4.6. The polarization of the probe beam is alternated $\cdots XY\, XY\, XY\, XY \cdots$ every 5 μs. A polarization bin is the amount of time where the probe beam is on continuously with a single polarization, typically around ~ 4 μs. The time between the start of adjacent polarization bins is 5 μs, and there is $\sim$1 μs of dead time where there is nominally no probe light. To extract the number of detector counts within single polarization bin, we average many traces together so that the modulation becomes clearly visible, as shown above. We then define polarization bins to use in the data analysis so that the bins are spaced by 5 μs, and the background signal (i.e. fluorescence signal before the molecules arrive) is flat. We integrate under each

polarization bin for each trace to obtain counts vs. time after ablation $S(t_i)$, where the time points t_i measure time after the ablation pulse and are spaced by 5 μs. The timing jitter in this experiment is $\ll$ 200 ns (the sampling time of the DAQ), so we don't have to worry about the polarization bin assignments drifting around. We always ensure that there is at least one millisecond at the beginning of each trace where there is no molecule signal so that we can perform background subtraction.

4.3.2 Extracting Asymmetry and Asymmetry Uncertainty

For pair of adjacent polarization bins, we compute the asymmetry bin

$$\widetilde{\mathcal{A}}(t_j) = \frac{S(t_i) - S(t_{i+1})}{S(t_i) + S(t_{i+1})}, \text{ where } t_j = \frac{1}{2}(t_i + t_{i+1}). \tag{4.10}$$

As long as $S(t_i), S(t_{i+1}) \gg 1$ and $|\widetilde{\mathcal{A}}(t_j)| \ll 1$, the quantity $\widetilde{\mathcal{A}}(t_j)$ should have Gaussian fluctuations (see Section 4.4). Since adjacent polarization bins have opposite sign, this is a measurement of the asymmetry between fluorescence from X vs. Y polarized light. Each polarization bin is only used in one asymmetry bin. The time points t_j measure time after the ablation pulse and are spaced by 10 μs. In order to reject portions of the trace with little or no signal-to-noise, we only consider values of $\widetilde{\mathcal{A}}(t_j)$ where the total number of counts per asymmetry bin is above some cutoff $(S(t_i) + S(t_{i+1})) > S_{cut}$. This cutoff is typically chosen such that points with signal-to-noise ratio of $\lesssim 1$ are rejected (see Section 4.3.4).

Next, we take a number N_{grp} of consecutive asymmetry bins (typically 10-30) and
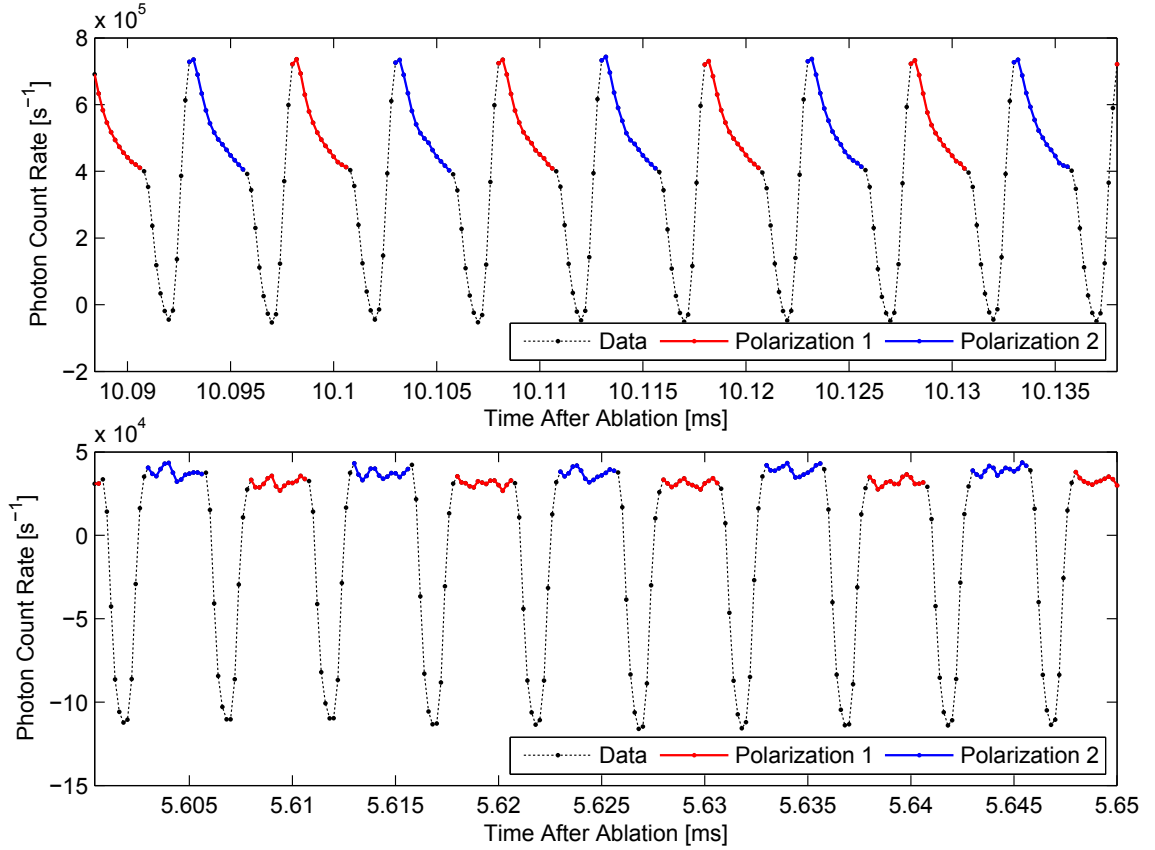
Figure 4.6: An average of many modulated photon signals from the PMTs. No background subtraction has yet occurred, so both plots have an arbitrary count rate offset. The bold, colored portions show which points were included in the polarization bins. The dots indicate measurements from the DAQ, while the lines are merely to guide the eye. Top: fluorescence signal from molecules. The colored points are added together to form the polarization bins. The sharp rise is due to the probe laser switching on, and the sharp drop is when the probe laser is switched off. Bottom: fluorescence signal before the arrival of the molecules.
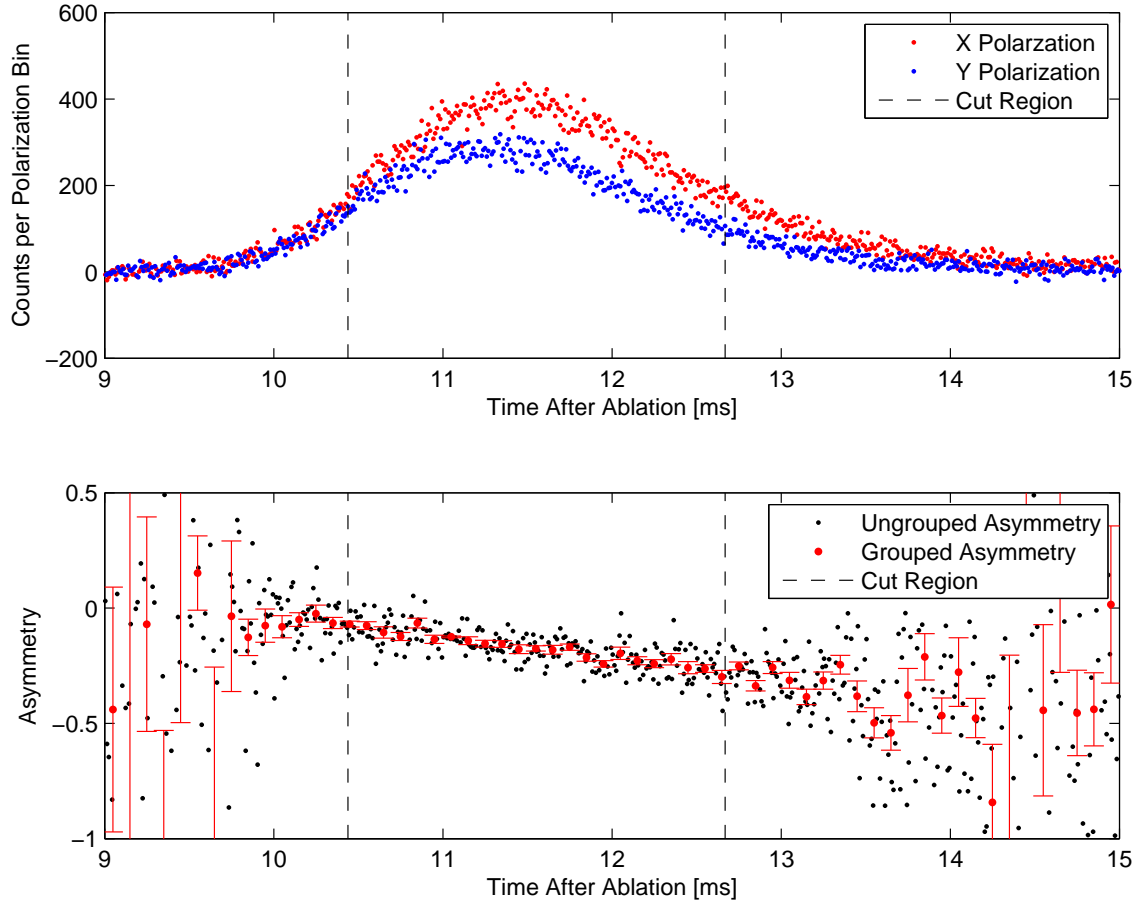
Figure 4.7: Turning polarization bins into asymmetry bins, and then asymmetry groups. Top: Counts per polarization bin, after background subtraction. The dashed lines indicate where the mean count rate is above a signal size cutoff. Bottom: Adjacent polarization bin counts are used to compute the asymmetry. For this figure, groups of 10 asymmetry bins are grouped together, and their mean and standard error are computed. In the actual data analysis, between 16 and 32 points are grouped together. The slope is due to the velocity dispersion in the molecular beam.

compute the standard mean and error of the asymmetry group:

$$\mathcal{A}(t_k) \;\; = \;\; \frac{1}{N_{grp}} \sum_{j=1}^{N_{grp}} \widetilde{\mathcal{A}}(t_j) \tag{4.11}$$

$$\delta\mathcal{A}(t_k) \;\; = \;\; \left[\frac{1}{N_{grp}} \sum_{j=1}^{N_{grp}} \left(\widetilde{\mathcal{A}}(t_j) - \mathcal{A}(t_k) \right)^2 \right]^{1/2} \tag{4.12}$$

$$t_k \;\; = \;\; \frac{1}{N_{grp}} \sum_{j=1}^{N_{grp}} t_j. \tag{4.13}$$

The time points t_k measure time after the ablation pulse and are spaced by $N_{grp} \times 10$ $\mu s \approx 100 - 300$ μs. Note that if N_{grp} is too large then the signal-to-noise will vary within a single asymmetry group, and will result in non-Gaussian behavior (see Section 4.4). This step is the first where we have computed any sort of uncertainty, and this uncertainty will be propagated to all computed quantities, including the final EDM result.

4.3.3 Computation of Contrast, τ, and Angular Frequencies

For this section, consider all of the states in a single block. For each of the 2^4 states we now have asymmetry as a function of time, $\mathcal{A}(t_k; \mathcal{N}, \mathcal{E}, \mathcal{B}, \theta)$. For small phase angle differences ϕ about the $\pi/4$ bias rotation, the $\mathcal{B}$-corrected asymmetry and phase are related by $\hat{\mathcal{A}} = 2\mathcal{C}\phi$, where $\mathcal{C}$ is the contrast. In our case, the measured phase angle $\phi = \theta + \phi_{mol}(\mathcal{N}, \mathcal{E}, \mathcal{B})$ depends both on the optical (pump-probe relative) polarization θ, and the spin precession of the molecules $\phi_{mol}(\mathcal{N}, \mathcal{E}, \mathcal{B})$. Since the precession of the molecules does not depend on θ, we can compute the contrast by

examining the θ−odd part of the measured phase,

$$\hat{\mathcal{A}}(t_k; \mathcal{N}, \mathcal{E}, \mathcal{B}, +\theta) - \hat{\mathcal{A}}(t_k; \mathcal{N}, \mathcal{E}, \mathcal{B}, -\theta) = \cdots$$

$$2\mathcal{C}(\phi_{mol}(\mathcal{N}, \mathcal{E}, \mathcal{B}) + \theta) - 2\mathcal{C}(\phi_{mol}(\mathcal{N}, \mathcal{E}, \mathcal{B}) - \theta) = 4\mathcal{C}\theta. \quad (4.14)$$

Since θ is a known experimental parameter, we can compute the contrast

$$\mathcal{C}(t_k; \mathcal{N}, \mathcal{E}, \mathcal{B}) = \frac{\hat{\mathcal{A}}(t_k; \mathcal{N}, \mathcal{E}, \mathcal{B}, +\theta) - \hat{\mathcal{A}}(t_k; \mathcal{N}, \mathcal{E}, \mathcal{B}, -\theta)}{4\theta}. \quad (4.15)$$

Notice that we have computed the contrast with a fixed choice of $\mathcal{N}, \mathcal{E}, \mathcal{B}$, but since the contrast should not depend on any of those quantities (which we can check), we can compute the contrast by averaging together all 2^3 possible choices of $\mathcal{N}, \mathcal{E}, \mathcal{B}$:

$$\mathcal{C}(t_k) = \frac{1}{8} \sum_{\tilde{\mathcal{N}}, \tilde{\mathcal{E}}, \tilde{\mathcal{B}}} \mathcal{C}(t_k; \tilde{\mathcal{N}}, \tilde{\mathcal{E}}|\mathcal{E}|, \tilde{\mathcal{B}}|\mathcal{B}|). \quad (4.16)$$

Since the contrast does not vary significantly vs. time after ablation (which we can experimentally verify), we can perform a weighted average over time to get the contrast

$$\mathcal{C} = \frac{\sum_{t_k} \mathcal{C}(t_k)/\delta\mathcal{C}(t_k)^2}{\sum_{t_k} 1/\delta\mathcal{C}(t_k)^2}, \quad (4.17)$$

where $\delta\mathcal{C}(t_k)$ is obtained by propagating the errors on the asymmetries. In practice, the contrast may vary over a single trace, but using an errorbar of $\delta\mathcal{C} = 0.05$ is very conservative, and will not dominate the uncertainty from shot noise. The contrast is typically $\mathcal{C} = 93 \pm 2\%$.

To compute the coherence time τ, we make use of the fact that ϕ_{mol} contains the term $-g\mu_B\mathcal{B}\tau$ (see Section 5.1.1). The magnetic g-factor is $g = -0.00440(5)$, and the typical value of $\mathcal{B}$ is 20 mG, so the angular frequency of spin precession in the applied magnetic field is ≈ 700 rad/sec, which is much larger than any other cause

of spin precession (EDM, precession in background fields, etc) by a factor of $\gtrsim 10^3$. The total amount of spin precession is therefore $-g\mu_{\mathrm{B}}\mathcal{B}\tau \approx \hat{B}\pi/4 + \phi_{mol}$ (when we use the magnetic field to provide a $\pi/4$ bias field), or $\phi_{mol} \approx -g\mu_{\mathrm{B}}\mathcal{B}\tau - \tilde{\mathcal{B}}\pi/4$. Here $\tilde{\mathcal{B}}$ indicates the sign of the $\tilde{\mathcal{B}}$. Since the quantity $g\mu_{\mathrm{B}}\mathcal{B}\tau$ changes sign with reversal of $\mathcal{B}$ but nothing else, we can perform a very similar computation to the one above,

$$\hat{\mathcal{A}}(t_k; \mathcal{N}, \mathcal{E}, +\mathcal{B}, \theta) - \hat{\mathcal{A}}(t_k; \mathcal{N}, \mathcal{E}, -\mathcal{B}, \theta)$$

$$= 2\mathcal{C}(\phi_{mol}(\mathcal{N}, \mathcal{E}, \mathcal{B}) + \theta) - 2\mathcal{C}(\phi_{mol}(\mathcal{N}, \mathcal{E}, -\mathcal{B}) + \theta) \tag{4.18}$$

$$= 2\mathcal{C}(g\mu_{\mathrm{B}}\mathcal{B}\tau + \pi/4 + \theta) - 2\mathcal{C}(-g\mu_{\mathrm{B}}\mathcal{B}\tau - \pi/4 + \theta) \tag{4.19}$$

$$= 4\mathcal{C}(\pi/4 + g\mu_{\mathrm{B}}\mathcal{B}\tau) \tag{4.20}$$

$$\tau(t_k; \mathcal{N}, \mathcal{E}, \theta) = \frac{1}{g\mu_{\mathrm{B}}\mathcal{B}} \left(\frac{\mathcal{A}(t_k; \mathcal{N}, \mathcal{E}, +\mathcal{B}, \theta) - \mathcal{A}(t_k; \mathcal{N}, \mathcal{E}, -\mathcal{B}, \theta)}{4\mathcal{C}} - \frac{\pi}{4} \right). \tag{4.21}$$

As before, the coherence time should not depend on $\mathcal{N}, \mathcal{E}$, or θ, so compute

$$\tau(t_k) = \frac{1}{8} \sum_{\mathcal{N}, \tilde{\mathcal{B}}, \tilde{\theta}} \tau(t_k; \mathcal{N}, \tilde{\mathcal{E}}|\mathcal{E}|, \tilde{\theta}|\theta|). \tag{4.22}$$

Since the molecule forward velocity is correlated with the time that the molecule left the cell, and because there is velocity dispersion, τ typically varies by $\sim 10\%$ over the a single trace. However, since the shot noise limit on all phases in a single block are much larger than 10%, we can take

$$\tau = \frac{\sum_{t_k} \tau(t_k)/\delta\tau(t_k)^2}{\sum_{t_k} 1/\delta\tau(t_k)^2}, \qquad \delta\tau = 0.1 \text{ ms}, \tag{4.23}$$

where $\delta\tau(t_k)$ is obtained by propagating the errors on the asymmetries. The uncertainty $\delta\tau = 0.1$ ms is conservative, and will not dominate the shot noise. The coherence time is typically $\tau = 1.05 \pm 0.05$ ms.

We will now define the angular frequency such that

$$\hat{\mathcal{A}} = 2\mathcal{C}\phi = 2\mathcal{C}\omega\tau, \tag{4.24}$$

where ω is in units of rad/sec. After computing $\mathcal{C}$ and τ, we obtain a set (for each block) of $2^3 = 8$ angular frequencies $\omega(t_k; \pm\mathcal{N}, \pm\mathcal{E}, \pm\mathcal{B})$, where

$$\omega(t_k; \mathcal{N}, \mathcal{E}, \mathcal{B}) = \frac{1}{2\mathcal{C}\tau}\left(\mathcal{A}(t_k; \mathcal{N}, \mathcal{E}, \mathcal{B}, +\theta) + \mathcal{A}(t_k; \mathcal{N}, \mathcal{E}, \mathcal{B}, -\theta)\right). \tag{4.25}$$

We choose to eliminate the dependence on θ since the θ switch is only used to compute the contrast, which we have already done. Notice that we have defined ω to be the precession frequency *not including* the $\pi/4$ bias precession. In other words, with perfect a perfect $\pi/4$ phase rotation, we would measure $\omega = 0$.

4.3.4 Data cuts: count rate, asymmetry, and χ^2

In order to ensure that the distribution of our measurements is Gaussian, we perform a number of tests which asymmetry bins must pass to be included in the data. As shown in Figure 4.9, our EDM result was very robust against the specific values chosen for these cuts. The values for each of these cuts was chosen before unblinding (see Section 4.3.6). These cuts are performed on each asymmetry bin for each trace. If an asymmetry bin (time point) fails one of the cuts for any trace, that asymmetry bin is thrown out for the entire block, otherwise there would be in imbalance between the experimental states and the parity sums would not be meaningful.

Count rate

This cut simply requires that an asymmetry bin has a signal count rate above some value to be included, typically around the background count rate. The motivation
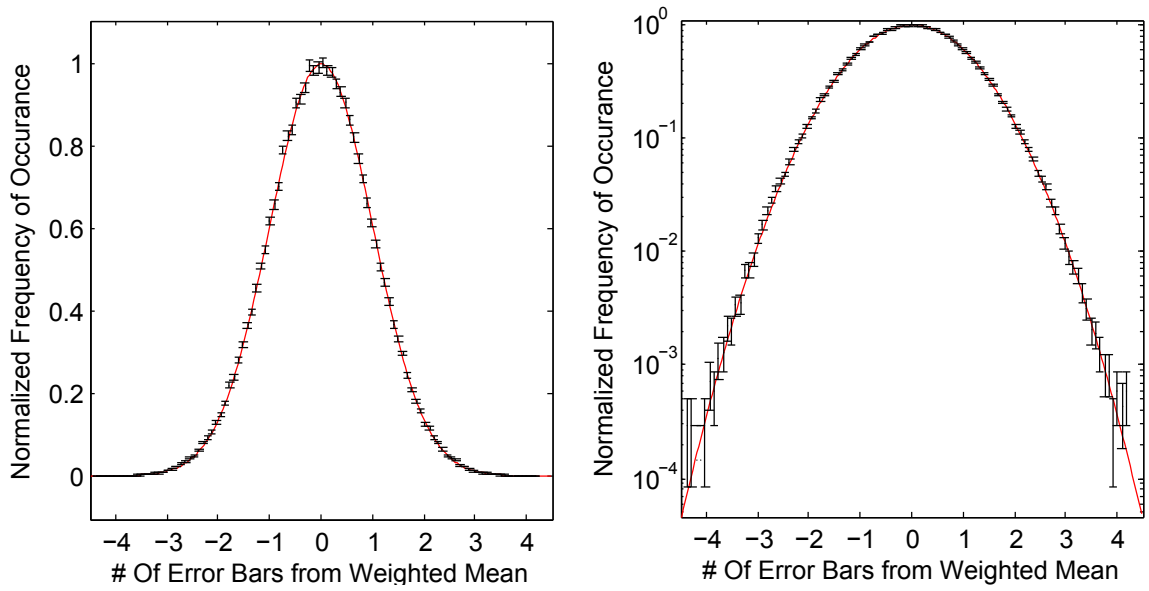
Figure 4.8: A histogram of all EDM measurements, for every time point and every block. We divide each measurement by the error bar (1σ uncertainty) to determine how many error bars that value is from the mean of all the data. As discussed in Section 4.4.4, this quantity should be a Gaussian with mean 0 and standard deviation 1. Here we have plotted this histogram on a linear (left) and log (right) scale, so that we can see the Gaussian character both near the center and in the tails. The Gaussian fit has $\sigma = 1.007$.

for this cut is that as we will see in Section 4.4.3, forming an asymmetry from data with a low signal-to-noise ratio results in non-Gaussian statistics. In Figure 4.9 we see the results of varying the count rate cut, and it appears to not have a significant effect. We generated similar plots for the other cuts discussed below, but they look nearly identical so we don't include them.
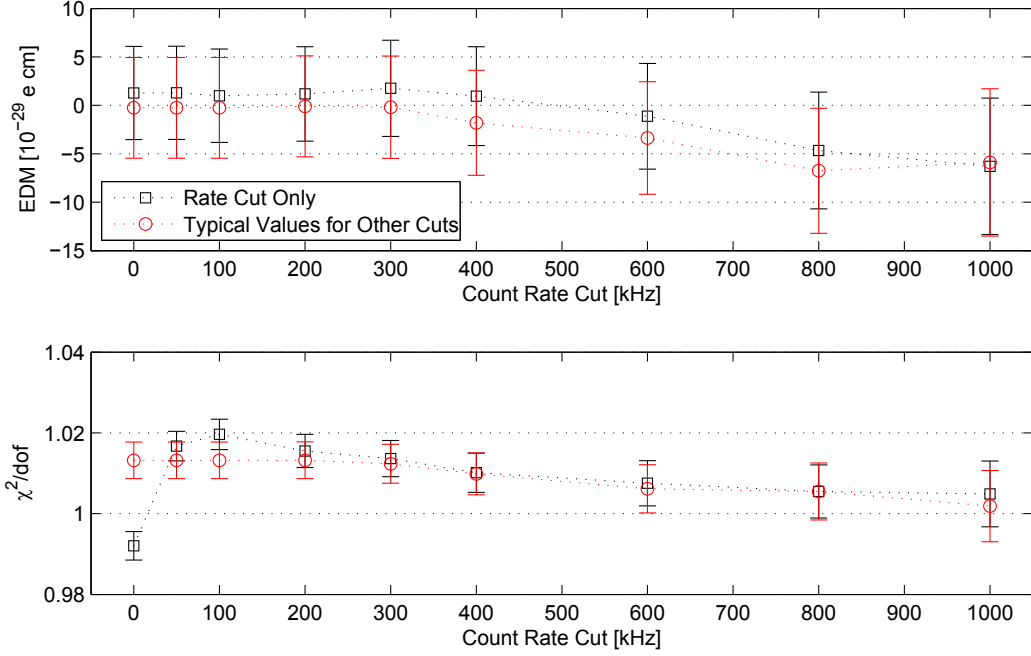
Figure 4.9: EDM value vs. count rate cut, varied from 1 to 1000 kHz. We can see that the count rate cut doesn't move the mean outside of the error bars, but that imposing a stricter cut results in larger error bars (due to the increased amount of rejected data). The black dashed line shows the result if we only use the count rate cut, while the red dashed line assumes standard values for the other cuts (χ^2 and asymmetry outlier). Our standard count rate cut is 300 kHz, which is approximately equal to the background rate. Here the χ^2 is computed according to the method outlined in Section 4.4.

Chi-square

In addition to the count rate cut, we try to protect against non-Gaussian statistics by performing a chi-square test. Specifically, we take all of the asymmetry values for a particular time bin in a block, form a histogram of the values, and test against the hypothesis that the histogram is described by a Gaussian. We then reject data if the p-value (i.e. statistical confidence that the hypothesis is correct) is below some cutoff, typically 0.1. In other words, if the statistical test is 99% confident that the data is not Gaussian, we reject it. Notice that this implies we will be throwing out approximately 1% of our perfectly good data, but that has a negligible effect on our final result.

Asymmetry

According to Eq. (4.9), the asymmetry resulting from a physical phase cannot be larger than 1. However, because of statistical fluctuations, the measured asymmetry can be larger than 1, so any asymmetry bin with $|\mathcal{A}|$ above some value (typically 1) is rejected.

4.3.5 Computation of Parity Sums, and the EDM

The previous section hinted at the idea of a "parity sum," or a way to extract a component of ϕ which has a particular behavior under reversals of $\mathcal{N}, \mathcal{E}, \mathcal{B}, \theta$. Let us make the assumption that all terms in the measured phase ϕ are linear in $\mathcal{N}, \mathcal{E}, \mathcal{B}, \theta$ (an assumption which we can test, and is quite valid). In particular, we will assume that upon reversal of $\mathcal{N}, \mathcal{E}, \mathcal{B}$, or θ (or any combination of them), each term contributing

to spin precession will either change sign, or not change at all. Let us then choose to express the measured angular frequency $\omega(\mathcal{N}, \mathcal{E}, \mathcal{B}, \theta)$ in the "parity basis,"

$$\omega(\mathcal{N}, \mathcal{E}, \mathcal{B}) = \omega^{(0)} + \tilde{\mathcal{B}}\omega^{\mathcal{B}} + \tilde{\mathcal{E}}\omega^{\mathcal{E}} + \tilde{\mathcal{E}}\tilde{\mathcal{B}}\omega^{\mathcal{EB}} + \tilde{\mathcal{N}}\omega^{\mathcal{N}} + \tilde{\mathcal{N}}\tilde{\mathcal{B}}\omega^{\mathcal{NB}} + \tilde{\mathcal{N}}\tilde{\mathcal{E}}\omega^{\mathcal{NE}} + \tilde{\mathcal{N}}\tilde{\mathcal{E}}\tilde{\mathcal{B}}\omega^{\mathcal{NEB}}$$

$$(4.26)$$

Here the tilde indicate the sign of a quantity. In words, we use a superscript to indicate the reversals under which this component is odd, assuming that it is even under all other quantities. The superscript (0) indicates the quantity which is even under all reversals. We will use this superscript notation very generally, for quantities other than ω and switches other than $\mathcal{N}, \mathcal{E}, \mathcal{B}, \theta$. The superscripts are often called "channels" or "parity indices," and terms ω^p for some parity index p are called "parity sums". By definition, the parity sums are chosen to not change sign under reversal of any experimental quantity.

These parity sums are useful for isolating terms in the Hamiltonian by their parity under reversals of $\mathcal{N}, \mathcal{E}, \mathcal{B}$ (or any other experimental quantity). We can compute these from our set of $2^3 = 8$ measured values of $\omega(\pm\mathcal{N}, \pm\mathcal{E}, \pm\mathcal{B})$ by adding them up with appropriate signs,

$$\omega^{(0)} = \frac{1}{8} \sum_{\tilde{\mathcal{N}}, \tilde{\mathcal{E}}, \tilde{\mathcal{B}}} \omega(\tilde{\mathcal{N}}, \tilde{\mathcal{E}}|\mathcal{E}|, \tilde{\mathcal{B}}|\mathcal{B}|), \tag{4.27}$$

$$\omega^{\mathcal{B}} = \frac{1}{8} \sum_{\tilde{\mathcal{N}}, \tilde{\mathcal{E}}, \tilde{\mathcal{B}}} \tilde{\mathcal{B}}\omega(\tilde{\mathcal{N}}, \tilde{\mathcal{E}}|\mathcal{E}|, \tilde{\mathcal{B}}|\mathcal{B}|), \tag{4.28}$$

$$\omega^{\mathcal{NE}} = \frac{1}{8} \sum_{\tilde{\mathcal{N}}, \tilde{\mathcal{E}}, \tilde{\mathcal{B}}} \tilde{\mathcal{N}}\tilde{\mathcal{E}}\omega(\tilde{\mathcal{N}}, \tilde{\mathcal{E}}|\mathcal{E}|, \tilde{\mathcal{B}}|\mathcal{B}|), \tag{4.29}$$

and so on. The uncertainties are found through standard error propagation of $\delta\omega$. Again, these relationships can be generalized for quantities other than ω, and switches other than $\mathcal{N}, \mathcal{E}, \mathcal{B}$. As we will discuss in Section 4.4.5, it is crucial that unweighted

sums are used to compute parity sums; using weighted sums will often give the wrong answer.

Though we have been suppressing the time index t_k, we have not yet eliminated it. This is because $\omega(t_k; \mathcal{N}, \mathcal{E}, \mathcal{B})$ is not a constant versus time after ablation due to the asymmetry slope; however, after computing the parity sums the slope vanishes for any parity sum which is odd in $\mathcal{N}$ or $\mathcal{E}$. This is because the slope is dominated by the spin precessing the magnetic field, so changing $\mathcal{N}$ or $\mathcal{E}$ doesn't change the slope (except, possibly, on the $\lesssim 10^{-3}$ level) so the slope gets subtracted away. We can then take a weighted mean over t_k of the parity sums,

$$\omega^p = \frac{\sum_{t_k} \omega^p(t_k)/\delta\omega^p}{\sum_{t_k} 1/\delta\omega^p(t_k)^2}, \quad \delta\omega^p = \left[\sum_{t_k} \omega^p(t_k)^{-2}\right]^{-1/2}, \tag{4.30}$$

where p is some parity index.

"Good" vs. "bad" channels, "fast" vs. "slow" switches

By computing parity sums we can extract components of the phase which are correlated with experimental reversals, and do not depend on the overall phase. However, if the overall phase changes over the amount of time it takes to perform a switch, then we will introduce noise (and possibly bias, if the phase tends to drift in one direction) into our parity sums and therefore measured phases. We therefore try to perform switches as quickly as we can. The fastest four switches are $\mathcal{N}$ every 0.5 seconds, $\mathcal{E}$ every 2 seconds, θ every 5 seconds, and $\mathcal{B}$ every 20 seconds. In order to see whether a switch p is being performed fast enough, we can perform a χ^2 test on the values for $\mathcal{A}^p$ (see Section 4.4.4). Since the uncertainty assigned to the asymmetry $\mathcal{A}$ ultimately derives from the signal variations between polarization bins (see Section

4.3.2 and [142]), additional variations from slow drifts between traces will cause the assigned uncertainties to be underestimates which will inflate the χ^2.

In Figure 4.10 we can see this analysis for four asymmetry channels: $\mathcal{B}, \theta, \mathcal{E}, \mathcal{NE}$. We can see that as the switch becomes faster, the histogram becomes more and more Gaussian indicating that there are no additional sources of error. We call the $\mathcal{B}$-odd channel (and similarly, the all-even channel) "bad" because these slow drifts prevent extraction of meaningful quantities. The θ-odd channel is reasonably good, while the $\mathcal{E}$ and $\mathcal{N}$ channels are "good," since the switching speed means that these channels are highly immune to drifts. Notice that any channel including an $\mathcal{E}$ or $\mathcal{N}$ switch is also good, so we shall refer to the $\mathcal{E}, \mathcal{EB}, \mathcal{N}, \mathcal{NB}, \mathcal{NE}$, and $\mathcal{NEB}$ as the good channels for our experiment. Since none of the superblock switches are faster than $\mathcal{B}$, they are all "bad" unless examined in a channel with a fast switch.

4.3.6   Blinded analysis

Very early in the experiment (well before we had accumulated enough statistics to improve the EDM limit), we added an unknown offset, or "blind," to the piece of data which allows us to calculate the EDM. We will discuss the interpretation of phases and frequencies in the next chapter, and will see that the EDM computed from $\omega^{\mathcal{NE}}$. Whenever we computed this value from our data, we would add the blind. Since we compute the parity sums for each block a single time (and then save the output), once we included this offset at the block level we knew that it would be included for all further analysis.

The blind was included to protect against subconscious bias[132]. Our measure-
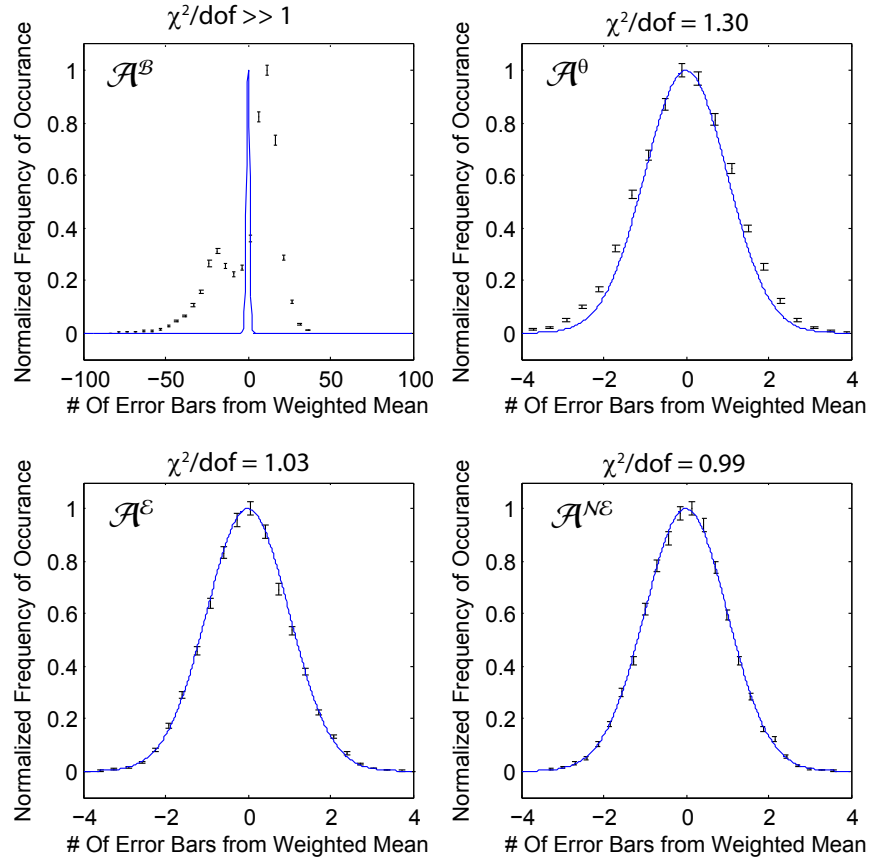
Figure 4.10: Histogram for various asymmetry channels: $\mathcal{B}, \theta, \mathcal{E}, \mathcal{NE}$. As the switch gets faster, the histograms become more Gaussian and the χ^2 approaches the expected value 1 ± 0.01 (see Section 4.4.4). The blue curves shown are Gaussians with mean 0 and variance 1

ment and analysis procedures have a large number of "judgment call" decisions, and while none of them moved the EDM value by a significant amount, the concern was that a large number of small, biased changes could accumulate into a large bias.

We made no attempt to protect the blind from purposeful revealing, though we did take two steps to prevent accidental revealing. The first step was to store the value as a binary file, so that a person who accidentally opened the file would not know the value. The second step was to only access the file through a script which would take an input value, and output the blinded value (input plus blind). The script would reject an attempt to blind zero. The file containing the blind was made available to all collaboration members, so that anybody who wanted to analyze the data could use the same blind. The blind used was labeled blind #0004 (the previous three were either used for diagnostics, or revealed after small data sets not used for our published results), and was equal to -107.2×10^{-29} e cm.

4.3.7 Superblock Switches

In this section we will discuss the superblock switches in more detail. As mentioned at the beginning of this section, there are four switches which we perform between blocks. A set of all $2^4 = 16$ combinations of superblock switches is called a superblock. These switches are not needed to compute the EDM (unlike $\mathcal{N}, \mathcal{E}, \mathcal{B}, \theta$), but instead are designed to search for and suppress systematic effects. Figure 4.11 shows a plot of the $\omega^{\mathcal{N}\mathcal{E}}$ channel versus each of the superblock states, as well as the two different electric fields, three different magnetic fields, and two different laser propagation directions in which we operated the experiment.
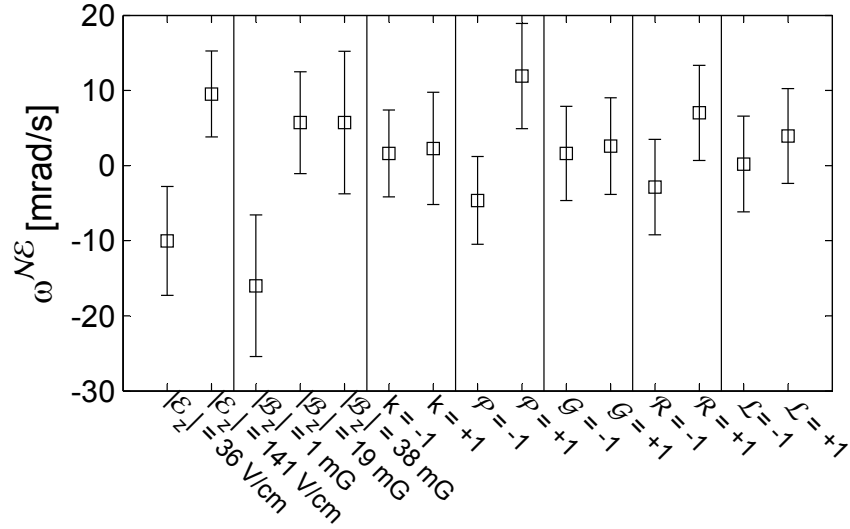
Figure 4.11: Published EDM value versus various states of the apparatus. The switches $\tilde{\mathcal{P}}, \tilde{\mathcal{L}}, \tilde{\mathcal{R}}, \tilde{\mathcal{G}}$ are described in the text.

$\tilde{\mathcal{P}}$: C-state switch

As shown in Figure 4.3, we can choose to address either Ω-doublet component in $|C, J = 1, M = 0\rangle$. We label these two states by $\tilde{\mathcal{P}} = \pm 1$. The value for $\tilde{\mathcal{P}}$ is chosen randomly at the beginning of each block, and is therefore switched every ~ 40 seconds. The primary implication of this switch is that the two $\tilde{P}$ states have opposite parity, and therefore the dark states prepared by these two choices of $\tilde{\mathcal{P}}$ are orthogonal[142]. This means that the bright and dark states are interchanged in Eq. (4.9), resulting in a sign change for the asymmetry due to molecular phases. Since the X and Y laser beams follow different optical paths, they will have slightly different pointing, power, etc. and could therefore cause measurable asymmetries not due to molecular phases. For example, if the X laser beam intersects with the molecule beam such that the fluorescence collection optics have a higher acceptance compared to the Y laser beam, then there will be an asymmetry offset. By changing the sign of the asymmetry

144

without (ideally) changing the molecule phase, we can eliminate these effects.

$\tilde{\mathcal{L}}$: **Electric field plate lead switch**

The voltages on the electric field plates are set by a computer controlled amplifier. Each plate is hooked up to a separate output channel, so voltage offsets on the outputs will result in non-reversing electric fields (see Section 5.2.1). We can search for these offsets through voltage measurements, but we can also reduce their effects by switching which output is connected to which plate. We installed relays between the amplifier and the field plates, and the relay reverses the wiring every 4 blocks, or every $\sim$ 3 minutes.

$\tilde{\mathcal{R}}$: **Readout laser polarization**

The X and Y readout laser beams travel through a $\lambda/2$ waveplate which can be rotated to rotate their polarizations. Since the X and Y beams have orthogonal linear polarization, a polarization rotation of 90° has the effect of interchanging the X and Y polarizations, which will result in a reversal of the asymmetry sign due to molecular phases and therefore has the same benefits of the $\tilde{\mathcal{P}}$ switch. Additionally, there is an important systematic which depends on the polarization of the lasers (see Figure 5.4) with a period of 180°, which this switch will therefore help to suppress. The experiment is operated with the waveplate at two different positions corresponding to 90° relative polarization rotation, labeled as $\tilde{\mathcal{R}} = \pm 1$. We switch $\tilde{\mathcal{R}}$ every 8 blocks, or every $\sim$ 5 minutes.

$\tilde{\mathcal{G}}$: Global polarization rotation

Like the X and Y readout laser beams, the preparation laser beam also travels through a $\lambda/2$ waveplate. We can therefore rotate the polarization of this beam arbitrarily, though we choose two values separated by 90° for experimental operation, labeled $\tilde{\mathcal{G}} = \pm 1$. We switch $\tilde{\mathcal{G}}$ every 16 blocks, or every ~ 10 minutes.

4.3.8   Analysis Checks

In order to ensure that our extracted values for the EDM and other quantities are robust, we want to check that none of the adjustable parameters described above change the value of the EDM significantly. Many such tests were performed, and here we shall describe some of the more important ones.

Sub-bin dependence

Exactly which portion (or "sub-bin") of the fluorescence trace shown in Figure 4.6 that we choose to include is somewhat arbitrary. As indicated in the that figure, we use the portion of the trace which corresponds to a steady-state background rate, *i.e.* the 1090 nm probe laser providing the background counts is at full intensity. In order to make sure that our choice of sub-bin is reasonable, we compute the EDM with varying choices and make sure that we obtain the same answer. The results of this variation are shown in Figure 4.12. As we can see, the choice of sub-bin appears to not be crucial. There was one instance when sub-bin dependence was very large, which was when we performed fast $\mathcal{N}$-switching, and is described in Section 6.4.4.
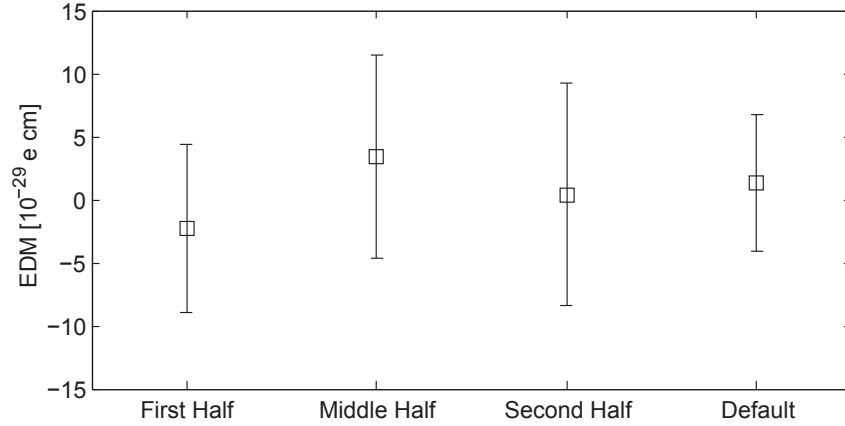
Figure 4.12: EDM value vs. choice of sub-bin. Here Default is the choice shown in Figure 4.6. First, Middle, and Second Half refer to using half the number of points as in Default, corresponding to the first, middle, and second half (respectively) of the Default polarization bin.

State-averaged contrast

In Eq. (4.24), we solved for the phase $\phi = \hat{\mathcal{A}}/2\mathcal{C}$ assuming that the contrast $\mathcal{C}$ is a constant. However, as discussed in Appendix E, the contrast typically depends on the $\tilde{\mathcal{N}}, \tilde{\mathcal{E}}, \tilde{\mathcal{B}}$ state of the system, so we can write contrast correlations such as $\mathcal{C}^{\mathcal{N}\mathcal{E}}$, etc. Such terms would be indistinguishable from phases if we follow the computation procedure described above; however, there are two techniques to deal with these contrast correlations. The first is to extract them from the data by looking at $\tilde{\theta}$-odd channels, since they provide useful diagnostic data, as discussed in Appendix E. The second technique is to use "state-averaged" contrast, where we compute the contrast for each $\tilde{\mathcal{N}}, \tilde{\mathcal{E}}, \tilde{\mathcal{B}}$ state of the system individually. This will cause contrast correlations to not appear as phases, at the expense of slightly increased uncertainty; the uncertainty on the denominator in the equation $\phi = \hat{\mathcal{A}}/2\mathcal{C}$ is now larger, since fewer traces were averaged together to compute the contrast. However, as discussed in

Section 4.3.3, the uncertainty on the contrast is far from dominant so the uncertainty is expanded by only around a few percent for our data. See the lablog posts by Ben Spaun from 3 and 31 October 2012 for the initial proposal of this method, and detailed discussion and analysis. In general, the values we report are computed using state averaged contrast.

Background subtraction

As shown in Figure 4.6, the modulated polarization results in a modulated background signal. Because the X and Y beams are not identical, the background rate is different; this could result in asymmetry offsets, so it is tempting to perform a background subtraction for the X,Y beams individually. However, doing so will introduce correlations into the data, resulting in χ^2 values which are inflated by a factor of ≈ 2. This is a general feature of the analysis procedure and was present in the Monte Carlo data analysis (see Section 4.4.6) as well. Performing single-value background subtraction results in χ^2 values much closer to 1.

Similarly, different experimental states (especially $\tilde{\mathcal{N}}$, since it involves changing the optical path) may have different background rates. We perform background subtraction which is calculated for each experimental state, which does not introduce correlations, and does not change the final result.

Asymmetry group size

The asymmetry group size (see Section 4.3.2) is essentially a free parameter, so we want to ensure that our chosen value is reasonable. If the group size is too small, then small sample effects begin to significantly perturb the statistics (see Section

4.4). On the other hand, if the group size is too large, then we will group together different parts of the trace with different asymmetry and signal to noise, therefore losing important information. The standard number we use is 20, but as shown in Figure 4.13 other choices work just as well.
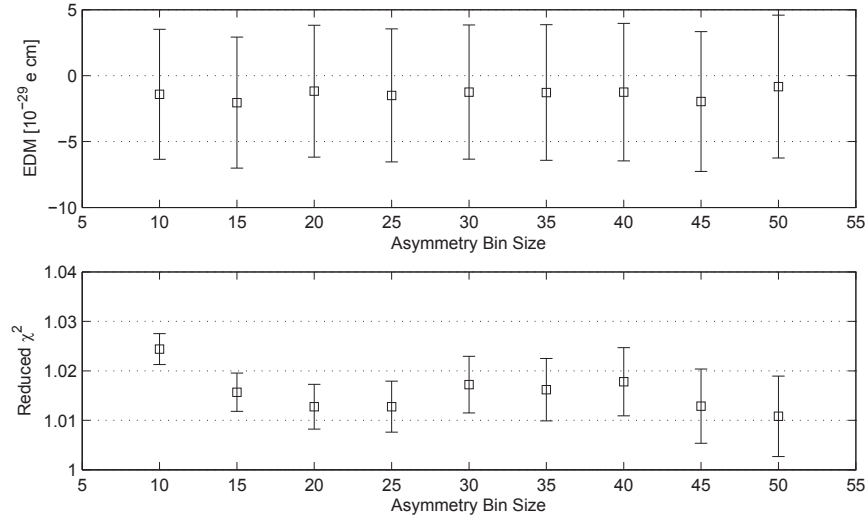
Figure 4.13: EDM versus asymmetry group size. We can see that there is no significant effect, and our choice of 20 is reasonable. Here the χ^2 is computed according to the method outlined in Section 4.4.

4.4 Notes about statistics

In this section, we will discuss some of the subtleties of our assignment of the means and uncertainties outlined in the preceeding sections. In particular, we will discuss how several of the steps which we casually mentioned, such as computation of standard error and weighted mean, are actually quite complicated. Since we have such a large data set, if any of these calculations have some systematic bias then we may have cause for concern. As we shall see, both of these very common calculations

are in fact biased, but in ways which are too small to matter for most experiments. Additionally, we shall see that our data is fundamentally non-Gaussian, which also requires some attention.

4.4.1   The shot noise limit

We mentioned in Section 4.3.2 that uncertainty is assigned to asymmetry bins, and then propagated to compute all further statistical uncertainties. Therefore, it is important to know what the smallest possible uncertainty is for a set of asymmetry values, so that we can ensure our uncertainties are near their expected value. This minimum uncertainty is called the shot noise limit[140], and ultimately derives from the fact that we are interrogating a molecular beam with Poissonian number fluctuations on the timescale of the polarization chopping[142].

Of course, we actually measure an asymmetry and then compute the phase using Eq. 4.9. We will now show that the asymmetry can be used to reach the shot noise limit in sensitivity, and find the effects of reduced contrast and finite signal-to-noise. Let's assume that we measure signal counts Y, X in the polarization bins. Define the asymmetry $\mathcal{A}$ and total counts N as

$$\mathcal{A} = \frac{Y - X}{Y + X}, \quad N = Y + X \quad \Rightarrow \quad Y = \frac{N}{2}(1 + \mathcal{A}), \quad X = \frac{N}{2}(1 - \mathcal{A}) \qquad (4.31)$$

Using the standard formula for propagation of uncertainty, we find

$$\delta \mathcal{A}^2 = \left(\frac{d\mathcal{A}}{dX}\right)^2 \delta X^2 + \left(\frac{d\mathcal{A}}{dY}\right)^2 \delta Y^2 = \frac{4}{(X + Y)^4} \left(Y^2 \delta X^2 + X^2 \delta Y^2\right). \qquad (4.32)$$

For times much shorter than the pumpout time of our buffer gas cell (see Section 3.3.1), which is the fastest timescale for macroscopic variations in the molecular beam

flux, the variations in beam flux are Poissonian and random in nature. This means that X and Y should be Poissonian as well, and therefore have uncertainty given by $\delta X^2 = X$ and $\delta Y^2 = Y$, assuming no other sources of noise. The shot noise limit on the uncertainty in our determination of $\mathcal{A}$ is therefore

$$\delta \mathcal{A}^2 = \frac{4}{(X+Y)^4}(Y^2 X + X^2 Y) = \frac{4XY}{(X+Y)^4}(Y+X) = \frac{4XY}{N^3} = \frac{1-\mathcal{A}^2}{N} \qquad (4.33)$$

For $\mathcal{A} = 0$, we recover the expected[243] relationship $\delta A = N^{-1/2}$. This discussion is only valid when the variables are all Gaussian, which we shall see in Section 4.4.3 requires $|\mathcal{A}| \ll 1$.

In reality, there are two important effects which prevent us from reaching the true shot noise limit in our determination of $\mathcal{A}$: background signal, and contrast. Assume that both X and Y have a background rate $B/2$, so that we have B background counts and N signal counts. If we subtract the background, we still have $X = Y = N/2$ (for $\mathcal{A} = 0$), but now $\delta X^2 = \delta Y^2 = (N+B)/2$, so

$$\delta \mathcal{A}^2 \;=\; \frac{4}{(X+Y)^4}\left(Y^2 \delta X^2 + X^2 \delta Y^2\right) = \frac{N+B}{N^2} \qquad (4.34)$$

$$\delta \mathcal{A} \;=\; \frac{1}{\sqrt{N}}\sqrt{1+B/N}, \qquad (4.35)$$

and the expected shot noise limit is increased by $\sqrt{1+B/N}$.

The angular frequency (again for $|\mathcal{A}| \ll 1$) is given by $\omega = \mathcal{A}/(2\mathcal{C}\tau)$. Since the contrast $\mathcal{C}$ and coherence time τ can be measured with fractional error smaller than other relevant quantities (see 4.3.3), we can simply write

$$\delta \omega = \frac{\delta \mathcal{A}}{2\mathcal{C}\tau} = \frac{1}{\sqrt{N}}\frac{\sqrt{1+B/N}}{\mathcal{C}\tau}. \qquad (4.36)$$

The statistical limit, obtained by taking a weighted mean of all EDM measurements (all time points, and all blocks), is 36×10^{-30} e cm. The one that we report is

slightly larger since it involves unweighted averaging between superblocks (see Section 4.4.5), and is 38×10^{-30} e cm. To compare to the expected shot noise limit, we calculate the total number of used photons, the mean background rate B (from the variance of the counts per bin in the background part of the trace), and the contrast $\mathcal{C}$ and coherence time τ averaged over all blocks. The estimated shot noise limit computed using this method is 31×10^{-30} e cm, which is about 20% lower than the reported statistical limit[142].

4.4.2 Bias of sample standard deviation

Consider a number N of normally distributed random variables $X_i \sim \mathcal{N}(\mu, \sigma^2)$ with true mean μ and true variance σ^2. We use the notation $\sim$ to mean "is distributed as," and $\mathcal{N}(\mu, \sigma^2)$ is a normal distribution with mean μ and variance σ^2. These "true" values are not known to the experimenter, so we form the sample mean and sample variance

$$\bar{X} = \frac{1}{N} \sum_{i=1}^{N} X_i, \qquad S^2 = \frac{1}{N-1} \sum_{i=1}^{N} (X_i - \bar{X})^2. \tag{4.37}$$

A standard result proven in most statistics textbooks is that the sample mean and variance are unbiased estimators of the true mean and variance, that is, $E[\bar{X}] = \mu$ and $E[S^2] = \sigma^2$, where E represents the expectation value. However, the sample standard deviation S is a *biased* estimator of the true standard deviation,

$$E[S] = E\left[\sqrt{\frac{1}{N-1} \sum_{i=1}^{N} (X_i - \bar{X})^2}\right] \neq \sigma. \tag{4.38}$$

It might seem very unusual that $E[S^2] = \sigma^2$ yet $E[S] \neq \sigma$, but the operations of taking a mean and taking a square root do not commute. The relationship between

$E[S]$ and σ is given by

$$\sigma = E[S]\sqrt{\frac{N-1}{2}}\frac{\Gamma((N-1)/2)}{\Gamma(N/2)}, \tag{4.39}$$

where Γ is the gamma function. This correction factor can be quite large, as shown in Figure 4.14. By modifying the formula for the sample standard deviation[40] to be

$$S' = \sqrt{\frac{1}{N-3/2}\sum_{i=1}^{N}(X_i - \bar{X})^2}, \tag{4.40}$$

we obtain a much better approximation to the true variance, as shown in Figure 4.14.
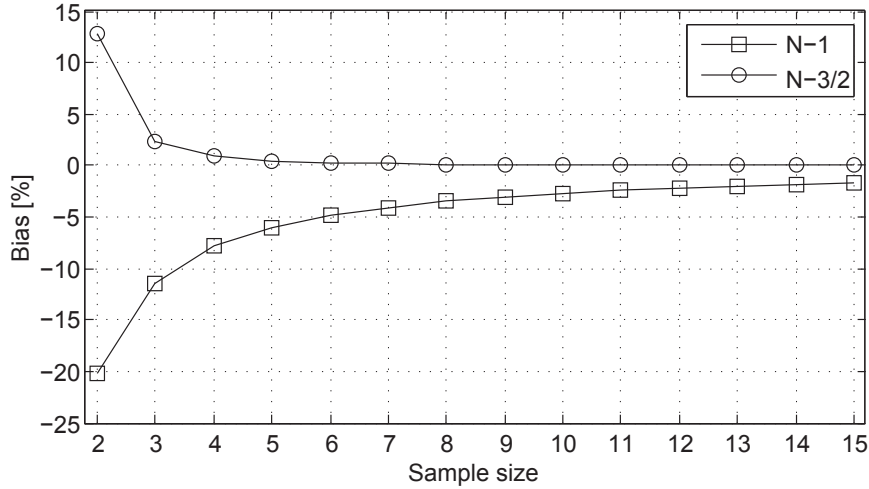
Figure 4.14: Bias of the usual formula for sample standard deviation (with $N-1$) in the denominator, and the modified formula with $N-3/2$ in the denominator. We can see that for sample sizes of $N > 4$, the modified formula is within 1% of the true standard deviation.

For all of our experimental analysis, we use the usual formula for standard deviation. We ensured that the bias was not having an appreciable effect on our result by varying the bin sizes, as discussed in Section 4.3.8.

4.4.3 Asymmetries

We infer molecular phases and spin precession frequencies from asymmetries using simple linear relationships (see Section 4.3.3), so the statistical properties of our measured asymmetries will determine the statistical properties of nearly everything that we compute. As we shall now see, the statistical properties of an asymmetry are non-trivial and, in particular, non-Gaussian.

Consider two independent random variables X_1 and X_2 with marginal distributions (probability density functions) $p_1(x)$ and $p_2(x)$. The ratio $Z = X_1/X_2$ is a random variable whose distribution is given by the formula[61]

$$p_Z(z) = \int_{-\infty}^{\infty} |y| p_1(zy) p_2(y) \, dy. \tag{4.41}$$

For the case of two Gaussians $X_1 \sim N(\mu_1, \sigma_1^2)$ and $X_2 \sim N(\mu_2, \sigma_2^2)$, we have

$$p_1(x) = \frac{e^{-(x-\mu_1)^2/2\sigma_1^2}}{\sqrt{2\pi}\sigma_1}, \qquad p_2(x) = \frac{e^{-(x-\mu_2)^2/2\sigma_2^2}}{\sqrt{2\pi}\sigma_2}. \tag{4.42}$$

The analytical form for $p_Z(z)$ is written out explicitly in [120], but is too long to include here. In the case where $\mu_1 = \mu_2 = 0$ and $\sigma_1 = \sigma_2 = \sigma$, the formula simplifies dramatically to

$$p_Z(z) = \frac{1}{\pi} \frac{1}{1 + z^2}, \tag{4.43}$$

which is a Lorentzian (or Cauchy Distribution) with FWHM $= 2$. Notice that this result does not depend on σ. This result tells us that the ratio of two Gaussians is not necessarily a Gaussian.

Now consider the situation for the signals that we have in the EDM experiment. In this case, $X_1 = N_y - N_x$ and $X_2 = N_y + N_x$, where N_y and N_x are the detector signals for neighboring polarization bins. The asymmetry is $\mathcal{A} = X_1/X_2 = (N_y - $

$N_x)/(N_y + N_x)$. Let $N_x \sim \mathcal{N}(\mu(1-\epsilon), \sigma^2)$ and $N_y \sim \mathcal{N}(\mu(1+\epsilon), \sigma^2)$ for some ϵ. Note that this means the true asymmetry is $\mathrm{E}[\mathcal{A}] = [\mu(1+\epsilon) - \mu(1-\epsilon)]/[\mu(1+\epsilon) + \mu(1-\epsilon)] = 2\mu\epsilon/2\mu = \epsilon$. We then have $X_1 = N_y - N_x \sim N(2\mu\epsilon, 2\sigma^2)$ and $X_2 = N_y + N_x \sim N(2\mu, 2\sigma^2)$. Plugging in $\mu_1 = 2\mu\epsilon, \mu_2 = 2\mu, \sigma_1 = \sigma_2 = \sigma\sqrt{2}$ into the Gaussian ratio distribution[120], we obtain the probability distribution for the asymmetry $\mathcal{A}$,

$$p_{\mathcal{A}}(a; \beta, \epsilon) = \frac{e^{-\beta^2(\epsilon^2+1)}}{\pi \left(a^2 + 1\right)^{3/2}} \times \cdots$$
$$\left(\beta(a\epsilon + 1)\sqrt{\pi} \exp\left(\frac{\beta^2(1 + \epsilon a)^2}{a^2 + 1}\right) \mathrm{erf}\left(\frac{\beta(1 + \epsilon a)}{\sqrt{a^2 + 1}}\right) + \sqrt{a^2 + 1}\right). \quad (4.44)$$

In the limit $\beta = 0$ (*i.e.* zero signal to noise), the distribution becomes a Cauchy (or Lorentzian) distribution centered at $a = 0$,

$$p_{\mathcal{A}}(a; \beta, \epsilon | \beta = 0) = \frac{1}{\pi} \frac{1}{1 + a^2}. \quad (4.45)$$

This makes intuitive sense; if there is no signal, then we couldn't possibly have any ϵ dependence in the distribution.

The opposite limit of large signal to noise ($\beta \gg 1$) is

$$p_{\mathcal{A}}(a; \beta, \epsilon | \beta \gg 1) \approx \frac{\beta|1 + a\epsilon|}{\sqrt{\pi} \left(1 + a^2\right)^{3/2}} \exp\left(-\frac{\beta^2(a - \epsilon)^2}{1 + a^2}\right). \quad (4.46)$$

Notice that this is also not Gaussian. However, in the limit where a, ϵ are small (i.e small asymmetry), we have

$$p_{\mathcal{A}}(a; \beta, \epsilon | \beta \gg 1, a^2 \ll 1, a\epsilon \ll 1) \approx \beta\pi^{-1/2} \exp\left(-(a - \epsilon)^2\beta^2\right) \sim N(\epsilon, (2\beta^2)^{-1}).$$
$$(4.47)$$

This also makes intuitive sense; in the limit of very large signal to noise, the data looks like a Gaussian centered at ϵ.

The fact that our asymmetry distribution can be Cauchy (or, generally, have polynomial tails) is dangerous, since a Cauchy distribution has a non-converging mean and standard deviation[203]. This is far from a mathematical technicality: if we a series of N Cauchy distributed points and take the mean, we find that the mean does not converge to the true mean even as $N \to \infty$, as depicted in Figure 4.15. This is because the large polynomial tails of the Cauchy distribution means that values "very far" from the mean are fairly common. Another dangerous observation is that the peak of the distribution moves from $a = 0$ to $a = \epsilon$ as β goes from 0 to ∞, so for $\beta \sim 1$ the center of the distribution will not be around ϵ!
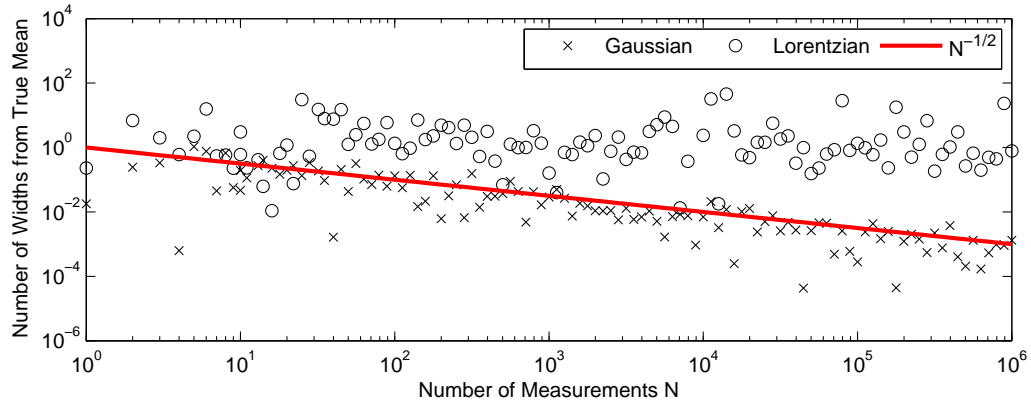
Figure 4.15: A demonstration that the mean of Cauchy distributed measurements does not converge. We generate N random Gaussian (Cauchy) distributed numbers with mean 0 and standard deviation (half-width at half-maximum) 1 and find the sample mean. We then calculate how many characteristic widths (standard deviation or half-width at half-maximum) the sample mean is from the true mean of 0. The Gaussian mean converges to the true mean as $1/\sqrt{N}$, while the Cauchy mean is still ~ 1 width away even after 10^6 measurements.

We now see precisely the motivation for the data cuts described in Section 4.3.4. The count rate cut enforces large β, while the asymmetry outlier cut enforces small asymmetries, both of which keep our data in the Gaussian regime. The fact that we

are so close to the shot noise limit (see Section 4.4.1), and that our histograms are highly Gaussian (see Figure 4.8), are evidence that these cuts are doing their jobs.

4.4.4 Chi-square Tests with Unknown Variance

A common statistical test for a large number of repeated measurements is a chi-squared (χ^2) test. Here we will discuss what exactly that means, and see how the way it is normally constructed in fact sweeps a large number of important subtleties under the rug.

Naive Application of a Chi-square Test to Binned Data

Caution: In this section, we will perform a naive chi-square test which involves making a number of false claims!

Consider a number N_x of data points x_i without any error bars. Say that the data is normally distributed $x_i \sim \mathcal{N}(\mu, \sigma^2)$, where the values μ, σ are not known to the experimenter. Let us gather these data points into groups of n, $G_1 = \{1, \ldots, n\}$, $G_2 = \{n+1, \ldots, 2n\}$, etc. Now compute the usual mean, standard deviation, and error in the mean (or standard error) of each group of points:

$$y_j = \frac{1}{n}\sum_{i \in G_i} x_i \qquad \sigma_j = \sqrt{\frac{\sum_{i \in G_i}(x_i - y_j)^2}{n-1}} \qquad \sigma_{yj} = \frac{1}{\sqrt{n}}\sigma_j. \tag{4.48}$$

Since each x_i is normally distributed, we can use the additivity of Gaussian random variables to determine the expected value, standard deviation, and standard error of

the y_j,

$$\text{E}[y_j] = \frac{1}{n} \sum_{j \in G_i} \text{E}[x_j] = \mu \tag{4.49}$$

$$\text{E}[\sigma_j] = \text{Std}[y_j] = \sqrt{\frac{1}{n} \sum_{j \in G_i} \text{Std}[x_j]^2} = \sigma \tag{4.50}$$

$$\text{E}[\sigma_{yj}] = \frac{1}{\sqrt{n}} \text{E}[\sigma_j] = \frac{\sigma}{\sqrt{n}} \tag{4.51}$$
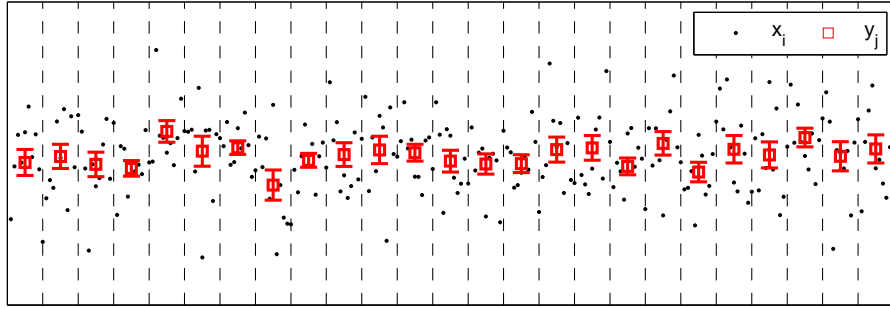
Figure 4.16: Illustration of the binning procedure. Each black point represents one of the x_i data points, which does not have an error bar associated with it. We will gather up n of the x_i points (sequentially) and compute the mean and standard error for each bin. The horizontal dashed lines indicate the bin size.

We have now "binned" our data into a smaller set of $N = N_x/n$ means y_j and "error bars" σ_{yj}. For a set of perfectly Gaussian points, like our x_i values, this might seem like a pointless exercise; however, binning the data into smaller groups could be useful for a number of reasons. If the data set is very large, binning can reduce memory requirements and computation time. Also, if the data is subject to varying conditions, either controlled or uncontrolled, gathering the data into bins where the conditions are the same can be useful to determine the effects of the changing parameters.

As a check to see whether the error bars are correctly capturing the statistical fluctuations of the data, we can perform a χ^2 test. We will follow the procedure

outlined in many standard texts[197, 28, 232]. We will be performing a χ^2 test of the hypothesis that the y_j are normally distributed about a constant $\bar{y}$, and that the error bars correctly describe the Gaussian fluctuations of the data about the mean. The χ^2 value of the data set is

$$\chi^2 = \sum_{j=1}^{N} \left(\frac{y_j - \bar{y}}{\sigma_{y_j}} \right)^2, \text{ where } \bar{y} = \frac{\sum_i y_j/\sigma_{yj}^2}{\sum_i 1/\sigma_{yj}^2} \tag{4.52}$$

is the weighted mean of the y data. The quantity $(y_j - \bar{y})/\sigma_{y_j}$ counts how many error bars each data point is from the mean, and therefore should be normally distributed with variance 1 and mean 0. The distribution of the quantity χ^2 is called, appropriately, the χ^2-distribution with $\nu = N - 1$ degrees of freedom, which has mean ν and variance 2ν. We therefore expect a reduced chi-squared value of $\chi^2_{red} = \chi^2/\nu = 1 \pm \sqrt{2/\nu}$, where the $\pm$ indicates the $\pm$ one sigma error bar. That is, the value of χ^2_{red} is itself a normally distributed random variable with mean 1 and standard deviation $\sqrt{2/\nu}$, in the case where the error bars σ_{yi} correctly reflect the Gaussian variations in the y_i.

Let's perform a simple test numerical of this analysis on some simulated data. Generate 1,000,000 points $x_i \sim \mathcal{N}(0, 1)$, bin into groups of 10, and then compute y_i, σ_{yi}, and χ^2_{red}.

```
Nx = 1000000; %Number of x values
nbin = 10; %Number of points to bin
for j = 1:(Nx/nbin) %Step over bins
    x = randn(1,nbin); %Generate nbin normally distributed points
    y(j) = mean(x); %Find the mean
    sigmayi(j) = std(x)/sqrt(nbin); %Find the standard deviation
end
ybar = sum(y./sigmayi.^2)/sum(1./sigmayi.^2); %Weighted mean
chi = (y-ybar)./sigmayi;
chi2 = sum(chi.^2); %Compute chi^2
```

```
dof = length(y)-1; %Degrees of freedom
redchi2 = chi2/dof %Reduced chi^2
redchi2sigma = sqrt(2/dof) %One sigma uncertainty on chi^2
```

If we run this simple piece of code, we will find `redchi2 = 1.2868` and `redchi2sigma`

`= 0.0045`. Of course `redchi2` will be slightly different each time due to the random

nature of the simulation, but we find that the value of the reduced χ^2 statistic for this

data is greater than the expected value of 1 by an amount much, much larger than

$\sqrt{2/\nu}$, and we would reject the hypothesis that this data has Gaussian fluctuations

described by the error bars. This is in serious disagreement with our expectation that

χ^2_{red} should have mean 1 and standard deviation $\sqrt{2/\nu}$. Making `Nx` larger and larger

will make $\sqrt{2/\nu}$ smaller and smaller, and we will find that `redchi2` converges to a

value of about 1.2857. If this test fails for perfect Gaussian data, there must be some-

thing fundamentally wrong. We shall see that the problem is indeed a fundamental

one, and arises from the fact that the quantities $\bar{y}$ and σ_{yi} are not the true values μ

and σ. This difference has a significant impact on our statistical tests, and is very

often glossed over in most treatments.

The χ^2 Distribution

First, let's try to understand the χ^2 statistic. Consider a collection of normally

distributed random variables $Y_j \sim \mathcal{N}(0, 1)$ for $j = 1, \ldots, N$. These variables Y_i could

be, for example, our y_i from above, which we claimed were distributed as $\mathcal{N}(0, 1)$. The

quantity $\chi^2 = \sum_j Y_j^2$ is also a random variable, and its distribution is appropriately

called the chi-squared distribution with N degrees of freedom, χ^2_N. The mean and

variance of this distribution are given by

$$\mathrm{E}[\chi_N^2] = N, \quad \mathrm{Var}[\chi_N^2] = 2N. \tag{4.53}$$

In the limit of large N, this distribution becomes a Gaussian with mean N and variance $2N$. The reduced chi-squared value $\chi_{red}^2 = \chi^2/N$ therefore has mean $N/N = 1$ and variance $2N/N^2 = 2/N$. This agrees with our earlier claim that $\chi_{red}^2 \sim \mathcal{N}(1, 2/N)$ for large N. Since our simulation above had large N (and adding more and more points does not solve the discrepancy), then the problem must be with the claim that $(y_j - \bar{y})/\sigma_{yi} \sim \mathcal{N}(0, 1)$.

The t Distribution

Consider the case we initially started with: we have values y_j and error bars σ_{yj} which are the mean and standard error, respectively, of a collection of n random variables distributed as $\mathcal{N}(\mu, \sigma^2)$. Since the sum of Gaussian random variables is itself Gaussian, then simple algebra tells us that

$$\frac{y_j - \mathrm{E}[y_j]}{\mathrm{Std}[y_j]} \sim \mathcal{N}(0, 1). \tag{4.54}$$

This relationship also holds with any Gaussian random variable in place of y_j. This would agree with our claim that $(y_i - \bar{y})/\sigma_{yi} \sim \mathcal{N}(0, 1)$, provided that $\bar{y} = \mathrm{E}[y_j]$ and $\sigma_{yi} = \mathrm{Std}[y_j]$, but *these relationships are not true*. The quantities $\bar{y}$ and σ_{yi} are computed from the data set, and are therefore *estimators* of the true mean and standard deviation, but are not equal to the true values. For this reason, let's redefine our uncertainty in y_i to be s_{yi},

$$y_j = \frac{1}{n}\sum_{j \in G_i} x_j \qquad s_j = \sqrt{\frac{\sum_{j \in G_j}(x_j - y_j)^2}{n-1}} \qquad s_{yj} = \frac{1}{\sqrt{n}}s_j, \tag{4.55}$$

where s denotes the *sample* standard deviation or *sample* error in the mean, as opposed to the true, unknown values. If we now count how many sample standard errors each data point is from the mean, the distribution is no longer a normal distribution but is instead a t distribution,

$$\frac{y_j - \mathrm{E}[y_j]}{s_{yj}} = \frac{y_j - \mu}{s_{yj}} \sim t_{n-1}, \tag{4.56}$$

where t_{n-1} is the $t-$distribution (or Student's $t-$distribution) with $n-1$ degrees of freedom. Recall that n is the number of x_i that were averaged together to create each y_j, so it appears that this number has been encoded in the distribution of the y_j in a non-trivial way. The above relationship is essentially the definition of the $t-$distribution: for a collection of Gaussian random variables $X_1, \ldots, X_N \sim \mathcal{N}(\mu, \sigma)$ with usual sample mean $\bar{X}$ and sample standard deviation S given by

$$\bar{X} = \frac{1}{N} \sum_{i=1}^{N} X_i \qquad S = \sqrt{\frac{1}{N-1} \sum_{i=1}^{N} (X_i - \bar{X})}, \tag{4.57}$$

the $t-$distribution with $N-1$ degrees of freedom is defined by

$$\frac{\bar{X} - \mu}{S/\sqrt{N}} \sim t_{N-1}. \tag{4.58}$$

If we replace the sample standard deviation with the true standard deviation, we recover the expected Gaussian behavior

$$\frac{\bar{X} - \mu}{\sigma/\sqrt{N}} \sim \mathcal{N}(0, 1). \tag{4.59}$$

There is an intuitive explanation of why we might expect these two very similar quantities to have different distributions. Say we compute some quantity $f(\sigma)$ with σ as an input. Of course, we do not know σ, so we actually compute $f(S)$. Since

S is a quantity computed from a finite set of data, it has some uncertainty; on the other hand, σ is a parameter with no uncertainty. Therefore, if we propagate the uncertainty on S we expect $f(S)$ to have additional uncertainty compared to $f(\sigma)$, or $\mathrm{Var}[f(S)] \geq \mathrm{Var}[f(\sigma)]$. This indeed holds for our case; we can look up the variance of the $t-$distribution in any standard statistics text to find

$$\mathrm{Std}\left[\frac{\bar{y}_j - \mu}{\sigma_{yj}}\right] = \mathrm{Std}[t_{n-1}] = \sqrt{\frac{n-1}{n-3}} > 1. \tag{4.60}$$

Notice that as $n \to \infty$, the standard deviation approaches 1; in fact, the distribution becomes a Gaussian in this limit: $\lim_{n\to\infty} t_{n-1} = \mathcal{N}(0,1)$. Intuitively, this tells us that if we have an infinite number of data points x_i making up each y_j, then we can known σ_{yj} to arbitrary precision and set $s_{yj} \to \sigma_{yj}$. In this case we recover the situation discussed in most treatments, where the sample and true standard deviations are considered equal.

There is still a glaring problem with our discussion so far: we are still using the true, unknown value μ for the mean! Just like with the standard deviation, we do not know the true mean exactly, so using the population mean in computing the χ^2 (which is, of course, our only choice) means that we have additional uncertainty that must be propagated to create additional variance. Addressing this fact turns out to be rather complicated[114], and we will not consider it here. However, we have a way around it; if we consider the case where $N_x \to \infty$ (but keeping n finite), then the uncertainty on $\bar{y}$ will approach zero and we can regard it as the true mean, $\bar{y} = \mu$. This is the relevant case with many precision measurements (such as ours), where the total set of data is very large, but it must be subdivided into smaller pieces to accommodate changing experimental conditions.

We can now see why our simple numerical χ^2 example failed above. The quantity

$$\tilde{\chi}^2_{red} = \frac{1}{N-1}\sum_{j=1}^{N}\tilde{\chi}^2_j = \frac{1}{N-1}\sum_{j=1}^{N}\tilde{\chi}^2_j, \text{ where } \tilde{\chi}_j \equiv \left(\frac{y_j - \bar{y}}{s_{yj}}\right) \tag{4.61}$$

is not a sum of squares of Gaussian variables, but a sum of squares of $t-$distributed variables. Here we are now using the notation $\tilde{\chi}^2_{red}$ to indicate the chi-squared statistic that is actually calculated from the data, where $\tilde{\chi}_j$ counts how many (signed) error bars the data point y_j is from the mean $\bar{y}$. The square of a $t-$distributed variable is known exactly; if $Y \sim t_{n-1}$, then $Y^2 \sim F_{(1,n-1)}$, where $F_{(1,n-1)}$ is called an $F-$distribution. Notice that the $F-$distribution has two input parameters. Fortunately, the mean and variance of the $F-$distribution have a simple form:

$$\mathrm{E}[F_{(1,n-1)}] = \frac{n-1}{n-3} \qquad \mathrm{Var}[F_{(1,n-1)}] = \left(\frac{n-1}{n-3}\right)^2 \frac{n-2}{n-5}. \tag{4.62}$$

These relationships will allow us to easily calculate the expected value of our reduced chi-squared statistic:

$$\mathrm{E}[\tilde{\chi}^2_{red}] = \frac{1}{N-1}\mathrm{E}\left[\sum_{j=1}^{N}\tilde{\chi}^2_j\right] = \frac{1}{N-1}\sum_{j=1}^{N}\mathrm{E}\left[\tilde{\chi}^2_j\right] = \frac{N}{N-1}\mathrm{E}[F_{(1,n-1)}] \approx \frac{n-1}{n-3}, \tag{4.63}$$

where in the last line we used the fact that we are considering the limit $N \to \infty$, so $N/(N-1) \approx 1$. The expectation of our reduced chi-square statistic is therefore

$$\mathrm{E}[\tilde{\chi}^2_{red}] = \mathrm{E}\left[\frac{1}{N}\sum_{i=1}^{N}\tilde{\chi}^2_j\right] = \frac{n-1}{n-3} > 1. \tag{4.64}$$

This might seem shocking: *the reduced chi-square statistic is not expected to be 1 for the type of data we are considering!* The variance in our reduced chi-square statistic

is also different from our simple discussion earlier, and is given by

$$
\begin{aligned}
\mathrm{Var}[\tilde{\chi}_{red}^2] &= \mathrm{Var}\left[\frac{1}{N-1}\sum_{j=1}^{N}\tilde{\chi}_j^2\right] \\
&= \frac{1}{(N-1)^2}\sum_{j=1}^{N}\mathrm{Var}\left[\tilde{\chi}_j^2\right] \\
&= \frac{\mathrm{Var}[F_{(1,n-1)}]}{N-1} \\
\mathrm{Var}[\tilde{\chi}_{red}^2] &= \frac{2}{N-1}\left(\frac{n-1}{n-3}\right)^2\left(\frac{n-2}{n-5}\right).
\end{aligned}
\tag{4.65}
$$

The standard deviation is therefore

$$
\mathrm{Std}[\tilde{\chi}_{red}^2] = \sqrt{\frac{2}{N-1}}\times\frac{n-1}{n-3}\sqrt{\frac{n-2}{n-5}}.
\tag{4.66}
$$

To summarize, the mean and one-sigma uncertainty on the sample reduced chi-squared statistic χ_{red}^2 is

$$
\chi_{red}^2 = \frac{n-1}{n-3}\pm\sqrt{\frac{2}{\nu}}\times\frac{n-1}{n-3}\sqrt{\frac{n-2}{n-5}}, \text{ where } \nu = N-1.
\tag{4.67}
$$

We see that both the mean and standard deviation of the the typically-quoted result of $\chi_{red}^2 = 1\pm\sqrt{2/\nu}$ must be multiplied by some correction factors which are larger than one. Figure 4.17 shows a plot of these correction factors as a function of n. Let's see if our initial numerical example passes the test. For $n = 10$ and $N = 100,000$, we expect $\chi_{red}^2 = 9/7 \approx 1.2857$ with an uncertainty of 0.0073. Our computed mean was 1.2868, which is within the one-sigma uncertainty.

Alternative Approach

We can compute the mean and variance of our chi-squared statistic through algebra alone, though it doesn't reveal anything about what is happening. We wish to
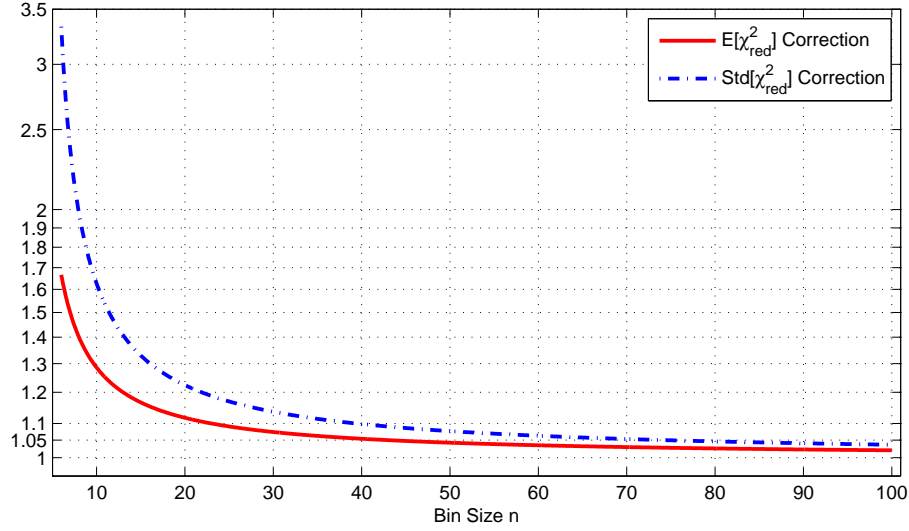
Figure 4.17: Correction factors to the mean and standard deviation of χ^2_{red}.

find the expected value and variance of the quantity

$$\tilde{\chi}^2_j = \left(\frac{y_j - \bar{y}}{\sigma_{yj}}\right)^2 = \underbrace{\left(\frac{y_j - \bar{y}}{\hat{\sigma}_{yj}}\right)^2}_{\equiv X^2} \underbrace{\left(\frac{\hat{\sigma}_{yj}}{\sigma_{yj}}\right)^2}_{\equiv \Sigma^2} \tag{4.68}$$

for a single value of j. Once we have these properties for a single j, we can easily obtain the expected value and variance of the sum over all j. The reason that we broke up the quantity into two parts is because each of those quantities has a known distribution. Specifically,

$$X^2 \sim \chi^2_1, \qquad \frac{\Sigma^2}{n-1} \sim \text{Inv-}\chi^2_{n-1}, \tag{4.69}$$

where Inv-χ^2 is the inverse chi-squared distribution. These relations rely on the assumption that we have a large enough set of data such that we can regard the weighted mean as the true mean, $\bar{y} = \mu$. The first relation is essentially the definition

of the χ^2 distribution,

$$X = \frac{y_j - \bar{y}}{\hat{\sigma}_{yj}} = \frac{y_j - \hat{\mu}}{\hat{\sigma}_{yj}} \sim \mathcal{N}(0,1) \quad \Rightarrow \quad X^2 \sim \chi_1^2, \ \mathrm{E}[X^2] = 1, \ \mathrm{Var}[X^2] = 2. \quad (4.70)$$

To find the distribution of Σ^2, we must make use of the following relation,

$$\frac{n-1}{\Sigma^2} = \frac{(n-1)\sigma_{yj}^2}{\hat{\sigma}_{yj}^2} \sim \chi_{n-1}^2, \quad (4.71)$$

which can be found in most standard textbooks. The the inverse chi-squared distribution with $n-1$ degrees of freedom Inv-χ^2 is defined as the distribution of the inverse of a random variable with the chi-squared distribution, and has the properties

$$\mathrm{E}[\text{Inv-}\chi_{n-1}^2] = \frac{1}{n-3}, \quad \mathrm{Var}[\text{Inv-}\chi_{n-1}^2] = \frac{2}{(n-3)^2(n-5)}, \quad (4.72)$$

and therefore

$$\mathrm{E}[\Sigma^2] = \frac{n-1}{n-3}, \quad \mathrm{Var}[\Sigma^2] = \frac{2(n-1)^2}{(n-3)^2(n-5)}. \quad (4.73)$$

One of these equations is significant enough that we will rewrite it in a more explicit form,

$$\mathrm{E}\left[\frac{\sigma^2}{S^2}\right] = \frac{n-1}{n-3} \quad \Rightarrow \quad \mathrm{E}\left[\frac{1}{S^2}\right] = \mathrm{E}\left[\frac{1}{\sigma^2}\right] \frac{n-1}{n-3} \quad (4.74)$$

In other words, the inverse of the sample variance is systematically smaller than the inverse of the true variance, a fact which will be important in the next section. We

are now ready to compute the mean and variance of our sample chi-squared value.

$$
\begin{aligned}
\mathrm{E}\left[\tilde{\chi}_j^2\right] &= \mathrm{E}[X^2\Sigma^2] \\
&= \mathrm{E}[X^2]\mathrm{E}[\Sigma^2] \\
&= \frac{n-1}{n-3} \\
\mathrm{Var}\left[\tilde{\chi}_j^2\right] &= \mathrm{Var}[X^2\Sigma^2] \\
&= (\mathrm{E}[X^2])^2\mathrm{Var}[\Sigma^2] + \mathrm{Var}[X^2](\mathrm{E}[\Sigma^2])^2 + \mathrm{Var}[X^2]\mathrm{Var}[\Sigma^2] \\
&= \frac{2}{(n-3)^2(n-5)} + 2\left(\frac{n-1}{n-3}\right)^2 + 2\frac{2(n-1)^2}{(n-3)^2(n-5)} \\
&= 2\left(\frac{n-1}{n-3}\right)^2\frac{n-2}{n-5}.
\end{aligned}
$$

$$(4.75)$$

$$(4.76)$$

Notice that $\mathrm{E}[X^2\Sigma^2] = \mathrm{E}[X^2]\mathrm{E}[\Sigma^2]$ holds since the sample mean and sample standard deviation are independent. The mean and variance of the reduced sample chi-square are then easy to find (again in the limit $N \to \infty$),

$$
\begin{aligned}
\mathrm{E}[\tilde{\chi}_{red}^2] &= \mathrm{E}\left[\frac{1}{N-1}\sum_{j=1}^{N}\tilde{\chi}_j^2\right] \\
&= \frac{N}{N-1}\mathrm{E}\left[\tilde{\chi}_j^2\right] \\
\mathrm{E}[\tilde{\chi}_{red}^2] &\approx \frac{n-1}{n-3} \\
\mathrm{Var}[\tilde{\chi}_{red}^2] &= \mathrm{Var}\left[\frac{1}{N-1}\sum_{j=1}^{N}\tilde{\chi}_j^2\right] \\
&= \frac{N}{(N-1)^2}\mathrm{Var}\left[\tilde{\chi}_j^2\right] \\
\mathrm{Var}[\tilde{\chi}_{red}^2] &\approx \frac{2}{N-1}\left(\frac{n-1}{n-3}\right)^2\frac{n-2}{n-5}
\end{aligned}
$$

$$(4.77)$$

$$(4.78)$$

General Case

We made a number of simplifying assumptions above (assuming a large data set, and ignoring the variance of the weighted mean) to make the problem tractable, since the general solution in fact does not have a closed form. The usual χ^2 test outlined in section Section 4.4.4 has modified versions which try to take into account the finite number of data points and variance of the weighted mean (both of which we completely ignored), and the reader is directed to the book by Hartung *et al.* (especially chapters 4 and 5) for more discussion[114].

We briefly considered using these modified statistical tests instead of the usual χ^2 approach, but ultimately decided against it. Instead, we prefer the approach where we simply vary the statistical properties of our data (varying points per bin, etc.) and show that the result does not change.

4.4.5   Weighted means

In the data analysis procedure outlined in Section 4.3, we used a weighted mean in several places. For a set of means x_i and variances σ_i^2, the weighted mean and variance is given by[232]

$$\bar{x} = \frac{\sum_i x_i/\sigma_i^2}{\sum_i 1/\sigma_i^2}, \quad \sigma_{\bar{x}}^2 = \frac{1}{\sum_i 1/\sigma_i^2}. \tag{4.79}$$

The weighted mean is the maximum likelihood estimator of the true mean, so it is the "best" way to combine the data points x_i and their uncertainties. However, there are two subtleties associated with this procedure that we will discuss.

Unknown variance

The weighted mean suffers from the exact same problem that we encountered in the previous section, namely that the variances σ_i^2 are unknown, and have distinctly different statistical properties compared to the sample variances[53, 170, 160, 31, 138, 114]. As in the previous section, we can do a very simple numerical simulation to clearly see the problem. Let's make a simulated data set of `Nx` points, drawn from a normal distribution $\mathcal{N}(0,1)$. Let's then bin those points into groups of `nbin`, compute the mean and standard errors, then form a weighted mean `w` and uncertainty `sigmaw` according to the usual equations above. Then, repeat to create a large number of `w`'s, and examine the actual variance.

```
Nx = 100; %Number of x values
nbin = 10; %Number of points to bin
Nw = 10000; %Number of weighted means to compute
for i = 1:Nw %Compute Nw weighted means
    for j = 1:(Nx/nbin) %Step over bins
        x = randn(1,nbin); %nbin normally distributed points
        y(j) = mean(x); %Find the mean
        sigmayi(j) = std(x)/sqrt(nbin); %Standard deviation
    end
    w(i) = sum(y./sigmayi.^2)/sum(1./sigmayi.^2); %Weighted mean
    sigmaw(i) = 1/sum(1./sigmayi.^2); %Uncertainty in w
end
mean_sigmaw = mean(sigmaw) %Mean estimated uncertainty in w
std_w = std(w) %Actual standard deviation of w
```

Running the above MATLAB code yields `mean_sigmaw=0.0894` and `std_w=0.1126`. Of course running the code over will give slightly different answers, but we can see that the formula for the variance in the weighted mean is underestimating the actual variance in the weighted means by about 25%. This means that if we use the usual formula to compute the weighted mean of 10 binned means and standard errors

170

based on 100 measurements, we will will report a weighted uncertainty that is 25% too low. If we re-run the code with `Nx = 30` and `nbin = 5`, we find that the formula underestimates the uncertainty by about 40%.

Based on our analysis above, we can pinpoint the source of the problem rather easily: the formula in Eq. (4.79) has several instances of the quantity σ_i^{-2}. However, we will of course only know the sample variance s_i^{-2}, which will is biased (see Eq. 4.74). In the limit when there are a very large number of bins, and each bin has the same number of points n, then we will compute

$$s_{\bar{x}}^2 = \frac{1}{\sum_i 1/s_i^2}. \tag{4.80}$$

Compared to the true variance $\sigma_{\bar{x}}$ from Eq. (4.79) (which contains the true variances and is therefore not known),

$$\mathrm{E}\left[\frac{s_{\bar{x}}^2}{\sigma_{\bar{x}}^2}\right] = \mathrm{E}[s_{\bar{x}}^2]\mathrm{E}[\sigma_{\bar{x}}^{-2}] = \mathrm{E}[s_i^2]\mathrm{E}[\sigma_i^{-2}] = \frac{n-3}{n-1}, \tag{4.81}$$

where we used Eq. (4.74). Therefore, we see that our sample weighted variance will underestimate by a factor of $(n-1)/(n-3)$. Notice that $n = 10$ means that we should underestimate the variance by about 30%, which is close to the 25% underestimation seen in our numerical example. The general case is very complex, and the reader is referred to the references given at the end of the first paragraph. The book by Hartung *et al.*[114] and the original article by Meier[170] are particularly good places to start.

Varying true mean

The formula for the weighted mean will give an unbiased estimate of the true mean of the data points x_i. If the data points x_i have different true means, then

the formula for weighted mean will not give a useful answer. For example, taking the weighted mean of the asymmetry values for a single trace (Figure 4.7) would yield a meaningless result. A slightly less obvious example of how this could cause problems is when there are data points with changing sign. For example, say we have measurements x_1 and x_2 which have true means $+\mu$ and $-\mu$. We might be tempted to use the weighted mean as a "weighted sum" to compute $\bar{x}$, which has an expected value of

$$\mathrm{E}[\bar{x}] = \frac{\mu/\sigma_1^2 - \mu/\sigma_2^2}{\sigma_1^{-2} + \sigma_2^{-2}}. \tag{4.82}$$

However, we can clearly see that if $\sigma_1 \neq \sigma_2$, then $\mathrm{E}[\bar{x}] \neq 0$ and we have a biased result. In our experiment, we use many such "switches" which have the effect of (ideally) only changing the sign of the asymmetry, which we add together to cancel out a number of undesired effects (see Section 4.3.7). This is especially relevant for the C-state switch $\tilde{\mathcal{P}}$, where one C-state systematically gives a larger signal (and therefore smaller uncertainty) than the other. In light of this discussion, we cannot take a weighted mean of measurements performed with different states, but must instead use an unweighted mean. The result will have a slightly larger uncertainty, but will not be biased.

4.4.6 Monte Carlo Simulation of Statistics

We want to make sure that our data has the expected statistical properties. However, in light of the discussions above, it is difficult to know what exactly those statistical properties are. One way to ensure that our data analysis routine is doing what we expect is to input simulated oscilloscope traces constructed to have certain

statistical properties, and then make sure that the data analysis code outputs the correct results. The general procedure is:

1. Generate ideal parity sums by inputting desired spin precession (including time dependence), waveplate dither, waveplate offset, and EDM.

2. Compute ideal asymmetry using these parity sums, an input contrast, and an input coherence time. The coherence time varies linearly in time after ablation (similar to the real data, see Figure 4.7).

3. Using this ideal asymmetry profile, compute an array of X and Y counts (i.e. fluorescence bins).

4. Add an input background level to the counts.

5. Add noise to the counts. We typically use Gaussian noise with standard deviation equal to the mean count rate, which is the large counts limit of Poissonian noise.

6. Put these count arrays into the same data analysis code as the real data.

We generally tried to match as many of the experimental conditions as possible, including drifting coherence time and signal size, asymmetry and contrast slopes vs. time after ablation, etc. An example comparison is shown in Figure 4.18, where we plot all EDM values for each time point at each block. Unlike the histogram shown in figure Figure 4.8, this histogram ignores the error bars on each point and is therefore not expected to be Gaussian, especially in the tails, when the signal to noise is not constant (which it is not). The actual expected distribution for this quantity is

essentially impossible to compute analytically, but we can see that the Monte Carlo

simulation gives good qualitative agreement.
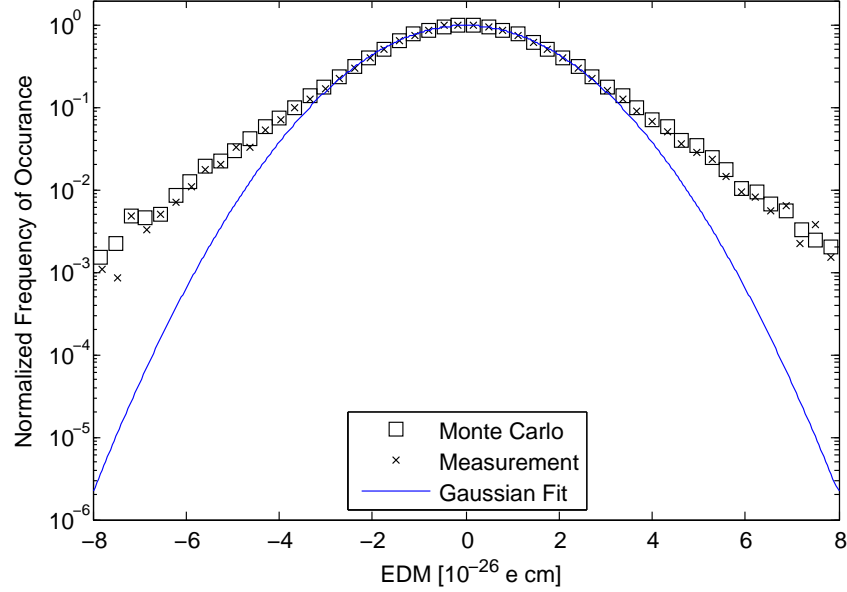
Figure 4.18: Comparison of real and Monte Carlo simulated data. Here we plot a histogram of all EDM values for each time point at each block. As discussed in the text, this histogram is not expected to be Gaussian.

Chapter 5

Interpretation of Measured Phases

In this chapter, we will deal with the most difficult and important part of any precision measurement: interpretation of the data to extract physical quantities.

5.1   Ideal system: applied fields, and an EDM

The Hamiltonian for an ideal experiment is

$$H = -Mg\mu_{\mathrm{B}}\mathcal{B}_z - \eta\tilde{\mathcal{N}}M\mu_{\mathrm{B}}|\mathcal{E}_z|\mathcal{B}_z - \tilde{\mathcal{N}}d|\mathcal{E}_z| - M\tilde{\mathcal{N}}\tilde{\mathcal{E}}\mathcal{E}_{\mathrm{eff}}d_{\mathrm{e}}. \tag{5.1}$$

The terms represent magnetic (Zeeman) spin precession, electric field dependence of the $g-$factors, the Stark shift, and the EDM, respectively. We will review the form of these terms in the following paragraphs. It is straightforward to determine in which

ω parity channel (see Section 4.3.5) these terms will appear:

$$\phi \;=\; \frac{\tau}{2}\left(E(M=+1) - E(M=-1)\right) \tag{5.2}$$

$$=\; \tau\left(-g\mu_{\mathrm{B}}\mathcal{B}_z - \eta\mu_{\mathrm{B}}\mathcal{N}|\mathcal{E}_z|\mathcal{B}_z - \mathcal{N}\tilde{\mathcal{E}}\mathcal{E}_{\mathrm{eff}}d_{\mathrm{e}}\right) \tag{5.3}$$

$$\hbar\omega \;=\; -g\mu_{\mathrm{B}}\mathcal{B}_z - \eta\mathcal{N}|\mathcal{E}_z|\mathcal{B}_z - \mathcal{N}\tilde{\mathcal{E}}\mathcal{E}_{\mathrm{eff}}d_{\mathrm{e}} \tag{5.4}$$

$$\hbar\omega^{\mathcal{B}} \;=\; -g\mu_{\mathrm{B}}|\mathcal{B}_z| \tag{5.5}$$

$$\hbar\omega^{\mathcal{NB}} \;=\; -\eta\mu_{\mathrm{B}}|\mathcal{E}_z\mathcal{B}_z| \tag{5.6}$$

$$\hbar\omega^{\mathcal{NE}} \;=\; -\mathcal{E}_{\mathrm{eff}}d_{\mathrm{e}}. \tag{5.7}$$

Notice that the Stark shift by itself does not cause spin precession since it does not depend on M.

5.1.1 Zeeman Shift

The convention that we use for $g-$factors is (see Section 2.5)

$$H_{Zeeman} = -\vec{\mu}_{\parallel} \cdot \vec{\mathcal{B}}_z = -M\mu_{\mathrm{B}}g\mathcal{B}_z. \tag{5.8}$$

Here we are making the assumption that $\vec{\mu}_{\parallel} = G_{\parallel}\vec{\Omega} = G_{\parallel}(\vec{J}_e \cdot \hat{n})\hat{n}$, that is, a positive $g-$factor means that the magnetic moment and the electron angular momentum $\vec{J}_e$ are aligned. This seems like a reasonable definition, but be warned that there is almost no consistency in definitions of the Zeeman shift signs. Previous measurements[244, 142] indicated that $|g| = 0.00440(5)$. Further measurements (see Section 6.4.3) indicated that the $g-$factor of the H state is negative.

5.1.2 g-factor Difference (η)

The term $\eta \tilde{\mathcal{N}} M \mu_{\mathrm{B}} |\mathcal{E}_z| \mathcal{B}_z$ describes the electric field dependence of the g-factors. This effect was first observed and understood in PbO[29]. Here η is a term which depends on the molecular electronic and rotational state, which for $|H, J = 1\rangle$ is 0.79(1) nm/V, as discussed further in Section 6.3. Measuring the correct value for η from the same data as the EDM is crucial; notice that only the EDM and the η term are odd under $\tilde{\mathcal{N}}$, so this term is a check to see if the $\tilde{\mathcal{N}}$ switch is behaving as expected. This term is the subject of Chapter 6.

5.1.3 Stark Shift

In the limit where the molecule is fully polarized, the opposite parity states $|H; J, M, \pm\rangle$ are fully mixed by the electric field and the good eigenstates are

$$|H; J, M, \pm\Omega\rangle = \frac{1}{\sqrt{2}} |H; J, M, +\rangle \pm \frac{1}{\sqrt{2}} |H; J, M, -\rangle. \tag{5.9}$$

The Stark shift of the states is given by[36, 117]

$$\langle H; J, M, \Omega | \vec{D} \cdot \vec{\mathcal{E}}_z | H; J, M, \Omega \rangle = \frac{M\Omega D_\| \mathcal{E}_z}{J(J+1)} = \frac{M\Omega D_\| |\mathcal{E}_z| \tilde{\mathcal{E}}}{J(J+1)} \equiv \frac{\mathcal{N} D_\| |\mathcal{E}_z|}{J(J+1)}, \tag{5.10}$$

where we have defined

$$\mathcal{N} = M\Omega\tilde{\mathcal{E}}, \tag{5.11}$$

$\tilde{\mathcal{E}} = \mathrm{sign}(\vec{\mathcal{E}}_z \cdot \hat{Z}_{lab})$ is the sign of the lab electric field relative to the lab $Z-$axis, and $D_\| = 1.67(4)ea_0 = 2.14(5)$ MHz/(V/cm) is the molecule-frame electric dipole moment[244]. The Stark Hamiltonian is given by

$$H_{Stark, J=1} = -\vec{D} \cdot \vec{\mathcal{E}}_z = -\mathcal{N}d|\mathcal{E}_z|, \tag{5.12}$$

where $d = D_\parallel/2$ is the dipole moment in the $J = 1$ state, so states with $\mathcal{N} = +1$ (-1) are shifted down (up) in energy.

5.1.4 Electron EDM

We must be very careful with this term, as it is susceptible to a number of sign errors due to differing conventions. Our convention is that the internuclear axis points from the negative (O) to the positive (Th) nucleus, so that the molecule dipole moment is aligned along $\hat{n}$. However, since electric fields point from positive to negative charges, the internal effective electric field points against $\hat{n}$, i.e. $\vec{\mathcal{E}}_{\text{eff}} = -\mathcal{E}_{\text{eff}}\hat{n}$. The electron EDM interaction is therefore

$$-\vec{d}_e \cdot \vec{\mathcal{E}}_{\text{eff}} = +d_e\mathcal{E}_{\text{eff}}\vec{S} \cdot \hat{n} = +d_e\mathcal{E}_{\text{eff}}\Sigma = -d_e\mathcal{E}_{\text{eff}}\Omega = -d_e\mathcal{E}_{\text{eff}}M\tilde{\mathcal{N}}\tilde{\mathcal{E}}, \qquad (5.13)$$

as claimed. Here we used the fact that $\Sigma = -\Omega$ for a $^3\Delta_1$ state, as shown in Figure 5.1.

5.2 Non-Ideal Effects Appearing in the Hamiltonian: "Systematics"

In this section, we will consider the "non-ideal" terms, which unfortunately (though not surprisingly) outnumber the ideal terms. In this section we shall limit our discussion to the physical origin of the terms; in the following section we will go into detail of the experimental implications, including suppression and systematic errors.
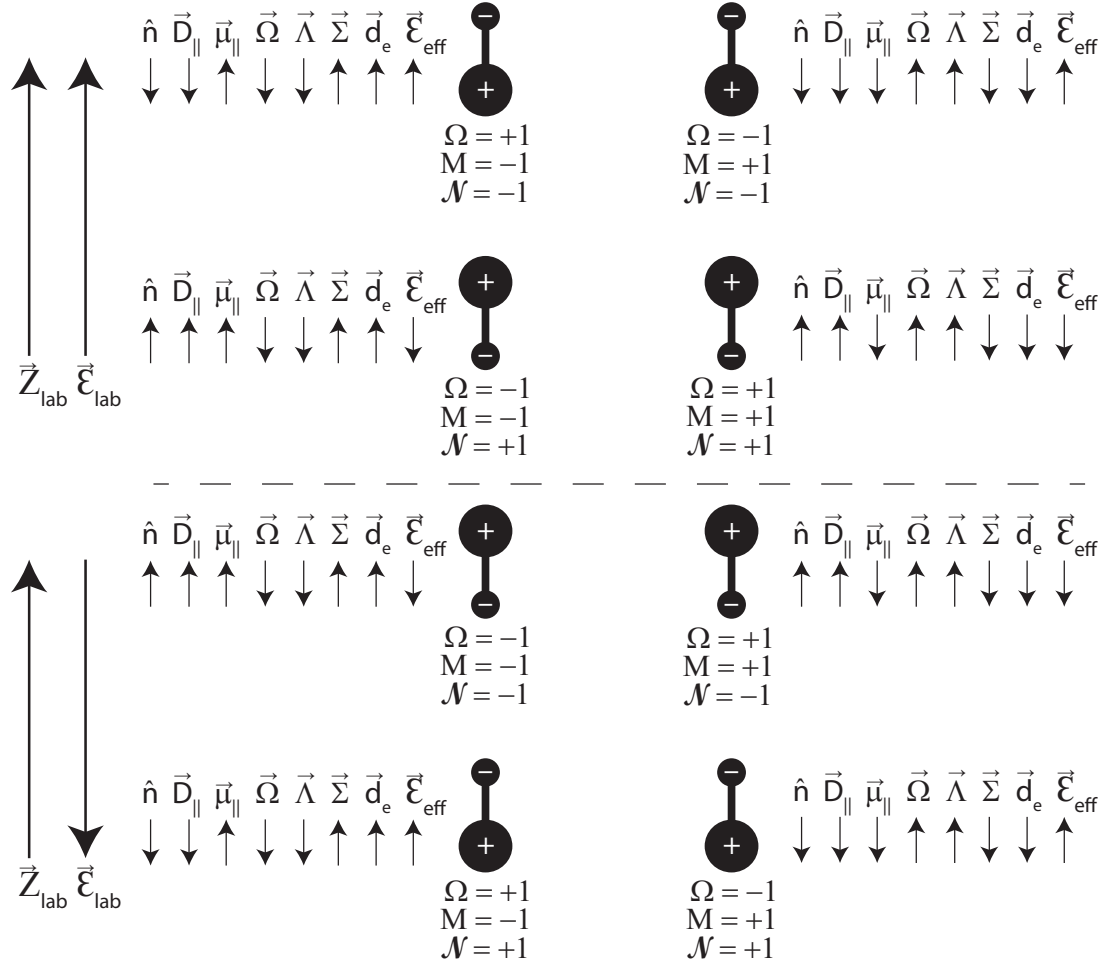
Figure 5.1: Signs of important parameters in the different molecular states, inspired by [155]. Notice the difference between scalar Ω and vector $\vec{\Omega}$. This figure assumes that the magnetic moment points against $\vec{\Omega}$, i.e that the molecule has a negative $g-$factor.

5.2.1 Non-reversing Fields

A non-reversing electric or magnetic field is a component of the field which does not reverse with the applied field. For example, we may write

$$\mathcal{E}^{\text{tot}} \;=\; \tilde{\mathcal{E}}|\mathcal{E}_z| + \mathcal{E}^{\text{nr}} \tag{5.14}$$

$$|\mathcal{E}^{\text{tot}}| \;=\; |\mathcal{E}_z| + \tilde{\mathcal{E}}\mathcal{E}^{\text{nr}}, \tag{5.15}$$

where tot indicates a total field, nr indicates non-reversing field, and we used that $|x+y| = |x| + \text{sign}(x)y$ if $|x| > |y|$. There are also identical formulas for the magnetic field, with $\mathcal{E} \to \mathcal{B}$. If we take the ideal Hamiltonian from Eq. (5.1) and include the effects of non-reversing fields, we will add a number of terms with different parities:

$$\hbar\omega^{(0)} \;=\; -g\mu_{\text{B}}\mathcal{B}^{\text{nr}} \tag{5.16}$$

$$\hbar\omega^{\mathcal{N}} \;=\; -\eta\mu_{\text{B}}|\mathcal{E}_z|\mathcal{B}^{\text{nr}} \tag{5.17}$$

$$\hbar\omega^{\mathcal{N}\mathcal{E}} \;=\; -\eta\mu_{\text{B}}\mathcal{E}^{\text{nr}}\mathcal{B}^{\text{nr}} \tag{5.18}$$

$$\hbar\omega^{\mathcal{N}\mathcal{E}\mathcal{B}} \;=\; -\eta\mu_{\text{B}}\mathcal{E}^{\text{nr}}\mathcal{B}_z. \tag{5.19}$$

Notice that the term $-\eta\mu_{\text{B}}\mathcal{E}^{\text{nr}}\mathcal{B}^{\text{nr}}$ has the same parity as the EDM, and will therefore cause a false EDM. However, with $\mathcal{E}_z = 100$ V/cm, $\mathcal{E}^{\text{nr}} = 5$ mV/cm (see Section D.2), and $\mathcal{B}^{\text{nr}} = 20$ μG (see Section 5.4.6), the false EDM would be $\approx 10^{-36}$ e cm, which is negligibly small. We shall see that an non-reversing electric field does result in a much larger EDM systematic in Section 5.3.1, due to an entirely different mechanism.

5.2.2 Light Shifts

The molecules experience a number of AC Stark shifts, or "light shifts," due to the preparation and readout lasers. The summary of important light shift effects is given by the equation

$$\phi_{\mathrm{LS}} = \alpha\Delta + \alpha^{\mathcal{B}}\mathcal{B}\Delta^2 + \beta\Omega_{\mathrm{r}} + \beta^{\mathcal{B}}\Omega_{\mathrm{r}}\mathcal{B}, \tag{5.20}$$

where Δ is the laser detuning, and Ω_{r} is the Rabi frequency. Both Δ and Ω_{r} are in units of angular frequency in this section. We shall discuss the origin of each of these terms in the following sections. We shall also see that there are $\mathcal{N}\mathcal{E}$-correlated detunings $\Delta^{\mathcal{N}\mathcal{E}}$ and Rabi frequencies $\Omega_{\mathrm{r}}^{\mathcal{N}\mathcal{E}}$ which give rise to $\mathcal{N}\mathcal{E}$-correlated phases not due to an EDM.

Light Shifts due to Polarization Gradients

The ellipticity of the lasers is important for understanding the light shifts, so let's consider the effect of the preparation laser when it has ellipticity

$$S = \frac{I_+ - I_-}{I_+ + I_-}, \quad I_\pm = \frac{1}{2}(1 \pm S)I, \tag{5.21}$$

where $I_\pm$ are the intensities of the right $(+)$ and left $(-)$ hand circular polarizations of the beam, and I is the total intensity. Notice that a linearly polarized laser has $S = 0$. If we consider the light polarization in the $\sigma_\pm$ basis,

$$\hat{\epsilon} = \frac{1}{\sqrt{2}}\left(-e^{-i\theta}\hat{\epsilon}_{+1} + e^{+i\theta}\hat{\epsilon}_{-1}\right), \tag{5.22}$$

then we can write the rotating wave Hamiltonian as

$$
H = \begin{pmatrix} \Delta & \frac{1}{2}\Omega_- e^{i\theta} & -\frac{1}{2}\Omega_+ e^{-i\theta} \\ \frac{1}{2}\Omega_- e^{-i\theta} & 0 & 0 \\ -\frac{1}{2}\Omega_+ e^{i\theta} & 0 & 0 \end{pmatrix},
\tag{5.23}
$$

where our basis is $\{|C, M = 0\rangle, |H, M = +1\rangle, |H, M = -1\rangle\} \equiv \{|0\rangle, |+1\rangle, |-1\rangle\}$, Δ is the laser detuning from resonance, and $\Omega_\pm$ is the Rabi frequency resulting from the laser intensity $I_\pm$. To simplify, let us assume that $\theta \ll 1$ and write

$$
H = \begin{pmatrix} \Delta & \frac{1}{2}\Omega_-(1 + i\theta) & -\frac{1}{2}\Omega_+(1 - i\theta) \\ \frac{1}{2}\Omega_-(1 - i\theta) & 0 & 0 \\ -\frac{1}{2}\Omega_+(1 + i\theta) & 0 & 0 \end{pmatrix}.
\tag{5.24}
$$

Since the total laser intensity $I = I_+ + I_-$ is a fixed experimental quantity, we can define $\Omega_+ = \Omega \sin(\varepsilon + \pi/4)$ and $\Omega_- = \Omega \cos(\varepsilon + \pi/4)$, where ε parameterizes the ellipticity. Notice that $\Omega_+^2 + \Omega_-^2 = \Omega^2$ is a fixed quantity since $\Omega^2 \propto I$, and $\Omega_\pm = \Omega/\sqrt{2}$ when $\varepsilon = 0$. If we restrict ourselves to the limit $S \ll 1$ and therefore $\varepsilon \ll 1$, we can see that ε is the asymmetry in the Rabi frequencies,

$$
\frac{\Omega_+ - \Omega_-}{\Omega_+ + \Omega_-} = \frac{(1 + \varepsilon) - (1 - \varepsilon)}{(1 + \varepsilon) + (1 - \varepsilon)} = \varepsilon,
\tag{5.25}
$$

which is related to the intensity ellipticity by

$$
\varepsilon = \frac{\Omega_+ - \Omega_-}{\Omega_+ + \Omega_-} = \frac{\sqrt{I_+} - \sqrt{I_-}}{\sqrt{I_+} + \sqrt{I_-}} = \frac{\sqrt{1 + S} - \sqrt{1 - S}}{\sqrt{1 + S} + \sqrt{1 - S}} = \frac{S}{2} + \mathcal{O}(S^2).
\tag{5.26}
$$

In this limit, our Hamiltonian becomes

$$
H = \begin{pmatrix}
\Delta & \frac{1}{2}\Omega(1-\varepsilon)(1+i\theta) & -\frac{1}{2}\Omega(1+\varepsilon)(1-i\theta) \\
\frac{1}{2}\Omega(1-\varepsilon)(1-i\theta) & 0 & 0 \\
-\frac{1}{2}\Omega(1+\varepsilon)(1+i\theta) & 0 & 0
\end{pmatrix} \tag{5.27}
$$

$$
= \begin{pmatrix}
\Delta & \frac{1}{2}\Omega(1-\Pi^*) & -\frac{1}{2}\Omega(1+\Pi^*) \\
\frac{1}{2}\Omega(1-\Pi) & 0 & 0 \\
-\frac{1}{2}\Omega(1+\Pi) & 0 & 0
\end{pmatrix}, \tag{5.28}
$$

where we have defined $\Pi = \varepsilon + i\theta$, and are only keeping terms to first order in ε, θ. Let us now change our basis to $\{|E\rangle, |D\rangle, |B\rangle\} = \{|0\rangle, (|+1\rangle + |-1\rangle)/\sqrt{2}, (|+1\rangle - |-1\rangle)/\sqrt{2}\}$, where the letters stand for Excited, Dark, and Bright. In this basis, our Hamiltonian takes the simpler form

$$
H = \begin{pmatrix}
\Delta & -\frac{\Pi^*\Omega}{\sqrt{2}} & \frac{\Omega}{\sqrt{2}} \\
-\frac{\Pi\Omega}{\sqrt{2}} & 0 & 0 \\
\frac{\Omega}{\sqrt{2}} & 0 & 0
\end{pmatrix}. \tag{5.29}
$$

If we define $\delta \equiv \Delta/(\sqrt{2}\Omega)$ and consider the limit $\delta \ll 1$, the eigenstates and energies (U) have a fairly simple form,

$$
\begin{align}
|D'\rangle &= |D\rangle - \Pi^* |B\rangle \tag{5.30} \\
U_{D'} &= 0 \tag{5.31} \\
|B'\rangle &= \frac{1}{\sqrt{2}}\left((-1+\delta)|E\rangle + \Pi|D\rangle + |B\rangle\right) \tag{5.32} \\
U_{B'} &= \hbar\frac{\Omega}{\sqrt{2}}(\delta-1) \tag{5.33} \\
|E'\rangle &= \frac{1}{\sqrt{2}}\left((+1+\delta)|E\rangle + \Pi|D\rangle + |B\rangle\right) \tag{5.34} \\
U_{E'} &= \hbar\frac{\Omega}{\sqrt{2}}(\delta+1). \tag{5.35}
\end{align}
$$

In addition to acquiring a light shift, the states $|B'\rangle$ and $|E'\rangle$ will decay radiatively due to their admixture of the $|E\rangle$ state. If the optical field is intense enough to saturate the transition, then the molecules will be in either $|B\rangle$ or $|E\rangle$ with equal probability and the states $|B'\rangle$ and $|E'\rangle$ with decay with time constant $2/\gamma_C = 1$ μs, where $\gamma_C \approx (500 \text{ ns})^{-1}$ is the decay rate of the C state. In this amount of time the molecules will travel ≈ 0.2 mm, so as long as the laser width is > 1 mm we should lose $> 99\%$ of these states to the ground electronic state. This means that the molecules will be only in state $|D'\rangle$, which is simply some rotation of the $|D\rangle, |B\rangle$ states described earlier and will, at worse, introduce some constant phase offset to the measurement.

Consider now what happens when an initial state $|\psi(t=0)\rangle = |D\rangle$ enters an optical field with $0 < |\Pi| \ll 1$ which is not strong enough to saturate the transition. First, we will project the state onto the new basis,

$$|\psi(0)\rangle = |E'\rangle \langle E'|D\rangle + |D'\rangle \langle D'|D\rangle + |B'\rangle \langle B'|D\rangle = \frac{\Pi}{\sqrt{2}} |E'\rangle + \frac{\Pi}{\sqrt{2}} |B'\rangle + |D'\rangle . \quad (5.36)$$

After time T, the state will evolve into

$$|\psi(T)\rangle = \frac{\Pi}{\sqrt{2}} e^{-iU_{E'}T/\hbar} |E'\rangle + \frac{\Pi}{\sqrt{2}} e^{-iU_{B'}T/\hbar} |B'\rangle + |D'\rangle . \quad (5.37)$$

For times much shorter than the Rabi period, the population fraction in the excited state will be $\frac{1}{4}\Omega^2 T^2 \ll 1$, so there will be negligible loss of molecules due to radiative decay of the excited state. However, we will now show that there is a light shift linear in ΔT. We shall continue to make the assumption that $\Delta \ll \Omega$, so as long as $\Delta \ll \Omega \ll T^{-1}$, we will have negligible loss from the excited state yet non-negligible light shift. Let the molecules abruptly leave the optical field so that $\Omega = 0$. If they

precess for a time much longer than $1/\gamma_C$ in no fields, the states $|D\rangle$ and $|B\rangle$ will not accumulate any additional phase (since they will be degenerate ground states in our three level system), and the $|E\rangle$ component will decay, leaving

$$
\begin{align}
|\psi(t')\rangle &= \frac{\Pi}{\sqrt{2}}e^{-iU_{B'}T/\hbar}\,|B'\rangle + |D'\rangle \tag{5.38}\\
&= \frac{\Pi}{2}e^{-iU_{E'}T/\hbar}\,|B\rangle + \frac{\Pi}{2}e^{-iU_{B'}T/\hbar}\,|B\rangle + |D\rangle - \Pi\,|B\rangle \tag{5.39}\\
&= |D\rangle + \Pi\left(e^{-i\delta\Omega T}\cos(\Omega T) - 1\right)|B\rangle \tag{5.40}\\
&\approx |D\rangle + \Pi\left(e^{-i\delta\Omega T + \Omega^2 T^2/2} - 1\right)|B\rangle, \tag{5.41}
\end{align}
$$

where we used that $\cos(x) \approx \exp(-x^2/2)$ for small x. Now assume that an optical field with $\varepsilon = \theta = 0$ performs the projective measurement. We must perform the spin readout with the polarization rotated by $45°$ for maximum phase sensitivity (see Section 4.2.1), so we must find the projection onto the dark and bright states in this new basis,

$$
\begin{align}
D(\theta) &= \cos(\theta)\,|D\rangle + i\sin(\theta)\,|B\rangle \tag{5.42}\\
D(\pi/4) &= \frac{1}{\sqrt{2}}\,|D\rangle + \frac{i}{\sqrt{2}}\,|B\rangle \tag{5.43}\\
B(\theta) &= i\sin(\theta)\,|D\rangle + \cos(\theta)\,|B\rangle \tag{5.44}\\
B(\pi/4) &= \frac{i}{\sqrt{2}}\,|D\rangle + \frac{1}{\sqrt{2}}\,|B\rangle \tag{5.45}\\
\mathcal{A} &= \frac{|\langle B(\pi/4)|\psi(t')\rangle|^2 - |\langle D(\pi/4)|\psi(t')\rangle|^2}{|\langle B(\pi/4)|\psi(t')\rangle|^2 + |\langle D(\pi/4)|\psi(t')\rangle|^2} \tag{5.46}\\
&\approx \Omega^2 T^2\theta - \Delta T\varepsilon \tag{5.47}
\end{align}
$$

where we are ignoring factors of order unity for this approximation, and have only kept terms to lowest order in Δ and Ω. If we use $\phi \approx \mathcal{A}/2\mathcal{C} \approx \mathcal{A}/2$, we will see an

"ellipticity light shift"

$$\phi_{\mathrm{ELS}} \approx \theta \Omega^2 T^2 - \varepsilon \Delta T. \tag{5.48}$$

This phase will be detected by our spin precession measurement, but overall phases are not important for our measurement. These phases become important when there are detunings or Rabi frequencies which are correlated with experimental switches, of which we shall see some examples later on. Since these correlated detunings and Rabi frequencies are small, we can linearize the light shift around the typical Rabi frequency of the experiment and write the light shift as

$$\phi_{\mathrm{ELS}} \approx \alpha \Delta + \beta \Omega_{\mathrm{r}}^{\mathrm{corr}}. \tag{5.49}$$

Here α and β are defined and measurable quantities which depend on experimental parameters such as ellipticity gradients, though their approximate form is given by comparing the above equation to Eq. (5.48). $\Omega_{\mathrm{r}}^{\mathrm{corr}} \ll \Omega_{\mathrm{r}}$ is a small Rabi frequency correlated with some experimental switches.

At this point, we could try to estimate what the values for α and β should be. However, it is much better to actually measure these values, which we will discuss in Section 5.3.1.

$\mathcal{B}$-odd light shifts

The light shifts discussed above do not depend on magnetic field. However, by including the Zeeman interaction (see Section 2.5) we obtain the Hamiltonian

$$\begin{pmatrix} \Delta & \frac{1}{2}\Omega_{\mathrm{r}} & -\frac{1}{2}\Omega_{\mathrm{r}} \\ \frac{1}{2}\Omega_{\mathrm{r}} & +\zeta & 0 \\ -\frac{1}{2}\Omega_{\mathrm{r}} & 0 & -\zeta \end{pmatrix}, \tag{5.50}$$

where $\zeta = g\mu_{\mathrm{B}}\mathcal{B}$. We won't go through the derivation, but by repeating the calculations above (treating $|\zeta|$ as a small parameter), we find a light shift phase

$$\phi_{LS}^{\mathcal{B}} = \alpha^{\mathcal{B}}\mathcal{B}\Delta^2, \tag{5.51}$$

where, similar to the previous section, $\alpha^{\mathcal{B}}$ depends on the time the molecules spend in the "intermediate strength" portion of the optical field. Since we have not included any imperfect polarizations, this should be a light shift present even in the ideal experiment. We can clearly see this light shift by varying the laser detuning and measuring the molecular phase with only a $\mathcal{B}$ switch, and obtain the typical $\mathcal{B}$-odd light shift

$$\alpha^{\mathcal{B}}\mathcal{B}\Delta^2 \approx (2 \ \mathrm{mrad/s}) \times \left(\frac{\Delta}{2\pi \times 1 \ \mathrm{MHz}}\right)^2 \times \left(\frac{\mathcal{B}}{20 \ \mathrm{mG}}\right) \tag{5.52}$$

5.2.3 Correlated detunings

Here we shall show that a non-reversing electric field $\mathcal{E}^{\mathrm{nr}}$ (see Section 5.2.1) gives rise to a correlated detuning $\delta^{\mathcal{N}\mathcal{E}}$, and that a modulation frequency offset gives rise to a correlated detuning $\delta^{\mathcal{N}}$. We shall use uppercase Δ to denote detunings with angular frequency units, and δ to detnote detunings with linear frequency units, so that $\Delta = 2\pi\delta$.

Figure 5.2 shows the upper and lower Ω-doublet states, split by an electric field $\mathcal{E}$, so that the upper and lower states are detuned from their center of mass by $\pm d\mathcal{E}$. Here $d = 1.07 \ \mathrm{MHz/(V/cm)}$[244]. The preparation and readout lasers are split by AOMs into two beams of frequency $\nu_c \pm \nu_m$, where ν_c is the carrier frequency, and $\delta\nu_c$ is the detuning of the carrier from the center-of-mass of the upper and lower spectral
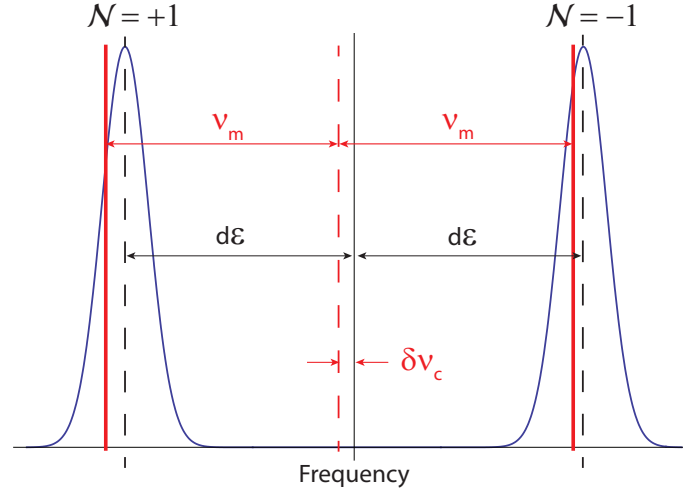
Figure 5.2: Spectral lines for $\mathcal{N} = \pm 1$ in an electric field. ν_m is a modulator frequency, $d\mathcal{E}$ is the Stark shift, and $\delta\nu_c$ is an overall detuning.

lines. By looking at Figure 5.2, we can see that the detuning of the upper and lower

laser lines from the spectral line centers is given by

$$\begin{aligned} \delta(\tilde{\mathcal{N}} = +1) &= d\mathcal{E} + \delta\nu_c - \nu_m \\ \delta(\tilde{\mathcal{N}} = +1) &= \delta\nu_c + \nu_m - d\mathcal{E} \end{aligned} \quad \Rightarrow \quad \delta(\tilde{\mathcal{N}}) = \tilde{\mathcal{N}}d\mathcal{E} - \tilde{\mathcal{N}}\nu_m + \delta\nu_c. \tag{5.53}$$

If we include the effects of a non-reversing electric field $\mathcal{E}^{\mathrm{nr}}$, and use the fact that for

$|a| > |b|$ we have $|a + b| = |a| + \mathrm{sign}(a)b$, then

$$\delta(\tilde{\mathcal{N}}, \mathcal{E}, \mathcal{E}^{\mathrm{nr}}, \delta\nu_c, \nu_m) = \tilde{\mathcal{N}}d|\mathcal{E} + \mathcal{E}^{\mathrm{nr}}| - \tilde{\mathcal{N}}\nu_m + \delta\nu_c = \tilde{\mathcal{N}}d\mathcal{E} + \tilde{\mathcal{N}}d\tilde{\mathcal{E}}\mathcal{E}^{\mathrm{nr}} - \tilde{\mathcal{N}}\nu_m + \delta\nu_c. \tag{5.54}$$

Define the difference between the modulation frequency and Stark shift as $\delta\nu_m = \nu_m - d\mathcal{E}$, so that

$$\delta(\tilde{\mathcal{N}}, \tilde{\mathcal{E}}, \mathcal{E}^{\mathrm{nr}}, \delta\nu_c, \delta\nu_m) = \tilde{\mathcal{N}}\tilde{\mathcal{E}}d\mathcal{E}^{\mathrm{nr}} - \tilde{\mathcal{N}}\delta\nu_m + \delta\nu_c. \tag{5.55}$$

We can now see that the effect of an $\mathcal{E}^{\mathrm{nr}}$ is to create a correlated detuning $\delta^{\mathcal{N}\mathcal{E}} = d\mathcal{E}^{\mathrm{nr}}$,

and an incorrect modulation frequency adds $\delta^{\mathcal{N}} = -\delta\nu_m = \nu_m - d\mathcal{E}$. The latter effect

is quite useful; a correlated detuning creates a correlated contrast $\mathcal{C}^{\mathcal{N}}$ (see Appendix E), so zeroing this quantity gives a precise way to set the AOM modulation frequency.

If we combine this fact with Eq. (5.49), we can see that there will be an $\mathcal{N}\mathcal{E}$-correlated phase given by

$$\phi^{\mathcal{N}\mathcal{E}}_{\mathcal{E}^{\mathrm{nr}}} = 2\pi\alpha d\mathcal{E}^{\mathrm{nr}}. \qquad (5.56)$$

In Figure 5.4 we see $\alpha \approx 5$ mrad/MHz, so with $d \approx 1.1$ MHz/(V/cm)[244] and $\mathcal{E}^{\mathrm{nr}} \approx 5$ mV/cm (see Section D.2), we would obtain an $\mathcal{N}\mathcal{E}$-correlated phase of ≈ 30 μrad, or a false EDM of $\approx 2 \times 10^{-28}$ e cm, which is unacceptably large. This effect was observed in the experiment, and is discussed further in Section 5.3.1.

5.2.4 Correlated Rabi frequencies

In addition to correlated detunings, there are correlated Rabi frequencies present in our experiment which lead to correlated phases via Eq. (5.49). These correlated Rabi frequencies and their implications were worked out by Brendon O'Leary, and the reader is referred to his lablog entries (for example, 18 July 2013) for more details.

We prepare the dark state by driving an electric dipole (E1) transition, leaving a dark state which is on-resonance but has no coupling and therefore zero Rabi frequency. However, there are other moments associated with the transition, for example the magnetic dipole (M1) transition moment. E1 and M1 transitions connect states of opposite parity[97]; however, since the electric and magnetic fields in the lasers are perpendicular, the bright state is driven by both the E1 and M1 components of the transition. Rabi frequency correlations can arise when the E1 and M1 components behave differently under reversals of experimental parameters, which indeed exist.

Specifically, it turns out (see Brendon's 18 July 2013 lablog entry, or Appendix B) that the signs of the E1 and M1 matrix elements are related by $k\hat{n} = k\tilde{\mathcal{N}}\tilde{\mathcal{E}}$, where $k = \hat{k} \cdot Z_{\text{lab}} = \pm 1$ is the propagation direction of the lasers. This means that for a fixed k, there is an effective $\mathcal{N}\mathcal{E}$-correlated Rabi frequency $\Omega_{\text{r}}^{\mathcal{N}\mathcal{E}}$.

There are multiple pieces of evidence supporting the existence of a non-zero $\Omega_{\text{r}}^{\mathcal{N}\mathcal{E}}$. First, there is an $\mathcal{N}\mathcal{E}$-correlated fluorescence signal with magnitude equal to $\approx 2\times10^{-3}$ times the total count rate. Second, this correlated fluorescence rate reversed sign with an experimental reversal of k. Third, there is a $\mathcal{N}\mathcal{E}\mathcal{B}$-correlated phase $\phi^{\mathcal{N}\mathcal{E}\mathcal{B}}$ due to $\Omega_{\text{r}}^{\mathcal{N}\mathcal{E}}$ coupling to the $\mathcal{B}$-odd, Ω_{r}-dependent light shift (see Section 5.2.2), as discussed further in Section 5.3.2.

5.2.5 Correlated magnetic fields: leakage current and switch ordering

Consider the effect of a magnetic field component which reverses with another switch, so that we may write $\mathcal{B}_{\text{tot}} = \tilde{\mathcal{B}}|\mathcal{B}_z| + \tilde{\mathcal{N}}\mathcal{B}^{\mathcal{N}} + \tilde{\mathcal{E}}\mathcal{B}^{\mathcal{E}} + \tilde{\mathcal{N}}\tilde{\mathcal{E}}\mathcal{B}^{\mathcal{N}\mathcal{E}}$. This will give rise to a number of terms, the most significant of which will be

$$\hbar\omega^{\mathcal{E}} = -g\mu_{\text{B}}\mathcal{B}^{\mathcal{E}} \tag{5.57}$$

$$\hbar\omega^{\mathcal{N}} = -g\mu_{\text{B}}\mathcal{B}^{\mathcal{N}} \tag{5.58}$$

$$\hbar\omega^{\mathcal{N}\mathcal{E}} = -g\mu_{\text{B}}\mathcal{B}^{\mathcal{N}\mathcal{E}} - \eta\mu_{\text{B}}|\mathcal{E}_z|\mathcal{B}^{\mathcal{E}}. \tag{5.59}$$

A term $\mathcal{B}^{\mathcal{E}}$ can arise from a "leakage current," that is, a current flowing from one electric field plate to the other[140]. A motional magnetic field is also $\mathcal{E}$-correlated, but that is a purely transverse field and is suppressed due to the large Stark shift

separating the $M = \pm1$ states (see [242, 192]); however, a leakage current field could be along the z axis. We can see two reasons why leakage currents are heavily suppressed in our system. First, even if $\mathcal{B}^{\mathcal{E}} \approx 1$ μG, large enough to see on the fluxgates which are inside the magnetic shields, the resulting false EDM would be only $\eta\mu_{\mathrm{B}}|\mathcal{E}_z|\mathcal{B}^{\mathcal{E}}/\mathcal{E}_{\mathrm{eff}} \approx 10^{-30}$ e cm. Second, the term $-g\mu_{\mathrm{B}}\mathcal{B}^{\mathcal{E}}$ appearing in $\omega^{\mathcal{E}}$ is larger than the term causing the false EDM by a factor of $g/(\eta|\mathcal{E}_z|) > 100$, so the effect would be significantly amplified and easily detected in another channel.

Terms like $\mathcal{B}^{\mathcal{N}}$ and $\mathcal{B}^{\mathcal{N}\mathcal{E}}$ might seem artificial since it is not physically reasonable to expect that the magnetic field changes with a laser detuning (provided that the frequency switching electronics are well isolated from the molecules, which they are.) However, terms with this behavior can give rise due to timing correlations and systematic drifts. Since we degauss the magnetic shields between each $\mathcal{B}$-switch, there is some systematic transient magnetic field which decays away after each switch. If we perform the other switches in a non-random order, then the first $\mathcal{N}$ (or $\mathcal{E}$) state will systematically see a different magnetic field than the second. This will give rise to an effective $\mathcal{B}^{\mathcal{E}}, \mathcal{B}^{\mathcal{N}}$, and $\mathcal{B}^{\mathcal{N}\mathcal{E}}$.

In run 0339, we purposefully applied $\mathcal{B}^{\mathcal{E}} = \pm1.4$ mG in the control system to see if we could measure the $\eta\mu_{\mathrm{B}}|\mathcal{E}_z|\mathcal{B}^{\mathcal{E}}$ component of $\omega^{\mathcal{N}\mathcal{E}}$. This term should give rise to a false EDM slope vs. $\mathcal{B}^{\mathcal{E}}$ of $d_{\mathrm{e,false}}/\mathcal{B}^{\mathcal{E}} = \hbar\eta\mu_{\mathrm{B}}|\mathcal{E}_z|/\mathcal{E}_{\mathrm{eff}} = 8 \times 10^{-28}$ e cm/mG. However, we measured a slope that was approximately 4 times larger than expected. Upon examining the $\mathcal{N}, \mathcal{E}, \mathcal{B}$ parity sums of the fluxgates readings, we found that there was a large $\mathcal{N}\mathcal{E}$-correlated magnetic field, which was due to the fact that the switching order was not randomized for this run. In run 0351, we repeated the $\mathcal{B}^{\mathcal{E}}$ measurement

with randomized switching and measured $|d_{\mathrm{e,false}}/\mathcal{B}^{\mathcal{E}}| = (7.2 \pm 1.8) \times 10^{-28}$ e cm/mG, in good agreement with our prediction. The bound of $|\mathcal{B}^{\mathcal{E}}| \lesssim 10^{-4}$ mG from the fluxgates means that this systematic is suppressed to the $< 10^{-31}$ e cm level.

5.2.6 Contrast correlations

As briefly mentioned earlier, the contrast needn't be a true constant and can be correlated with experimental switches. In light of Section 5.2.3, the existence of $\mathcal{N}$- and $\mathcal{N}\mathcal{E}$-correlated detunings naturally leads to correlated contrasts $\mathcal{C}^{\mathcal{N}}$ and $\mathcal{C}^{\mathcal{N}\mathcal{E}}$, respectively. Therefore, we could replace $\mathcal{C} \to \mathcal{C}^{(0)} + \tilde{\mathcal{N}}\tilde{\mathcal{E}}\mathcal{C}^{\mathcal{N}\mathcal{E}} + \mathcal{N}\mathcal{C}^{\mathcal{N}}$ in Eq. (4.24), which would lead to a dramatic increase in the number of possible terms. However, as discussed in Section 4.3.8, these terms can be eliminated from the measured phases by computing asymmetry and contrast for each state of the experiment, so we will relegate further discussion to Appendix E.

5.2.7 Summary of terms in the Hamiltonian, including known systematics

We will now combine all of the effects listed earler to obtain a reasonably complete description of the Hamiltonian. Instead of writing out the full Hamiltonian, we will break up all of the terms into the different ω parities, since these are ultimately the quantities which we seek to compute. These terms are shown in Table 5.1.

Table 5.1: Table of different ω parities arising from the effects we have considered in this section. τ is the coherence time; $\mathcal{C}$ is the contrast; θ is the pump/probe relative polarization dither; g is the g-factor and d is the electric dipole moment of $|H, J = 1\rangle$; η quantifies the electric field dependence of the g-factors; $\mathcal{B}, \mathcal{E}$ are the applied magnetic, electric fields, and $\mathcal{B}^{\mathrm{nr}}$, $\mathcal{E}^{\mathrm{nr}}$ are their non-reversing components; $\alpha, \alpha^{\mathcal{B}}, \beta, \beta^{\mathcal{B}}$ are light shifts given by Eq. (5.20); Δ represents a laser detuning; k is the direction of the laser pointing relative to the lab Z_{lab} axis; $\Omega_{\mathrm{r}}^{\mathcal{N}\mathcal{E}}$ is the intrinsic $\mathcal{N}\mathcal{E}$ correlated Rabi frequency; μ_{B} is the Bohr Magneton; d_{e} and $\mathcal{E}_{\mathrm{eff}}$ are the electron EDM and internal effective field of ThO.

Channel	Terms
$\hbar\omega^{(0)}$	$-\theta\tau^{-1}$
	$-\mathcal{B}^{\mathrm{nr}}g\mu_{\mathrm{B}}$
	$-\alpha\tau^{-1}\Delta^{(0)}$
	$-\tau^{-1}\mathcal{B}^{\mathrm{nr}}\alpha^{\mathcal{B}}(\Delta^{\mathcal{N}})^2$
	$-\tau^{-1}\mathcal{B}^{\mathrm{nr}}\alpha^{\mathcal{B}}(\Delta^{(0)})^2$
	$-\tau^{-1}\mathcal{B}^{\mathrm{nr}}d\alpha^{\mathcal{B}}(\mathcal{E}^{\mathrm{nr}})^2$
$\hbar\omega^{\mathcal{B}}$	$-|\mathcal{B}|g\mu_{\mathrm{B}}$
	$-\tau^{-1}|\mathcal{B}|\alpha^{\mathcal{B}}(\Delta^{\mathcal{N}})^2$
	$-\tau^{-1}|\mathcal{B}|\alpha^{\mathcal{B}}(\Delta^{(0)})^2$
	$-\tau^{-1}|\mathcal{B}|d\alpha^{\mathcal{B}}(\mathcal{E}^{\mathrm{nr}})^2$
$\hbar\omega^{\mathcal{E}}$	$-2\tau^{-1}\mathcal{B}^{\mathrm{nr}}d\alpha^{\mathcal{B}}\Delta^{\mathcal{N}}\mathcal{E}^{\mathrm{nr}}$
$\hbar\omega^{\mathcal{E}\mathcal{B}}$	$-2\tau^{-1}|\mathcal{B}|d\alpha^{\mathcal{B}}\Delta^{\mathcal{N}}\mathcal{E}^{\mathrm{nr}}$
$\hbar\omega^{\mathcal{N}}$	$-\alpha\tau^{-1}\Delta^{\mathcal{N}}$
	$-\eta|\mathcal{E}|\mathcal{B}^{\mathrm{nr}}\mu_{\mathrm{B}}$
	$-2\tau^{-1}\mathcal{B}^{\mathrm{nr}}\alpha^{\mathcal{B}}\Delta^{(0)}\Delta^{\mathcal{N}}$
$\hbar\omega^{\mathcal{N}\mathcal{B}}$	$-\eta|\mathcal{B}||\mathcal{E}|\mu_{\mathrm{B}}$
	$-2\tau^{-1}|\mathcal{B}|\alpha^{\mathcal{B}}\Delta^{(0)}\Delta^{\mathcal{N}}$
$\hbar\omega^{\mathcal{N}\mathcal{E}}$	$-d_{\mathrm{e}}\mathcal{E}_{\mathrm{eff}}$
	$-\alpha\tau^{-1}d\mathcal{E}^{\mathrm{nr}}$
	$-2\tau^{-1}\mathcal{B}^{\mathrm{nr}}d\alpha^{\mathcal{B}}\Delta^{(0)}\mathcal{E}^{\mathrm{nr}}$
	$-\eta\mathcal{B}^{\mathrm{nr}}\mathcal{E}^{\mathrm{nr}}\mu_{\mathrm{B}}$
	$-k\beta\tau^{-1}\Omega_{\mathrm{r}}^{\mathcal{N}\mathcal{E}}$
	$-k\tau^{-1}\mathcal{B}^{\mathrm{nr}}\beta^{\mathcal{B}}\Omega_{\mathrm{r}}^{\mathcal{N}\mathcal{E}}$
$\hbar\omega^{\mathcal{N}\mathcal{E}\mathcal{B}}$	$-2\tau^{-1}|\mathcal{B}|d\alpha^{\mathcal{B}}\Delta^{(0)}\mathcal{E}^{\mathrm{nr}}$
	$-\eta|\mathcal{B}|\mathcal{E}^{\mathrm{nr}}\mu_{\mathrm{B}}$
	$-k\tau^{-1}|\mathcal{B}|\beta^{\mathcal{B}}\Omega_{\mathrm{r}}^{\mathcal{N}\mathcal{E}}$

5.3 Measurement and Suppression of Systematic Effects

Here we will discuss how the effects discussed in the previous section were measured and suppressed (when possible) in our experiment.

5.3.1 False EDM from light shifts and non-reversing $\mathcal{E}$-field

Figure 5.3 shows our first[1] systematic check with an applied $\mathcal{E}^{\mathrm{nr}}$, Run 0110. The slope from this run was $d_e/\mathcal{E}^{\mathrm{nr}} = (2.8 \pm 0.1) \times 10^{-29}$ e cm/(mV/cm), which was considerably larger than expected from the $\mathcal{E}^{\mathrm{nr}}\mathcal{B}^{\mathrm{nr}}$ cross term. With an $\mathcal{E}^{\mathrm{nr}}$ of 5 mV/cm (see Section D.2), this would lead to a false EDM of $\approx 1.4 \times 10^{-28}$ e cm, which is 3-4 times larger than our final statistical uncertainty (see Table 5.6).

This large slope was due to the ellipticity light shift α (see Eq. (5.49)) coupled to a correlated detuning $\delta^{\mathcal{N}\mathcal{E}} = d\mathcal{E}^{\mathrm{nr}}$ (see Section 5.2.3). There will be an $\mathcal{N}\mathcal{E}$-correlated phase $\phi^{\mathcal{N}\mathcal{E}} = \alpha d\mathcal{E}^{\mathrm{nr}}$ from these two effects, which will cause a false EDM $d_{e,\mathrm{false}}/\mathcal{E}^{\mathrm{nr}} = \alpha d/\mathcal{C}\tau$. To make sure that the numbers for this model make sense we measured α directly by measuring the overall molecule phase (with no switches, and no magnetic field) as a function of laser detuning, and obtained the results shown in Figure 5.4. In that figure, the blue curve shows the light shift with no corrections, and the slope is ≈ 4 mrad/MHz near the center, which should lead to $d_{e,\mathrm{false}}/\mathcal{E}^{\mathrm{nr}} \approx 3 \times 10^{-29}$ e cm/(mV/cm), very close to what was actually measured

---

[1]Run 0110 was not truly the first, but it was the first with multiple values of $\mathcal{E}^{\mathrm{nr}}$ interleaved, and was the first with an applied $\mathcal{E}^{\mathrm{nr}}$ which would mimic an actual non-reversing field, say from patch potentials. See my lablog entry from 14 November 2012 for details.
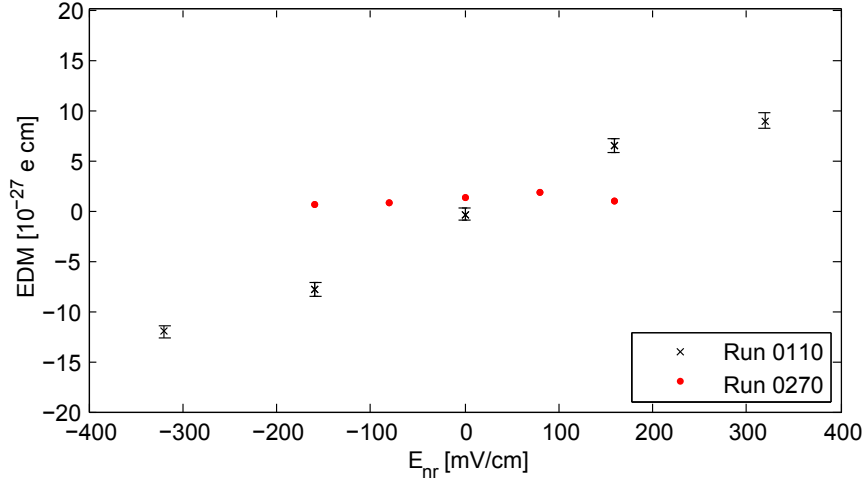
Figure 5.3: EDM vs. applied non-reversing electric field, before correcting (Run 0110) and after correcting (Run 0270). The error bars for Run 0270 are approximately the size of the marker.

with the $\mathcal{E}^{\mathrm{nr}}$ systematic check. At this point we could have simply subtracted away this effect, but we instead decided to try and directly reduce it.

As discussed in Appendix A, the ellipticity light shift is due to a polarization structure imprinted on the lasers by thermal stress birefringence in the electric field plates. Therefore, we are not able to eliminate this effect simply with better polarization optics. There are three simple tricks to reduce this effect, each of which we perform.

1. Align the laser polarizations with the birefringent axes of the plates. This is the most obvious solution, but doesn't work in all situations. As discussed in Section 4.2.1, if we operate with a fringe number of 1, that is, with a magnetic field which causes a $\pi/4$ rotation of the molecules, then we must have a 45° relative polarization rotation between the pump and probe. Since the birefringent axes will be perpendicular, this means that we cannot satisfy this alignment with

both pump and probe.

2. Reduce the heat load on the plates with a chopper wheel. If we only shine the lasers through the plates when there are molecules present, the net thermal load will be reduced. We verified that this indeed reduces the ellipticity gradient. It is important that the lasers be on for the entire oscilloscope trace so that we can perform a background subtraction (see Section 4.3.8); since our scope traces are 9 ms long and come every 20 ms, we simply have a 50% chopper wheel with a full period of 20 ms. This reduces the effect by half.

3. Eliminate the low-intensity part of the laser beams. As discussed in Section 5.2.2, the light shift comes from the molecules spending time in an optical field with varying ellipticity that is not bright enough to pump away the dark state. If we impose a sharp drop in intensity after the dark state is prepared, the light shift should be reduced. This method gives us the most significant suppression of the light shift (see Figure 5.4), and works for all magnetic fields.

By combining these effects, we were able to reduce this systematic below our statistical uncertainty. The calculation of the systematic shift and uncertainty is discussed in Section 5.4.2.

We briefly considered compensating for the effect by imprinting the "inverse" polarization before sending the light through the field plates, but quickly decided that simply reducing the effect below our experimental sensitivity was much more attractive.
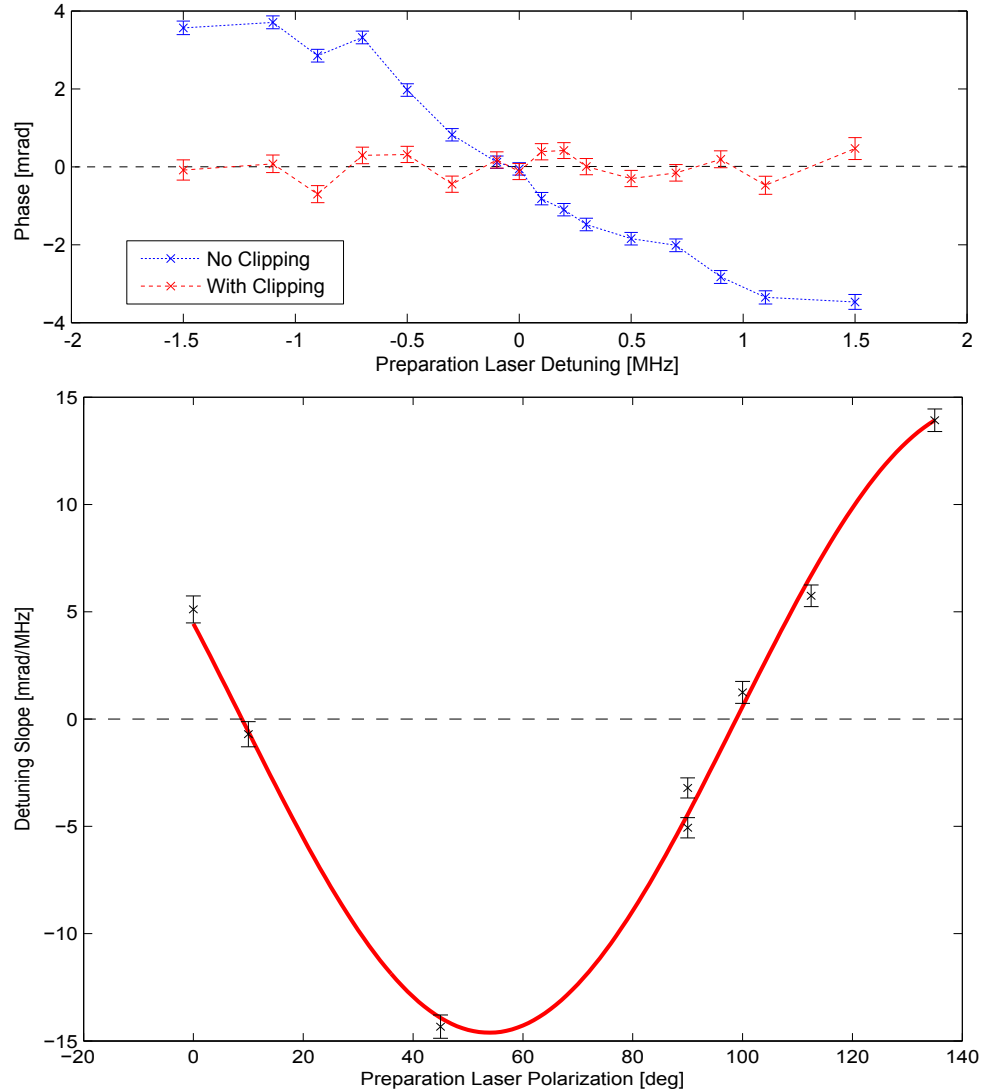
Figure 5.4: Top: Light shift with (Run 0144) and without (Run 0139) clipping the Gaussian tail of the preparation laser beam. The lines connecting the data points are to guide the eye. Bottom: Slope of light shift vs. detuning for various angles of preparation laser polarization. The fit is to a sine curve with 180° period, which is expected for a birefringent effect.

5.3.2 False EDM from light shifts and correlated Rabi frequency

As discussed in Section 5.2.2, the light shift due to a linear polarization gradient will couple to the $\mathcal{NE}$-correlated Rabi frequency $\Omega_{\mathrm{r}}^{\mathcal{NE}}$ to cause an $\mathcal{NE}$-correlated phase $\phi^{\mathcal{NE}} = \beta\Omega_{\mathrm{r}}^{\mathcal{NE}}$ and therefore a false EDM $d_{\mathrm{e,false}} = \beta\Omega_{\mathrm{r}}^{\mathcal{NE}}/\mathcal{E}_{\mathrm{eff}}$. Since $\Omega_{\mathrm{r}}^{\mathcal{NE}}$ is an intrinsic molecular property, we cannot directly change it in order to try and observe this term. However, we can simulate a $\Omega_{\mathrm{r}}^{\mathcal{NE}}$ by applying an $\mathcal{NE}$-correlated fractional laser power, $P^{\mathcal{NE}}$. This is achieved by sending the lasers through a AOM, using the undiffracted beam in the experiment, and blocking the diffracted beams. We chose this method over a more robust method to control laser power, for example with waveplates and polarizers, because it is very fast. In theory we could also change β by adding a linear polarization gradient (or enhancing the existing one), but we could not think of a simple method of doing so. The thermal stress birefringence which causes the ellipticity gradient causes a linear polarization gradient which is too small to measure (see Appendix A).

Unlike the non-reversing $\mathcal{E}$-field systematic, we were never able to induce a very large effect in the EDM channel. However, we did find that the slope of $d_{\mathrm{e}}/P^{\mathcal{NE}}$ did depend on laser alignment and shaping, and and background subtraction method. Specifically, we found subtracting a constant value of the background for each trace resulted in a large $\mathcal{NE}$-correlated asymmetry; this asymmetry was canceled by the C-state switch $\tilde{\mathcal{P}}$ and pump X/Y interchange $\tilde{\mathcal{R}}$ (see Section 4.3.7), but we generally performed an X, Y dependent background subtraction on runs with an applied $P^{\mathcal{NE}}$ to avoid this effect.
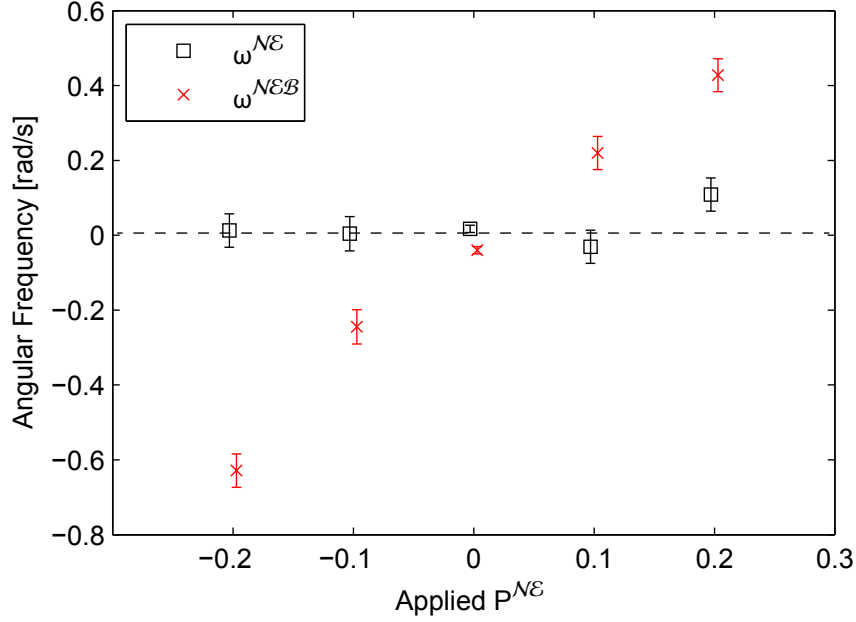
Figure 5.5: $\omega^{\mathcal{NE}}$ and $\omega^{\mathcal{NEB}}$ vs. applied fractional $\mathcal{NE}$-correlated laser power.

An important parameter for this systematic is the mean $\Omega_{\mathrm{r}}^{\mathcal{NE}}$ at our typical laser intensities. Since the parameter we apply is $P^{\mathcal{NE}}$, and since the laser power and Rabi frequency are linearly related for small deviations around their means, we typically discuss the "intrinsic" $P_{\mathrm{eff}}^{\mathcal{NE}}$, i.e. which applied $P^{\mathcal{NE}}$ would be needed to cancel the effect of the non-zero $\Omega_{\mathrm{r}}^{\mathcal{NE}}$. To compute $P_{\mathrm{eff}}^{\mathcal{NE}}$, we measure $\omega^{\mathcal{NEB}}$ as a function of applied $P^{\mathcal{NE}}$ and find the value where $\omega^{\mathcal{NEB}} = 0$, meaning that the correlated Rabi frequency has been canceled. The value we find, which we treat as a constant, is $P_{\mathrm{eff}}^{\mathcal{NE}} = 0.0158(2)$.

5.3.3 False EDM from contrast correlations and phase offsets

Even though contrast correlations can be eliminated from the measured phases as discussed in Section 4.3.8, it is worth mentioning them since they can lead to false

EDMs if not properly dealt with. We know there are generic ways (see Appendix E) for a $\mathcal{C}^{\mathcal{N}}$ or $\mathcal{C}^{\mathcal{N}\mathcal{E}}$ to appear in the system, and the $\mathcal{C}^{\mathcal{N}\mathcal{E}}$ term is the most dangerous: it can couple to any overall phase (which does not change under experimental switches) to create a false EDM. For example, if the polarization difference between the pump and probe is not exactly equal to the phase added to the molecules by the magnetic field (which it never will be), then there will be a false EDM $d_{\mathrm{e,false}} = \theta^{\mathrm{nr}} \mathcal{C}^{\mathcal{N}\mathcal{E}}$, where θ^{nr} is the amount by which the polarization is offset. Fortunately, such a false EDM can be eliminated by performing the phase computation on a state-by-state basis (see Section 4.3.8), or by measuring $\mathcal{C}^{\mathcal{N}\mathcal{E}}$ and θ^{nr} and making sure that it is small

Figure 5.6 shows the result of some runs with both an applied $\mathcal{E}^{\mathrm{nr}}$ and θ^{nr}. We see that there is indeed an $\mathcal{N}\mathcal{E}$-correlated phase (which would cause a false EDM) if we use the block-averaged contrast to compute the phase, but that this phase vanishes if we instead use state-averaged contrast.

5.3.4 $\mathcal{N}\mathcal{E}\mathcal{B}$-correlated precession from light shifts and correlated Rabi frequency

Our measurement always showed a non-zero value of $\omega^{\mathcal{N}\mathcal{E}\mathcal{B}}$, though we never realized its statistical significance until our first long data set in June 2013. The frequency appeared to depend linearly on $\mathcal{B}$, and did not change under any of our superblock switches or $|\mathcal{E}|$. The signal was eventually determined by Brendon O'Leary to be an $\mathcal{N}\mathcal{E}$-correlated Rabi Frequency $\Omega_{\mathrm{r}}^{\mathcal{N}\mathcal{E}}$ (see Section 5.2.2) coupling to the $\mathcal{B}$-odd, Rabi frequency-dependent light shift (see Section 5.2.2) $\phi^{\mathcal{N}\mathcal{E}\mathcal{B}} = \beta^{\mathcal{B}\Omega} |\mathcal{B}| \Omega_{\mathrm{r}}^{\mathcal{N}\mathcal{E}}$. The smoking gun for this model was that the phase switched sign almost exactly
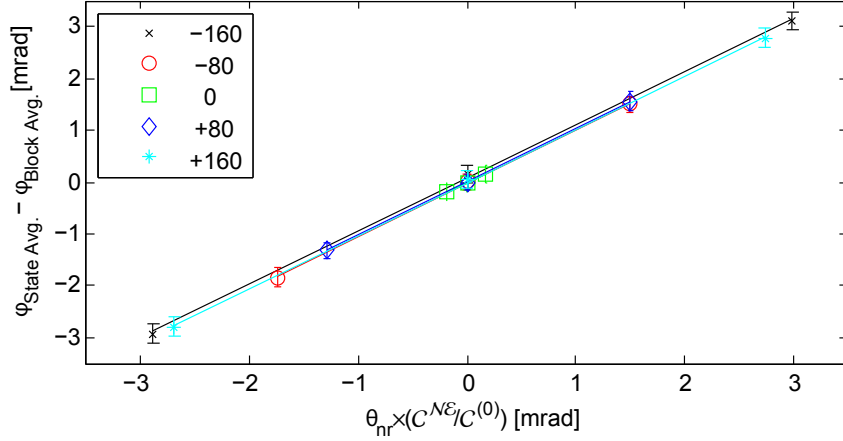
Figure 5.6: Suppression of $\mathcal{C}^{\mathcal{NE}}$ false EDM by using state-averaged contrast (Runs 0097-0102). Each line represents data taken with a different value of $\mathcal{E}^{\mathrm{nr}}$ (indicated in the legend in mV/cm), and therefore a different $\mathcal{C}^{\mathcal{NE}}$. The y-axis is the difference between the $\phi^{\mathcal{NE}}$ computed with block-averaged and state-averaged contrast, and the x-axis gives the applied θ^{nr} times the calculated $\mathcal{C}^{\mathcal{NE}}$. The mean slope of these lines is 1.03 ± 0.03, indicating that the block-averaged $\phi^{\mathcal{NE}}$ does indeed have a term caused by $\theta^{\mathrm{nr}} \times \mathcal{C}^{\mathcal{NE}}$, but that using state-averaged contrast suppresses it.

when the direction of the lasers (and therefore $\Omega_{\mathrm{r}}^{\mathcal{NE}}$) was reversed, as shown in Figure 5.7.

5.3.5 $\mathcal{N}$-correlated Laser Pointing

For a number of runs with high $\mathcal{E}$ field (141 V/cm), there was an $\mathcal{N}$-correlated laser pointing, $k^{\mathcal{N}}$. This was discovered by examining parity sums on the laser monitor photodiode voltages, and observing a large $\mathcal{N}$-correlated signal. Since the photodiodes would not be able to distinguish between a power or pointing correlation, a beam profiler confirmed that the laser pointing did in fact shift when the $\mathcal{N}$ state of the lasers was changed. While there was never any evidence that this effect showed up in the EDM channel (see Section 5.4.3), we did observe changes in $\omega^{\mathcal{N}}$ due to this effect. In particular, runs where there was a non-zero (or drifting) $k^{\mathcal{N}}$ tended to have
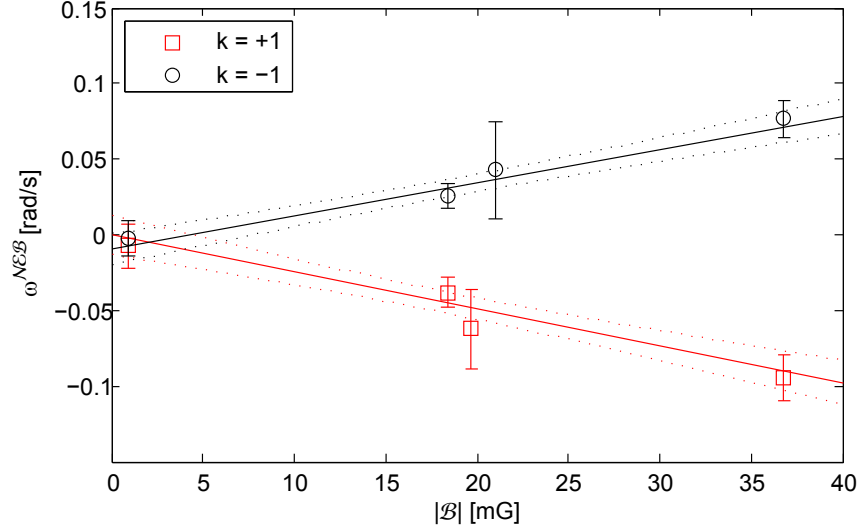
Figure 5.7: Plot of $\omega^{\mathcal{NEB}}$ vs. magnetic field for two different laser propagation directions. The slope for $k = \hat{k} \cdot Z_{\text{lab}} = +1, -1$ is given by -2.4(6) mrad/s/mG, +2.2(5) mrad/s/mG, respectively.

a non-zero (or drifting) measured $\omega^{\mathcal{N}}$.

While we never did figure out exactly why this effect caused a drifting value of $\omega^{\mathcal{N}}$, the $k^{\mathcal{N}}$ was eliminated with better optical alignment of the lasers into the fiber amplifier. A good overview of this effect can be found in Brendon O'Leary's lablog entry dated 11 September 2013.

5.4 Determination of Systematic Shift and Uncertainty

For a parameter P, we measure the slope $S = \partial P / \partial \omega^{\mathcal{NE}}$ and slope uncertainty δS by measuring $\omega^{\mathcal{NE}}$ at varying values of P and using standard line fitting techniques[197]. We then compute the systematic uncertainty due to P as $\delta\omega_P^{\mathcal{NE}} = (\delta S')P$, and sys-
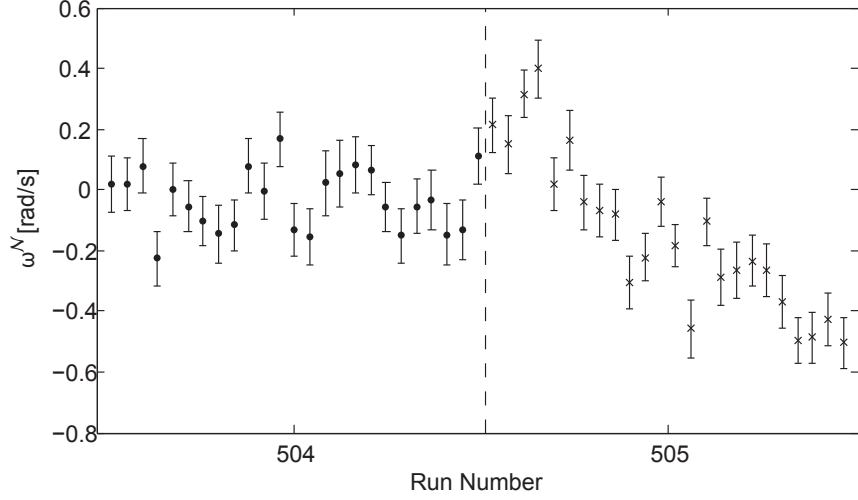
Figure 5.8: Drifting value of $\omega^{\mathcal{N}}$ for two different runs. Run 0505 had high $\mathcal{E}$-field and large drifting $k^{\mathcal{N}}$ (as indicated by the laser monitor photodiodes) compared to the low $\mathcal{E}$ run 0504. Each point represents an average of a complete superblock.

tematic shift $\omega_P^{\mathcal{N}\mathcal{E}} = S'P^{(0)}$, where $S' = \sqrt{S^2 + (\delta S)^2}$ is an upper bound for S'. Notice that $\delta\omega_P^{\mathcal{N}\mathcal{E}}$ is therefore strictly larger than the 1σ Gaussian uncertainty, which would be given by $(\delta S)P$. Unless specified otherwise, we ignore uncertainty on the parameter P, since $\delta P/P \ll \delta S/S$ is typical for our experimental parameters.

It is important to stress that the procedure for determining the systematic uncertainty was decided before unblinding (see Section 4.3.6). Additionally, the numbers reported in this section differ slightly from those published in our result paper[16]. Those values were obtained by taking the average value of the mean and standard deviation for the three different sets of results computed by myself, Ben Spaun, and Brendon O'Leary.

5.4.1 Criteria for inclusion

In order an effect to be included in our systematic uncertainty, it must satisfy at least one of the following three criteria:

1. A parameter moved the EDM by a statistically significant amount,

2. A parameter causes a known, calculable false EDM,

3. One of "good" data channels had unexplained behavior,

4. A parameter caused a not-entirely-explained false EDM in a similar experiment.

If an effect satisfies one of the first two criteria, we apply a correction to the mean value as well as adding the uncertainty in quadrature. Otherwise, we do not shift the mean and add the uncertainty in quadrature.

Criteria 1 and 2 are clear and straightforward. In this generation of the experiment, we were fortunate that every effect which satisfied criterion 1 also satisfied criterion 2; that is, unlike the YbF EDM measurement[126], we did not have to apply any shifts to the EDM mean which we did not understand. The non-reversing $\mathcal{E}$-field and correlated Rabi frequency effects satisfy criteria 1 and 2, while $\mathcal{E}$ odd phases coupling to the g-factor difference of the Ω-doublet states satisfy only criterion 2. We neglect effects which satisfy only criterion 2 which are $\lesssim 10^{-31}$; for example, we know there is a term in $\omega^{\mathcal{NE}}$ due to combined non-reversing electric and magnetic fields $\eta\mu_{\mathrm{B}}\mathcal{B}^{\mathrm{nr}}\mathcal{E}^{\mathrm{nr}} \approx 1$ μrad/sec, which would cause a false EDM of $< 10^{-32}$ e cm, so we do not consider this effect as satisfying criterion 2.

In criterion 3, by a "good" channel we mean one which has fast switches (i.e. anything which is $\mathcal{E}$ or $\mathcal{N}$ odd), and should therefore have a consistent, robust

value (see Section 4.3.5). In other words, we claim to be able to accurately measure $\omega^{\mathcal{E}}, \omega^{\mathcal{EB}} \omega^{\mathcal{N}} \omega^{\mathcal{NB}} \omega^{\mathcal{NE}}$, and $\omega^{\mathcal{NEB}}$, so if one of these values (apart from $\omega^{\mathcal{NE}}$, which gives the EDM) cannot be understood, then we will include some systematic uncertainty. If one of these channels drifts (as was the case with $\omega^{\mathcal{N}}$, as discussed in Section 5.4.5), we treat the drifting channel as a varying parameter and compute the systematic uncertainty in the usual way. Notice that we do not have a criterion for how to deal with a "good" channel which is not drifting but has an unexplained value, but fortunately we were not in that situation.

Criterion 4 is perhaps the most unusual, and is included for the sake of being cautious. If another similar experiment saw an effect which they did not understand, then we therefore cannot say that it is not present in our experiment. We choose the PbO and YbF experiments for this criterion; PbO because it has a similar molecular structure, and YbF because it is a pulsed beam experiment. PbO saw not-entirely-understood false EDMs due to magnetic field offsets and gradients[77], while YbF saw not-entirely-understood false EDMs due to detunings and electric field plate voltage offsets[126, 135].

5.4.2 Non-reversing $\mathcal{E}$-field

Since application of a non-reversing $\mathcal{E}$-field caused a measurable false EDM, this parameter satisfied the first two criteria. The effect was ultimately due to a light shift which depended on the laser polarization and shape, so we computed the correction and uncertainty for each value of k (since the new optical setup likely resulted in a change to the beam shape), and for each value of the magnetic field (since the

Table 5.2: Table of systematic corrections and uncertainties due to a non-reversing $\mathcal{E}$-field. The details are discussed in the text. $*$ We did not monitor this slope during the run, so we choose to use the quadrature sum of the mean and uncertainty on $d_{\text{e,false}}$ for $k = -1$, $\text{mod}(N_{\text{fringe}}, 2) = 0$ as an uncertainty and do not apply a correction to the mean.

k	$+1$	$+1$	-1	-1
$\text{mod}(N_{\text{fringe}}, 2)$	0	1	0	1
$\mathcal{E}^{\text{nr}}[\text{mV/cm}]$	-4 ± 1	-4 ± 1	-5 ± 1	-5 ± 1
$d_{\text{e,false}}/\mathcal{E}^{\text{nr}}$ $[10^{-30}$ e cm/(mV/cm)]	$*$	0.3 ± 1.1	4.8 ± 1.1	1.7 ± 1.2
$d_{\text{e,false}}[10^{-30}$ e cm]	$0 \pm 25.1^{*}$	-1.2 ± 4.6	-24.0 ± 7.3	-8.5 ± 6.2

polarization is rotated to bias the measurement on the maximum fringe slope). Since the polarizations for $N_{\text{fringe}} = 0$ and 2 are the same, we combine these and consider the "fringe parity," $\text{mod}(N_{\text{fringe}}, 2)$. The non-reversing electric field data was measured with microwave spectroscopy, and is discussed in Section D.2. The slopes of $d_{\text{e,false}}$ vs. $\mathcal{E}^{\text{nr}}$ were measured every few hours during the EDM data sets. Table 5.2 shows the systematic correction and uncertainty from non-reversing electric fields. The table assumes that $\mathcal{E}^{\text{nr}}$ is the same at the pump and probe, though they are in fact slightly different (see Section D.2). However, that difference is encoded in the uncertainty on $\mathcal{E}^{\text{nr}}$.

5.4.3 Correlated Rabi frequency

As with $\mathcal{E}^{\text{nr}}$, the correlated Rabi systematic likely changes with polarization and beam shape, so we break up the data by laser pointing direction and fringe parity. Table 5.3 shows the systematic corrections and uncertainty from this effect.

Table 5.3: Table of systematic corrections and uncertainties due to an effective $\mathcal{NE}$-correlated laser power $P^{\mathcal{NE}}$. The details are discussed in the text. We use $P^{\mathcal{NE}} = -0.0158 \pm 0.002$ for all states. $*$ We did not monitor this slope during the run, so we do not apply a shift to the mean.

k	$+1$	$+1$	-1	-1
$\mathrm{mod}(N_{\mathrm{fringe}}, 2)$	0	1	0	1
$d_{\mathrm{e,false}}/P^{\mathcal{NE}}$ $[10^{-30}$ e cm$]$	668 ± 1130	-1238 ± 1101	1792 ± -764	-837 ± 725
$d_{\mathrm{e,false}}[10^{-30}$ e cm$]$	$0 \pm 21^{*}$	$0 \pm 26^{*}$	-28 ± 12	-13 ± 12

5.4.4 $\mathcal{E}$-odd phases

Since the g-factors in the upper and lower Ω-doublet states differ by an amount $\Delta = 2\eta|\mathcal{E}|$ (see Section 6.3), any $\mathcal{E}$-odd magnetic spin precession $\omega^{\mathcal{E}}$ will contribute an $\mathcal{NE}$-correlated spin precession $\approx (\Delta g/g)\omega^{\mathcal{E}} \approx 10^{-3}$. Since there are a large class of effects which are $\mathcal{E}$-odd, such as leakage currents, certain geometric phases, and motional fields, we can use our measured value of $\omega^{\mathcal{E}} = -3.9 \pm 4.3$ mrad/s to conclude that these effects will only contribute on the $< 10^{-2}$ mrad/s or $< 10^{-31}$ e cm level. However, since we know that these effects will cause a false EDM, they satisfy inclusion criterion # 2 so we include a conservative systematic correction of $(1 \pm 1) \times 10^{-31}$ e cm.

5.4.5 Drifting $\omega^{\mathcal{N}}$

As discussed in Section 5.4.5, $\omega^{\mathcal{N}}$ drifted and was generally non-zero for a subset of our high $\mathcal{E}$ data. Since $\omega^{\mathcal{N}}$ is a value which we think we should be able to measure very well (see Section 4.3.5), yet it displayed unexplained behavior, we choose to include a systematic uncertainty (criterion # 3). Specifically, we create a plot of $\omega^{\mathcal{N}}$ vs. EDM

and fit a line[254] to obtain a slope of $d_{e,false}/\omega^{\mathcal{N}} = 3(2) \times 10^{-29}$ e cm/(rad/s). Since the spread in the means is comparable to the uncertainties on each point, we must inflate the slope by the reliability ratio of 1.5[49]. The data points were taken from all EDM data runs, as well as any run where a large $k^{\mathcal{N}}$ was artificially added (0520-0523,0534). Once we have a slope, we use the mean value of $\omega^{\mathcal{N}} = -0.29(5)$ mrad/s and follow the outlined at the beginning of this section to obtain a systematic EDM uncertainty of 10.1×10^{-30} e cm. We do not apply a shift to the mean since there was no evidence that the EDM was actually correlated with $\omega^{\mathcal{N}}$.
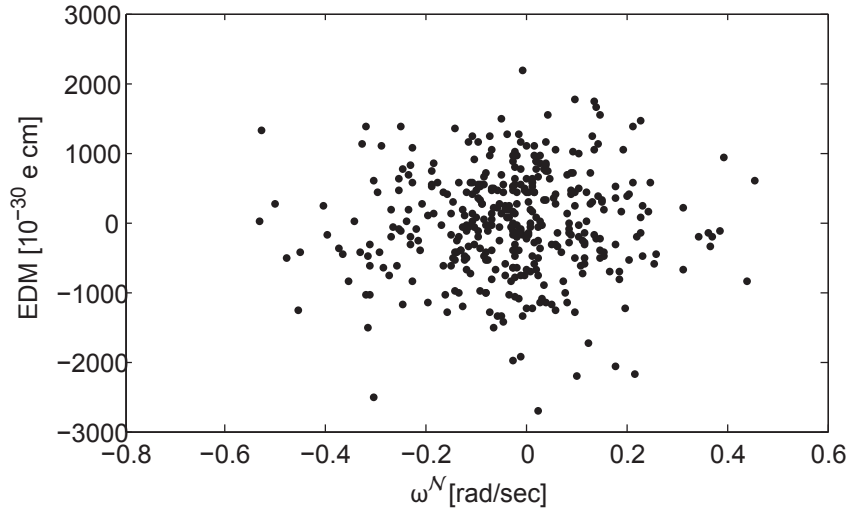
Figure 5.9: Scatter plot of $\omega^{\mathcal{N}}$ vs EDM. All data points have both error bars on both axes, but they are not indicated since the plot would be too dense to read.

5.4.6 Magnetic field offsets and gradients

Because the PbO EDM experiment observed not-entirely-understood false EDMs caused by magnetic field gradients[77], we choose to include these effects in our systematic uncertainty (criterion # 4). Specifically, we include all non-reversing mag-

Table 5.4: Systematic uncertainties due to magnetic field offsets and gradients.

Parameter	Measured	δd_{e} [10^{-30} e cm]
$\mathcal{B}_x^{\mathrm{nr}}$	0.1 mG	4.5
$\mathcal{B}_y^{\mathrm{nr}}$	0.65 mG	6.9
$\mathcal{B}_z^{\mathrm{nr}}$	0.02 mG	6.0
Total $\mathcal{B}^{\mathrm{nr}}$	–	10.2
$\partial\mathcal{B}_x/\partial x$	2 μG/cm	0.7
$\partial\mathcal{B}_y/\partial x$	8 μG/cm	5.0
$\partial\mathcal{B}_y/\partial y$	4 μG/cm	6.4
$\partial\mathcal{B}_y/\partial z$	8 μG/cm	4.4
$\partial\mathcal{B}_z/\partial x$	1 μG/cm	4.1
$\partial\mathcal{B}_z/\partial z$	4 μG/cm	6.3
Total gradients	–	11.9
Total magnetic	–	15.7

netic fields $\mathcal{B}_x^{\mathrm{nr}}$, $\mathcal{B}_y^{\mathrm{nr}}$, $\mathcal{B}_z^{\mathrm{nr}}$, and all applied magnetic field gradients $\partial\mathcal{B}_x/\partial x$, $\partial\mathcal{B}_y/\partial x$, $\partial\mathcal{B}_y/\partial y$, $\partial\mathcal{B}_y/\partial z$, $\partial\mathcal{B}_z/\partial x$, $\partial\mathcal{B}_z/\partial z$. Since there was no evidence that these shifted the EDM, we include only a systematic uncertainty and no correction to the mean. The measured values for the non-reversing fields and gradients are taken from fluxgate measurements along the molecular beam line, and are discussed in Brendon O'Leary's lablog entry dated 7 October 2013.

5.4.7 Laser detunings

Because the YbF EDM experiment observed not-entirely-understood false EDMs caused by detunings[126, 135], we choose to include these effects in our systematic uncertainty (criterion # 4). The detunings in the YbF experiment were microwave detunings, but we feel that the role of their microwaves and our lasers were similar enough that this inclusion was justified. We include $\delta^{\mathcal{N}}$, $\delta^{\mathcal{N}} \times \delta^{(0)}$, $\delta_{\mathrm{pump}}^{(0)}$, and $\delta_{\mathrm{probe}}^{(0)}$.

Table 5.5: Systematic uncertainties due to laser detunings.

Parameter	Measured [kHz]	δd_e [10^{-30} e cm]
$\delta^{\mathcal{N}}$	20	6.7
$\delta^{\mathcal{N}} \times \delta^{(0)}$	4	3.5
$\delta^{(0)}_{\text{pump}}$	70	10.4
$\delta^{(0)}_{\text{probe}}$	10	6.7
Total detuning	−	14.5

We choose $\delta^{\mathcal{N}} \times \delta^{(0)}$ since this quantity has a known, large effect in a good channel ($\omega^{\mathcal{NB}}$, see Section 4.3.5). The experimental values for these detunings come from the $\mathcal{N}$-correlated contrast for $\delta^{\mathcal{N}}$ (see Appendix E), and Doppler scans for $\delta^{(0)}$.

Electric field plate ground offset

Because the YbF EDM experiment observed not-entirely-understood false EDMs caused by adding a voltage offset to their electric field plates[126, 135], we choose to include this effect in our systematic uncertainty (criterion # 4). Specifically, we set the voltage supply to the two field plates to be $\pm V + V_0$, where $V_0 \neq 0$ and $\pm V$ are the usual operating voltages. The typcal operating voltage offset was determined to be < 5 mV using a voltmeter, so by applying $V_0 = \pm 1$ Volt we found a slope of $0.0 \pm 0.3 \times 10^{-30}$ e cm/Volt, for an uncertainty of 1.5×10^{-30} e cm.

Systematic checks not included in our error budget

We performed a number of systematic checks which did not pass the criteria for inclusion in our systematic uncertainty. However, they were useful checks to make sure that we understood what was happening in our system. Here is a partial list of

these checks:

- Application of $\mathcal{E}$-correlated $\mathcal{B}$-field, $\mathcal{B}^{\mathcal{E}}$. We did not directly include this parameter, but we did account for it by general inclusion of $\mathcal{E}$-odd effects as described in Section 5.4.4.

- Laser detunings correlated with C-state, $\Delta^{\mathcal{P}}$.

- Laser power correlated with $\mathcal{N}$, $P^{\mathcal{N}}$.

- Temporal overlap of lasers to address the different $\mathcal{N}$ states. Specifically, for the first 5 shots of the 25 shots averaged together to obtain a trace, the lasers to address both $\mathcal{N}$ states were present.

- Pointing offset of preparation and readout lasers.

- Relative pointing offset of X and Y readout beams.

- Power reduction in both preparation and readout lasers.

- Change in number of shots averaged to form a trace, from 25 to 10 and then 50. In addition to changing the statistics, this changed the time scale of the switches to be about a factor of two both faster and slower.

- Molecular beam clipping with the adjustable collimators, both horizontal and vertical. Specifically, we moved the collimators in from their fully retracted positions until the signal dropped by about half. At one point we observed a significant change in $\omega^{\mathcal{NB}}$ by moving the horizontal collimators, but it was not repeatable.

- Preparation laser ellipticity.

- Rotational state. We performed a short EDM measurement in $|H, J = 2\rangle$, but did not accumulate much statistics. The primary motivation of operating in $J = 2$ was to measure the electric field dependence of the g-factors (η) in this state, as discussed in Chapter 6.

- Fast electric field lead switching, that is, switching the leads instead of the signs of the voltages on the field plate voltage supply.

- Applied non-reversing $\mathcal{E}$-field with an applied $\mathcal{NE}$-correlated detuning to compensate for the induced detuning correlations (see Section 5.2.3)

- Reducing the polarization switching frequency

- Blocking the preparation laser (i.e. zero contrast), and ensuring that the parity sums were all zero.

5.4.8   Rejected Methods

Here are are two methods which were proposed, along with the reasons for why we rejected them.

Add all systematic checks in quadrature

The procedure is very simple: add all of the uncertainties in Table 5.6 in quadrature, and report that as the systematic uncertainty. Apart from the practical drawback that this would result in a systematic uncertainty many times larger than our statistical uncertainty, it has a several fundamental drawbacks. First, our systematic

uncertainty will become larger as we perform more systematic checks, even if those checks do not show any evidence of shifting the EDM. Second, we could arbitrarily subdivide the data into any number of "parameters," and if we have no rejection criteria for inclusion in our systematic uncertainty then we are essentially obligated to do this. For example, we could divide the data into "which day of the week was this data taken," make a plot of EDM vs. "day of the week", and then get a "day of the week" uncertainty. The "day of the week" example is somewhat frivolous, but there are other parameters, such as room temperature, human operator, chamber pressure, etc. which certainly have physical effects on the apparatus. If we started including such systematic effects, the systematic uncertainty would balloon to unreasonable values.

Add systematic checks whose uncertainty is below some cutoff

One solution is to simply include all of the systematic checks whose uncertainty is below some cutoff value. The problem with this approach is that with a large number of systematic checks with a large range of uncertainties (such as ours), this is inescapably equivalent to setting the systematic uncertainty to whatever value the experimenter chooses. In this case, the value of the systematic uncertainty is independent of the results of the actual systematic checks, as long as there are a large number of them with a large range of values, which hardly seems reasonable.

Table 5.6: Final error budget and result.

Parameter	Mean [10^{-30} e cm]	Uncertainty [10^{-30} e cm]
Non-reversing $\mathcal{E}$-field ($\mathcal{E}^{\mathrm{nr}}$)	-8.1	5.5
Correlated Rabi frequency ($\Omega_{\mathrm{r}}^{\mathcal{NE}}$)	-12.5	8.6
$\mathcal{E}$-odd effects ($\Omega^{\mathcal{E}}$)	$+0.1$	0.1
Drifting $\Omega^{\mathcal{N}}$	-	10.2
Magnetic effects	$-$	15.7
Detuning effects	$-$	14.5
Field plate voltage offset	$-$	1.5
Total Systematic	$+21$	26
Statistical	-32	38
Final Result	-11	46

5.5 Final Error Budget and Result

Table 5.6 summarizes our final error budget, based on the statistical result and systematic corrections and uncertainties discussed above. Notice that the final value is $\approx 1 \times 10^{-29}$ e cm closer to zero than the published value[16] $d_{\mathrm{e}} = (-2.1 \pm 4.5) \times 10^{-29}$ e cm $= (-2.1 \pm 3.7_{\mathrm{stat}} \pm 2.5_{\mathrm{sys}}) \times 10^{-29}$ e cm, and therefore would result in a slightly lower limit for d_{e}.

The upper limit is obtained using the Feldman-Cousins approach to computing confidence intervals[90], and yields $d_{\mathrm{e}} < 8.7 \times 10^{-29}$ e cm with 90% confidence. A good description of this procedure, and its application to our specific case, can be found in Elizabeth Petrik's lablog entry dated 10 July 2013.

5.5.1 A new limit on the electron-nucleon pseudoscalar coupling, C_S

In addition to the electron EDM, there is another quantity manifests itself in exactly the same way in a molecule[147, 55, 76, 87, 196, 133]: a CP-violating coupling

electron-nucleon pseudoscalar coupling, quantified by a unitless coupling constant C_S. This quantity is discussed much less frequently, though it has essentially the same implications for physics beyond the Standard Model as an electron EDM. The CP violating term in the molecular Hamiltonian (for our $\Omega = 1$ state) can be written as

$$H_{CP} = -d_e \mathcal{E}_{\text{eff}} - C_S W_S, \tag{5.60}$$

where W_S is a molecule specific constant, which is $h \times 300$ kHz for the H state in ThO[224]. Note that the pseudoscalar enhancement factor is reported as $k_{T,P} = h \times 116$ kHz in the paper where it is calculated, which differs from C_S by (atomic mass number)/(proton number) $= 232/90$ for the Thorium atom in ThO[76].

In reporting our EDM limit, we take the traditional approach and assume $C_S = 0$ for the reported value. We can also assume that $d_e = 0$, in which case we find

$$C_S = (-0.8 \pm 3.1) \times 10^{-9}, \tag{5.61}$$

which we can obtain from our final EDM result in Table 5.6 and multiplying by $\mathcal{E}_{\text{eff}}/W_S = (84 \text{ GV/cm})/(h \times 300 \text{ kHz}) = 6.77 \times 10^{19}/(\text{e cm})$. Notice that this differs slightly from the reported[16] value of $(-1.3 \pm 3.0) \times 10^{-9}$, which resulted in a 90% confidence upper limit of $|C_S| < 5.9 \times 10^{-9}$, a six-fold improvement over the previous limit[108].

Chapter 6

Effective Zeeman Hamiltonian in ThO $H^3\Delta_1$

Here we compute the energy shifts of the ThO H state in a magnetic field, including perturbations from an external electric field and other electronic and rotational states. The main result of this computation is to understand the dependence of the magnetic spin precession rate on J, $\mathcal{E}$, and $\mathcal{N}$, where $\mathcal{N} = M\Omega\tilde{\mathcal{E}} = -1(+1)$ for the state where the molecule is anti-aligned (aligned) in a large external electric field and therefore has higher (lower) energy. Recall that $\tilde{\mathcal{E}} = \text{sign}(\vec{\mathcal{E}} \cdot Z_{\text{lab}})$, and in general a $\sim$ over a quantity indicates the sign of that quantity. We compare the calculations to our measured values for a few different J levels.

As we claimed in Section 2.5, the Zeeman Hamiltonian is

$$H_{mag} = -Mg(J)\mu_B\mathcal{B} - M\mathcal{N}|\mathcal{E}|\eta(J)\mu_B\mathcal{B}, \tag{6.1}$$

which we shall now derive. The first term is the usual Zeeman shift due to the mean $g-$factor of the upper and lower energy states, which depends on J. The second term

is the electric field and orientation dependent $g-$factor[29], where $\Delta g = 2|\mathcal{E}|\eta$ is the difference in $g-$factor between the upper and lower energy states. Our convention is that a positive $g-$factor means that the spin and magnetic moment are aligned, meaning that an electron has an orbital and spin g-factor of $g_L = -1$ and $g_S \approx -2$, respectively.

We will not consider any terms which could change M (for example, transverse fields) so we will leave M out of the kets. Additionally, since we only measure energy differences between Zeeman sublevels we will ignore any energy shifts which do not depend on M. Lastly, we will always work in an electric field large enough to fully polarize the $\Omega-$doublet states (see Section 2.4.2).

Many of the theoretical calculations in this Appendix were performed much more rigorously by A. N. Petrov, L.V. Skripnikov, and A. V. Titov of St. Petersburg State University and the Petersburg Nuclear Physics Institute. As of the time of writing this thesis, we are preparing a collaborative paper combining their theoretical calculations with our experimental results.

6.1   Summary of perturbations

Table 6.1 summarizes some of the perturbations that we discussed in 2.6, along with their selection rules, and which states are connected to H by the perturbation. In the next sections, we will see what effect these perturbations have on the Zeeman interaction.
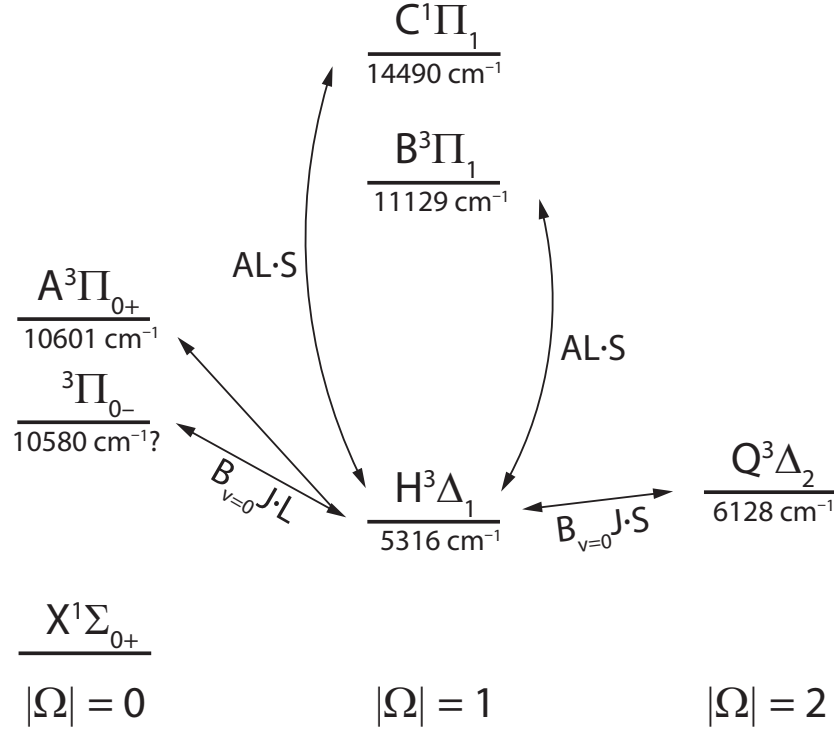
Figure 6.1: Summary of relevant electronic states, their energies above the ground state, and the perturbations that connect them. The $2S + 1\Lambda_\Omega$ term symbols are taken from Paulovič *et al.*[189], and are approximate. The $^3\Pi_{0-}$ state has not been observed, but is estimated to be within 100 cm^{-1} below $A^3\Pi_0$. The energies (except $^3\Pi_{0-}$) are measurements from Edvinsson *et al.*[80].

Table 6.1: A summary of the relevant perturbations that we will discuss in this chapter, adapted from Table 3.2 of [157]. We show the selection rules, and the states to which H is connected by the perturbation.

Perturbation	Operator	$\Delta\Omega$	$\Delta\Lambda$	$\Delta\Sigma$	ΔS	Connected to H
Spin-Orbit	$AL \cdot S$	0	$0, \pm1$	$0, \pm1$	$0, \pm1$	$C^1\Pi_1, B^3\Pi_1$
Spin Uncoupling	$-2B_{v=0}J \cdot S$	±1	0	±1	0	$Q^3\Delta_2$
L Uncoupling	$-2B_{v=0}J \cdot L$	±1	±1	0	0	$A^3\Pi_{0+}, ^3\Pi_{0-}$

6.2 $g-$factor

As discussed in Section 2.5, a pure Hund's case (a) molecule will satisfy $g(J) = G_\parallel[J(J+1)]^{-1}$, where $G_\parallel$ is a constant of the molecular state. In this section we will attempt to compute the Zeeman interaction by including perturbations from other electronic states, and will find that the g-factors do not follow this simple scaling. This effect has been observed in a number of other molecules[240, 198, 39, 168, 106, 176, 239, 174], and are usually some small perturbation to the usual parallel g-factor scaling. However, since the parallel g-factor is so small in the ThO $^3\Delta_1 H$ state, these perturbations are a significant fraction of the total Zeeman interaction.

6.2.1 Parallel g-factor in a $^3\Delta_1$ state

First consider the parallel molecule frame g-factor $G_{^3\Delta_1}$ in a pure $^3\Delta_1$ state. As discussed in Section 2.1.2, the fact that the spin projection Σ and orbital projection Λ have opposite sign means that $G_{^3\Delta_1} = 2g_L - g_S \approx -2 + 2.002 \approx +0.002$. Recall our convention that the signs of $g-$factors are with respect to $\vec{J}$ and therefore $\vec{\Omega} = \Omega(\vec{J} \cdot \hat{n})\hat{n} = \Omega(\vec{J_e} \cdot \hat{n})\hat{n}$, that is, a positive $g-$factor means that the magnetic moment points along $\vec{\Omega}$ and therefore along $\vec{J}$. The direction of $\vec{\Omega}$ in this state is aligned with $\vec{\Lambda}$, therefore $\vec{\Sigma}$ points against $\vec{\Omega}$. Since $|g_S| > 2|g_L|$, the magnetic moment direction is determined by the direction of $\vec{\Sigma}$, and since an electron has a negative $g-$factor (in our convention), the magnetic moments points against $\vec{\Sigma}$, and therefore along $\vec{\Omega}$. Thus our conclusion that $G_{^3\Delta_1} > 0$ makes physical sense. Recall that we are always working in a large electric field, and are not considering the difference between the e and f (opposite parity) states at zero field.

6.2.2 Spin-Orbit mixing with B and C states

Here we shall see that spin-orbit mixing of the excited B and C electronic states is the dominant contribution to the H state parallel g-factor. Let's make the simplifying assumption that the spin-orbit Hamiltonian is $H^{SO} = A\vec{L} \cdot \vec{S}$ (which is not strictly true, see 3.4.2 in [157]), where $A \approx 405$ cm^{-1} from the $Q - H$ energy splitting $E_{QH} \approx 2A = 810$ cm^{-1}. Note that $E_{QH} \approx 2A$ really is an approximation that neglects some molecular constants[37]; more accurate determination of A would require advanced calculations, or the energy of the unobserved $W^3\Delta_3$ state. The spin-orbit Hamiltonian will mix $H^3\Delta_1$ with $B^3\Pi_1$ and $C^1\Pi_1$. The B and C states they are actually each a spin-orbit mixture of $^3\Pi_1$ and $^1\Pi_1$[189], but this won't matter since we will make the simple approximation $\langle ^3\Pi_1 | H^{SO} | ^3\Delta_1 \rangle \approx \langle ^1\Pi_1 | H^{SO} | ^3\Delta_1 \rangle \approx A$. The admixtures of these states into H is

$$\begin{aligned}
|H\rangle &= |^3\Delta_1\rangle + \frac{\langle ^3\Pi_1 | H^{SO} | ^3\Delta_1 \rangle}{E_H - E_B} |^3\Pi_1\rangle + \frac{\langle ^1\Pi_1 | H^{SO} | ^3\Delta_1 \rangle}{E_H - E_C} |^1\Pi_1\rangle & (6.2) \\
&\equiv |^3\Delta_1\rangle - \epsilon_{HB} |^3\Pi_1\rangle - \epsilon_{HC} |^1\Pi_1\rangle . & (6.3)
\end{aligned}$$

If we use $E_{BH} = 5800$ cm^{-1} and $E_{CH} = 9200$ cm^{-1} for the energy splittings (see Figure 6.1), we find $\epsilon_{HB} \approx 0.07$ and $\epsilon_{HC} \approx 0.04$, which is close to the result from the full *ab initio* calculation[189] $\epsilon_{HB} = \sqrt{0.01} = 0.1$ and $\epsilon_{HC} = \sqrt{0.005} = 0.07$. We will use the *ab initio* values. The Zeeman interaction in this state is

$$\begin{aligned}
\langle H | -\mu \cdot \mathcal{B} | H \rangle &= \langle ^3\Delta_1 | -\mu \cdot \mathcal{B} |^3\Delta_1\rangle + \epsilon_{HB}^2 \langle ^3\Pi_1 | -\mu \cdot \mathcal{B} |^3\Pi_1\rangle + \epsilon_{HC}^2 \langle ^1\Pi_1 | -\mu \cdot \mathcal{B} |^1\Pi_1\rangle \\
&= -M\mu_B\mathcal{B}\frac{(G_{^3\Delta_1} + \epsilon_{HB}^2 G_{^3\Pi_1} + \epsilon_{HC}^2 G_{^1\Pi_1})}{J(J+1)} \\
&\equiv -M\mu_B\mathcal{B}\frac{G_\parallel}{J(J+1)}, & (6.4)
\end{aligned}$$

where we used the fact that $\langle {}^3\Delta_1| - \mu \cdot \mathcal{B}|{}^1\Pi_1\rangle = \langle {}^3\Delta_1| - \mu \cdot \mathcal{B}|{}^3\Pi_1\rangle = 0$ since a magnetic field cannot change Σ and Λ simultaneously. Above we saw that $G_{{}^3\Delta_1} \approx +0.002$, so consider $G_{{}^3\Pi_1}$ and $G_{{}^1\Pi_1}$. Both have ${}^3\Pi_1$ and ${}^1\Pi_1$ have $\Omega = \Lambda = 1$ and $\Sigma = 0$, so $G_{{}^3\Pi_1} = G_{{}^1\Pi_1} = g_L = -1$. Therefore, our predicted parallel g-factor is $G_\| = G_{{}^3\Delta_1} + \epsilon_{HB}^2 G_{{}^3\Pi_1} + \epsilon_{HC}^2 G_{{}^1\Pi_1} = -0.01$, which is fairly close to the measured value[142] of $G_\| = -0.0088(1)$ (though that paper did not report the sign; we will discuss the sign in Section 6.4.3).

6.2.3 Zeeman/Spin-uncoupling Perturbation

We will now consider the effect of the spin-uncoupling operator (see Section 2.6) $H_{SU} = -2B_{v=0}J \cdot S$ on the Zeeman interaction. As shown in Table 6.1, the selection rules for this operator are $\Delta\Sigma = \Delta\Omega = \pm 1, \Delta\Lambda = \Delta S = \Delta J = 0$, so it will connect the $H^3\Delta_1$ and $Q^3\Delta_2$ states. Since there is no $Q, J = 1$ state, the $H, J = 1$ state is not affected by this perturbation. This perturbation will lead to anomalous $J-$dependence of the molecular $g-$factors, as opposed to the usual $g_J = G_\|/[J(J+1)]$ scaling. A particularly accessible discussion of this perturbation can be found in [21].

The perturbative energy shift for the $H^3\Delta_1$ state is

$$\Delta E^{(2)} = \frac{|\langle H, J| - \mu \cdot \mathcal{B}H_{SU}|Q, J\rangle|^2}{-2A}, \tag{6.5}$$

$$\Delta E^{(2)}(M) = -2\frac{1}{2A}\langle H, J| - \mu \cdot \mathcal{B}|Q, J\rangle \langle H, J|H_{SU}|Q, J\rangle, \tag{6.6}$$

where we used that these matrix elements (and all others in this discussion) are real. These matrix elements can be found in references [212, 157] as well as Section 2.6,

and are

$$\langle Q, J, \Omega \pm 1, \Sigma \pm 1| - \mu \cdot \mathcal{B}|H, J, \Omega, \Sigma\rangle$$

$$= \frac{M\mu_B\mathcal{B}}{J(J+1)} \left[(J \mp \Omega)(J \pm \Omega + 1)(S \mp \Sigma)(S \pm \Sigma + 1)\right]^{1/2} \tag{6.7}$$

$$= \frac{M\mu_B\mathcal{B}}{J(J+1)} \left[2(J-1)(J+2)\right]^{1/2} \tag{6.8}$$

$$\langle H, J, \Omega, \Sigma|H_{SU}|Q, J, \Omega \pm 1, \Sigma \pm 1\rangle$$

$$= -B_{v=0} \left[S(S+1) - \Sigma(\Sigma \pm 1)\right]^{1/2} \left[J(J+1) - \Omega(\Omega \pm 1)\right]^{1/2} \tag{6.9}$$

$$= -B_{v=0} \left[2(J-1)(J+2)\right]^{1/2}. \tag{6.10}$$

Here Ω and Σ are the values in the H state. In order to eliminate the $\pm$ signs, we use the fact that H has $|\Omega| = 1$ and Q has $|\Omega| = 2$, so if we start in the $\Omega = -1$ $(+1)$ state in H then we must use the $-$ $(+)$ sign to obtain a non-zero matrix element. This means that we can replace $\pm$ with Ω in the expressions above, and then use $\pm\Omega = \Omega^2 = 1$. We use a similar argument to replace $\pm\Sigma$ with $-\Sigma^2 = -1$. Notice that Schadee[212] uses $H = \mu \cdot \mathcal{B}$, but also uses positive $g-$factors for the electron, so the signs in his matrix elements are indeed correct. Combining these, we find

$$\Delta E^{(2)}(M) = +2\frac{B_{v=0}}{A} M\mu_B\mathcal{B} \left(1 - \frac{2}{J(J+1)}\right), \tag{6.11}$$

which changes the $g-$factor of states in H with $J > 1$. We can write the $g-$factor as the combination of the usual body-fixed dipole moment contribution and the contribution due to spin-uncoupling,

$$g(J) = \underbrace{\frac{G_\parallel}{J(J+1)}}_{g_\parallel(J)} - \underbrace{2\frac{B_{v=0}}{A}\left(1 - \frac{2}{J(J+1)}\right)}_{g_{SU}(J)}. \tag{6.12}$$

We can also write this in terms in a manner similar to [154], to show that our correction has the same functional form:

$$g(J) = \frac{G_\parallel - \frac{2B_{v=0}}{A}(J-1)(J+2)}{J(J+1)}.$$

(6.13)

Table 6.2 shows $g(J)$ for $J = 2, 3$ compared with the measurement. The perturbation from the Q state has a large contribution, and including it makes the measured and predicted values much closer to each other. Here we are assuming that the measured value $G_\parallel = -0.0088(1) = 2g(J = 1)$ inferred from the $J = 1$ level[142] is correct.

Table 6.2: Table of perturbations to the g-factor with changing J, and the measured values. The measurements are discussed in 6.4. We can see that the pure Hund's case (a) scaling, represented by the $g_\parallel(J)$ column, is badly violated.

J	$g_\parallel(J)$	$g_{SU}(J)$	$g_\parallel(J) + g_{SU}(J)$	$g_{meas}(J)$
2	-0.0015	-0.0011	-0.0026	$-0.0027(1)$
3	-0.0007	-0.0014	-0.0021	$-0.0024(2)$

6.3 Electric field-dependent $g-$factor Difference between $\mathcal{N}$ states

We shall now try to understand the term $-M\mathcal{N}\eta|\mathcal{E}|\mu_\mathrm{B}\mathcal{B}$ which appears in the Hamiltonian. In this section, we are assuming (as usual) a large enough lab electric field to fully polarize the molecule (see Section 2.4.2), and are ignoring any effects related to the zero-field $g-$factor difference. If we use $\mathcal{N} = \Omega M\tilde{\mathcal{E}}$, we can see that

this term is $\propto \Omega \mathcal{E} \mathcal{B}$ since $M^2 = 1$. This observation will help us rule our a large class

of perturbations as not being able to contribute to this term, since we need to have

some matrix element in the perturbation which contains Ω, of which there are few.

We can also see that we need a Stark term to get a factor of $\mathcal{E}$, and a Zeeman term

to get a factor of $\mathcal{B}$.

If we look at a table of Zeeman matrix elements (for example, equation (4) in

[212]), we will see that any Zeeman term connecting states with $\Delta J = \pm 1$ contains

a factor of Ω. For example, we can use Eq. (2.37) (and the identical equation with

$S \to L$) to obtain the J-changing Zeeman matrix element within an electronic state

$(\Delta \Omega = \Delta \Sigma = \Delta \Lambda = \Delta S = 0)$,

$$\langle J, M, \Omega; \Lambda, S, \Sigma | \vec{\mu} \cdot \vec{\mathcal{B}} | J+1, M, \Omega; \Lambda, S, \Sigma \rangle =$$

$$\mathcal{B} \left[(2J+1)(2J'+1) \right]^{1/2} \begin{pmatrix} J & 1 & J+1 \\ -\Omega & 0 & \Omega \end{pmatrix} \begin{pmatrix} J & 1 & J+1 \\ -M & 0 & M \end{pmatrix} \times \cdots$$

$$\left[g_S \left[S(S+1)(2S+1) \right]^{1/2} \begin{pmatrix} S & 1 & S \\ -\Sigma & 0 & \Sigma \end{pmatrix} + g_L \left[L(L+1)(2L+1) \right]^{1/2} \begin{pmatrix} L & 1 & L \\ -\Lambda & 0 & \Lambda \end{pmatrix} \right]$$

$$= \mathcal{B}(g_S \Sigma + g_L \Lambda) \frac{1}{J+1} \left[\frac{[(J+1)^2 - M^2][(J+1)^2 - \Omega^2]}{(2J+1)(2J+3)} \right]^{1/2}$$

$$= \mathcal{B} \Omega G_\| \frac{1}{J+1} \left[\frac{[(J+1)^2 - M^2][(J+1)^2 - \Omega^2]}{(2J+1)(2J+3)} \right]^{1/2}, \tag{6.14}$$

where we defined the parallel g-factor $G_\|$ as in Section 2.5, which is a constant of the

molecular state. The factor of Ω may not be as obvious for transitions which change

both J and Σ, for example (see Eq. 2.37, and Schadee's[212] Eq. (4d)),

$$\langle J+1, M, \Omega \pm 1; \Lambda, S, \Sigma \pm 1 | \vec{S} \cdot \vec{\mathcal{B}} | J, M, \Omega; \Lambda, S, \Sigma \rangle =$$
$$\pm \frac{1}{J+1} \left[\frac{(J \pm \Omega + 1)(J \pm \Omega + 2)(J + M + 1)(J - M + 1)(S \pm \Sigma)(S \pm \Sigma + 1)}{(2J+1)(2J+3)} \right]$$

$$(6.15)$$

does not obviously give us a factor of Ω. However, we shall now argue that the $\pm$ sign is equivalent to a factor of Ω. In our $^3\Delta_1$ state, we have $\Omega = \pm 1$ and $\Sigma = \mp 1$. Say that we start in the state with $\Omega = +1, \Sigma = -1$. In this case, we have to use the upper sign (i.e. $+$ in $\pm$, $-$ in $\mp$) in Eq. (6.15) to connect to the state with $\Omega = 2$, $\Sigma = 0$, since there is no state with $\Omega = 0, \Sigma = -2$ to which we can connect. We can make the same argument to show that if we start in the state with $\Omega = -1$, $\Sigma = +1$, we must use the lower sign in the equation. Due to the overall $\pm$ sign out front, the sign of this matrix element will change with with Ω, as needed (the absolute value will not change, however). We can go through the same algebra to see that the Stark shift will not be able to give us the required factor of Ω due to perturbations from other states, so η must come for perturbations involving J-changing Zeeman interactions.

6.3.1 Second Order Stark/Zeeman Perturbation

In this section we will discuss the modification of the Zeeman interaction caused by Stark mixing of the $|H, J\rangle$ state with the $|H, J \pm 1\rangle$ states. Our perturbing Hamiltonian will include the Stark and Zeeman effects, $H' = -D \cdot \mathcal{E} - \mu \cdot \mathcal{B}$, and we will consider the three rotational states $J - 1, J, J + 1$ in H. This perturbation is what was initially used to explain the observed Stark/Zeeman effect in the PbO electron EDM search[29], and fit their data very well.
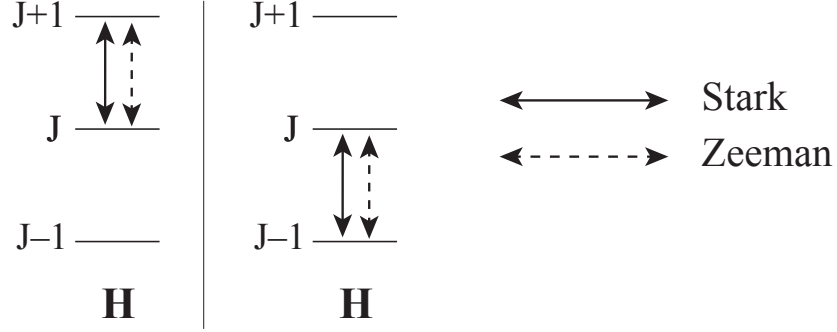
Figure 6.2: Schematic of the second-order perturbations to $\eta(J)$.

The second order energy shift of $|H, J=1\rangle$ will be

$$
\begin{aligned}
\Delta E^{(2)} &= \frac{|\langle H, J, \Omega|H'|H, J+1, \Omega\rangle|^2}{E_{H,J} - E_{H,J+1}} + \frac{|\langle H, J, \Omega|H'|H, J-1, \Omega\rangle|^2}{E_{H,J} - E_{H,J-1}} \\
&= \frac{(\langle H, J, \Omega|H'|H, J+1, \Omega\rangle)^2}{-2B_{v=0}(J+1)} + \frac{(\langle H, J, \Omega|H'|H, J-1, \Omega\rangle)^2}{+2B_{v=0}J}, \quad (6.16)
\end{aligned}
$$

where we used that all matrix elements are real to replace $|\ |^2$ with $(\ )^2$. The matrix elements are

$$
(\langle H, J, \Omega|H'|H, J+1, \Omega\rangle)^2
$$

$$
= (\langle H, J, \Omega| - D \cdot \mathcal{E} - \mu \cdot \mathcal{B}|H, J \pm 1, \Omega\rangle)^2
$$

$$
= \langle H, J, \Omega| - D \cdot \mathcal{E}|H, J \pm 1, \Omega\rangle^2 + \langle H, J, \Omega| - \mu \cdot \mathcal{B}|H, J \pm 1, \Omega\rangle^2 + \cdots
$$

$$
2\langle H, J, \Omega| - D \cdot \mathcal{E}|H, J \pm 1, \Omega\rangle\langle H, J, \Omega| - \mu \cdot \mathcal{B}|H, J \pm 1, \Omega\rangle. \quad (6.17)
$$

The first two terms have no M dependence, and will therefore cause no spin precession. The second term can be computed with the matrix elements (see Sections 2.5 and

2.4)

$$\langle H, J, \Omega| - G_\parallel \mu_B \mathcal{B}|H, J+1, \Omega\rangle = \frac{-G_\parallel \mu_B \mathcal{B}\Omega J(J+2)}{(J+1)[(2J+1)(2J+3)]^{1/2}} \quad (6.18)$$

$$\langle H, J, \Omega| - D_\parallel \mathcal{E}|H, J+1, \Omega\rangle = \frac{-D_\parallel \mathcal{E} J(J+2)}{(J+1)[(2J+1)(2J+3)]^{1/2}} \quad (6.19)$$

$$\langle H, J, \Omega| - G_\parallel \mu_B \mathcal{B}|H, J-1, \Omega\rangle = \frac{-G_\parallel \mu_B \mathcal{B}\Omega(J-1)(J+1)}{J[(2J-1)(2J+1)]^{1/2}} \quad (6.20)$$

$$\langle H, J, \Omega| - D_\parallel \mathcal{E}|H, J-1, \Omega\rangle = \frac{-D_\parallel \mathcal{E}(J-1)(J+1)}{J[(2J-1)(2J+1)]^{1/2}}, \quad (6.21)$$

where we have used $\Omega^2 = 1$. Therefore, the $M-$dependent first term in the second-order energy shift is given by

$$\Delta E^{(2)}(M) = \frac{((\langle H, J, \Omega|H'|H, J+1, \Omega\rangle)^2}{-2B_{v=0}(J+1)} + \frac{((\langle H, J, \Omega|H'|H, J-1, \Omega\rangle)^2}{+2B_{v=0}J}$$

$$= -\frac{G_\parallel \mu_B \mathcal{B}\Omega D_\parallel \mathcal{E}}{B_{v=0}}\alpha(J) \quad (6.22)$$

$$\eta^{(2)}(J) = -\frac{\Delta E^{(2)}(M)}{\Omega \mathcal{E} \mathcal{B}}$$

$$= \frac{G_\parallel D_\parallel}{B_{v=0}}\alpha(J), \quad (6.23)$$

where we have defined

$$\alpha(J) \equiv \frac{J^2(J+2)^2}{(J+1)^3(2J+1)(2J+3)} - \frac{(J-1)^2(J+1)^2}{J^3(2J-1)(2J+1)} \quad (6.24)$$

and used $\Omega = \mathcal{N}M\tilde{\mathcal{E}}$. This looks like an electric field and $\mathcal{N}$ dependent $g-$factor, and was first observed and calculated for the PbO molecule[29]. We shall find that there is a third-order term which has an identical contribution, which is large enough in the ThO H state that it cannot be neglected.

6.3.2 Stark/Spin-uncoupling/Zeeman Perturbation

We will now consider perturbations which mix the $|H, J, \Omega\rangle$ state with other rotation levels in the H and Q states. Recall that Q is a $^3\Delta_2$ state and therefore has

$S = 1, \Sigma = 0, \Lambda = \Omega = \pm 2$. The spacing between the H and Q states is $2A$, where $A = 405$ cm^{-1} = 12.1 THz is the spin-orbit constant of the $^3\Delta$ manifold containing H and Q.

Our perturbing Hamiltonian will be $H' = -D \cdot \mathcal{E} - \mu \cdot \mathcal{B} + H_{SU}$, where $H_{SU} = -2B_{v=0}J \cdot S$ (see Table 6.1). We must now consider six states: the $J - 1, J, J + 1$ rotational levels in H and Q. To shorten the expressions, we will suppress Ω in the kets since Ω is determined by the electronic state.
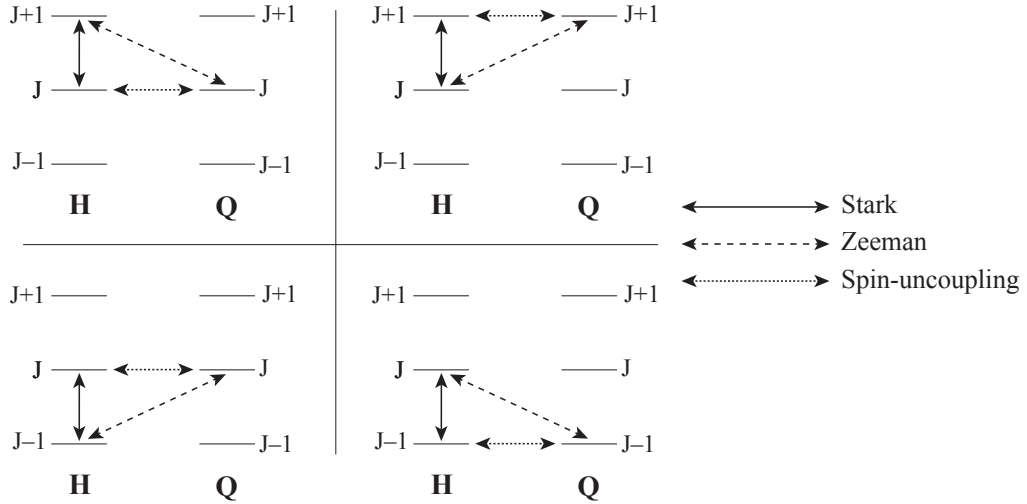

Figure 6.3: Schematic of the third-order pertubations to η.

The third order energy shift of the H, J state (due to the two perturbing states under consideration) is

$$
\begin{aligned}
\Delta E^{(3)} &= \sum_{J',J''} 2\frac{\langle H, J, |H'|H, J'\rangle \langle H, J', |H'|Q, J''\rangle \langle Q, J''|H'|H, J\rangle}{(E_{H,J} - E_{H,J'})(E_{H,J} - E_{Q,J''})} \\
&= \sum_{J',J''} 2\frac{\langle H, J, |H'|H, J'\rangle \langle H, J'|H'|Q, J''\rangle \langle Q, J''|H'|H, J\rangle}{2AB_{v=0}[(J'(J' + 1) - J(J + 1)]}
\end{aligned}
\tag{6.25}
$$

Notice that both terms in the energy denominator are negative, so the sign in the

second line is correct. We can eliminate most of the terms in the sum by making a few observations.

- We need precisely one of the matrix elements to be a $J-$changing Zeeman interaction in order to produce a $g-$factor difference, as discussed earlier.

- A Zeeman operator connected two levels in the H state will be suppressed by the small value of $G_\parallel$ in the $H-$state.

- The spin-uncoupling operator can only appear in a term which couples $H - Q$ and doesn't change J.

- A Stark operator in an $H - Q$ coupling term is suppressed by the fact that an electric field cannot re-orient a spin.

By using these facts, we can reduce the number of terms in the sum to four dominant terms:

$$\Delta E^{(3)}/2 =$$
$$\frac{\langle H, J| - D \cdot \mathcal{E} |H, J+1\rangle \langle H, J+1|H_{SU}|Q, J+1\rangle \langle Q, J+1| - \mu \cdot B|H, J+1\rangle}{4AB_{v=0}(J+1)} + \cdots$$
$$\frac{\langle H, J| - D \cdot \mathcal{E} |H, J-1\rangle \langle H, J-1|H_{SU}|Q, J-1\rangle \langle Q, J-1| - \mu \cdot B|H, J\rangle}{-4AB_{v=0}J} + \cdots$$
$$\frac{\langle H, J| - D \cdot \mathcal{E} |H, J+1\rangle \langle H, J+1| - \mu \cdot B|Q, J\rangle \langle Q, J|H_{SU}|H, J\rangle}{4AB_{v=0}(J+1)} + \cdots$$
$$\frac{\langle H, J| - D \cdot \mathcal{E} |H, J-1\rangle \langle H, J-1| - \mu \cdot B|Q, J\rangle \langle Q, J|H_{SU}|H, J\rangle}{-4AB_{v=0}J} \qquad (6.26)$$

The Stark matrix elements are given in Section 6.3.1; the others are given by[157,

212] (or worked out in Section 2.6),

$$\langle H, J, \Omega | H_{SU} | Q, J, \Omega \pm 1 \rangle = -B_{v=0}[2J(J+1) - 4]^{1/2}]$$

$$= -B_{v=0}[2(J+2)(J-1)]^{1/2}] \tag{6.27}$$

$$\langle Q, J+1, \Omega \pm 1 | -\mu \cdot \mathcal{B} | H, J, \Omega \rangle = \mp \mu_B \mathcal{B} \frac{J+2}{J+1} \left[\frac{2J(J+3)}{(2J+3)(2J+3)} \right]^{1/2}$$

$$= -\Omega \mu_B \mathcal{B} \frac{J+2}{J+1} \left[\frac{2J(J+3)}{(2J+3)(2J+3)} \right]^{1/2} \tag{6.28}$$

$$\langle Q, J-1, \Omega \pm 1 | -\mu \cdot \mathcal{B} | H, J, \Omega \rangle = \Omega \mu_B \mathcal{B} \frac{J-1}{J} \left[\frac{2(J+1)(J-2)}{(2J+1)(2J-1)} \right]^{1/2} \tag{6.29}$$

where the $\pm$ refers to the sign of Ω in the H state, but since $|\Omega| = 1$ we can replace $\pm \to \Omega$ as described below Eq. (6.15). The $M-$dependent energy shift is

$$\Delta E^{(3)}(M) = -\frac{4\Omega \mu_B \mathcal{B} D_{\parallel} \mathcal{E}}{A} \alpha(J) \tag{6.30}$$

$$\eta^{(3)}(J) = \frac{4D_{\parallel}}{A} \alpha(J) \tag{6.31}$$

Fortunately, this has the same functional form as the second order perturbation.

6.3.3 Combined effect of perturbations

If we combine the contributions to η from the second and third order perturbations, we obtain

$$\eta = \eta^{(2)} + \eta^{(3)} = \underbrace{\left(\frac{G_{\parallel} D_{\parallel}}{B_{v=0}} + \frac{4D_{\parallel}}{A} \right)}_{-11.8 \text{ nm/volt}} \underbrace{\left(\frac{J^2(J+2)^2}{(J+1)^3(2J+1)(2J+3)} - \frac{(J+1)^2(J-1)^2}{J^3(2J-1)(2J+1)} \right)}_{\alpha(J)},$$

$$\tag{6.32}$$

where we used the measured values $G_{\parallel} = -0.0088$, $D_{\parallel} = 2.07$ MHz/(volt/cm), $B_{v=0} = 9.77$ GHz, and $A = 405$ cm^{-1}. Table 6.3.3 summarizes calculated values versus measurements. For the two values where we have measured values of η, including

the third-order perturbation results in much better agreement between theory and experiment.

Table 6.3: Table of perturbations to the η with changing J, and the measured values. The units on η are nm/V. The measurements are discussed in 6.4. We can see that the third-order perturbation including spin-uncoupling is of comparable size to the second-order perturbation[29].

J	$\alpha(J)$	$\eta^{(2)}$	$\eta^{(3)}$	$\eta^{(2)} + \eta^{(3)}$	η_{meas}
1	$+3/40$	-1.40	$+0.51$	-0.88	$-0.79(1)$
2	$-11/1512$	$+0.14$	-0.05	$+0.08$	$+0.03(2)$

6.3.4 Smaller Effects

Here we list a number of smaller effects which we have thought about, but are not able to compute beyond a simple approximation: mixing with higher energy $^3\Pi_1$ and $^1\Pi_1$ states, the nuclear rotation magnetic moment, mixing with the $A^3\Pi_0$ state, and off-diagonal terms in the perturbations. These effects can:

- *Change $G_\parallel$.* A perturbation which introduces a correction to the $g-$factor that scaled as $[J(J+1)]^{-1}$ would modify $G_\parallel$. This would not change our measured value of $G_\parallel$, $g(J)$, or $\eta(J)$, so it would only help us understand the origin of the value for $G_\parallel$. For example, mixing of higher energy $^3\Pi_1$ and $^1\Pi_1$ states would have change the prediction for $G_\parallel$ (but not the measurement), similar to the mixing with the B and C states. Many higher energy $\Omega = 1$ states are known, but their term assignments are generally not.

- *Add anomalous $J-$scaling to the $g-$factor.* Perturbations can add terms to the effective $g-$factor which do not scale like $[J(J+1)]^{-1}$, similar to the Q state mixing. In addition to helping us better understand our measured $g-$factor

scaling with J, such perturbations can change our calculated value of $G_\parallel$, and therefore η. Specifically, we measure $g(J = 1)$ and then solve for $G_\parallel$ by assuming that $g(J = 1) = G_\parallel/2$ from the expression for $g(J)$ derived earlier. However, there are other terms which shift the value of $g(J = 1)$ independently of $G_\parallel$, making the calculation $g(J = 1) = G_\parallel/2$ invalid. Here are two such terms:

- The nuclear rotation magnetic moment will add a term $g_{rot}\mu_N J$ to the effective $g-$factor. If we assume $g_{rot} \approx 0.1$[210], then $g_{rot}\mu_N \approx 5 \times 10^{-5}\mu_B$, which would change our determination of $G_\parallel$ by about 1%.

- The $L-$uncoupling interaction $-2B_{v=0}J \cdot L$ with the $A^3\Pi_0$ state. The size of this effect will be $\sim B_{v=0}/E_{HA} = (0.33 \text{ cm}^{-1})/(5300 \text{ cm}^{-1}) \approx 6 \times 10^{-5}$, so this is another $\sim 1\%$ correction to $G_\parallel$.

- *Directly change η.* We only considered the largest terms in the perturbations, but there are others which are non-zero. For example, the term

$$2\frac{\langle H, J, \Omega| - D \cdot \mathcal{E}|Q, J \pm 1, \Omega \pm 1\rangle \langle H, J, \Omega| - \mu \cdot \mathcal{B}|Q, J \pm 1, \Omega \pm 1\rangle}{-2A}$$

$$\sim \frac{D_{HQ}\mathcal{E}\Omega\mu_B\mathcal{B}}{A} \quad (6.33)$$

appears in the expression for $\Delta E^{(2)}$, where D_{HQ} is the transition dipole moment between H and Q. This term will give rise to an η correction of $\sim D_{HQ}/A$. The matrix element D_{HQ} must come from the spin-orbit admixtures of H and Q (since $\langle^3\Delta_1|D \cdot \mathcal{E}|^3\Delta_2\rangle = 0$ in the pure Hund's case (a) approximation), so we can estimate that it is $D_{HQ} \approx 0.01D_\parallel$ since the spin-orbit admixtures are on the $\sim 1\%$ level. The correction to η is therefore approximately $0.01D_\parallel/A \approx 0.01$

nm/volt. There are similarly a number of terms in the third order perturbation which were neglected, which should also be small; for example, we could interchange the Stark and Zeeman interactions in the perturbation, though the result would be suppressed by a factor of $\sim G_{\parallel} \times (D_{HQ}/D_{\parallel}) \sim 10^{-4}$.

Many of these effects were taken into consideration by our theory collaborators, and will be reported in our upcoming paper.

Second Order Zeeman/L-uncoupling Perturbation

Now consider the interaction from the $A^3\Pi_0$ state, which is 5284 cm^{-1} away from H. The A state has $\Lambda = 1, \Sigma = -1, \Omega = 0, S = 1$, so it can be connected to the H state by the $L-$uncoupling operator $-2B_{v=0}\vec{J} \cdot \vec{L}$. Let's make the simplifying assumption that $L = 2$ for the H and A states, so that we can copy the formulas from above but with $S \rightarrow L$,

$$
\begin{aligned}
\langle A, J, \Omega \pm 1 | \mu \cdot \mathcal{B} | H, J, \Omega \rangle &= \frac{1}{2} \frac{M\mu_B \mathcal{B}}{J(J+1)} \left[(J \mp \Omega)(J \pm \Omega + 1)(L \mp \Lambda)(L \pm \Lambda + 1) \right]^{1/2} \\
&= \frac{M\mu_B \mathcal{B}}{[J(J+1)]^{1/2}} \qquad\qquad (6.34)
\end{aligned}
$$

This looks functionally different from the analogous Q state matrix element because now for the upper sign we must use $\Omega = -1$, and vice-versa. The additional factor of 1/2 comes from g_L/g_S. Simlarly,

$$
\langle H, J, \Omega | -2B_{v=0}J \cdot L | A, J, \Omega \pm 1 \rangle
$$

$$
= B_{v=0} \left[L(L+1) - \Lambda(\Lambda \pm 1) \right]^{1/2} \left[J(J+1) - \Omega(\Omega \pm 1) \right]^{1/2} \quad (6.35)
$$

$$
= 2B_{v=0} \left[J(J+1) \right]^{1/2}, \qquad\qquad (6.36)
$$

The second-order energy shift is therefore

$$\Delta E^{(2)} = \frac{|\langle H, J| - \mu \cdot \mathcal{B} - 2B_{v=0}J \cdot L|A, J\rangle|^2}{-\Delta_{HA}} \tag{6.37}$$

$$\Delta E^{(2)}(M) = -\frac{1}{\Delta_{HA}} \langle H, J|\mu \cdot \mathcal{B}|A, J\rangle \langle H, J|2B_{v=0}J \cdot L|A, J\rangle \tag{6.38}$$

$$= -\frac{B_{v=0}}{\Delta_{HA}}M\mu_B\mathcal{B} \tag{6.39}$$

$$g_{HA} = \frac{B_{v=0}}{\Delta_{HA}}\mu_B = 6 \times 10^{-5}\mu_B \tag{6.40}$$

This effect modifies our determination of $G_\parallel$ (and therefore η) on the $\approx 1\%$ level. Detailed calculations performed by our theory collaborators show that this effect is a factor of a few larger than our simple estimate.

6.4 Measurement of g and η

We measured g and η in the $J = 1, 2, 3$ rotational levels in H, and the results are shown in Table 6.5. We always worked in the $M = \pm 1$ states, otherwise our readout scheme (see Section 4.2) would not work. To populate $H, J = 1$ we pump through the $A, J = 0$ state, which can only decay to the $J = 1$ state in H since there is no $H, J = 0$ state. To populate the higher rotational levels we pump into higher rotational states in A, which reduces our population transfer efficiency and signal sizes and limited the number of rotational levels which we were able to probe.

Table 6.4: Measured values of $\eta(J)$ in different electric and magnetic fields. We expect $\eta(J)$ to not depend on either $\mathcal{E}$ or $\mathcal{B}$ in the limit where the molecule is fully polarized. We also measured η with $\mathcal{B} \approx 1$ mG, but do not include those values due to the large uncertainty resulting from the relatively small value of $\omega^{\mathcal{NB}}$.

$\mathcal{E}$ [V/cm]	$\mathcal{B}$ [mG]	$\eta(1)$ [nm/V]	$\eta(2)$ [nm/V]
36	19	$-0.81(2)$	$-$
36	38	$-0.79(2)$	$-$
141	19	$-0.80(1)$	$-$
141	38	$-0.80(1)$	$-$
141	59	$-0.78(2)$	$-$
106	38	$-$	$+0.03(2)$

Table 6.5: Summary of measurements. The value reported for $\eta(1)$ is a weighted mean of the entries in Table 6.4. $\eta(3)$ was not measured due to small signal sizes.

	$g(J)$	$\eta(J)$
$J = 1$	$-0.00440(5)[142]$	$-0.79(1)$ nm/V
$J = 2$	$-0.0027(1)$	$+0.03(2)$ nm/V
$J = 3$	$-0.0024(2)$	Not measured

6.4.1 Measurement of η

We can extract $\omega^{\mathcal{NB}}$ from our data, and use the known $\mathcal{E}$ and $\mathcal{B}$ fields to compute η,

$$\eta^{\text{meas}} = -\frac{\hbar\omega^{\mathcal{NB}}}{\mu_B |\mathcal{EB}|}. \tag{6.41}$$

With the exception of the $\mathcal{B} = 59$ mG and $J = 2$ measurements in Table 6.4, we computed η from the same data set which was used to compute an upper limit on the electron EDM. By computing η for several values of $|\mathcal{E}|$ and $|\mathcal{B}|$, as shown in Table 6.4, we can ensure that the value of η is indeed a constant which does not depend on applied fields.

The uncertainty on η comes from a combination of statistical uncertainty on $\omega^{\mathcal{NB}}$, and from a systematic uncertainty. Specifically, an $\mathcal{N}$-dependent laser detuning δ^N (caused by imperfect acousto-optical modulator frequencies) and overall detuning $\delta^{(0)}$
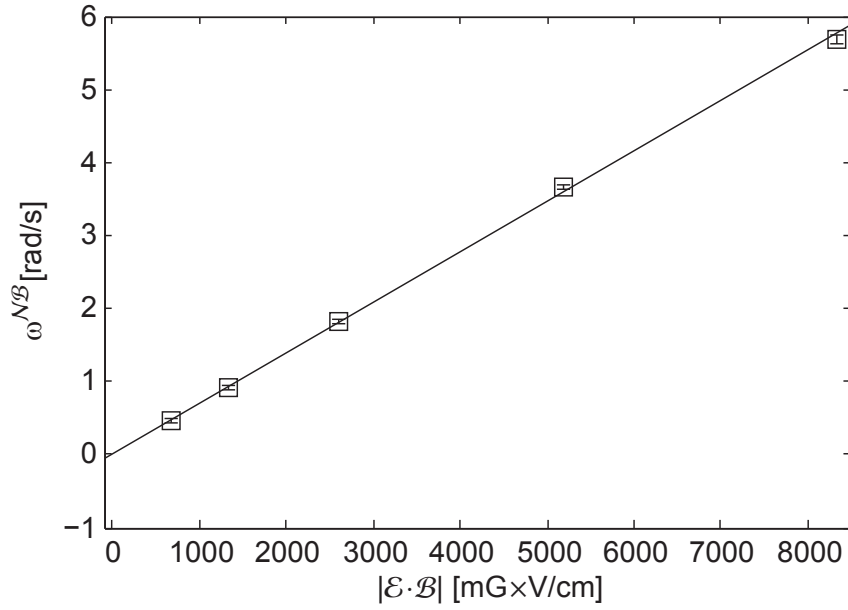
Figure 6.4: Plot of $\omega^{\mathcal{NB}}$ vs. $|\mathcal{E}\cdot\mathcal{B}|$ for $J=1$ with a linear fit. According to Eq. (6.41) the slope is $\omega^{\mathcal{NB}}/|\mathcal{EB}| = -\eta(1)\mu_{\mathrm{B}}/\hbar$, from which we can extract $\eta(1) = 0.79(1)$, which agrees with the weighted mean reported in Table 6.5. Error bars are combined statistical and systematic, as in Table 6.5. The fit parameters and their uncertainties are determined by χ^2 minimization, as outlined in Ref. [197]. The reduced χ^2 value of the fit is 1.5, which agrees with the expected value of 1 ± 0.7 for 4 degrees of freedom.

couple to an AC Stark shift to cause a spin precession frequency $\hbar\omega^{\mathcal{NB}} \propto \delta^{(0)}\delta^{\mathcal{N}}|\mathcal{B}|$ (see Section 5.2.2). Since we determine η from $\omega^{\mathcal{NB}}$, this will systematically change our determination of η. By applying a non-zero $\delta^{(0)}$ and $\delta^{\mathcal{N}}$, we measured $\eta^{\mathrm{meas}}/(\delta^{(0)}\delta^{\mathcal{N}}) = 2.61(2)$ nm V^{-1} MHz^{-2} with $|\mathcal{E}| = 141$ V/cm, where η^{meas} is the value determined by η if we ignore the AC Stark shift. Given our measured average $\delta^{(0)}_{\mathrm{RMS}} \approx 70$ kHz and $\delta^{\mathcal{N}}_{\mathrm{RMS}} \approx 20$ kHz (see Table 5.5), this gives rise to a systematic uncertainty in η of ≈ 0.01 nm/V, which is approximately the size of the statistical uncertainty. The values of $\mathcal{E}$ and $\mathcal{B}$ are known to $\sim 10^{-3}$ fractionally[16], so we do not include those uncertainties in our error budget.

The small value of $\eta(2)$ means that the $H, J = 2$ state should be even more robust against a number of systematic effects compared to $H, J = 1$. Since the energy shift due to d_{e} does not depend on J when the molecule is fully polarized[146], performing an EDM measurement in multiple rotational levels could be a powerful method to search for and reject systematics.

6.4.2   Measurement of the g-factor

The measurement of $g(1)$ was performed in a previous publication[142], and we will use the value reported there of $g(1) = -0.00440(5)$. The previous measurement did not report the sign, but the spin precession measurement reported here is sensitive to signs so we know that $g(1) < 0$ (that is, the magnetic moment and angular momentum are anti-aligned in the molecule). This sign also agrees with the theoretical calculations discussed earlier in Section 6.2.2.

To measure the g-factor in the higher rotational (J) levels, we find the smallest

magnetic field which results in a $\pi/4$ phase rotation of each Zeeman sublevel. Because our spin precession measurement is time-resolved, we choose the magnetic field $\mathcal{B}_J$ which results in a $\pi/4$ rotation for the molecules in the center of the beam pulse. We measure this magnetic field for $J = 1, 2, 3$, and find that a magnetic field of magnitude $19.7, 29.6, 35.5$ mG (respectively) are required to impart a $\pi/4$ phase.

In terms of the flight time τ, the fields $\mathcal{B}_J$ are given by $g(J)\mu_B\mathcal{B}_J\tau = \pi/4$. If we make the assumption that τ (≈ 1.1 ms) does not change during the time it takes to change the lasers to address/populate the other rotational levels, we can see that $g(J)/g(J') = \mathcal{B}_{J'}/\mathcal{B}_J$ for any J, J'. Since $g(1)$ is known, we can solve $g(J) = g(1) \times (\mathcal{B}_J/\mathcal{B}_1)$ with the values reported above. To compute an uncertainty, we make use of the fact that τ typically drifts on the $\pm1\%$ level for short time scales, and that the magnetic fields were only set with a resolution of 0.7 mG, so the overall uncertainty on the g-factor measurements (for $J > 1$) is $\approx \pm3\%$.

6.4.3   Checking the sign

Our measurement procedure gives signed values for the molecular phase, so if we are careful with our signs then we should be able to determine the sign of the g-factor from the spin precession. However, there are many, many signs to keep track of, so a double-check is definitely worthwhile. Figure 6.5 shows a plot of asymmetry vs. the polarization angle of the readout beam with respect to the preparation beam for various magnetic fields. Signs of rotations are with respect to the Z_{lab} axis and using the right hand rule. From $\mathcal{A} = \cos(2(\theta - \phi))$, where ϕ is the molecular phase, we see that $\mathcal{A} = 1$ when $\theta = \phi = -\hbar\tau g\mu_B\mathcal{B}$ (if we ignore other small phases). Therefore,

when $\mathcal{A} = 1$ we have $\text{sign}(\theta) = \text{sign}(-gB)$. For $\mathcal{B} > 0$ we have $\mathcal{A} = 1$ when $\theta > 0$, which implies $g < 0$.
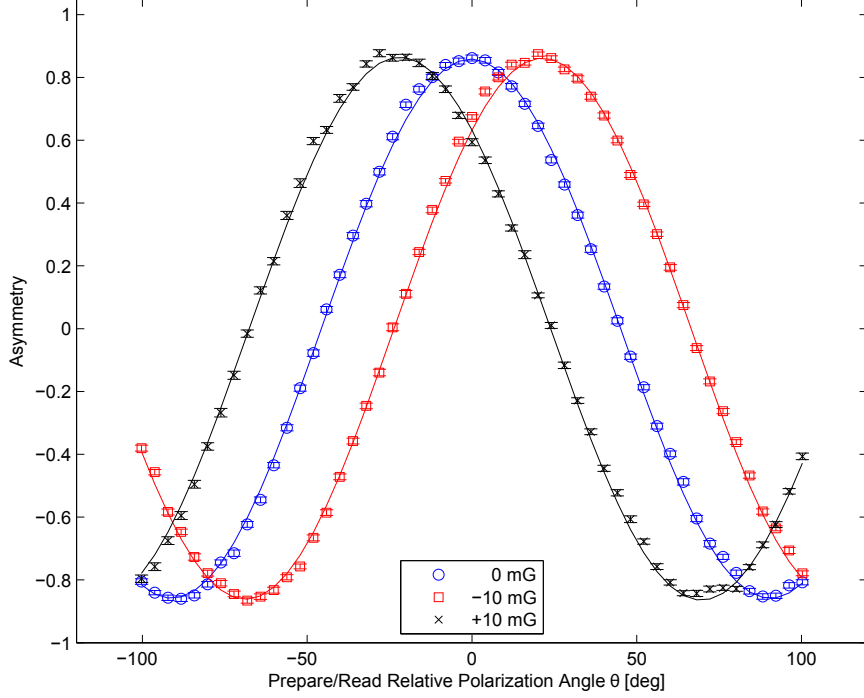

Figure 6.5: Asymmetry vs. preparation laser polarization rotation θ and magnetic field $\mathcal{B}$ (Run 0031)

We can also interpret this behavior classically. First, note that a positive $g-$factor rotates around a magnetic field in a *negative* sense. Say that the spins are aligned so that $\langle \vec{\mu} \rangle = \mu \hat{X}$ at $t = 0$. The magnetic field is $\vec{\mathcal{B}} = \mathcal{B}\hat{Z}$, so the torque is $\vec{\tau} = \vec{\mu} \times \vec{B} = \mu\mathcal{B}\hat{X} \times \hat{Z} = -\mu\mathcal{B}\hat{Y}$. A positive magnetic moment would therefore cause a torque in the $-\hat{Y}$ direction, which is a negative rotation. A positive magnetic field causes our molecules to rotate in a positive sense, which is why we have to rotate the waveplate in a positive fashion to line up the molecule dipoles and the light polarization ($\mathcal{A} = 1$) as shown in Figure 6.5. This also implies that the g-factor is negative.

6.4.4 Fast $\mathcal{N}$ switching

While the value of η computed from our data has typically been very robust, there was one experimental configuration which resulted in consistently bad behavior of the $\omega^{\mathcal{NB}}$ channel. As described in Section 4.2, the value for $\mathcal{N}$ is switched between pulses, so each molecule packet sees only a single laser frequency. For a while we attempted "fast Ω-doublet switching", where after each XY polarization chop we would switch Ω-doublets. This doubled our signal, since molecules in both upper and lower states (which are populated equally by the optical pumping) could be prepared and detected. However, the $\omega^{\mathcal{NB}}$ channel behaved quite badly, and had a very unreliable value. Specifically, we found that $\omega^{\mathcal{NB}}$ was very dependent on laser power, and had sub-bin structure (see Section 4.3.8) as shown in Figure 6.6. The effects seemed to come from the presence of the off-resonant light (i.e. not a technial problem), but we never figured out the exact mechanism. We spent a while trying to salvage this technique before decided that it was too severe of a perturbation on our measurement and it was abandoned.
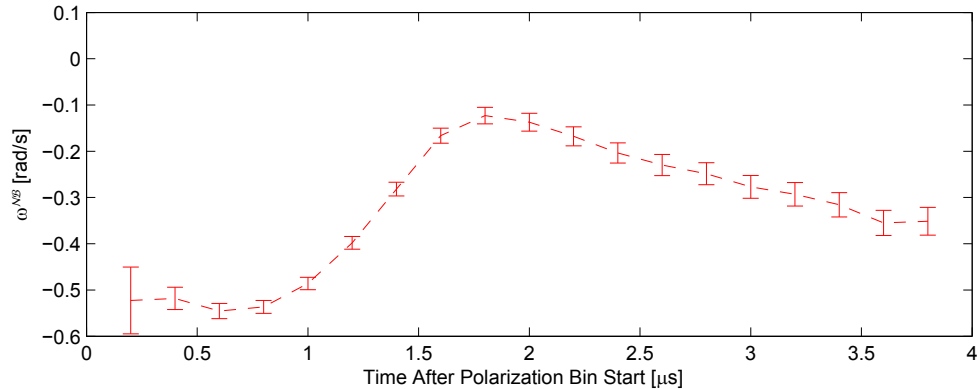

Figure 6.6: Sub-bin dependence of $\omega^{\mathcal{NB}}$ with fast Ω-doublet switching.

Appendix A

Thermal Stress Birefringence

In Section 5.2.2, we discussed how an ellipticity gradient across the preparation and readout lasers could cause an AC stark shift. In this appendix, we will show that this gradient is due to thermal stress induced birefringence in the electric field plates. Similar effects have been seen before in YAG rods[144] and on the windows in intense copper vapor lasers[86].

A.1 Size of Effect

If we send 45° polarized light through an optic with retardance $\Gamma \ll 1$, the Jones vector transformation is[208]

$$\begin{pmatrix} 1 & 0 \\ 0 & e^{-i\Gamma} \end{pmatrix} \begin{pmatrix} 1/\sqrt{2} \\ 1/\sqrt{2} \end{pmatrix} = \frac{1}{\sqrt{2}} \begin{pmatrix} 1 \\ e^{-i\Gamma} \end{pmatrix} \tag{A.1}$$

$$\approx \frac{1}{\sqrt{2}} \begin{pmatrix} 1 \\ 1-i\Gamma \end{pmatrix} \tag{A.2}$$

$$= \frac{(1-\Gamma)-i}{2} \begin{pmatrix} 1/\sqrt{2} \\ i/\sqrt{2} \end{pmatrix} + \frac{(1+\Gamma)+i}{2} \begin{pmatrix} 1/\sqrt{2} \\ -i/\sqrt{2} \end{pmatrix}. \tag{A.3}$$

The vectors $(1/\sqrt{2}, \pm i/\sqrt{2})^T$ represent right/left circular polarizations, so the difference of the absolute value squares of the prefactors gives the ellipticity,

$$\epsilon = \left| \frac{(1+\Gamma)+i}{2} \right|^2 - \left| \frac{(1-\Gamma)-i}{2} \right|^2 = \Gamma. \tag{A.4}$$

According to direct polarimetry measurements by Paul Hess (some of which are shown in Figure A.2), the ellipticity gradient across the lasers is a few percent. Therefore, we are searching for an effect which gives $\epsilon = \Gamma \sim 0.01$, corresponding to a retardance of $\sim 0.01/(2\pi) \sim 0.002$ waves, or about 2 nm at 1090 nm. The length scale of interaction with optical materials (except for coatings) is 1 cm, so we are sensitive to retardance/length of $\sim$ few nm/cm. In terms of index difference we have $\Delta n = n_\perp - n_\parallel = \epsilon\lambda/(2\pi t) \sim 10^{-7}$.

A.1.1   Relationship to Linear Gradient

A linear polarization gradient can lead to an EDM systematic through correlated Rabi rates (see Section 5.2.2). An optic with retardance Γ will also cause a linear polarization rotation, which we discuss here. If we repeat the above calculation but include $\mathcal{O}(\Gamma^2)$ terms, we find

$$\begin{pmatrix} 1 & 0 \\ 0 & e^{-i\Gamma} \end{pmatrix} \begin{pmatrix} 1/\sqrt{2} \\ 1/\sqrt{2} \end{pmatrix} = \frac{1}{\sqrt{2}} \begin{pmatrix} 1 \\ e^{-i\Gamma} \end{pmatrix} \approx \frac{1}{\sqrt{2}} \begin{pmatrix} 1 \\ 1 - i\Gamma - \Gamma^2/2 \end{pmatrix}. \tag{A.5}$$

The linear polarization θ for a Jones vector $\hat{J}$ is given by $\mathrm{Re}(\hat{J} \cdot \hat{y})/\mathrm{Re}(\hat{J} \cdot \hat{x})$, so the linear polarization for our light after traveling through the retarder is rotated by $\Gamma^2/4$. This quantity is small, and was never resolved with the Paul Hess's direct polarimetry measurements.

A.2   Thermal Stress Induced Birefringence

The steady-state relationship between stress and internal heat generation is given by Barber's[14] Eqs. (14.6) and (14.18),

$$\nabla^4 \phi = \frac{E\alpha_V}{\kappa} Q, \tag{A.6}$$

where E, α_V, κ are the young's modulus, coefficient of thermal expansion, and thermal conductivity of the material, and Q is the heat deposited per unit volume. If the heat generation is due to absorption of a laser of intensity I, then $Q = \alpha I$ where α is the absorbance of the material. ϕ is the Airy stress, related to the usual stress by

$$\frac{\partial^2 \phi}{\partial x^2} = \sigma_{yy}, \quad \frac{\partial^2 \phi}{\partial y^2} = \sigma_{xx}. \tag{A.7}$$

This formula looks like we have mixed up x and y in the derivatives, but we haven't! See Chapter 4 in [14] for details.

Consider the case where the laser is much taller than it is wide, so that we can estimate the heat deposited as a function of only x, i.e. $Q(x, y) = Q(x)$. Since the width in the x direction of the pump and probe lasers is about 1.3 mm, and the beams are stretched to have (one sigma) height 2 cm and 4 cm at the preparation and readout stages, respectively, this approximation is fairly valid. In Cartesian coordinates (with no z-dependence), the biharmonic operator ∇^4 becomes

$$\nabla^4 \phi = \frac{E\alpha_V}{\kappa}Q \quad = \quad \frac{\partial^4 \phi}{\partial y^4} + \frac{\partial^4 \phi}{\partial x^4} + \frac{\partial^4 \phi}{\partial x^2 \partial y^2} \tag{A.8}$$

$$= \quad \frac{\partial^2 \sigma_{xx}}{\partial y^2} + \frac{\partial^2 \sigma_{yy}}{\partial x^2} + \frac{\partial^2}{\partial x \partial y} \frac{\partial^2 \phi}{\partial x \partial y} \tag{A.9}$$

$$= \quad \frac{\partial^2 \sigma_{xx}}{\partial y^2} + \frac{\partial^2 \sigma_{yy}}{\partial x^2}. \tag{A.10}$$

To eliminate the cross terms, we used that for thermal stresses the off-diagonal (shear) elements $\sigma_{xy} = \partial^2 \phi / \partial x \partial y$ are zero. By symmetry, neither σ_{xx} nor σ_{yy} can depend on y, so the equation simplifies to

$$\frac{E\alpha_V}{\kappa}Q = \frac{\partial^2 \sigma_{yy}}{\partial x^2} = \sigma_{yy}''(x). \tag{A.11}$$

The heat deposited per unit volume is related to the absorbance α of the material by $Q(x) = I(x)\alpha$, where I is the laser intensity. The equation then becomes

$$\sigma_{yy}''(x) = \frac{E\alpha_V \alpha I(x)}{\kappa}. \tag{A.12}$$

The stress-optic law[62] states that the birefringence and stress are related by $\Delta n = K(\sigma_{xx} - \sigma_{yy})$, where K is the stress-optical coefficient, which is $K \approx 4 \times 10^{-3}$ GPa^{-1} for borofloat glass[215]. Since we have determined that σ_{xx} is constant, and we only

care about changes in Δn, let's set it to be zero so that

$$\Delta n(x) = -K\sigma_{yy}(x). \tag{A.13}$$

We usually discuss ellipticity instead of Δn, so in terms of $\Delta\epsilon$ we have $\Delta\epsilon(x) = \frac{2\pi t}{\lambda}\Delta n(x)$, where t is the material thickness and λ is the wavelength of light. Combining the above equations, we obtain

$$\Delta\epsilon''(x) = \frac{\beta t}{\lambda}I(x), \tag{A.14}$$

where we have defined the material-specific constant

$$\beta = \frac{2\pi K E\alpha_V\alpha}{\kappa}, \tag{A.15}$$

which is 26×10^{-6} W^{-1} for borofloat glass. If we wish to write this as an integral, we can specify $\Delta\epsilon(0) = 0$ (since constant offsets to ellipticity are not relevant for the experiment) and $\Delta\epsilon'(0) = 0$, which should hold for a symmetric intensity distribution, to obtain

$$\Delta\epsilon(x) = \frac{\beta t}{\lambda}\int_0^x \int_0^{x'} I(x)\, dx''\, dx' = \frac{\beta t I_0}{\lambda}\int_0^x \int_0^{x'} f(x'')\, dx''\, dx', \tag{A.16}$$

where $I(x) = I_0 f(x)$ and $f(0) = 1$.

We can make some rough estimates to understand how this effect should scale with the important parameters. We can guess that a figure of merit is the derivative (gradient) of the ellipticity at the position $x = w_x$, the characteristic horizontal half-width of the intensity profile, which is about where the laser light starts to become weak. Therefore, we wish to compute

$$\Delta\epsilon'(w_x) = \beta\frac{tI_0}{\lambda}\int_0^{w_x} f(x')\, dx'. \tag{A.17}$$

Since the integral has units of length and is related to the horizontal beam profile, it would be $\approx w_x$. If we also approximate $I_0 \approx P_{tot}/(2w_x \times 2w_y)$, then

$$\Delta\epsilon'(w_x) \approx \frac{\beta t P_{tot}}{4\lambda w_y}. \tag{A.18}$$

If we use $t = 25$ mm, $\lambda = 1090$ nm, $w_y = 10$ mm, and $P_{tot} = 4$ W, then we can estimate $\Delta\epsilon'(w_x) \approx 5\%$/mm, which is fairly close to the measured value (see Figure A.2).

We can obtain a closed-form solution for the case of a stretched Gaussian, $f(x) = \exp(-x^2/2w_x^2)$,

$$\Delta\epsilon(x) = -\beta\frac{tI_0}{\lambda}\left[w_x^2 e^{-x^2/2w_x^2} + \sqrt{\frac{\pi}{2}}w_x x \ \mathrm{erf}\left(\frac{x}{w_x\sqrt{2}}\right)\right]. \tag{A.19}$$

The relationship between the total power P_{tot} and peak intensity I_0 for a 2D Gaussian beam is $I_0 = P_{tot}/2\pi w_x w_y$, so

$$\Delta\epsilon(x) = -\beta\frac{tP_{tot}}{2\pi w_x w_y \lambda}\left[w_x^2 e^{-x^2/2w_x^2} + \sqrt{\frac{\pi}{2}}w_x x \ \mathrm{erf}\left(\frac{x}{w_x\sqrt{2}}\right)\right]. \tag{A.20}$$

If we treat that prefactor as a parameter and perform a fit to measured data, we would expect to find the value to be about 0.03 mm^{-2} given our experimental parameters.

The data in Figure A.2 shows some data taken by Paul on 10 December 2012 along with some fits. The first fit assumes the function described above, and gives the prefactor as $u = 0.024(2)$ mm^{-1}, in good agreement with our estimate. There is also a "low power" fit with the power reduced by a factor of 8, and we see that the thermoelastic fit prefactor changes by a factor of 6 ± 1. The plots also include a schematic representation of the laser profile, to show that the shape is definitely not a Gaussian with the same width as the laser.

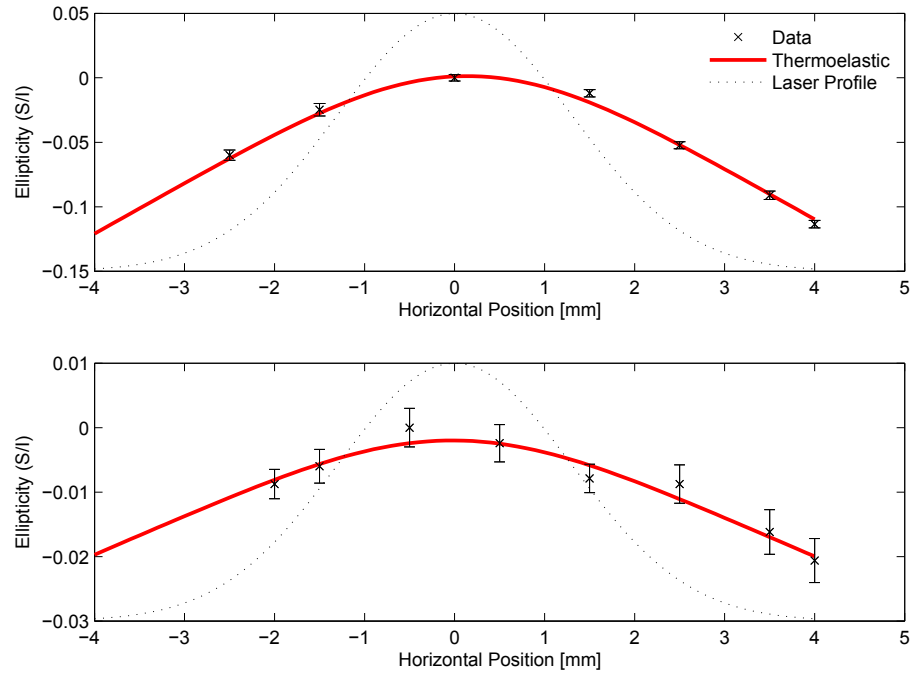Figure A.1: Measured ellipticity with fit from thermal stress birefringence model. The measurements were performed by Paul Hess. Top: Full power, 4.9 W laser. The fit prefactor $u = 0.024 \pm 0.002$ mm^{-1} agrees fairly well with the estimate in the text. Bottom: lower power, 0.6 W laser. We expect reduction by a factor of $4.9/0.6 = 8$, and see a reduction of 6 ± 1, which is fairly close.

Another case which can be solved analytically is that of a horizontally flat-topped beam, $f(x) = \text{If}(|x| < w)$. In this case,

$$
\int_0^x \int_0^{x'} f(x'') \, dx'' \, dx' =
\begin{cases}
\frac{1}{2}x^2 & |x| \leq w \\[2mm]
-\frac{1}{2}w^2 + w|x| & |x| > w
\end{cases}
\tag{A.21}
$$

The relationshipbetween total power and peak intensity is now $I_0 = P_{tot}/(2w_x \times 2w_y)^2 = P_{tot}/4w_x w_y$, so

$$
\Delta\epsilon(x) = \beta \frac{tP_{tot}}{4w_x w_y \lambda} \times
\begin{cases}
\frac{1}{2}x^2 & |x| \leq w \\[2mm]
-\frac{1}{2}w^2 + w|x| & |x| > w
\end{cases}
\tag{A.22}
$$

Compared to the expression for the stretched Gaussian, the prefactor should be a factor of $2\pi/4 = \pi/2 = 1.6$ larger.

We can also analytically solve the case for an unstretched Gaussian beam. In polar coordinates with no angular dependence, the Airy stress equation becomes

$$
\frac{E\alpha_V}{\kappa}Q = \nabla^4\phi = \frac{1}{r}\frac{\partial}{\partial r}\left(r\frac{\partial}{\partial r}\left(\frac{1}{r}\frac{\partial}{\partial r}\left(r\frac{\partial\phi}{\partial r}\right)\right)\right),
\tag{A.23}
$$

which looks very difficult, but can be solved analytically in Mathematica with the input $Q = Q_0 \exp(-r^2/2w^2) = I_0\alpha \exp(-r^2/2w^2)$, though the solution is too long to include here. Now that we have ϕ, we can compute the birefringence using the stress-optic law,

$$
\Delta n = K(\sigma_{xx} - \sigma_{yy}) = K\left(\frac{\partial^2\phi}{\partial y^2} - \frac{\partial^2\phi}{\partial x^2}\right),
\tag{A.24}
$$

where we assume that the light sent through the medium is linearly polarized in the $\hat{x} + \hat{y}$ direction. Using Mathematica, we find

$$
\Delta n = \frac{KE\alpha_V I_0\alpha}{\kappa} \frac{w^2\left(r^2 + 2\left(-1 + e^{-r^2/2w^2}\right)w^2\right)\cos(2\theta)}{2r^2},
\tag{A.25}
$$

where r and θ are polar coordinate with respect to the Gaussian beam center. Notice that we recover the expected $\cos(2\theta)$ dependence. If we set $y = 0$ and measure $\Delta\epsilon$ as a function of x, which we do in the experiment, we find (throwing away constant offsets),

$$\Delta\epsilon(x) = \frac{2\pi t K E \alpha_V I_0 \alpha}{\lambda \kappa} \frac{\left(1 - e^{-x^2/2w^2}\right) w^4}{x^2} = \beta \frac{t I_0}{\lambda} \frac{\left(1 - e^{-x^2/2w^2}\right) w^4}{x^2}. \tag{A.26}$$

Using $I_0 = P_{tot}/2\pi w^2$,

$$\Delta\epsilon(x) = \beta \frac{t P_{tot}}{2\pi\lambda} \frac{\left(1 - e^{-x^2/2w^2}\right) w^2}{x^2}. \tag{A.27}$$

Notice that this effect scales linearly with the heat deposited (and therefore the laser intensity), and is not a Gaussian. The FWHM of this shape is about $3.6w$, compared to $2.3w$ for a Gaussian.

To estimate the timescale of thermal effects, consider the volume illuminated by the laser, $4w_x w_y t$. The heat energy (due to laser heating) stored in this volume is $Q = 4\Delta T \rho C w_x w_y t$, where $\rho = 2.2$ g/cm^3 and $C = 0.8$ J/g/K are the density and specific heat of borofloat, respectively. The rate of heat transfer through the plates is $\dot{Q} = \kappa(2w_y t)(\Delta T/w_x) = 2\kappa t \Delta T w_y/w_x$, where $2w_y t$ is the surface area of the volume within the plate, and $\Delta T/w_x$ is the temperature gradient in the $x-$direction. The timescale for thermal effects is therefore

$$\frac{Q}{\dot{Q}} \approx \frac{4\Delta T \rho C w_x w_y t}{2\kappa t \Delta T w_y/w_x} \approx \frac{2\rho C w_x^2}{\kappa} \approx 10 \text{ s} \tag{A.28}$$

A.2.1 Different substrates

One simple way to reduce the size of this effect in future experimental generations is to use a substrate with better stress-optical properties. In Eqs. (A.15) and (A.18),

Table A.1: A comparison of estimated thermal stress birefringence in various materials. BK7[216] and Borofloat 33[215]are borosilicate glasses manufactured by Schott. 7980[59] is a fused silica manufactured by Corning. Other higher quality fused silica glasses, such as Suprasil, offer similar parameters with a much higher price.

	BK7	Borofloat 33	7980
Young's Modulus E [GPa]	82	64	73
Thermal Conductivity κ [W m^{-1} K^{-1}]	1.1	1.2	1.4
Thermal Expansion α_V [K^{-1}]	8.3×10^{-6}	3.3×10^{-6}	0.6×10^{-6}
1090 nm Absorbance α [cm^{-1}]	$\lesssim 10^{-3}$	≈ 0.05	$\lesssim 10^{-3}$
Stress-optical Coefficient K [GPa^{-1}]	3×10^{-3}	4×10^{-3}	3×10^{-3}
$KE\alpha_V/\kappa$ [μm/W]	1.9	0.7	0.1

we found that the magnitude of the effect should scale with $KE\alpha_V/\kappa$ times some geometric and laser properties. We can therefore calculate this quantity for various optical materials and see if they offer any improvement. Fused silica seems to be the most promising, mainly due to its small thermal expansion. We also considered using YAG as a substrate due to its large thermal conductivity, but it is not likely to reduce the effect due to it's large Young's Modulus. A thinner ITO coating could also be used to reduce the net absorbance.

A.2.2 Optical Properties of ITO

Optical properties of ITO are difficult to come by, likely due to manufacturing inhomogeneities. Zhang *et al.*[257] measured the optical properties of a similar coating, from which we can estimate the extinction coefficient $\kappa = \mathrm{im}(n) \approx 0.06$ at 1090 nm. In terms of absorbance, we can use the relationship $\alpha = 4\pi\kappa/\lambda = \kappa \times 1.2 \times 10^5$ cm^{-1} at 1090 nm to obtain $\alpha = 7000$ cm^{-1}. Their film thickness was 60 nm, which gives an absorption fraction of $A = 1 - \exp(-100 \text{ nm} \times 7000 \text{ cm}^{-1}) = 4\%$. Notice that they also give data for another coating with different preparation and different

optical constants; we choose their Figure 1 instead of their Figure 2 since it looks more like the transmission data provided by the manufacturer of our plates, shown in Figure A.2. However, the transmission does not exactly match up, and the measured resistivity is smaller than our specified resistivity, but hopefully this estimate of α is good to within a factor of a few.
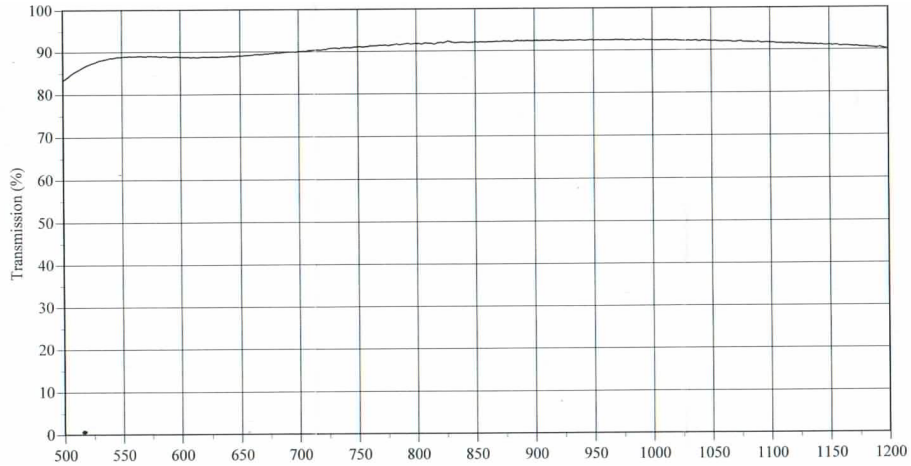

Figure A.2: Transmission of field plates supplied by Custom Scientific. The "nominal film thickness" is 125 nm.

The birefringence of an ITO film depends on how it was deposited[121, 113]. Films deposited at normal incidence have very small birefringence, but films made through oblique deposition typically have $\Delta n \sim 10^{-3} \times \theta [\text{deg}]$ for angles $\gtrsim 20°$, or $\Delta n \sim 5 \times 10^{-5} \times (\theta [\text{deg}])^2$ for angles $\lesssim 10°$ with a 100 nm thick coating. The origin of this birefringence is due to the anisotropic structure of ITO coated at oblique angles, and is discussed in Ref. [121]. This effect could be causing some local birefringence effects, but shouldn't be intensity dependent and therefore not of serious concern.

A.3   Other Effects

Here we will discuss some effects which do not cause the observed ellipticity gradient, but could in different situations.

A.3.1   Vacuum Stress Induced Birefringence

We can make the rough estimate that the stress on the BK7 vacuum window results in birefringence of magnitude $\Delta n_{atm} = K \times (1 \text{ atm}) = 4 \times 10^{-7}$, which we have argued might be large enough to cause a problem. The length scale of this index change is the window clear radius ~ 1 cm, which is of the same order as the laser beam.

If we assume that the window is a thin plate, stress at the window center is[14]

$$\sigma_{max} = \frac{3(3+\nu)P_0 r_0^2}{8t^2} = 0.8 \text{ MPa} \approx 8 \text{ atm}, \tag{A.29}$$

where we used the Poisson ratio $\nu = 0.2$[216]. Using $K \approx 3 \times 10^{-6}$ MPa^{-1} for the vacuum windows, we find $\Delta n_{atm} = K \times (0.8 \text{ MPa}) = 3 \times 10^{-6}$, over a length of ~ 1 cm. Given other experimental data[225], the real value is likely to be even higher.

The thickness is $t = 6$ mm and the unsupported radius is $r_0 \sim 15$ mm, so we might be concerned that the thin plate approximation is not a valid one. The full formula is[14]

$$\sigma_{max}/P_0 = \frac{3(3+\nu)r_0^2}{8t^2} + \frac{2+\nu}{10} = 0.2 + 1.2(r_0/t)^2, \tag{A.30}$$

where for the last equality we substituted $\nu = 0.2$. This means that even for $r_0/t = 1$, the thin plate equation is good to about 15%.

While it seems possible that this effect could cause ellipticity gradients large enough to be observed, we simply do not observe them; the polarimetry measurements performed by Paul Hess show very small gradients with a weak laser, so we only need to consider intensity dependent effects.

A.3.2 Optically Induced Birefringence

Non-linearities in an optical material can cause birefringence which depends on intensity[35], though we shall see that they are too small. Specifically, a third-order susceptibility $\chi = \chi_{1221}^{(3)}$ gives rise to a birefringence

$$\Delta n = \frac{3\chi}{n}(|E_-|^2 - |E_+|^2), \tag{A.31}$$

where we have used Eqs. (4.2.24) and (4.2.12c) from Boyd[35]. Here $E_\pm$ are the right/left hand circular components of the optical electric field. Notice that since the birefringence depends on the third order polarizability, we might suspect that it is very small. If we use $I = 2nc\epsilon_0 |E|^2$ and $I_+ + I_- = I$,

$$\Delta n = \frac{3\chi}{n}\frac{1}{2nc\epsilon_0}(I_- - I_+) = \frac{3\chi I}{2n^2 c\epsilon_0}\frac{S}{I}, \tag{A.32}$$

where $S/I = (I_- - I_+)/(I_- + I_+)$ is the fractional ellipticity. If we use that $\chi \approx 10^{-21}$ m^2/V^2 (see Boyd's table 4.1.2[35]), $I = 1$ W/cm^2, $S/I = 0.1$, and $n = 1.5$, we find $\Delta n \sim 10^{-16}$. Owyoung *et al.*[181] present data specifically for $\chi_{1212}^{(3)}$ in BK7 glass, and their value is $\chi = 2.3 \times 10^{-15}$ esu. To convert back to MKS units, we use Boyd's (C.12), $\chi = 1.4 \times 10^{-8} \times 2.3 \times 10^{-15}$ m^2/V^2 = 3×10^{-23} m^2/V^2, which is even smaller than the value that we used.

Appendix B

$\mathcal{N}\mathcal{E}$-correlted Rabi Frequency

In Section 5.2.2, we discussed how correlated Rabi frequencies can cause measurable phases in the molecule spin precession. Here we take an alternative approach to Brendon's original writeup proposing these Rabi Frequency correlations (see his Lablog post dated 18 July 2013) to arrive at the same answer. Consider an optical field with electric field $\mathcal{E}$ oscillating in the $\hat{x}$ direction, and magnetic field $k\mathcal{B} = \mathcal{E}/c$ oscillating in the $\hat{y}$ direction. Here $k = \pm 1$ is the sign of the $k-$vector of the light relative to Z_{lab}. The $\omega^{\mathcal{N}\mathcal{E}\mathcal{B}}$ channel did not change sign under rotation of the pump polarization, so we should be able to pick the polarization arbitrarily, and later we will show that the ratio of the E1 and M1 matrix elements does not depend on this choice. The E1 and M1 transitions come from the electric and magnetic parts of the optical field, respectively. The quantization axis is set by the lab electric field and is $\hat{z}$. We are considering transitions between $|H, J = 1\rangle$ and $|C, J = 0, M = 0\rangle$, so our states will be $|H; M, \Omega\rangle$ and $|C; \Omega\rangle$ where $M, \Omega = \pm 1$. In terms of spherical tensors, $\mathcal{E}\hat{x} = 2^{1/2}[T_1^1(\mathcal{E}) - T_{-1}^1(\mathcal{E})]$ and $\mathcal{B}\hat{y} = i2^{1/2}[T_1^1(\mathcal{B}) + T_{-1}^1(\mathcal{B})]$. In other words,

254

$\mathcal{E}_{\pm 1} = \pm 2^{-1/2}\mathcal{E}$ and $\mathcal{B}_{\pm 1} = i2^{-1/2}\mathcal{B}$. The Stark matrix element is given by

$$\langle H; M, \Omega | D \cdot \mathcal{E} | C; \Omega \rangle$$

$$= 2^{1/2} \sum_{p=\pm 1} D_\| \langle H; M, \Omega | pT_p^1(\mathcal{E}) | C; \Omega \rangle$$

$$= D_\| 2^{1/2} \sum_{p=\pm 1} (-1)^p \mathcal{E}_{-p} (-1)^{J-M} (-1)^{J-\Omega} (2J+1) \begin{pmatrix} J & 1 & J \\ -M & p & 0 \end{pmatrix} \begin{pmatrix} J & 1 & J \\ -\Omega & 0 & \Omega \end{pmatrix}$$

$$= D_\| M \mathcal{E} (-1)^M (-1)^{J-M} (-1)^{J-\Omega} (2J+1) \begin{pmatrix} J & 1 & J \\ -M & M & 0 \end{pmatrix} \begin{pmatrix} J & 1 & J \\ -\Omega & 0 & \Omega \end{pmatrix}$$

$$= 2^{-1/2} M D_\| \mathcal{E} (-1)^{2J-\Omega} (2J+1) \left(M(-1)^J \left[\frac{J(J+1)}{2J(J+1)(2J+1)} \right]^{1/2} \right) \times \cdots$$

$$(-1)^{J-\Omega} \frac{\Omega}{[2J(J+1)(2J+1)]^{1/2}}$$

$$= 2^{-1/2} M^2 \Omega D_\| \mathcal{E} (-1)^{4J-2\Omega} (2J+1) \frac{[J(J+1)]^{1/2}}{2J(J+1)(2J+1)}$$

$$= \frac{2^{-3/2} \Omega D_\| \mathcal{E}}{[J(J+1)]^{1/2}}$$

$$= 2^{-1} \Omega D_\| \mathcal{E}, \qquad\qquad\qquad\qquad\qquad\qquad\qquad (\text{B.1})$$

where $D_\|$ is the parallel transition electric dipole moment between H and C. We know from Section 2.5 that Zeeman matrix elements which are on-diagonal in J and either on or off diagonal in Ω have a reduced magnetic dipole matrix element which looks like $\mu\Omega$, where μ is a constant.

$$\langle H; M, \Omega | \mu \cdot \mathcal{B} | C; \Omega \rangle$$

$$= 2^{1/2} \sum_{p=\pm 1} \mu_{\|} \Omega k \langle H; M, \Omega | i T_p^1(\mathcal{B}) | C; \Omega \rangle$$

$$= i\mu_{\|} \Omega k 2^{1/2} \sum_{p=\pm 1} (-1)^p \mathcal{B}_p (-1)^{J-M} (-1)^{J-\Omega} (2J+1) \begin{pmatrix} J & 1 & J \\ -M & p & 0 \end{pmatrix} \begin{pmatrix} J & 1 & J \\ -\Omega & 0 & \Omega \end{pmatrix}$$

$$= i\mu_{\|} \Omega k \mathcal{B} (-1)^M (-1)^{J-M} (-1)^{J-\Omega} (2J+1) \begin{pmatrix} J & 1 & J \\ -M & M & 0 \end{pmatrix} \begin{pmatrix} J & 1 & J \\ -\Omega & 0 & \Omega \end{pmatrix}$$

$$= i 2^{-1} M k \mu_{\|} \mathcal{B}, \tag{B.2}$$

$$\tag{B.3}$$

where $\mu_{\|}$ is the parallel magnetic transition dipole moment between H and C. To perform that last step, notice that this looks exactly the same as the Stark matrix element but with $M D_{\|} \mathcal{E} \to i\mu_{\|} \Omega \mathcal{B} k$, so we can take the Stark result and multiply by $i\mu_{\|} \Omega \mathcal{B} k / M D_{\|} \mathcal{E}$ and use the fact that $M^2 = \Omega^2 = 1$ and therefore $\Omega^{-1} = \Omega$, $M^{-1} = M$.

In the experiment, the relevant states are symmetric and anti-symmetric combinations of the states we wrote above. Let $P = \pm 1$ denote the parity of the C state, and $\Pi = \pm 1$ denote the polarization of the H state (i.e. X vs Y.) The relevant states are then

$$|C; P\rangle = 2^{-1/2}(|C; \Omega = +1\rangle + P |C; \Omega = -1\rangle) \tag{B.4}$$

$$|H; \hat{n}, \Pi\rangle = 2^{-1/2}(|H; M = +1, \Omega = -\hat{n}\rangle + \Pi |H; M = -1, \Omega = +\hat{n}\rangle), \tag{B.5}$$

where $\hat{n} = \mathcal{N} \hat{\mathcal{E}}_{lab}$ is the molecule dipole orientation in the lab frame. The matrix

elements between these states are

$$
\begin{aligned}
2\left\langle \hat{n}, \Pi | D \cdot \mathcal{E} | C; P \right\rangle &= \left\langle M=+1, \Omega=-\hat{n} | D \cdot \mathcal{E} | \Omega=+1 \right\rangle + \cdots \\
&\quad P \left\langle M=+1, \Omega=-\hat{n} | D \cdot \mathcal{E} | \Omega=-1 \right\rangle + \cdots \\
&\quad \Pi \left\langle M=-1, \Omega=+\hat{n} | D \cdot \mathcal{E} | \Omega=+1 \right\rangle + \cdots \\
&\quad P\Pi \left\langle M=-1, \Omega=+\hat{n} | D \cdot \mathcal{E} | \Omega=-1 \right\rangle \\
&= 2^{-1} D_{\|} \mathcal{E} \left(-\hat{n}\delta_{-\hat{n},+1} + P(-\hat{n})\delta_{-\hat{n},-1} + \Pi\hat{n}\delta_{\hat{n},+1} + P\Pi\hat{n}\delta_{\hat{n},-1} \right) \\
&= 2^{-1} D_{\|} \mathcal{E}\hat{n} \left(-\delta_{-\hat{n},+1} - P\delta_{-\hat{n},-1} + \Pi\delta_{\hat{n},+1} + P\Pi\delta_{\hat{n},-1} \right) \\
&= 2^{-1} D_{\|} \mathcal{E}\hat{n} \times
\begin{cases}
-\delta_{\hat{n},-1} - P\delta_{\hat{n},+1} + \delta_{\hat{n},+1} + P\delta_{\hat{n},-1} & \Pi=+1 \\[2ex]
-\delta_{\hat{n},-1} - P\delta_{\hat{n},+1} - \delta_{\hat{n},+1} - P\delta_{\hat{n},-1} & \Pi=-1
\end{cases} \\
&= 2^{-1} D_{\|} \mathcal{E}\hat{n} \times
\begin{cases}
(-\delta_{\hat{n},-1} + \delta_{\hat{n},+1})(1-P) & \Pi=+1 \\[2ex]
-(\delta_{\hat{n},-1} + \delta_{\hat{n},+1})(1+P) & \Pi=-1
\end{cases} \\
&= 2^{-1} D_{\|} \mathcal{E}\hat{n} \times
\begin{cases}
\hat{n}(1-P) & \Pi=+1 \\[2ex]
-(1+P) & \Pi=-1
\end{cases} \\
\left\langle \hat{n}, \Pi | D \cdot \mathcal{E} | C; P \right\rangle &= \frac{D_{\|}\mathcal{E}}{4} \times
\begin{cases}
(1-P) & \Pi=+1 \\[2ex]
-\hat{n}(1+P) & \Pi=-1,
\end{cases}
\end{aligned}
\tag{B.6}
$$

where we used that $\delta_{\hat{n},-1} + \delta_{\hat{n},+1} = 1$ and $-\delta_{\hat{n},-1} + \delta_{\hat{n},+1} = \hat{n}$ since $\hat{n} = \pm1$. The above looks complicated, but the final result makes sense; the answer is non-zero only when

$P \neq \Pi$, which is the E1 parity selection rule. Similarly,

$$
\begin{aligned}
2\langle \hat{n}, \Pi | \mu \cdot \mathcal{B} | C; P \rangle &= \langle M = +1, \Omega = -\hat{n} | \mu \cdot \mathcal{B} | \Omega = +1 \rangle + \cdots \\
&\quad P \langle M = +1, \Omega = -\hat{n} | \mu \cdot \mathcal{B} | \Omega = -1 \rangle + \cdots \quad \text{(B.7)} \\
&\quad \Pi \langle M = -1, \Omega = +\hat{n} | \mu \cdot \mathcal{B} | \Omega = +1 \rangle + \cdots \\
&\quad P\Pi \langle M = -1, \Omega = +\hat{n} | \mu \cdot \mathcal{B} | \Omega = -1 \rangle \\
&= 2^{-1} i k \mu_\parallel \mathcal{B} \left(\delta_{-\hat{n},+1} + P\delta_{-\hat{n},-1} - \Pi\delta_{\hat{n},+1} - P\Pi\delta_{\hat{n},-1} \right) \\
&= 2^{-1} i k \mu_\parallel \mathcal{B}
\begin{cases}
\delta_{-\hat{n},+1} + P\delta_{-\hat{n},-1} - \delta_{\hat{n},+1} - P\delta_{\hat{n},-1} & \Pi = +1 \\[2ex]
\delta_{-\hat{n},+1} + P\delta_{-\hat{n},-1} + \delta_{\hat{n},+1} + P\delta_{\hat{n},-1} & \Pi = -1
\end{cases} \\
&= 2^{-1} i k \mu_\parallel \mathcal{B}
\begin{cases}
(\delta_{-\hat{n},+1} - \delta_{\hat{n},+1}) + P(\delta_{-\hat{n},-1} - \delta_{\hat{n},-1}) & \Pi = +1 \\[2ex]
(\delta_{-\hat{n},+1} + \delta_{\hat{n},+1}) + P(\delta_{-\hat{n},-1} + \delta_{\hat{n},-1}) & \Pi = -1
\end{cases}
\end{aligned}
$$

$$
\langle \hat{n}, \Pi | \mu \cdot \mathcal{B} | C; P \rangle = -\frac{i k \mu_\parallel \mathcal{B}}{4}
\begin{cases}
\hat{n}(1 - P) & \Pi = +1 \\[2ex]
(1 + P) & \Pi = -1.
\end{cases}
\quad \text{(B.8)}
$$

The M1 and E1 amplitudes differ by a factor of $ik\hat{n}$, which agrees with Brendon's result. Since $\hat{n} = \tilde{\mathcal{N}}\tilde{\mathcal{E}}$, this means that we have an $\mathcal{NE}$-correlated Rabi frequency which reverses with k.

Appendix C

Fluorescence Collection

One of the significant advantages of transparent electric field plates is that a large solid angle of fluorescence can be collected from the molecules. The current design is a set of 8 lens doublets, each of which focuses the light into a fiber bundle. There are four doublets behind each electric field plate. The fiber bundles are combined into a single face coupled to a fused quartz light pipe. The light pipe penetrates the vacuum and is connected to a photomultiplier tube. Here we will discuss the design, construction, and characteristics of the system.

C.1   Design

The primary constraints of the design are that the system should not come within ≈ 1 mm of the field plates (to avoid damaging them), and that there should be at least 25 mm diameter of clearance for the lasers to pass through. The figure of merit we shall discuss for the lens system is f_{lens}, the fraction of photons emitted by the

molecules which are incident on the fiber bundles. This quantity does not take into account the finite transmission of the bundles, bundle-light pipe coupling, or PMT quantum efficiency, which will be discussed later. Ideally, we want each lens system to focus the light onto as small an area as possible, since smaller area photodetectors will have less dark noise.

The original design was to use elliptic reflectors. The advantage of this design was that behind each plate there would be a single collector, and a single light pipe. However, the design ended up being unavoidably complex and would have been very costly, so we started searching for a more modular solution. The requirement that there be a clear aperture for the lasers naturally suggests a number of collectors placed symmetrically around the fluorescing molecules. We tried a various combinations of collector number and geometry, and found that four collectors was a reasonable compromise between maximizing f_{lens} and minimizing complexity.

With eight collectors, we need eight ways to get the light out of the vacuum chamber and into PMTs. We explored the idea of getting bent fused silica light pipes (bent acrylic would be simpler to make, but would have more outgassing and lower transmission), but quickly realized that option would be expensive, complicated, and not modular. After shopping around we found a company (Fiberoptic Systems of Simi Valley, CA) who manufactures custom fiberoptic bundles with high numerical aperture and low cost. Shopping around was important - one company quoted $50,000 for an item that Fiberoptic Systems sold for $100! We obtained two "quadfurcated" bundles, that is, bundles with four input faces and one output face. This easily combined the four collectors on each side into a single light pipe to be sent to a single

PMT. We opted for a 19 mm (3/4") diameter light pipe, since it is a standard size and the PMT face is 18 mm diameter.

The next step is to choose the lens diameter. Before performing any sort of simulations, it is reasonable to assume that the lens axis should be aligned such that it intersects the molecule fluorescence (i.e. it is looking right at the molecules). If we then do a simple geometric calculation, we find that 50 mm diameter lenses will not give the required clearance for the lasers, but 75 mm lenses will. This lens size is also the largest which is easily obtainable, and is therefore a reasonable choice.

After trying a few different combinations of lens configuration, we found that the setup shown in Figure C.1 was a good balance between maximizing f_{lens}, and design simplicity. The lenses are standard items at CVI Melles-Griot, and are standard diameters which can be put into lens tubes. The first lens collimates the light, and the second lens focuses the light into a fiber bundle. A keen observer might notice that the first, large lens seems to be backwards; the curved face of a plano-convex lens usually faces collimated light to focus to a point source, not the other way around. However, these lenses are so thick that having the flat face look toward the "point source" of molecule fluorescence resulted in a large fraction of the light being totally internally reflected at the curved face.

Numerical ray tracing simulations with LightTools indicate that $f_{lens} = 4.6\%$ for the configuration shown in Figure C.1. The simulation assumes a 10 mm diameter, 1 mm thick disc as the light source. The ITO coated side of the field plates is assumed to scatter 10%, while the opposite side features an AR coating. The lenses are AR coated as well. The value of f_{lens} is fairly robust to misalignment, as shown in Figure
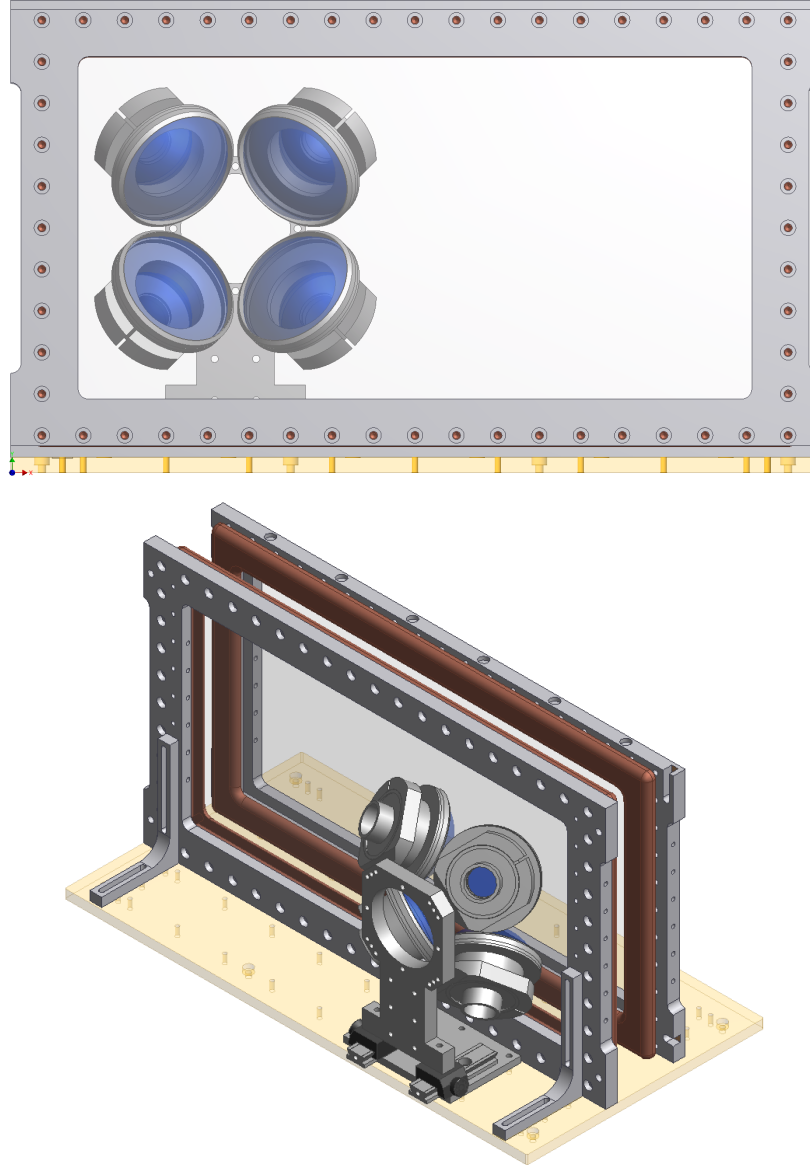
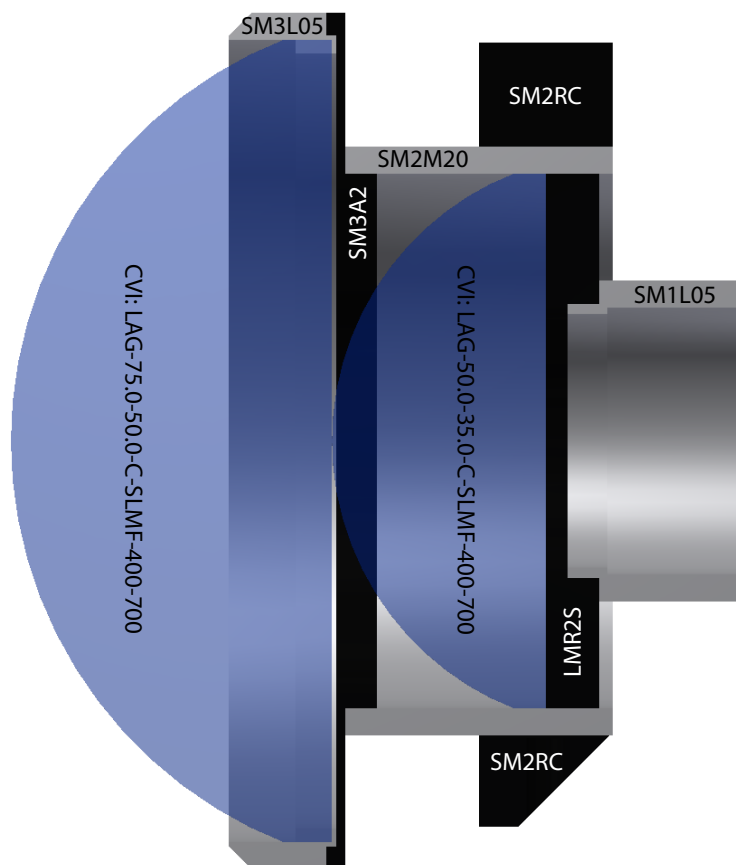Figure C.1: Two views of the electric field plates and fluorescence collection system.

Figure C.2: Cut-away of the lens tube assembly, with part numbers indicated. Apart from the lenses from CVI, all parts are from ThorLabs. Some of the parts of additional machining, for example SM3L05 is cut to be 0.25" in length, and SM2RC has a 45° cut on the bottom for mounting.

Table C.1: Estimated collection efficiency. The entries in the first part of the table are rounded to the nearest multiple of 5%. Tests by Ben Spaun with the fully assembled system indicate that the detection efficiency is $\approx 1.3\%$.

Quantity	Value	Notes
Lens Efficiency	35%	Single lens doublet = 4.6%
Bundle Coupling	60	65% core filling fraction, 5% Fresnel
Bundle Transmission	95	Attenuation = 0.67 dB/m, length = 1 foot
Light Pipe Exit	95	
Light Pipe Contact	95	O-ring seal, mounting collar
PMT Face Reflection	95	
Estimated collection efficiency	17	
PMT Quantum efficiency	10	
Estimated detection efficiency	$\approx 1.7\%$	

C.3.

We also considered using compound parabolic concentrators (CPCs, or "Winston Cones") instead of lenses. These objects have a large input face, a smaller output face, and over a large ranges of incidence angles will spatially compress incoming light from the large to the small face. The drawback with using these objects is that they spatially compress the light at the expense of an increased angular spread, which is not compatible with the fiber bundles acceptance angle of $\approx 40°$. CPCs could be used after the light pipe if we wanted a smaller PMT, but since dark noise is not our dominant noise source (see Section 4.4.1), we did not bother implementing this.

C.2   Construction

The assembly is shown in Figure C.1. All of the lens tubes are standard Thorlabs items, though they were ordered without anodization to reduce outgassing (exceptions to this were any time there was a moving metal-on-metal contact, such as the optical rails or lens tube threads, in which case one of the surfaces was left anodized.) The

fiber bundle ferrule is mounted with a shaft collar into a lens tube, and the other ferrule is held against the face of a fused quartz light pipe. A small amount of Dow Corning Q2-3067 Optical Couplant, a gel with index of refraction close to that of glass, is placed between the bundle and light pipe to prevent losses at the interfaces. The light pipe leaves the vacuum chamber through a "Quick Coupling" port on a KF flange, which uses an o-ring to seal directly against the light pipe. The light pipe is then incident on a Hamamatsu R8900U-20 PMT, which has $\approx 10\%$ quantum efficiency at 690 nm.

C.3   Testing

We performed bench tests of the fluorescence collection system in order to ensure that the numerical simulations were reasonably accurate. To simulate the fluorescing molecular cloud, we inserted an optical fiber into a Delrin ball with a small hole drilled into it. We modulated the light coming out of the fiber at about 1 kHz to reject background due to room lights. We calibrated the total light emitted by the Delrin ball by placing a large area photodiode (Hamamatsu S3584) at a set distance from it and noting the voltage. Next, we placed the Delrin ball at a distance of 12 mm from a 12.7 mm thick piece of glass, to simulate the field plate. We then aligned one of the lens doublets as we would behind the real field plates, and placed the same photodiode behind a lens doublet. Figure C.3 shows an example of some data taken with the bench setup, showing the variation of collection efficiency with varying misalignment.
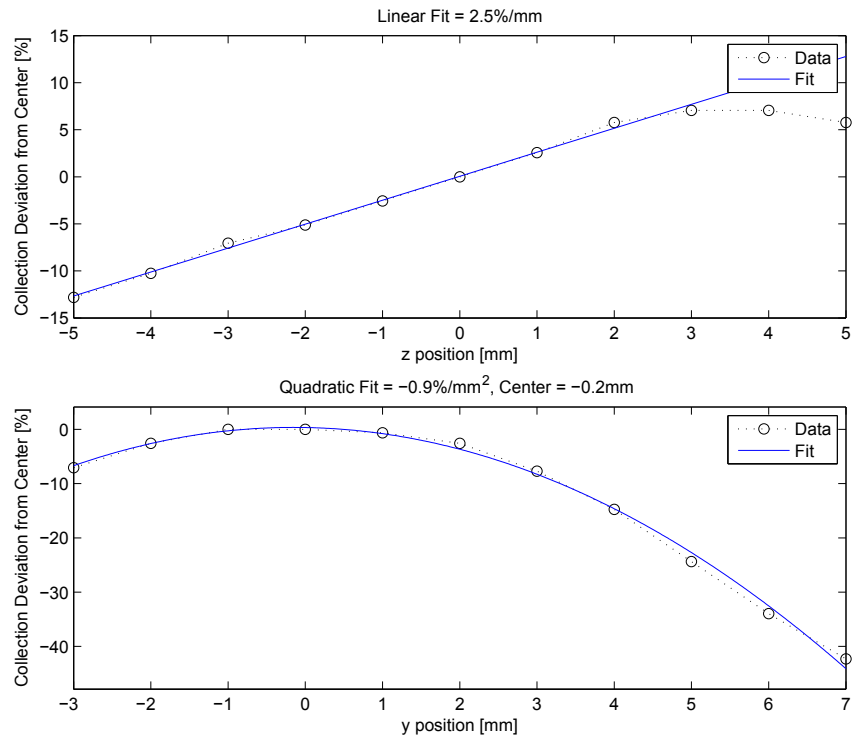
Figure C.3: Measured change in collection efficiency with varying source. The source is a 1 cm diameter Delrin ball with an optical fiber stuck into the center. Here z is the direction perpendicular to the plate face, and y is parallel to the plate face.

C.4   Next Generation

One of the ideas being considered for the next generation apparatus is to have the laser propagate between the field plates, instead of through them. There are a large number of considerations with this prospect, and we will not discuss them here. However, one advantage would be that the laser clearance constraint would vanish and we could increase our collected solid angle. We did not pursue careful studies of this scenario, but did put together a simple simulation of the system shown in Figure C.4. The system consists of two elliptic reflectors, one behind each field plate. Each reflector has a hole in the center which is occupied by a light pipe. One of the foci is located on the fluorescing molecules, while the other is located on the light pipe for the opposite reflector. This preliminary design indicated $f_{lens} \approx 50\%$, suggesting that significant count rate improvements could be had with such a setup. The downside would be added complexity and cost.

Jul 18, 2011
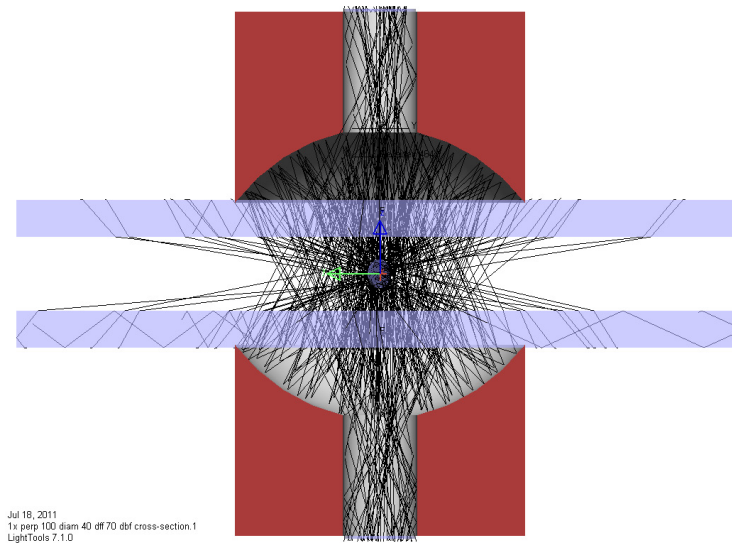1x perp 100 diam 40 dff 70 dbf cross-section.1
LightTools 7.1.0

Figure C.4: Ray tracing simulation of an elliptic reflector-based fluorescence collection system. This system was not optimized, but offered ≈ 50% geometric collection efficiency.

Appendix D

H State Microwave Spectroscopy

As we saw in Section 5.3.1, non-reversing electric fields are behind one of our most significant systematic effects. While the effect we observed only relied on the non-reversing electric field near the preparation and readout lasers (to create a correlated detuning), it motivated us to measure the electric field uniformity and reversibility along the entire molecule flight length. We performed this measurement by using microwave spectroscopy to measure the Stark shift as a function of distance from the readout laser, as will be described in this Appendix. These measurements also allowed us to obtain improved measurements of the Ω-doublet splitting, and the rotational constant.

Microwaves are emitted by a horn at the end of the apparatus, and counter-propagate with respect to the molecular beam. We drive the $|H, J = 1\rangle \rightarrow |H, J = 2\rangle$ transition, which has a frequency of ≈ 39 GHz. Given the typical molecular beam velocity of 200 ± 20 m/s and width (FWHM) of ≈ 40 m/s[130], we expect a first order Doppler shift of 26(2) kHz, and a Doppler broadened linewidth of ≈ 5 kHz. We

269

can typically find the line centers to ≈ 1 kHz, so our total uncertainty on frequency measurements is ≈ 3 kHz.

D.1 Stark spectroscopy in the H state

We shall first discuss the Stark shifts of the microwave transitions in the H state, in particular of transitions between the $J = 1$ and $J = 2$ states.

D.1.1 Zero Field

We will always assume that there is no magnetic field, but for this section we assume no electric field as well, $\mathcal{E}_{ext} = 0$. In this section we will make the assertion that $H, J = 1^{+}$ is the lower state of the Ω-doublet, which we will prove in Section D.3. Since we start the optical pumping from the $X, J = 1^{-}$ state, and the pumping involves two $E1$ transitions, we will populate the negative parity (upper) $H, J = 1^{-}$ state. The Ω-doublet splitting is given by[37] $aJ(J+1)$ where a is a constant, and the mean splitting between the $H, J = 1$ and $H, J = 2$ state is $4B_{v=0}$, where $B_{v=0}$ is the rotational constant in the $H, v = 0$ state. The frequency of the microwave transition will therefore be $(4B_{v=0} + 3a) - a = 4B_{v=0} + 2a$, as shown in Figure D.1
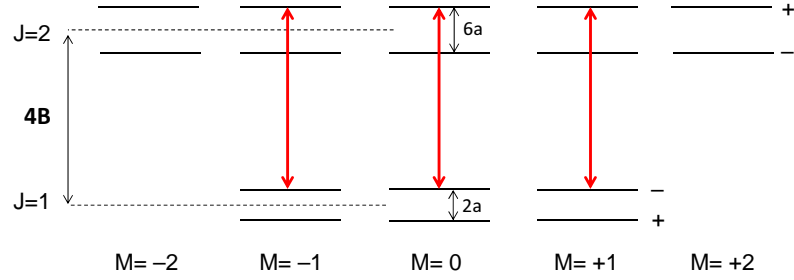
Figure D.1: Microwave absorption in zero field.

D.1.2 Transitions in the Linear Stark Regime

The linear Stark shifts (see Section 2.4) are given by

$$E_{stark} = \frac{D_\| M \Omega \mathcal{E}_{ext}}{J(J+1)} = D_\| |\mathcal{E}_{ext}| \times \begin{cases} 0 & M = 0 \\[2mm] \pm\frac{1}{2} & J = 1, M\Omega = \mp 1 \\[2mm] \pm\frac{1}{6} & J = 2, M\Omega = \mp 1 \\[2mm] \pm\frac{1}{3} & J = 2, M\Omega = \mp 2. \end{cases} \tag{D.1}$$

From Figure D.2, we see that there are a total of 11 lines: 3 with $z-$polarization, and 8 with y-polarization (x-polarized microwaves could also drive these transitions, but the microwaves propagate along $\hat{x}$ in our setup). Note that we cannot drive from the upper state to the lower state, or vice-versa, because the upper/lower states have the same sign of $M\Omega$, where M and Ω are both ≥ 1 in absolute value. Therefore to change the sign of $M\Omega$ we either need to change M by > 1, or change Ω by > 1, neither of which is allowed.

The Stark shift will never be truly linear (see Section 2.4.2), but we can determine how large of an electric field is required such that the departure from linearity is small
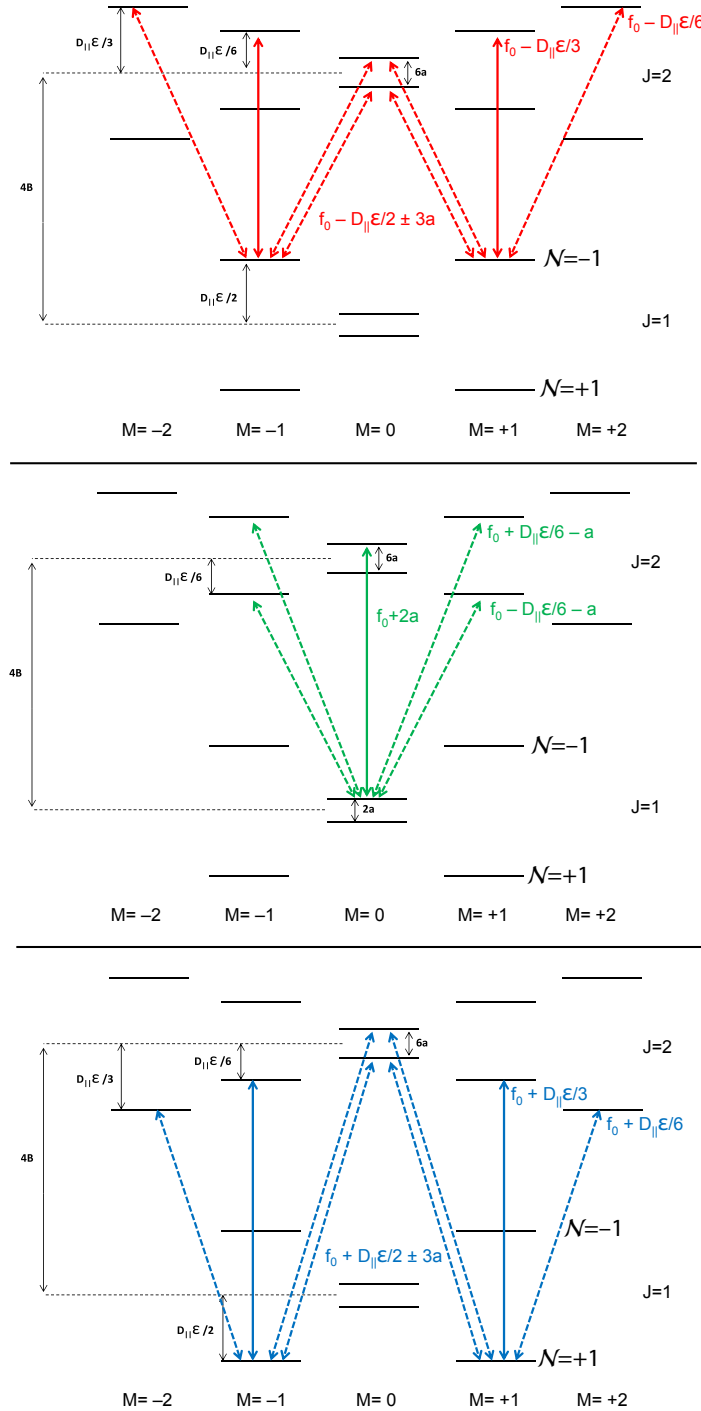
Figure D.2: Linear stark shifts in $H, J = 1$. The quadratic stark shift is ignored here since it is much smaller than the linear shift, but it is typically larger than the Doppler shift and therefore must be included to determine molecular constants.

compared to the Doppler width. The stark shift is

$$E_{stark} = -\mathcal{N} \left[\left(\frac{D_{\parallel}\mathcal{E}_{ext}}{J(J+1)} \right)^2 + \left(\frac{aJ(J+1)}{2} \right)^2 \right]^{1/2}, \tag{D.2}$$

and the transition frequency (for the $M = \pm 1$ levels) is therefore

$$E_{stark}(J=2) - E_{stark}(J=1) = -\mathcal{N}\frac{D_{\parallel}\mathcal{E}_{ext}}{3} + \mathcal{N}\frac{26a^2}{D_{\parallel}\mathcal{E}_{ext}} + \mathcal{O}\left(\frac{a^4}{(D_{\parallel}\mathcal{E}_{ext})^3} \right). \tag{D.3}$$

Since $a^4/(D_{\parallel}\mathcal{E}_{ext})^3 < 1$ kHz even for $\mathcal{E}_{ext} = 1$ V/cm, we are justified in ignoring higher order terms. If we apply $\mathcal{E}_{ext} = 100$ V/cm, then $26a^2/D_{\parallel}\mathcal{E}_{ext} < 5$ kHz (the Doppler width). Our measurements were reported in $\mathcal{E}_{ext} = 141$ V/cm, so the linear Stark approximation is valid.

D.1.3   Quadratic Stark Shift

The molecules will also see a quadratic stark shift from the applied electric field. The quadratic shifts for $J = 1$ are

$$\Delta E(J=1, M=0) = -\frac{|\langle 1,0,\pm| H_{\mathcal{E}} |2,0,\pm\rangle|^2}{4B_{v=0}} \tag{D.4}$$

$$\Delta E(J=1, M=\pm1) = -\frac{|\langle 1,\pm1,\pm\Omega| H_{\mathcal{E}} |2,\pm1,\pm\Omega\rangle|^2}{4B_{v=0}}, \tag{D.5}$$

where $H_{\mathcal{E}} = -D \cdot \mathcal{E}$, while the quadratic shifts for $J = 2$ are

$$\Delta E(J=2, M=0) = \frac{|\langle 1,0,\pm| H_{\mathcal{E}} |2,0,\pm\rangle|^2}{4B_{v=0}} - \frac{|\langle 2,0,\pm| H_{\mathcal{E}} |3,0,\pm\rangle|^2}{6B_{v=0}} \tag{D.6}$$

$$\Delta E(J=2, M=\pm1) = \frac{|\langle 1,\pm1,\pm1| H_{\mathcal{E}} |2,\pm1,\pm1\rangle|^2}{4B_{v=0}} - \cdots$$
$$\frac{|\langle 2,\pm1,\pm1| H_{\mathcal{E}} |3,\pm1,\pm1\rangle|^2}{6B_{v=0}}. \tag{D.7}$$

The difference in $J = 1 \to 2$ transition frequency is therefore

$$\Delta E(M = 0) = 2 \frac{|\langle 1, 0, \pm | H_{\mathcal{E}} | 2, 0, \pm \rangle|^2}{4 B_{v=0}} - \frac{|\langle 2, 0, \pm | H_{\mathcal{E}} | 3, 0, \pm \rangle|^2}{6 B_{v=0}} \quad (D.8)$$

$$\Delta E(M = \pm 1) = 2 \frac{|\langle 1, \pm 1, \pm 1 | H_{\mathcal{E}} | 2, \pm 1, \pm 1 \rangle|^2}{4 B_{v=0}} - \cdots$$

$$\frac{|\langle 2, \pm 1, \pm 1 | H_{\mathcal{E}} | 3, \pm 1, \pm 1 \rangle|^2}{6 B_{v=0}}. \quad (D.9)$$

The $J = 2 \to 3$ matrix elements are easy to find using the equations from Section 2.4:

$$\langle 2, M, \Omega | H_{\mathcal{E}} | 3, M, \Omega \rangle = D_{\|} \mathcal{E}_{ext} \sqrt{35} \begin{pmatrix} 2 & 1 & 3 \\ -M & 0 & M \end{pmatrix} \begin{pmatrix} 2 & 1 & 3 \\ -\Omega & 0 & \Omega \end{pmatrix} \quad (D.10)$$

$$= D_{\|} \mathcal{E} \times \begin{cases} \sqrt{\frac{8}{35}} & M = 0, \Omega = \pm 1 \\[2ex] \sqrt{\frac{64}{318}} & M = \pm 1, \Omega = \pm 1. \end{cases} \quad (D.11)$$

Plugging these in, we find

$$\Delta E(M = 0) = \frac{13}{210} \frac{(D_{\|} \mathcal{E}_{ext})^2}{B_{v=0}} \approx 27.163 \text{ Hz} \times (\mathcal{E}[\text{V/cm}])^2 \quad (D.12)$$

$$\Delta E(M = \pm 1) = \frac{311}{7560} \frac{(D_{\|} \mathcal{E}_{ext})^2}{B_{v=0}} \approx 18.051 \text{ Hz} \times (\mathcal{E}[\text{V/cm}])^2, \quad (D.13)$$

$$(D.14)$$

where we used $D_{\|} = 2070$ kHz/(V/cm) from Raman measurements performed by Paul Hess (see his Lablog entry dated 29 March 2013), and $B_{v=0} = 9765.4(3)$ MHz[79].

We are making the simplifying assumption in Eq. (D.6) that the two Ω-doublet states have equal energy spacing. If we include the Ω-doubling, we will need to modify the denominators in Eq. (D.6) to be $4B_{v=0} \pm 4a$ and $6B_{v=0} \pm 6a$, which will result

in a fractional energy shift of $a/B_{v=0} \sim 10^{-5}$ in the quadratic Stark shift. However, we shall see that the quadratic shifts are < 1 MHz with a 141 V/cm applied field, and therefore the modification to the transition frequencies are below the ~ 1 kHz sensitivity of our measurements.

D.2   Measurement of the electric field

Because the H state has large Stark shifts of order ~ 1 MHz/(V/cm), our frequency sensitivity of ~ 1 kHz means that we should be sensitive to $\sim$ mV/cm $\mathcal{E}$-fields. The first direct measurements of the $\mathcal{E}$-field were Raman measurements performed by Paul Hess, as described in his Lablog entries (see 29 March 2013, for example). These measurements indicated that the non-reversing $\mathcal{E}$-fields in the preparation and readout regions were a few mV/cm. Given non-reversing $\mathcal{E}$-field systematic (see Section 5.3.1) depends only on the non-reversing $\mathcal{E}$-field in these regions (to cause correlated detunings), these measurements were sufficient to put limits on this systematic. However, we still wanted to measure the $\mathcal{E}$-field along the entire beam path, including where there was no optical access. To achieve this, we used the counter-propagating microwave field to spin-polarize the molecules, and then used our normal readout procedure (see Section 4.2) to measure the asymmetry.

Specifically, we waited until the peak of the molecule packet was half way between the preparation and readout lasers, which we call $t = 0$. At $t = 0$ we would shine a burst of y-polarized, resonant microwaves for ≈ 5 μs. The microwaves were resonant with the $|H, J = 1, M = \pm 1\rangle$ levels in either the $\mathcal{N} = \pm 1$ state, and the $|H, J = 2, M = 0\rangle$ level (see Figure D.2). This Λ-system will prepare a coherent su-

perposition of the $M = \pm 1$ levels, exactly as described in Section 4.2.

If the molecules take time τ to travel from the preparation to the readout laser, then we will obtain a spin precession signal between time $t = 0$ and $t = \tau$. Since there is no magnetic field, the spin polarization imprinted on the molecules from the microwave pulse will remain fixed (neglecting the very small phases accumulated from stray fields and other effects) until read out. A molecule read out at time t' will have been spin-polarized at a distance of vt' from the readout laser, where v is the molecule velocity. If we fix our attention on the asymmetry signal at time t' and perform a microwave frequency scan, we can obtain a contrast lineshape as in Appendix E. Since the contrast lineshape is centered at the resonant frequency of the transition, which gives the Stark shift as described in the previous section, we can determine the Stark shift as a function of position along the plates by examining all values of t'.

D.3 Determination of rotational and Ω-doubling constants

First, we measured the $H, J = 1 \rightarrow H, J = 2$ transition in zero field to be $39,065,540$ kHz. From Section D.1.1, this tells us that

$$4B_{v=0} + 2a = 39,065,566(3) \text{ kHz}, \tag{D.15}$$

after including the 26 kHz Doppler shift.

Next, we measured the $|H, J = 1, M = \pm 1, \mathcal{N} = -1\rangle \rightarrow |H, J = 2, M = 0\rangle$ transitions in a 141 V/cm electric field. From Figure D.2, we can see that there should be two transitions (to the two Ω-doublet states in $J = 2$) with frequencies that differ by
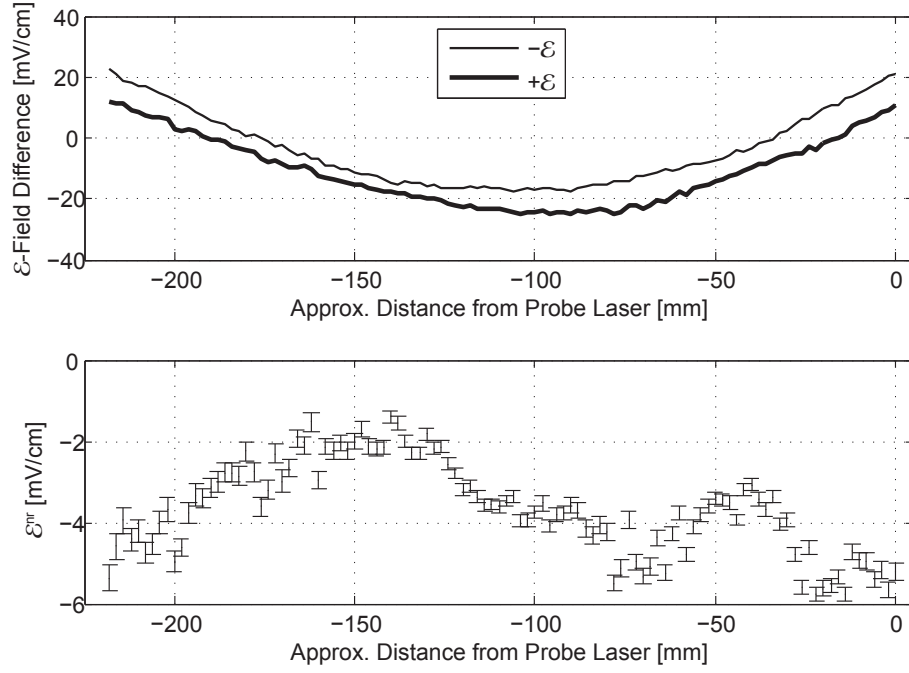
Figure D.3: Electric field map using microwave spectroscopy. We assume that the molecule velocity is the typical value of 200 m/s. Top: Electric field with the field plates in the two configurations with the applied voltages on the plates reversed, or "$+\mathcal{E}$" and "$-\mathcal{E}$" configuration. This method is mainly sensitive to $\mathcal{E}$-field differences, so the above plot has an arbitrary offset. The parabolic shape is in good agreement with the plate spacing as measured by Ivan Kozyryev using an interferometer. Error bars are not shown since they are too small to be visible with this scale. Bottom: half the difference between the $+\mathcal{E}$ and $-\mathcal{E}$ configurations, which gives the non-reversing $\mathcal{E}$-field, $\mathcal{E}^{\mathrm{nr}}$. The error bars are determined by the contrast linewidth.

6a, independent of the Doppler shift and electric field. The frequencies were measured

to be 38,919,036(3) kHz and 38,920,120(3) kHz, so their difference yields

$$a = 181(1) \text{ kHz} = 6.04(3) \times 10^{-6} \text{ cm}^{-1}. \tag{D.16}$$

We can then solve Eq. (D.15) to obtain

$$B_{v=0} = 9,766,301(1) \text{ kHz} = 0.3257687(1) \text{ cm}^{-1}. \tag{D.17}$$

These numbers agree with the previously reported values of $B_{v=0} = 0.32574(1) \text{ cm}^{-1}$

and $a = 6.2(4) \times 10^{-6} \text{ cm}^{-1}$[79], but with higher precision. Notice that some papers[78]

report the rotational constant as $B_e = 0.326427(7) \text{ cm}^{-1}$, which differs from $B_{v=0}$ by

$\alpha_e/2$, where $\alpha_e = 0.00128(1) \text{ cm}^{-1}$ for the ThO H state[78].

The determination of $B_{v=0}$ above relied on the assertion made in Section D.1.1

that the lower Ω-doublet state in $H, J = 1$ is the positive parity state. To prove

this, we can calculate $B_{v=0}$ using transitions which do not rely on this parity ordering

and check that the results agree. According to Figure D.2 and Section D.1.3, the

mean frequency of the $|H, J = 1 \mathcal{N} = \pm 1\rangle \rightarrow |H, J = 2, \mathcal{N} = \pm 1\rangle$ transitions should

be equal to $4B_{v=0}$ plus the quadratic Stark shift. We measure this mean frequency to

be (39,162,900 kHz + 38,968,168 kHz)/2 = 39,065,534 kHz with 141 V/cm applied

field, so

$$4B_{v=0} + \frac{311}{7560} \frac{(D_{\parallel}\mathcal{E}_{ext})^2}{B_{v=0}} = 39,065,534 \text{ kHz}$$

$$4B_{v=0} + 18.051 \text{ Hz} \times (141)^2 = 39,065,534 \text{ kHz}$$

$$B_{v=0} = 9,766,295(3) \text{ kHz}, \tag{D.18}$$

which agrees with our determination above fairly well (especially when considering

that we have ignored uncertainty on $D_{\parallel}\mathcal{E}_{ext}$). If the lower $H, J = 1$ state was the

negative parity state, then we would compute $4B_{v=0} - 2a = 39,065,566(3)$ or $B_{v=0} = 9,766,482(1)$ kHz, which disagrees significantly.

D.4   Rotational Constant - Correction to Dewberry

et al. (2007)

The paper by Dewberry *et al.*[71], to which we will refer as Dewberry 2007, reports the value $Y_{01} = 9971.7767(35)$ MHz for the X state of $^{232}\text{Th}^{16}\text{O}$. We will argue that because the paper neglected to include the Dunham coefficient (see Section 2.2.2) $D_e = Y_{02}$ in the fits, which is known to be non-zero[83], the reported value of Y_{01} should be shifted by $2Y_{02} \approx 11$ kHz. This is a small shift, but is larger than the reported uncertainty.

In Dewberry 2007, the transition frequency for $|X, J = 0\rangle \rightarrow |X, J = 1\rangle$ was measured within several different vibrational levels V. The frequency was then fit to the function $f(V)$, where

$$
\begin{aligned}
F(J, V) &= Y_{01}(V + 1/2)^0[J(J+1)]^1 + Y_{11}(V + 1/2)^1[J(J+1)]^1 + \cdots \\
&\quad Y_{21}(V + 1/2)^2[J(J+1)]^1 \tag{D.19} \\
&= \left(Y_{01} + Y_{11}(V + 1/2) + Y_{21}(V + 1/2)^2\right)[J(J+1)] \tag{D.20} \\
f(V) &= F(J = 1, V) - F(J = 0, V) \tag{D.21} \\
&= 2Y_{01} + 2Y_{11}(V + 1/2) + 2Y_{11}(V + 1/2)^2. \tag{D.22}
\end{aligned}
$$

Now let's consider including the Y_{02} term in the fit function $f^*(V)$,

$$F^*(J, V) = Y_{01}^*[J(J+1)] + Y_{11}^*(V+1/2)[J(J+1)] + \cdots$$

$$Y_{21}^*(V+1/2)^2[J(J+1)] + Y_{02}^*[J(J+1)]^2 \qquad \text{(D.23)}$$

$$f^*(V) = F^*(J=1, V) - F^*(J=0, V) \qquad \text{(D.24)}$$

$$= 2Y_{01}^* + 2Y_{11}^*(V+1/2) + 2Y_{21}^*(V+1/2)^2 + 4Y_{02}^*. \qquad \text{(D.25)}$$

Notice that if we identify $Y_{11}^* = Y_{11}$, $Y_{21}^* = Y_{21}$, and $Y_{01}^* + 2Y_{02}^* = Y_{01}$, then we will obtain exactly the same fit for the data points taken. However, the transition frequencies for other rotational transitions will shift. Edvinsson et al.[83] report $Y_{02}^* = -5.50(1)$ kHz, so including this term in the fit will result in $Y_{01}^* = Y_{01} - 2Y_{02}^* = 9971.7877(35)$ MHz. Notice that Edvinsson *et al.* use the convention $Y_{02} = -D_e$, and since they were unable to resolve the difference between $D_{v=0}$ and $D_{v=1}$ we will simply use $D_e = D_{v=0}$.

As an experimental test, we drove the $J=2, V=0 \leftarrow J=1, V=0$ transition in the X state of $^{232}\text{Th}^{16}\text{O}$. The two fit functions predict that the transition frequency should be

$$F(J=1, V=0) - F(J=0, V=0) = 4Y_{01} + 4Y_{11}/2 + 4Y_{11}/4$$

$$= 39,808,962(14) \text{ kHz}$$

$$F^*(J=1, V=0) - F^*(J=0, V=0) = 4Y_{01}^* + 4Y_{11}^*/2 + 4Y_{11}^*/4 + 32Y_{02}^*$$

$$= 39,808,830(14) \text{ kHz}.$$

The experimentally determined frequency was 39,808,820(5) kHz, so it appears that the fit function which includes Y_{02}^* gives more accurate results.

To summarize, the entry $Y_{01} = 9971.7767(35)$ in Table 2 of Dewberry 2007 should be replaced with two entries reading $Y_{01} = 9971.7877(35)$ MHz and $Y_{02} = -0.00550(1)$ MHz, where the value of Y_{02} is from Edvinsson *et al.*[83].

Appendix E

Contrast

In Section 4.2 we found the relationship between the measured asymmetry $\mathcal{A}$ and spin precession phase ϕ to be

$$\mathcal{A} = \mathcal{C} \cos(2(\phi - \theta)), \tag{E.1}$$

where θ is the linear polarization angle between the preparation and readout lasers. The contrast $\mathcal{C}$ was mentioned in passing, but is clearly very important for our measurement, especially considering the possible systematic effects due to correlated contrast, as discussed in Section 5.2.6. In this Appendix, we will derive how the contrast relates to our ability to prepare the bright/dark states, and to the correlated laser detunings which arise due to experimental imperfections.

E.1   Dark/bright population

This section is similar to Section 4.2, but we will go into some more detail. Say that at $t = 0$, which is the moment when the molecules enter the state preparation

laser, the population in the bright $|B\rangle$ and dark $|D\rangle$ states (see Section 4.2) are $N_B(0)$ and $N_D(0)$ respectively. Here the bright and dark states are $|X\rangle$ and $|Y\rangle$, the polarization readout states. Let $|C\rangle$ be the Zeeman level in the C state through which the molecules in $|B\rangle$ are pumped into the ground state, so that the state preparation laser is driving $|B\rangle \leftrightarrow |C\rangle$. First, consider the situation where we neglect decay of the $|C\rangle$ state. Now we have a simple two-level-system, and can therefore use the standard result (we will follow the treatment from §3.7 of [42]) that the time-averaged number of molecules N_C in the $|C\rangle$ state under resonant excitation is given by

$$N_C = \frac{\kappa}{1 + 2\kappa}(N_B + N_C), \qquad \kappa = \frac{d_{CB}^2 \mathcal{E}_0^2}{\Gamma_{CB}} \tag{E.2}$$

where d_{CB} is the transition dipole moment, Γ_{CB} is the radiative decay rate, and κ is the saturation parameter.

Now, say that the excitation has a lineshape $f(\Delta)$, where Δ is the detuning of the state preparation laser from resonance, and the lineshape is normalized such that $f(0) = 1$. In this case, the excited fraction is obtained by replacing $\kappa \to \kappa f(\Delta)$,

$$N_C(\Delta) = \frac{\kappa f(\Delta)}{1 + 2\kappa f(\Delta)}(N_B + N_C) \equiv F(\Delta)(N_B + N_C). \tag{E.3}$$

Assume that molecules leave the $|B\rangle \leftrightarrow |C\rangle$ system only through radiative decay $|C\rangle \rightsquigarrow |X\rangle$, which occurs with rate $\Gamma_C \approx 1/(500 \text{ ns})$. Since this is the dominant decay channel for both $|B\rangle$ and $|C\rangle$, this is a good assumption. We may write

$$\frac{d}{dt}(N_B + N_C) = -\Gamma_C N_C = -\Gamma_C F(\Delta)(N_B + N_C) \tag{E.4}$$

$$(N_B + N_C)(t) = (N_B + N_C)(0)e^{-\Gamma_C t F(\Delta)t}. \tag{E.5}$$

At $t = 0$ there should be no molecules in the C state, so we can write $(N_B + N_C)(0) = N_B(0)$. Similarly, as soon as the molecules leave the 1090 driving field, which occurs at

$t = T$, the C state will rapidly decay to the ground state, so $(N_B + N_C)(T) = N_B(T)$. Therefore,

$$N_B(T) = N_B(0)e^{-\Gamma_C T F(\Delta)}, \quad N_D(T) = N_D(0). \tag{E.6}$$

Note that we have made the assumption that H state decay is negligible during time T, but we shall later see that $T \ll \tau_H$ so the assumption is valid.

Beginning at time T, the molecules precess in the magnetic field and acquire a phase ϕ, so

$$|B\rangle \rightarrow \cos(\phi)|B\rangle + \sin(\phi)|D\rangle \tag{E.7}$$

$$|D\rangle \rightarrow -\sin(\phi)|B\rangle + \cos(\phi)|D\rangle. \tag{E.8}$$

If we then shine X or Y polarized light onto the molecules, we will collect fluorescence intensities

$$
\begin{aligned}
I_X &= N_B(T)|\langle X|B\rangle|^2 + N_D(T)|\langle X|D\rangle|^2 \tag{E.9} \\
&= N_B(T)\cos^2(\phi) + N_D(T)\sin^2(\phi) \tag{E.10} \\
I_Y &= N_B(T)|\langle Y|B\rangle|^2 + N_D(T)|\langle Y|D\rangle|^2 \tag{E.11} \\
&= N_B(T)\sin^2(\phi) + N_D(T)\cos^2(\phi) \tag{E.12}
\end{aligned}
$$

Note we are neglecting radiative decay of the $|B\rangle, |D\rangle$ states since it will occur in equal proportion, and we will end up caring only about relative populations. If we calculate the contrast from the fluorescence intensities, we will find

$$\mathcal{A} = \frac{I_Y - I_X}{I_Y + I_X} = \frac{N_B(T) - N_D(T)}{N_B(T) + N_D(T)}\cos^2(\phi) \equiv \mathcal{C}\cos^2(\phi). \tag{E.13}$$

The contrast is therefore given by

$$\mathcal{C}(\Delta) = \mathcal{C}_{max}\frac{N_B(T) - N_D(T)}{N_B(T) + N_D(T)} = \mathcal{C}_{max}\frac{e^{-\Gamma_C TF(\Delta)} - 1}{e^{-\Gamma_C TF(\Delta)} + 1} = \mathcal{C}_{max}\tanh\left(\Gamma_C TF(\Delta)/2\right),$$

(E.14)

where we have made the (valid) assumption that $N_B(0) = N_D(0)$. Here the value $\mathcal{C}_{max}$ is the maximum possible contrast after accounting for the velocity dispersion[242].

E.2 Contrast Correlations

As we saw in Section 5.2.3, a non-reversing electric field $\mathcal{E}^{\mathrm{nr}}$ creates a correlated detuning $\delta^{\mathcal{NE}} = d\mathcal{E}^{\mathrm{nr}}$, and an incorrect AOM frequency adds $\delta^{\mathcal{N}} = -\delta\nu_m = \nu_m - d\mathcal{E}$. We can plug these detuning correlations into Eq. (E.14) to determine how the contrast will be correlated with these quantities, but first let's make some simplifying assumptions. Assume that the contrast is near the maximum (valid when the overall detuning is small), so that

$$\tanh(\Gamma_C TF(\Delta)/2) \approx 1.$$

(E.15)

We may now use the approximation

$$1 - \tanh(x) = 1 - \frac{e^{2x} - 1}{e^{2x} + 1} = \frac{2}{e^{2x} - 1} \approx 2e^{-2x},$$

(E.16)

which is good to better than $\sim 10\%$ when $x > 2$ (and therefore contrast within $\sim 95\%$ of maximum). Therefore, for large contrast, we may approximate

$$\mathcal{C}(\Delta) = \mathcal{C}_{max}\tanh\left(\Gamma_C TF(\Delta)/2\right) \approx \mathcal{C}_{max}\left(1 - 2e^{-\Gamma_C TF(\Delta)}\right)$$

(E.17)

Let us also replace the un-broadened lineshape by a Gaussian $f^*(\Delta) = \exp(-\Delta^2/2\Gamma_{tot}^2)$ with width $\Gamma_{tot} \approx \Gamma_{laser}/2 + \Gamma_{rad}/2 + \Gamma_{dop}$ (the factors of $1/2$ come from the fact that

the homogeneous widths are full widths, while Gaussian widths are roughly half-widths). We may then perform a Taylor expansion to obtain

$$\mathcal{C}(\Delta) = \mathcal{C}_{max} - \mathcal{C}_{max}\exp\left(-\frac{N_{rad}\kappa}{1+2\kappa}\right)\left(2 + \frac{\Delta^2}{\Gamma_{tot}^2}\frac{N_{rad}\kappa}{(1+2\kappa)^2}\right), \qquad \text{(E.18)}$$

where $N_{rad} = \Gamma_C T$ is the number of radiative decay times that the molecules experience in the laser. Since this is a series expansion in Δ, we can see that the approximation is valid as long as

$$\frac{\Delta^2}{\Gamma_{tot}^2}\frac{N_{rad}\kappa}{(1+2\kappa)^2} \ll 1 \quad \Rightarrow \quad \Delta^2 \ll \Gamma_{tot}^2, \quad N_{rad}\kappa \gg 1+2\kappa. \qquad \text{(E.19)}$$
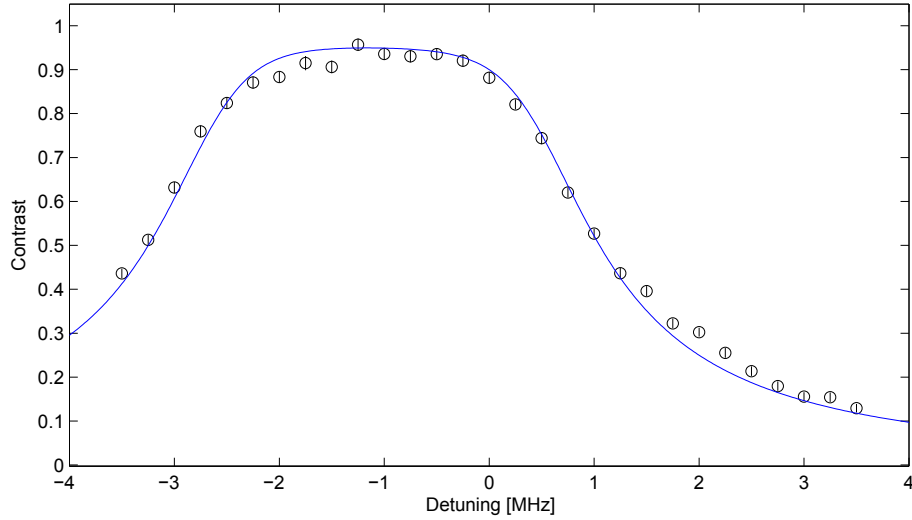

Figure E.1: Contrast lineshape with fit using a 3.5 W state preparation laser. The fit is given by Eq. (E.18), with parameters $\kappa = 1$, Doppler width (1σ) of 600 kHz, homogeneous FWHM = 800 kHz, and $N_{rad} = 15$.

We may compute contrast correlations following the procedure outlined in Section 4.3.5 to obtain

$$\begin{pmatrix} \mathcal{C}^{\mathcal{N}} \\ \mathcal{C}^{\mathcal{E}} \\ \mathcal{C}^{\mathcal{N}\mathcal{E}} \end{pmatrix} = \mathcal{C}_{max}\exp\left(-\frac{N_{rad}\kappa}{1+2\kappa}\right)\frac{2N_{rad}\kappa}{(1+2\kappa)^2}\begin{pmatrix} (\delta\nu_c/\Gamma_{tot}) \times (\delta\nu_m/\Gamma_{tot}) \\ (d\mathcal{E}_{nr}/\Gamma_{tot}) \times (\delta\nu_m/\Gamma_{tot}) \\ -(d\mathcal{E}_{nr}/\Gamma_{tot}) \times (\delta\nu_c/\Gamma_{tot}) \end{pmatrix} \qquad \text{(E.20)}$$

This formula shows how non-reversing fields and laser frequency offsets can cause correlated contrasts. As mentioned in Sections 4.3.8 and 5.3.3, these correlations can be eliminated from the molecular phases mathematically, and are therefore not a serious concern for our experiment. However, they can give useful information about non-reversing fields, and laser offsets.

Bibliography

[1] R J Ackermann and E G Rauh. High-temperature properties of the thorium-oxygen system: A Revision of the Thermodynamic Properties of ThO(g) and ThO$_2$(g). *High Temp. Sci.*, 5:463, 1973.

[2] R. J. Ackermann, E. G. Rauh, R J Thorn, and M. C. Cannon. A Thermodynamic Study of the Thorium-Oxygen System at High Temperatures. *Journal of Physical Chemistry*, 67(4):762–769, April 1963.

[3] R. J. Ackermann and M. Tetenbaum. High-Temperature Thermodynamic Properties of the Thorium-Oxygen System. *High Temperature Science*, 13:91–105, 1980.

[4] Wolfgang Altmannshofer, Roni Harnik, and Jure Zupan. Low energy probes of PeV scale sfermions. *Journal of High Energy Physics*, 2013(11):202, November 2013.

[5] Aviv Amirav, Uzi Even, and Joshua Jortner. Absorption spectroscopy of ultracold large molecules in planar supersonic expansions. *Chemical Physics Letters*, 83(1):1–4, 1981.

[6] David T Anderson, Scott Davis, Timothy S Zwier, and David J Nesbitt. An intense slit discharge source of jet-cooled molecular ions and radicals (T_{rot} <30 K). *Chemical Physics Letters*, 258(1-2):207–212, 1996.

[7] James B Anderson. Separation of Gas Mixtures in Free Jets. *AlChE Journal*, 13(6):1188–1192, 1967.

[8] M H Anderson, J R Ensher, M R Matthews, C E Wieman, and E A Cornell. Observation of Bose-Einstein Condensation in a Dilute Atomic Vapor. *Science*, 269:198, 1995.

[9] A André, D DeMille, J M Doyle, M D Lukin, S E Maxwell, P Rabl, R J Schoelkopf, and P Zoller. A coherent all-electrical interface between polar molecules and mesoscopic superconducting resonators. *Nat. Phys.*, 2:636, 2006.

[10] H Ashkenas and F S Sherman. *The Structure and Utilization of Supersonic Free Jets in Low Density Wind Tunnels*, pages 84–105. Academic Press, 1966.

[11] P Balakrishna, B P Varma, T S Krishnan, T R R Mohan, P Ramakrishnan, and Nuclear Fuel Complex. Low-temperature sintering of thoria. *Journal of Materials Science Letters*, 7(6):657–660, June 1988.

[12] C D Ball and F C De Lucia. Direct observation of Λ-doublet and hyperfine branching ratios for rotationally inelastic collisions of NO-He at 4.2 K. *Chem. Phys. Lett.*, 300(1-2):227, 1999.

[13] Christopher D Ball, Frank C De Lucia, and Frank C De Lucia. Direct Measurement of Rotationally Inelastic Cross Sections at Astrophysical and Quantum Collisional Temperatures. *Phys. Rev. Lett.*, 81:305, 1998.

[14] J R Barber. Thermoelasticity. In *Elasticity*, chapter 14, pages 201–205. Kluwer Academic Publishers, 2nd edition, 2002.

[15] L M Barkov and M Zolotorev. Observation of parity non-conservation in atomic transitions. *JETP Lett.*, 26:379–383, 1978.

[16] Jacob Baron, Wesley C Campbell, D Demille, John M Doyle, Gerald Gabrielse, Yulia V Gurevich, Paul W Hess, Nicholas R Hutzler, Emil Kirilov, Ivan Kozyryev, Brendon R. O'Leary, Cristian D Panda, M. F. Parsons, Elizabeth S Petrik, Ben Spaun, Amar C Vutha, and Adam D West. Order of Magnitude Smaller Limit on the Electric Dipole Moment of the Electron. *Science*, 343(6168):269–272, January 2014.

[17] S.M. Barr. A Review of CP Violation in Atoms. *International Journal of Modern Physics A*, 08(02):209–236, January 1993.

[18] J F Barry, E S Shuman, and D DeMille. A bright, slow cryogenic molecular beam source for free radicals. *Physical chemistry chemical physics : PCCP*, 13(42):18936–47, November 2011.

[19] J. F. Barry, E. S. Shuman, E. B. Norrgard, and D. DeMille. Laser Radiation Pressure Slowing of a Molecular Beam. *Physical Review Letters*, 108(10):103002, March 2012.

[20] R Benz. Thorium-thorium dioxide phase equilibria. *Journal of Nuclear Materials*, 29(1):43–49, January 1969.

[21] S V Berdyugina and S K Solanki. The molecular Zeeman effect and diagnostics of solar and stellar magnetic fields. *Astronomy and Astrophysics*, 385(2):701–715, April 2002.

[22] K Bergmann, H Theuer, and B W Shore. Coherent population transfer among quantum states of atoms and molecules. *Rev. Mod. Phys.*, 70(3):1003, 1998.

[23] J. Beringer, J. F. Arguin, R. M. Barnett, K. Copic, O. Dahl, D. E. Groom, C. J. Lin, J. Lys, H. Murayama, C. G. Wohl, W. M. Yao, P. A. Zyla, C. Amsler, M. Antonelli, D. M. Asner, H. Baer, H. R. Band, T. Basaglia, C. W. Bauer, J. J. Beatty, V. I. Belousov, E. Bergren, G. Bernardi, W. Bertl, S. Bethke, H. Bichsel, O. Biebel, E. Blucher, S. Blusk, G. Brooijmans, O. Buchmueller, R. N. Cahn, M. Carena, A. Ceccucci, D. Chakraborty, M. C. Chen, R. S. Chivukula, G. Cowan, G. D'Ambrosio, T. Damour, D. de Florian, A. de Gouvêa, T. De-Grand, P. de Jong, G. Dissertori, B. Dobrescu, M. Doser, M. Drees, D. A. Edwards, S. Eidelman, J. Erler, V. V. Ezhela, W. Fetscher, B. D. Fields, B. Foster, T. K. Gaisser, L. Garren, H. J. Gerber, G. Gerbier, T. Gherghetta, S. Golwala, M. Goodman, C. Grab, A. V. Gritsan, J. F. Grivaz, M. Grünewald, A. Gurtu, T. Gutsche, H. E. Haber, K. Hagiwara, C. Hagmann, C. Hanhart, S. Hashimoto, K. G. Hayes, M. Heffner, B. Heltsley, J. J. Hernández-Rey, K. Hikasa, A. Höcker, J. Holder, A. Holtkamp, J. Huston, J. D. Jackson, K. F. Johnson, T. Junk, D. Karlen, D. Kirkby, S. R. Klein, E. Klempt, R. V. Kowalewski, F. Krauss, M. Kreps, B. Krusche, Yu. V. Kuyanov, Y. Kwon, O. Lahav, J. Laiho, P. Langacker, A. Liddle, Z. Ligeti, T. M. Liss, L. Littenberg, K. S. Lugovsky, S. B. Lugovsky, T. Mannel, A. V. Manohar, W. J. Marciano, A. D. Martin, A. Masoni, J. Matthews, D. Milstead, R. Miquel, K. Mönig, F. Moortgat, K. Nakamura, M. Narain, P. Nason, S. Navas, M. Neubert, P. Nevski, Y. Nir, K. A. Olive, L. Pape, J. Parsons, C. Patrignani, J. A. Peacock, S. T. Petcov, A. Piepke, A. Pomarol, G. Punzi, A. Quadt, S. Raby, G. Raffelt, B. N. Ratcliff, P. Richardson, S. Roesler, S. Rolli, A. Romaniouk, L. J. Rosenberg, J. L. Rosner, C. T. Sachrajda, Y. Sakai, G. P. Salam, S. Sarkar, F. Sauli, O. Schneider, K. Scholberg, D. Scott, W. G. Seligman, M. H. Shaevitz, S. R. Sharpe, M. Silari, T. Sjöstrand, P. Skands, J. G. Smith, G. F. Smoot, S. Spanier, H. Spieler, A. Stahl, T. Stanev, S. L. Stone, T. Sumiyoshi, M. J. Syphers, F. Takahashi, M. Tanabashi, J. Terning, M. Titov, N. P. Tkachenko, N. A. Törnqvist, D. Tovey, G. Valencia, K. van Bibber, G. Venanzoni, M. G. Vincter, P. Vogel, A. Vogt, W. Walkowiak, C. W. Walter, D. R. Ward, T. Watari, G. Weiglein, E. J. Weinberg, L. R. Wiencke, L. Wolfenstein, J. Womersley, C. L. Woody, R. L. Workman, A. Yamamoto, G. P. Zeller, O. V. Zenin, J. Zhang, R. Y. Zhu, G. Harper, V. S. Lugovsky, and P. Schaffner. Review of Particle Physics. *Physical Review D*, 86(1):010001, July 2012.

[24] W Bernreuther and M Suzuki. The electric dipole moment of the electron. *Reviews of Modern Physics*, 63(2):313, 1991.

[25] H L Bethlem and G Meijer. Production and application of translationally cold molecules. *Int. Rev. Phys. Chem.*, 22(1):73, 2003.

[26] Hendrick L Bethlem, Giel Berden, Floris M H Crompvoets, Rienk T Jongma, Andre J A VanRoij, G Meijer, Berden G., Jongma R T., and vanRoij A. J. A. Electrostatic trapping of ammonia molecules. *Nature*, 406(August):491–494, August 2000.

[27] Hendrick L Bethlem, Floris M H Crompvoets, Rienk T Jongma, Sebastiaan Y T van de Meerakker, and Gerard Meijer. Deceleration and trapping of ammonia using time-varying electric fields. *Physical Review A*, 65(5):053416, May 2002.

[28] Philip R. Bevington and D. Keith Robinson. *Data reduction and error analysis for the physical sciences*. McGraw-Hill, Boston, 3rd edition, 2003.

[29] S Bickman, P Hamilton, Y Jiang, and D DeMille. Preparation and detection of states with simultaneous spin alignment and selectable molecular orientation in PbO. *Physical Review A*, 80:023418, August 2009.

[30] S Blatt, A Ludlow, G Campbell, J Thomsen, T Zelevinsky, M Boyd, J Ye, X Baillard, M Fouché, R Le Targat, A Brusch, P Lemonde, M Takamoto, F.-L. Hong, H Katori, and V Flambaum. New Limits on Coupling of Fundamental Constants to Gravity Using ^{87}Sr Optical Lattice Clocks. *Physical Review Letters*, 100(14):140801, April 2008.

[31] Annette Böckenhoff and Joachim Hartung. Some Corrections of the Significance Level in Meta-Analysis. *Biometrical Journal*, 40(8):937–947, December 1998.

[32] A Von Bornstedt and G Edvinsson. Rotational Analysis of two Mutually Interacting Electronic States of $^1\Pi$ Character in ThO. *Physica Scripta*, 2(4-5):205–210, October 1970.

[33] A Von Bornstedt, G Edvinsson, A Lagerqvist, and I Renhorn. The Spectrum of ThO: Rotational Analysis of the $L^1\Pi - X^1\Sigma^+$ and $N^1\Pi - X^1\Pi^+$ Systems. *Physica Scripta*, 20(5-6):599–602, November 1979.

[34] M A Bouchiat and C C Bouchiat. Weak Neutral Currents in Atomic Physics. *Physics Letters*, 48B(2):111–114, 1974.

[35] Robert W. Boyd. *Nonlinear Optics*. Elsevier, 2008.

[36] J Brown and A Carrington. *Rotational Spectroscopy of Diatomic Molecules*. Cambridge University Press, 2003.

[37] J.M Brown, A.S-C Cheung, and A.J Merer. Λ-Type doubling parameters for molecules in Δ electronic states. *Journal of Molecular Spectroscopy*, 124(2):464–475, August 1987.

[38] J.M. Brown, M. Kaise, C.M.L. Kerr, and D.J. Milton. A determination of fundamental Zeeman parameters for the OH radical. *Molecular Physics*, 36(2):553–582, August 1978.

[39] John M Brown, Helga Körsgen, Stuart P Beaton, and Kenneth M Evenson. The rotational and fine-structure spectrum of FeH, studied by far-infrared laser magnetic resonance. *The Journal of chemical physics*, 124(23):234309, June 2006.

[40] Richard M. Brugger. A Note on Unbiased Estimation of the Standard Deviation. *The American Statistician*, 23(4):32–32, October 1969.

[41] A A Buchachenko. Communication: Electric properties of the ThO($^1X^+$) molecule. *The Journal of Chemical Physics*, 133(4):41102, 2010.

[42] Dmitry Budker, Derek Kimball, and David DeMille. *Atomic physics: An exploration through problems and solutions*. Oxford University Press, USA, 2008.

[43] N E Bulleid, S M Skoff, R J Hendricks, B E Sauer, E A Hinds, and M R Tarbutt. Characterization of a cryogenic beam source for atoms and molecules. *Physical chemistry chemical physics : PCCP*, 15(29):12299–307, August 2013.

[44] R. Campargue. Progress in overexpanded supersonic jets and skimmed molecular beams in free-jet zones of silence. *J. Phys. Chem.*, 88(20):4466, September 1984.

[45] Wesley Campbell, Gerrit Groenenboom, Hsin-I Lu, Edem Tsikata, and John Doyle. Time-Domain Measurement of Spontaneous Vibrational Decay of Magnetically Trapped NH. *Physical Review Letters*, 100(8):83003, February 2008.

[46] Wesley C Campbell and John M Doyle. Cooling, Trap Loading, and Beam Production Using a Cryogenic Helium Buffer Gas. In Roman V Krems, W C Stwalley, and B Friedrich, editors, *Cold molecules: theory, experiment, applications*, chapter 13, pages 473–508. CRC Press, 2009.

[47] Wesley C Campbell, Timur V Tscherbul, Hsin-I Lu, Edem Tsikata, Roman V Krems, and John M Doyle. Mechanism of Collisional Spin Relaxation in $^3\Sigma$ Molecules. *Phys. Rev. Lett.*, 102:13003, 2009.

[48] Lincoln D Carr, David Demille, Roman V Krems, and Jun Ye. Cold and ultracold molecules: science, technology and applications. *New J. Phys.*, 11(5):55049, May 2009.

[49] Raymond J. Carroll, David Ruppert, and Leonard A. Stefanski. *Measurement Error in Nonlinear Models*. CRC Press, 1995.

[50] B N Chichkov, C Momma, S Nolte, F von Alvensleben, and A Tunnermann. Femtosecond, picosecond and nanosecond laser ablation of solids. *Appl. Phys. A*, 63:109–115, 1996.

[51] C Chin, M Bartenstein, A Altmeyer, S Riedl, S Jochim, J Hecker Denschlag, and R Grimm. Observation of the pairing gap in a strongly interacting Fermi gas. *Science*, 305:1128, 2004.

[52] C Chin, V V Flambaum, and M G Kozlov. Ultracold molecules: new probes on the variation of fundamental constants. *New Journal of Physics*, 11(5):55048, May 2009.

[53] W. G. Cochran. Problems Arising in the Analysis of a Series of Similar Experiments. *Supplement to the Journal of the Royal Statistical Society*, 4(1):102–118, 1937.

[54] E Commins. Electric Dipole Moments of Leptons. *Advances in Atomic, Molecular, and Optical Physics*, 40:1–55, 1999.

[55] E D Commins and D DeMille. The Electric Dipole Moment of the Electron. In B L Roberts and W J Marciano, editors, *Lepton Dipole Moments*, chapter 14, pages 519–581. World Scientific, 2010.

[56] Eugene D. Commins. Berrys geometric phase and motional fields. *American Journal of Physics*, 59(12):1077, 1991.

[57] Eugene D Commins, J D Jackson, and David P DeMille. The electric dipole moment of the electron: An intuitive explanation for the evasion of Schiffs theorem. *American Journal of Physics*, 75(6):532, 2007.

[58] R Conti, P Bucksbaum, S Chu, E Commins, L. Hunter, and L Hunter. Preliminary Observation of Parity Nonconservation in Atomic Thallium. *Physical Review Letters*, 42(6):343–346, 1979.

[59] Corning. Corning 7980 Fused Silica Datasheet. Technical report, 2003.

[60] J P Coughlin. Heats and Free Energies of Formation of Inorganic Oxides. *Bulletin of the Bureau of Mines*, (542), 1954.

[61] J. H. Curtiss. On the Distribution of the Quotient of Two Chance Variables. *The Annals of Mathematical Statistics*, 12(4):409–421, December 1941.

[62] James W. Dally and William F. Riley. Theory of Photoelasticity. In *Experimental Stress Analysis*, chapter 13, pages 406–412. McGraw-Hill, 2nd edition, 1978.

[63] G M Davis, M C Gower, C Fotakis, T Efthimiopoulos, and P Argyrakis. Spectroscopic studies of ArF laser photoablation of PMMA. *Appl. Phys. A*, 36(1):27, 1985.

[64] K B Davis, M.-O. Mewes, M R Andrews, N J van Druten, D S Durfee, D M Kurn, and W Ketterle. Bose-Einstein Condensation in a Gas of Sodium Atoms. *Phys. Rev. Lett.*, 75:3969, 1995.

[65] R DeCarvalho, J M Doyle, B Friedrich, T Guillet, J Kim, D Patterson, and J D Weinstein. Buffer-gas loaded magnetic traps for atoms and molecules: A primer. *Eur. Phys. J. D*, 7(3):289, 1999.

[66] D DeMille. Quantum Computation with Trapped Polar Molecules. *Phys. Rev. Lett.*, 88(6):67901, January 2002.

[67] D. DeMille, F. Bay, S Bickman, D. Kawall, L. Hunter, D. Krause, S. Maxwell, and K. Ulmer. Search for the electric dipole moment of the electron using metastable PbO. In *AIP Conference Proceedings*, volume 596, pages 72–83. AIP, 2001.

[68] D DeMille, F Bay, S Bickman, D Kawall, D Krause, S Maxwell, and L Hunter. Investigation of PbO as a system for measuring the electric dipole moment of the electron. *Physical Review A*, 61(5):52507, April 2000.

[69] D DeMille, S B Cahn, D Murphree, D a. Rahmlow, and M G Kozlov. Using Molecules to Measure Nuclear Spin-Dependent Parity Violation. *Phys. Rev. Lett.*, 100(2):23003, January 2008.

[70] D DeMille, S Sainis, J Sage, T Bergeman, S Kotochigova, and E Tiesinga. Enhanced Sensitivity to Variation of m_e/m_p in Molecular Spectra. *Physical Review Letters*, 100:43202, 2008.

[71] C T Dewberry, K C Etchison, and S A Cooke. The pure rotational spectrum of the actinide-containing compound thorium monoxide. *Physical Chemistry Chemical Physics*, 9(35):4895–4897, 2007.

[72] T G Dietz, M A Duncan, D E Powers, and R E Smalley. Laser production of supersonic metal cluster beams. *The Journal of Chemical Physics*, 74(11):6511, 1981.

[73] Michael Dine and Alexander Kusenko. Origin of the matter-antimatter asymmetry. *Reviews of Modern Physics*, 76(January):1–30, 2004.

[74] J. Doyle, B. Friedrich, R. V. Krems, and F. Masnou-Seeuws. Editorial: Quo vadis, cold molecules? *Eur. Phys. J. D*, 31(2):149, November 2004.

[75] V A Dzuba and V V Flambaum. Current trends in searches for new physics using measurements of parity violation and electric dipole moments in atoms and molecules. *arXiv:1009.4960v2*, 2010.

[76] V. A. Dzuba, V. V. Flambaum, and C. Harabati. Relations between matrix elements of different weak interactions and interpretation of the parity-nonconserving and electron electric-dipole-moment measurements in atoms and molecules. *Physical Review A*, 84(5):052108, November 2011.

[77] S. Eckel, P. Hamilton, E. Kirilov, H. W. Smith, and D. DeMille. Search for the electron electric dipole moment using Ω-doublet levels in PbO. *Physical Review A*, 87(5):052130, May 2013.

[78] G Edvinsson, A Bornstedt, and P Nylén. Rotational Analysis for a Perturbed $^1\Pi$ state in ThO. *Ark. Phys.*, 38:193, 1968.

[79] G Edvinsson and A Lagerqvist. Rotational analysis of yellow and near infrared bands in ThO. *Physica Scripta*, 30(5):309–320, 1984.

[80] G Edvinsson and A Lagerqvist. A low-lying $\Omega = 2$ state in the ThO molecule. *J. Mol. Spectrosc.*, 113:93, 1985.

[81] G Edvinsson and A Lagerqvist. Rotational Analysis of two Red Band Systems in the ThO Spectrum. *Physica Scripta*, 32(6):602–610, December 1985.

[82] G Edvinsson and A Lagerqvist. Two new band systems in ThO. *Physica Scripta*, 41:316–320, 1990.

[83] G Edvinsson, L.-E. Selin, and N Aslund. On the band spectrum of ThO. *Ark. Phys.*, 30(22):283–319, 1965.

[84] Gunnar Edvinsson and Albin Lagerqvist. Rotational analysis of some violet and green bands in the ThO spectrum. *Journal of Molecular Spectroscopy*, 122(2):428–439, April 1987.

[85] Gunnar Edvinsson and Albin Lagerqvist. Two band systems of ThO in the near ultraviolet. *Journal of Molecular Spectroscopy*, 128(1):117–125, March 1988.

[86] Shlomo Eisenbach, Haim Lotem, Zvi Horvitz, G Miron, Mordechai Lando, and Shimon Gabay. Thermally induced window birefringence in high power copper vapor laser. *Proc. SPIE 1972, 8th Meeting on Optical Engineering in Israel*, 1972:13–26, 1992.

[87] Jonathan Engel, Michael J. Ramsey-Musolf, and U. van Kolck. Electric dipole moments of nucleons, nuclei, and atoms: The Standard Model and beyond. *Progress in Particle and Nuclear Physics*, 71:21–74, July 2013.

[88] U. Even, J. Jortner, D. Noy, N. Lavie, and C. Cossart-Magos. Cooling of large molecules below 1 K and He clusters formation. *J. Chem. Phys.*, 112:8068, 2000.

[89] JiJi Fan and Matthew Reece. Probing charged matter through $h \to \gamma\gamma$, gamma ray lines, and EDMs. *Journal of High Energy Physics*, 2013(6):4, June 2013.

[90] Gary J. Feldman and Robert D. Cousins. Unified approach to the classical statistical analysis of small signals. *Physical Review D*, 57(7):3873–3889, April 1998.

[91] J Fernandez De La Mora and J Rosell-Llompart. Aerodynamic focusing of heavy molecules in seeded supersonic jets. *J. Chem. Phys.*, 91(4):2603–2615, 1989.

[92] V Flambaum and M Kozlov. Enhanced Sensitivity to the Time Variation of the Fine-Structure Constant and m_p/m_e in Diatomic Molecules. *Physical Review Letters*, 99(15):1–4, October 2007.

[93] V Flambaum and M Kozlov. Limit on the Cosmological Variation of m_p/m_e from the Inversion Spectrum of Ammonia. *Physical Review Letters*, 98(24):240801, June 2007.

[94] V V Flambaum and I V B Khriplovich. On the enhancement of parity nonconserving effects in diatomic molecules. *Physics Letters*, 110A(3):121–125, 1985.

[95] V V Flambaum and M G Kozlov. Variation of Fundamental Constants as Revealed by Molecules. In *Cold molecules: theory, experiment, applications*, pages 597–625. Taylor and Francis, 2009.

[96] D A Fletcher, K Y Jung, C T Scurlock, and T C Steimle. Molecular beam pump/probe microwave-optical double resonance using a laser ablation source. *The Journal of Chemical Physics*, 98(3):1837, 1993.

[97] C J Foot. *Atomic Physics*. Oxford University Press, USA, 2005.

[98] R Fox and A McDonald. *Introduction to Fluid Mechanics*. John Wiley and Sons, 1998.

[99] Frank Pobell. *Matter and Methods at Low Temperatures*. Springer-Verlag, 1996.

[100] Bretislav Friedrich and John M Doyle. Why are Cold Molecules so Hot? *ChemPhysChem*, 10:604, 2009.

[101] A. F. Gerds and M. W. Mallett. Surface Reaction between Oxygen and Thorium. *Journal of The Electrochemical Society*, 101(4):171, 1954.

[102] R. M. Gilgenbach, C. H. Ching, J. S. Lash, and R. A. Lindley. Laser diagnostic experiments on KrF laser ablation plasma-plume dynamics relevant to manufacturing applications. *Phys. Plasmas*, 1(5):1619, 1994.

[103] Joop J Gilijamse, Steven Hoekstra, Sebastiaan Y T van de Meerakker, Gerrit C Groenenboom, and Gerard Meijer. Near-Threshold Inelastic Collisions Using Molecular Beams with a Tunable Velocity. *Science*, 313:1617, 2006.

[104] J S M Ginges and V V Flambaum. Violations of fundamental symmetries in atoms and tests of unification theories of elementary particles. *Phys. Rep.*, 397(2):63, July 2004.

[105] Vasiliy Goncharov, Jiande Han, Leonid A Kaledin, and Michael C Heaven. Ionization energy measurements and electronic spectra for ThO. *J. Chem. Phys.*, 122(20):204311, May 2005.

[106] Jeffrey A Gray, Mingguang Li, and Robert W Field. Zeeman spectroscopy and deperturbation of the low-lying states of NiH. *The Journal of Chemical Physics*, 92(8):4651, 1990.

[107] M Greiner, O Mandel, T Esslinger, T W Hänsch, and I Bloch. Quantum Phase Transition from a Superfluid to a Mott Insulator in a Gas of Ultracold Atoms. *Nature*, 415:39, 2002.

[108] W Griffith, M Swallows, T Loftus, M Romalis, B Heckel, and E Fortson. Improved Limit on the Permanent Electric Dipole Moment of 199Hg. *Physical Review Letters*, 102(10):101601, March 2009.

[109] David Griffiths. *Introduction to Elementary Particles*. John Wiley & Sons, 1987.

[110] J Guèna, M Lintz, M.-A. A Bouchiat, and J Guena. Atomic Parity Violation: Principles, Recent Results, Present Motivations. *Modern Physics Letters A*, 20(6):375–389, 2005.

[111] H. J. Metcalf and P. van der Straten. *Laser Cooling and Trapping*. Springer-Verlag, 1999.

[112] D. Hanneke, S. Fogwell, and G. Gabrielse. New Measurement of the Electron Magnetic Moment and the Fine Structure Constant. *Physical Review Letters*, 100(12):120801, March 2008.

[113] Kenneth D. Harris, Andy C. van Popta, Jeremy C. Sit, Dirk J. Broer, and Michael J. Brett. A Birefringent and Transparent Electrical Conductor. *Advanced Functional Materials*, 18(15):2147–2153, August 2008.

[114] Joachim Hartung, Guido Knapp, and Bimal K. Sinha. *Statistical Meta-Analysis with Applications*. Wiley-Interscience, 2008.

[115] J B Hasted. *Physics of Atomic Collisions*. Elsevier, 1972.

[116] A Hatakeyama, K Enomoto, N Sugimoto, and T Yabuzaki. Atomic alkali-metal gas cells at liquid-helium temperatures: Loading by light-induced atom desorption. *Phys. Rev. A*, 65(2):22904, January 2002.

[117] G Herzberg. *Molecular Spectra and Molecular Structure: Spectra of Diatomic Molecules , 2nd ed.* Krieger, 1989.

[118] D. L. Hildenbrand. Mass spectrometric studies of gaseous ThO and ThO_2. *The Journal of Chemical Physics*, 61(3):1232, 1974.

[119] Matthias Hillenkamp, Sharon Keinan, and Uzi Even. Condensation limited cooling in supersonic expansions. *The Journal of Chemical Physics*, 118(19):8699, 2003.

[120] D. V. Hinkley. On the ratio of two correlated normal random variables. *Biometrika*, 56(3):635–639, 1969.

[121] Ian Hodgkinson, Qi Hong Wu, and Simon Collett. Dispersion Equations for Vacuum-Deposited Tilted-Columnar Biaxial Media. *Applied Optics*, 40(4):452, 2001.

[122] F Hoogeveen. The standard model prediction for the electric dipole moment of the electron. *Nuclear Physics B*, 341(2):322–340, September 1990.

[123] J. B. Hopkins, P. R. R. Langridge-Smith, M. D. Morse, and R. E. Smalley. Supersonic metal cluster beams of refractory metals : Spectral investigations of ultracold Mo_2. *The Journal of Chemical Physics*, 78(4):1627, 1983.

[124] Eric R Hudson, H J Lewandowski, Brian C Sawyer, and Jun Ye. Cold Molecule Spectroscopy for Constraining the Evolution of the Fine Structure Constant. *Physical Review Letters*, 96(14):143004, April 2006.

[125] J Hudson, B Sauer, M Tarbutt, and E Hinds. Measurement of the Electron Electric Dipole Moment Using YbF Molecules. *Physical Review Letters*, 89(2):8–11, June 2002.

[126] J J Hudson, D M Kara, I J Smallman, B E Sauer, M R Tarbutt, and E A Hinds. Improved measurement of the shape of the electron. *Nature*, 473(7348):493–6, May 2011.

[127] Matthew Hummon, Wesley Campbell, Hsin-I Lu, Edem Tsikata, Yihua Wang, and John Doyle. Magnetic trapping of atomic nitrogen (^{14}N) and cotrapping of NH ($X^3\Sigma$). *Physical Review A*, 78(5):50702, November 2008.

[128] Matthew T. Hummon, Mark Yeo, Benjamin K. Stuhl, Alejandra L. Collopy, Yong Xia, and Jun Ye. 2D Magneto-Optical Trapping of Diatomic Molecules. *Physical Review Letters*, 110(14):143001, April 2013.

[129] Nicholas R. Hutzler, Hsin-I Lu, and John M. Doyle. The buffer gas beam: an intense, cold, and slow source for atoms and molecules. *Chemical Reviews*, 112(9):4803–27, September 2012.

[130] Nicholas R Hutzler, Maxwell F Parsons, Yulia V Gurevich, Paul W Hess, Elizabeth Petrik, Ben Spaun, Amar C Vutha, David DeMille, Gerald Gabrielse, and John M Doyle. A cryogenic beam of refractory, chemically reactive molecules with expansion cooling. *Physical chemistry chemical physics : PCCP*, 13(42):18976–85, November 2011.

[131] T. Isaev, S. Hoekstra, and R. Berger. Laser-cooled RaF as a promising candidate to measure molecular parity violation. *Physical Review A*, 82(5):052521, November 2010.

[132] Monwhea Jeng. A selected history of expectation bias in physics. *American Journal of Physics*, 74(7):578, 2006.

[133] Martin Jung. A robust limit for the electric dipole moment of the electron. *Journal of High Energy Physics*, 2013(5):168, May 2013.

[134] T. Junglen, T. Rieger, S. A. Rangwala, P. W. H. Pinkse, G. Rempe, and P W H Pinske. Slow ammonia molecules in an electrostatic quadrupole guide. *Eur. Phys. J. D*, 31(2):365, November 2004.

[135] D M Kara, I J Smallman, J J Hudson, B E Sauer, M R Tarbutt, and E A Hinds. Measurement of the electron's electric dipole moment using YbF molecules: methods and data analysis. *New Journal of Physics*, 14(10):103051, October 2012.

[136] Leonard I. Katzin. Concerning a Lower Oxide of Thorium and Related Compounds of the Last Row Elements. *J. Am. Chem. Soc.*, 80(22):5908–5910, 1938.

[137] D. Kawall, F. Bay, S. Bickman, Y. Jiang, and D. DeMille. Progress towards measuring the electric dipole moment of the electron in metastable PbO. In *AIP Conference Proceedings*, volume 698, pages 192–195. AIP, 2004.

[138] Timothy Keller and Ingram Olkin. Combining correlated unbiased estimators of the mean of a normal distribution. *Institute of Mathematical Statistics Lecture Notes Monograph Series*, 45:218–227, 2004.

[139] I B Khriplovich. *Parity Nonconservation in Atomic Phenomena*. CRC Press, 1991.

[140] Iosif B Khriplovich and Steve K Lamoreaux. *CP Violation Without Strangeness*. Springer, 1997.

[141] J Kim. *Buffer-gas Loading and Magnetic Trapping of Atomic Europium*. PhD thesis, Harvard University, 1997.

[142] E. Kirilov, W. C. Campbell, J. M. Doyle, G. Gabrielse, Y. V. Gurevich, P. W. Hess, N. R. Hutzler, B. R. O'Leary, E. Petrik, B. Spaun, A. C. Vutha, and D. DeMille. Shot-noise-limited spin measurements in a pulsed molecular beam. *Physical Review A*, 88(1):013844, July 2013.

[143] W Klemperer. Interstellar chemistry. *Proc. Nat. Acad. Sci.*, 103:12232, 2006.

[144] W Koechner. Thermal Lensing in a Nd:YAG Laser Rod. *Applied optics*, 9(11):2548–2553, November 1970.

[145] István Kovács. *Rotational Structure in the Spectra of Diatomic Molecules*. American Elsevier, New York, NY, 1969.

[146] M. Kozlov and D. DeMille. Enhancement of the Electric Dipole Moment of the Electron in PbO. *Physical Review Letters*, 89(13):133001, September 2002.

[147] M G Kozlov and L N Labzowsky. Parity violation effects in diatomics. *Journal of Physics B: Atomic, Molecular and Optical Physics*, 28(10):1933–1961, May 1995.

[148] R V Krems. Cold controlled chemistry. *Phys. Chem. Chem. Phys.*, 10:4079, 2008.

[149] Roman V Krems, W C Stwalley, and B Friedrich. *Cold molecules: Theory, experiment, applications*. CRC Press, 2009.

[150] S G Krishnamurty. The Band Systems of Thorium Oxide and Hafnium Oxide. *Proceedings of the Physical Society. Section A*, 64(9):852–852, September 1951.

[151] W Kuchle, M Dolg, H Stoll, H Preuss, W Kikhle, and H Stall. Energy-adjusted pseudopotentials for the actinides. Parameter sets and test calculations for thorium and thorium monoxide. *J. Chem. Phys.*, 100(10):7535–7542, 1994.

[152] L N Labzovskii. Lambda doubling and parity-nonconservation effects in spectra of diatomic molecules. *Sov. Phys. JETP*, 48(3):434–439, 1978.

[153] T Lahaye, C Menotti, L Santos, M Lewenstein, and and T. Pfau. The physics of dipolar bosonic quantum gases. *Rep. Prog. Phys.*, 72:126401, 2009.

[154] J Lee, J Chen, L V Skripnikov, A N Petrov, A V Titov, N S Mosyagin, and A E Leanhardt. Optical spectroscopy of tungsten carbide for uncertainty analysis in electron electric-dipole-moment search. *Physical Review A*, 87(2):022516, February 2013.

[155] J Lee, E R Meyer, R Paudel, J L Bohn, and A E Leanhardt. An electron electric dipole moment search in the $X^3\Delta_1$ ground state of tungsten carbide molecules. *Journal of Modern Optics*, 56(18-19):2005–2012, 2009.

[156] J. Lees, V Poireau, V Tisserand, J. Garra Tico, E Grauges, A Palano, G Eigen, B Stugu, D. Brown, L. Kerth, Yu. Kolomensky, G Lynch, H Koch, T Schroeder, D. Asgeirsson, C Hearty, T. Mattison, J. McKenna, R. So, A Khan, V. Blinov, A. Buzykaev, V. Druzhinin, V. Golubev, E. Kravchenko, A. Onuchin, S. Serednyakov, Yu. Skovpen, E. Solodov, K. Todyshev, A. Yushkov, M. Bondioli, D. Kirkby, A. Lankford, M. Mandelkern, H. Atmacan, J. Gary, F. Liu, O. Long, G. Vitug, C. Campagnari, T. Hong, D. Kovalskyi, J. Richman, C. West, A. Eisner, J. Kroseberg, W. Lockman, A. Martinez, B. Schumm, A. Seiden, D. Chao, C. Cheng, B. Echenard, K. Flood, D. Hitlin, P. Ongmongkolkul, F. Porter, A. Rakitin, R. Andreassen, Z. Huard, B. Meadows, M. Sokoloff, L. Sun, P. Bloom, W. Ford, A. Gaz, U. Nauenberg, J. Smith, S. Wagner, R. Ayad, W. Toki, B. Spaan, K. Schubert, R. Schwierz, D. Bernard, M. Verderi, P. Clark, S. Playfer, D. Bettoni, C. Bozzi, R. Calabrese, G. Cibinetto, E. Fioravanti, I. Garzia, E. Luppi, M. Munerato, L. Piemontese, V. Santoro, R. Baldini-Ferroli, A. Calcaterra, R. de Sangro, G. Finocchiaro, P. Patteri, I. Peruzzi, M. Piccolo, M. Rama, A. Zallo, R. Contri, E. Guido, M. Lo Vetere, M. Monge, S. Passaggio, C. Patrignani, E. Robutti, B. Bhuyan, V. Prasad, C. Lee, M. Morii, A. Edwards, A. Adametz, U. Uwer, H. Lacker, T. Lueck, P. Dauncey, U. Mallik, C. Chen, J. Cochran, W. Meyer, S. Prell, A. Rubin, A. Gritsan, Z. Guo, N. Arnaud, M. Davier, D. Derkach, G. Grosdidier, F. Le Diberder, A. Lutz, B. Malaescu, P. Roudeau, M. Schune, A. Stocchi, G. Wormser, D. Lange, D. Wright, C. Chavez, J. Coleman, J. Fry, E. Gabathuler, D. Hutchcroft, D. Payne, C. Touramanis, A. Bevan, F. Di Lodovico, R. Sacco, M. Sigamani, G. Cowan, C. Davis, A. Denig, M. Fritsch, W. Gradl, K. Griessinger, A. Hafner, E. Prencipe, R. Barlow, G. Jackson, G. Lafferty, E. Behn, R. Cenci, B. Hamilton, A. Jawahery, D. Roberts, C. Dallapiccola, R. Cowan, D. Dujmic, G. Sciolla, R. Cheaib, D. Lindemann, P. Patel, S. Robertson, P. Biassoni, N. Neri, F. Palombo, S. Stracka, L. Cremaldi,

R. Godang, R. Kroeger, P. Sonnek, D. Summers, X. Nguyen, M. Simard, P. Taras, G. De Nardo, D. Monorchio, G. Onorato, C. Sciacca, M. Martinelli, G. Raven, C. Jessop, J. LoSecco, W. Wang, K. Honscheid, R. Kass, J. Brau, R. Frey, N. Sinev, D. Strom, E. Torrence, E. Feltresi, N. Gagliardi, M. Margoni, M. Morandin, A. Pompili, M. Posocco, M. Rotondo, G. Simi, F. Simonetto, R. Stroili, S. Akar, E. Ben-Haim, M. Bomben, G. Bonneaud, H. Briand, G. Calderini, J. Chauveau, O. Hamon, Ph. Leruste, G. Marchiori, J. Ocariz, S. Sitt, M. Biasini, E. Manoni, S. Pacetti, A. Rossi, C. Angelini, G. Batignani, S. Bettarini, M. Carpinelli, G. Casarosa, A. Cervelli, F. Forti, M. Giorgi, A. Lusiani, B. Oberhof, E. Paoloni, A. Perez, G. Rizzo, J. Walsh, D. Lopes Pegna, J. Olsen, A. Smith, A. Telnov, F. Anulli, R. Faccini, F. Ferrarotto, F. Ferroni, M. Gaspero, L. Li Gioi, M. Mazzoni, G. Piredda, C. Bünger, O. Grünberg, T. Hartmann, T. Leddig, H. Schröder, C. Voss, R. Waldi, T. Adye, E. Olaiya, F. Wilson, S. Emery, G. Hamel de Monchenault, G. Vasseur, Ch. Yèche, D. Aston, D. Bard, R. Bartoldus, J. Benitez, C. Cartaro, M. Convery, J. Dorfan, G. Dubois-Felsmann, W. Dunwoodie, M. Ebert, R. Field, M. Franco Sevilla, B. Fulsom, A. Gabareen, M. Graham, P. Grenier, C. Hast, W. Innes, M. Kelsey, P. Kim, M. Kocian, D. Leith, P. Lewis, B. Lindquist, S. Luitz, V. Luth, H. Lynch, D. MacFarlane, D. Muller, H. Neal, S. Nelson, M. Perl, T. Pulliam, B. Ratcliff, A. Roodman, A. Salnikov, R. Schindler, A. Snyder, D. Su, M. Sullivan, J. Vavra, A. Wagner, W. Wisniewski, M. Wittgen, H. Wulsin, C. Young, V. Ziegler, W. Park, M. Purohit, R. White, J. Wilson, A. Randle-Conde, S. Sekula, M. Bellis, P. Burchat, T. Miyashita, E. Puccio, M. Alam, J. Ernst, R. Gorodeisky, N. Guttman, D. Peimer, A. Soffer, P. Lund, S. Spanier, J. Ritchie, A. Ruland, R. Schwitters, B. Wray, J. Izen, X. Lou, F. Bianchi, D. Gamba, S. Zambito, L. Lanceri, L. Vitale, J. Bernabeu, F. Martinez-Vidal, A. Oyanguren, P. Villanueva-Perez, H. Ahmed, J. Albert, Sw. Banerjee, F. Bernlochner, H. Choi, G. King, R. Kowalewski, M. Lewczuk, I. Nugent, J. Roney, R. Sobie, N. Tasneem, T. Gershon, P. Harrison, T. Latham, H. Band, S. Dasu, Y. Pan, R. Prepost, and S. Wu. Observation of Time-Reversal Violation in the B^0 Meson System. *Physical Review Letters*, 109(21):211801, November 2012.

[157] H Lefebvre-Brion and R W Field. *The Spectra and Dynamics of Diatomic Molecules.* Elsevier, 2004.

[158] D. H. Levy, L. Wharton, and R. E. Smalley. Laser Spectroscopy in Supersonic Jets. In C B Moore, editor, *Chemical and Biochemical Applications of Lasers*, chapter 1, pages 1–41. Academic Press, 1977.

[159] Kun Li, Raymond S. Fellers, Mark R. Viant, Ryan P. McLaughlin, Mac G. Brown, and Richard J. Saykally. A long path length pulsed slit valve appropriate

for high temperature operation: Infrared spectroscopy of jet-cooled large water clusters and nucleotide bases. *Rev. Sci. Instrum.*, 67:410, 1996.

[160] Yuanzhang Li, Li Shi, and H. Daniel Roth. The bias of the commonly-used estimate of variance in meta-analysis. *Communications in Statistics - Theory and Methods*, 23(4):1063–1085, January 1994.

[161] Christopher M. Lovejoy and David J. Nesbitt. Slit pulsed valve for generation of long-path-length supersonic expansions. *Rev. Sci. Instrum.*, 58(5):807, 1987.

[162] Hsin-I Lu, Julia Rasmussen, Matthew J Wright, Dave Patterson, and John M Doyle. A cold and slow molecular beam. *Physical chemistry chemical physics : PCCP*, 13(42):18986–90, November 2011.

[163] Mei-Ju Lu and Jonathan D Weinstein. Cold TiO-He Collisions. *New Journal of Physics*, 11:055015, 2009.

[164] K Luria, W Christen, and U Even. Generation and propagation of intense supersonic beams. *J. Phys. Chem. A*, 115(25):7362–7, June 2011.

[165] Christel M Marian, U L F Wahlgren, O D D Gropen, and P Pyykko. Bonding and electronic structure in diatomic ThO: quasirelativistic effective core potential calculations. *J. Mol. Struct.*, 169:339, 1987.

[166] F. Martin, R. Bacis, J. Vergès, J. Bachar, and S. Rosenwaks. High resolution Fourier transform spectroscopy of the PbO molecule from investigation of the $O_2(^1\Delta_g)-Pb$ reaction. *Spectrochimica Acta Part A: Molecular Spectroscopy*, 44(9):889–897, January 1988.

[167] S E Maxwell, N Brahms, R DeCarvalho, D R Glenn, J S Helton, S V Nguyen, D Patterson, J Petricka, D DeMille, and J M Doyle. High-Flux Beam Source for Cold, Slow Atoms or Molecules. *Physical Review Letters*, 95(17):173201, October 2005.

[168] Michael C. McCarthy, Hideto Kanamori, Timothy C Steimle, Mingguang Li, and Robert W. Field. Sideband opticaloptical double resonance Zeeman spectroscopy. II. Studies of NiH, PdD, and PtH. *The Journal of Chemical Physics*, 107(11):4179, 1997.

[169] David McKeen, Maxim Pospelov, and Adam Ritz. Modified Higgs branching ratios versus CP and lepton flavor violation. *Physical Review D*, 86(11):113004, December 2012.

[170] Paul Meier. Variance of a Weighted Mean. *Biometrics*, 9(1):59, March 1953.

[171] Lorenzo Mercolli and Christopher Smith. EDM constraints on flavored CP-violating phases. *Nuclear Physics B*, 817(1-2):1–24, August 2009.

[172] J K Messer and Frank C De Lucia. Measurement of Pressure Broadening Parameters for the CO-He System at 4K. *Physical Review Letters*, 53(27):2555, December 1984.

[173] A. Micheli, G. K. Brennen, and P. Zoller. A toolbox for lattice-spin models with polar molecules. *Nat. Phys.*, 2(5):341, April 2006.

[174] Terry A Miller. Alternative Explanation for Anomalous Molecular Parameters from Electron Resonance Experiments. *The Journal of Chemical Physics*, 54(7):3156, 1971.

[175] Michael D Morse. Supersonic Beam Sources. In *Experimental Methods in the Physical Sciences, vol. 29B: Atomic, Molecular, and Optical Physics*, volume 29, Part B, pages 21–47. Academic Press, 1996.

[176] Thomas Nelis, Stuart P. Beaton, Kenneth M. Evenson, and John M Brown. A determination of the molecular parameters for NiH in its $^2\Delta$ ground state by laser magnetic resonance. *Journal of Molecular Spectroscopy*, 148(2):462–478, August 1991.

[177] K-K Ni, S Ospelkaus, M H G de Miranda, A Pe'er, B Neyenhuis, J J Zirbel, S Kotochigova, P S Julienne, D S Jin, and J Ye. A high phase-space-density gas of polar molecules. *Science*, 322(5899):231–235, October 2008.

[178] K.-K. Ni, S Ospelkaus, D Wang, G Quéméner, B Neyenhuis, M H G de Miranda, J L Bohn, J Ye, and D S Jin. Dipolar collisions of polar molecules in the quantum regime. *Nature*, 464(7293):1324–8, April 2010.

[179] D R Olander. Laser-pulse-vaporization of refractory materials. *Pure Appl. Chem.*, 62(1):123, 1990.

[180] S Ospelkaus, K.-K. Ni, D Wang, M H G de Miranda, B Neyenhuis, G Quéméner, P S Julienne, J L Bohn, D S Jin, and J Ye. Quantum-state controlled chemical reactions of ultracold potassium-rubidium molecules. *Science (New York, N.Y.)*, 327(5967):853–7, February 2010.

[181] Adelbert Owyoung, R. W Hellwarth, and Nicholas George. Intensity-Induced Changes in Optical Polarizations in Glasses. *Physical Review B*, 5(2):628–633, January 1972.

[182] R K Pathria. *Statistical Mechanics*. Butterworth-Heinemann, 1996.

[183] David Patterson and John M Doyle. Bright, guided molecular beam with hydrodynamic enhancement. *The Journal of Chemical Physics*, 126(15):154307, April 2007.

[184] David Patterson and John M. Doyle. Sensitive Chiral Analysis via Microwave Three-Wave Mixing. *Physical Review Letters*, 111(2):023008, July 2013.

[185] David Patterson, Julia Rasmussen, and John M Doyle. Intense atomic and molecular beams via neon buffer-gas cooling. *New Journal of Physics*, 11(5):055018, May 2009.

[186] David Patterson, Melanie Schnell, and John M. Doyle. Enantiomer-specific detection of chiral molecules via microwave spectroscopy. *Nature*, 497(7450):475–477, May 2013.

[187] David Patterson, Edem Tsikata, and John M Doyle. Cooling and collisions of large gas phase molecules. *Physical Chemistry Chemical Physics*, (April):9736–9741, 2010.

[188] J Paulovic, T Nakajima, and K Hirao. Third-order Douglas–Kroll ab initio model potential for actinide elements. *J. Chem. Phys.*, 117:3597, 2002.

[189] J Paulovic, T Nakajima, K Hirao, R Lindh, and P A Malmqvist. Relativistic and correlated calculations on the ground and excited states of ThO. *J. Chem. Phys.*, 119(2):798–805, 2003.

[190] H Pauly. *Atom, Molecule, and Cluster Beams I*. Springer, 2000.

[191] J Petricka. *A New Cold Molecule Source: The Buffer Gas Cooled Molecular Beam*. PhD thesis, Yale University, 2007.

[192] M A Player and P G H Sandars. An experiment to search for an electric dipole moment in the $^3P_2$ metastable state of xenon. *J. Phys. B*, 3:1620–1635, 1970.

[193] S. G. Porsev, M. S. Safronova, and M. G. Kozlov. Electric Dipole Moment Enhancement Factor of Thallium. *Physical Review Letters*, 108(17):173001, April 2012.

[194] M E Pospelov and I B Khriplovich. Electric Dipole Moment of the W boson and the Electron in the Kobayashi-Maskawa Model. *Yad. Fiz.*, 53:1030–1033, 1991.

[195] Maxim Pospelov and Adam Ritz. Electric dipole moments as probes of new physics. *Ann. Phys.*, 318(1):119–169, July 2005.

[196] Maxim Pospelov and Adam Ritz. CKM benchmarks for electron EDM experiments. *arXiv:1311.5537*, November 2013.

[197] William H Press, Saul A. Teukolsky, William T. Vetterling, and Brian P. Flannery. *Numerical Recipes*. Cambridge University Press, 3rd edition, 2007.

[198] Chengbing Qin, Colan Linton, and Timothy C Steimle. Optical Zeeman spectroscopy of the (0,0) $B^4\Gamma - X^4\Phi$ band systems of titanium monohydride, TiH, and titanium monodeuteride, TiD. *The Journal of chemical physics*, 137(7):074301, August 2012.

[199] P Rabl, D DeMille, J M Doyle, M D Lukin, R J Schoelkopf, and P Zoller. Hybrid Quantum Processors: Molecular Ensembles as Quantum Memory for Solid State Circuits. *Phys. Rev. Lett.*, 97:33003, 2006.

[200] David Rahmlow. *Towards a measurement of parity nonconservation in diatomic molecules*. PhD thesis, Yale University, 2010.

[201] Norman Ramsey. *Molecular beams*. Oxford University Press, 1985.

[202] B. Regan, Eugene Commins, Christian Schmidt, and David DeMille. New Limit on the Electron Electric Dipole Moment. *Physical Review Letters*, 88(7):18–21, February 2002.

[203] John A Rice. *Mathematical Statistics and Data Analysis*. Cengage Learning, 2006.

[204] T Rosenband, D B Hume, P O Schmidt, C W Chou, A Brusch, L Lorini, W H Oskay, R E Drullinger, T M Fortier, J E Stalnaker, S A Diddams, W C Swann, N R Newbury, W M Itano, D J Wineland, and J C Bergquist. Frequency ratio of Al$^+$ and Hg$^+$ single-ion optical clocks. *Science*, 319(5871):1808–12, March 2008.

[205] B. R. Rowe, G. Dupeyrat, J. B. Marquette, and P. Gaucherel. Study of the reactions $N_2^+ + 2N_2 \rightarrow N_4^+ + N_2$ and $O_2^+ + 2O_2 \rightarrow O_4^+ + O_2$ from 20 to 160 K by the CRESU technique. *The Journal of Chemical Physics*, 80(10):4915, 1984.

[206] Robert G. Sachs. *The Physics of Time Reversal*. University of Chicago Press, 1987.

[207] A. D. Sakharov. Violation of CP Invariance, C Asymmetry, and Baryon Asymmetry of the Universe. *JETP Lett.*, 5:27–30, 1967.

[208] Bahaa E. A. Saleh and Malvin Carl Teich. *Fundamentals of Photonics*. Wiley-Interscience, 2nd edition, 2007.

[209] P G H Sandars. The Electric Dipole Moment of an Atom. *Physics Letters*, 14(3):194, February 1965.

[210] Stephan P.A. Sauer. A relation between the rotational g-factor and the electric dipole moment of a diatomic molecule. *Chemical Physics Letters*, 297(5-6):475–483, December 1998.

[211] Brian C Sawyer, Benjamin K Stuhl, Mark Yeo, Timur V Tscherbul, Matthew T Hummon, Yong Xia, J Klos, David Patterson, John M Doyle, Jun Ye, and Jacek Kos. Cold heteromolecular dipolar collisions. *Physical chemistry chemical physics*, 13(42):19059, September 2011.

[212] Aert Schadee. On the Zeeman effect in electronic transitions of diatomic molecules. *Journal of Quantitative Spectroscopy and Radiative Transfer*, 19(5):517–531, May 1978.

[213] L I Schiff. Measurability of Nuclear Electric Dipole Moments. *Physical Review*, 132(5):2194, 1963.

[214] Melanie Schnell and Gerard Meijer. Cold Molecules: Preparation, Applications, and Challenges. *Angew. Chem. Int. Ed.*, 48:6010, 2009.

[215] Schott Inc. Schott Borofloat Glass Product Information. Technical Report 502.

[216] Schott Inc. Optical Glass Datasheets. Technical report, 2013.

[217] G Scoles. *Atomic and molecular beam methods*. Oxford University Press, 1988.

[218] E S Shuman, J F Barry, and D Demille. Laser cooling of a diatomic molecule. *Nature*, 467(7317):820–823, September 2010.

[219] E S Shuman, J F Barry, D R Glenn, and D DeMille. Radiative Force from Optical Cycling on a Diatomic Molecule. *Phys. Rev. Lett.*, 103(22):223001, 2009.

[220] Jonathan Simon, Waseem S Bakr, Ruichao Ma, M Eric Tai, Philipp M Preiss, and Markus Greiner. Quantum simulation of antiferromagnetic spin chains in an optical lattice. *Nature*, 472(7343):307–12, April 2011.

[221] Vijay Singh, Kyle S. Hardman, Naima Tariq, Mei-Ju Lu, Aja Ellis, Muir J. Morrison, and Jonathan D. Weinstein. Chemical Reactions of Atomic Lithium and Molecular Calcium Monohydride at 1 K. *Physical Review Letters*, 108(20):203201, May 2012.

[222] S M Skoff, R J Hendricks, C D J Sinclair, J J Hudson, D M Segal, B E Sauer, E A Hinds, and M R Tarbutt. Diffusion, thermalization, and optical pumping of YbF molecules in a cold buffer-gas cell. *Physical Review A*, 83(2):23418, February 2011.

[223] Sarah Margaretha Skoff. *Buffer gas cooling of YbF molecules*. PhD thesis, Imperial College London, 2011.

[224] L V Skripnikov, A N Petrov, and A V Titov. Communication: theoretical study of ThO for the electron electric dipole moment search. *The Journal of chemical physics*, 139(22):221103, December 2013.

[225] Neal Solmeyer, Kunyan Zhu, and David S Weiss. Note: mounting ultra-high vacuum windows with low stress-induced birefringence. *The Review of scientific instruments*, 82(6):066105, June 2011.

[226] Christian Sommer, Laurens D van Buuren, Michael Motsch, Sebastian Pohle, Josef Bayerl, Pepijn W H Pinkse, and Gerhard Rempe. Continuous guided beams of slow and internally cold polar molecules. *Faraday Discussions*, 142:203, 2009.

[227] Y Sone. *Molecular gas dynamics*. Birkhauser, Boston, 2007.

[228] Russell Stutz and Eric Cornell. Search for the electron EDM using trapped molecular ions. *Bulletin of the American Physical Society*, 89:76, 2004.

[229] O P Sushkov, V V Flarnbaurn, and V V Flambaum. Parity breaking effects in diatomic molecules. *Sov. Phys. JETP*, 48(4):608–611, 1978.

[230] M R Tarbutt, J J Hudson, B E Sauer, and E A Hinds. *Preparation and Manipulation of Molecules for Fundamental Physics Tests*, chapter 15, page 555. CRC Press, 2009.

[231] M R Tarbutt, J J Hudson, B E Sauer, E A Hinds, V A Ryzhov, V L Ryabov, and V F Ezhov. A jet beam source of cold YbF radicals. *J. Phys. B*, 35(24):5013–5022, 2002.

[232] J R Taylor. *An Introduction to Error Analysis*. University Science Books, 2nd edition, 1996.

[233] S. Truppe, R. J. Hendricks, E. A. Hinds, and M. R. Tarbutt. Measurement of the Lowest Millimeter-Wave Transition Frequency of the CH Radical. *The Astrophysical Journal*, 780(1):71, January 2014.

[234] S Truppe, R J Hendricks, S K Tokunaga, H J Lewandowski, M G Kozlov, Christian Henkel, E A Hinds, and M R Tarbutt. A search for varying fundamental constants using hertz-level frequency measurements of cold CH molecules. *Nature communications*, 4:2600, January 2013.

[235] K Tsigutkin, D Dounas-Frazer, A. Family, J Stalnaker, V Yashchuk, and D Budker. Observation of a Large Atomic Parity Violation Effect in Ytterbium. *Phys. Rev. Lett.*, 103(7):71601, August 2009.

[236] Ming-Feng Tu, Jia-Jung Ho, Chih-Chiang Hsieh, and Ying-Cheng Chen. Intense SrF radical beam for molecular cooling experiments. *The Review of scientific instruments*, 80(11):113111, November 2009.

[237] L. D van Buuren, C. Sommer, M. Motsch, S. Pohle, M. Schenk, J. Bayerl, P. W H Pinkse, and G. Rempe. Electrostatic Extraction of Cold Molecules from a Cryogenic Reservoir. *Physical Review Letters*, 102(3):033001, January 2009.

[238] S Y T van de Meerakker, H L Bethlem, and G Meijer. *Slowing, Trapping, and Storing of Polar Molecules by Means of Electric Fields*, chapter 14, page 509. CRC Press, 2009.

[239] L. Veseth. Theory of high-precision Zeeman effect in diatomic molecules. *Journal of Molecular Spectroscopy*, 63(2):180–192, November 1976.

[240] Wilton L Virgo, Timothy C Steimle, and John M Brown. Optical Zeeman Spectroscopy of the (0, 0) Bands of the $B^3\Pi - X^3\Delta$ and $A^3\Phi - X^3\Delta$ Transitions of Titanium Monoxide, TiO. *The Astrophysical Journal*, 628(1):567–573, July 2005.

[241] T Von Kármán and T Von Karman. *From Low-Speed Aerodynamics to Astronautics*. Pergamon Press, 1963.

[242] A C Vutha. *A search for the electric dipole moment of the electron using thorium monoxide*. PhD thesis, Yale University, 2011.

[243] A C Vutha, W C Campbell, Y V Gurevich, N R Hutzler, M Parsons, D Patterson, E Petrik, B Spaun, J M Doyle, G Gabrielse, and D DeMille. Search for the electric dipole moment of the electron with thorium monoxide. *Journal of Physics B: Atomic, Molecular and Optical Physics*, 43(7):74007, April 2010.

[244] A. C. Vutha, B. Spaun, Y. V. Gurevich, N. R. Hutzler, E. Kirilov, J. M. Doyle, G. Gabrielse, and D. DeMille. Magnetic and electric dipole moments of the $H^3\Delta_1$ state in ThO. *Physical Review A*, 84(3):034502, September 2011.

[245] Amar Vutha and David DeMille. Geometric phases without geometry. *arXiv:0907.5116*, July 2009.

[246] Fang Wang, Anh Le, Timothy C Steimle, and Michael C Heaven. Communication : The permanent electric dipole moment of thorium monoxide , ThO. *Journal of Chemical Physics*, (134):31102, 2011.

[247] Fang Wang and Timothy C Steimle. Optical Zeeman spectroscopy of the [17.6]2-$X^3\Delta_1$(1,0) band system of tungsten monocarbide, WC. *The Journal of chemical physics*, 135(10):104313, September 2011.

[248] Y Watanabe and O Matsuoka. All-electron Dirac–Fock–Roothaan calculations for the ThO molecule. *J. Chem. Phys.*, 107(9):3738–3739, 1997.

[249] Jonathan D Weinstein, Robert DeCarvalho, Thierry Guillet, Bretislav Friedrich, and John M Doyle. Magnetic trapping of calcium monohydride molecules at milliKelvin temperatures. *Nature*, 395(June):148–150, 1998.

[250] T Wentink and R J Spindler. The isoelectronic series ScF through ThO, I notes on the band spectra of TiO, HfO and ThO. *Journal of Quantitative Spectroscopy and Radiative Transfer*, 12(11):1569–1590, November 1972.

[251] C S Wood, S C Bennett, D Cho, B P Masterson, J L Roberts, C E Tanner, and C E Wieman. Measurement of Parity Nonconservation and an Anapole Moment in Cesium. *Science*, 275:1759–1763, 1997.

[252] C S Wu. Experimental Test of Parity Conservation in Beta Decay, February 1957.

[253] Bo Yan, Steven A. Moses, Bryce Gadway, Jacob P. Covey, Kaden R. A. Hazzard, Ana Maria Rey, Deborah S Jin, and Jun Ye. Observation of dipolar spin-exchange interactions with lattice-confined polar molecules. *Nature*, 501(7468):521–5, September 2013.

[254] Derek York, Norman M. Evensen, Margarita Lopez Martnez, and Jonas De Basabe Delgado. Unified equations for the slope, intercept, and standard errors of the best straight line. *American Journal of Physics*, 72(3):367, 2004.

[255] R Zare. *Angular Momentum*. Wiley-Interscience, 1991.

[256] Y B Zel'dovich. Electromagnetic interaction with parity violation. *Sov. Phys. JETP*, 33(6):1184, 1957.

[257] K Zhang, A R Forouhi, and I Bloomer. Accurate and rapid determination of thickness, n and k spectra, and resistivity of indiumtinoxide films. *Journal of Vacuum Science and Technology A*, 17(4):1843, 1999.

[258] M W Zwierlein, J R Abo-Shaeer, A Schirotzek, C H Schunck, and W Ketterle. Vortices and superfluidity in a strongly interacting Fermi gas. *Nature*, 435:1047, 2005.